ΠΑΝΕΠΙΣΤΗΜΙΟ ΚΡΗΤΗΣ

ΣΧΟΛΗ ΘΕΤΙΚΩΝ ΚΑΙ ΤΕΧΝΟΛΟΓΙΚΩΝ ΕΠΙΣΤΗΜΩΝ

ΤΟΜΕΑΣ ΦΥΣΙΚΗΣ

Διερεύνηση της σύλληψης ηλεκτρονίου σε κρούσεις ταχέων C^{4+} (1s2s ^{3}S) ιόντων με αέριους στόχους, χρησιμοποιώντας τη διάταξη φασματοσκοπίας Auger ηλεκτρονίων ιόντων στις 0° που κατασκευάστηκε με τη γραμμή L45 στον 5.5 MV tandem επιταχυντή του ΕΚΕΦΕ ¨Δημόκριτος¨.

Διδακτορική Διατριβή

του

Ιωάννη Μαδέση

που υποβάλλεται σε μερική εκπλήρωση των απαιτήσεων για τον τίτλο

ΔΙΔΑΚΤΩΡ

του Τμήματος Φυσικής του Πανεπιστημίου Κρήτης

Επιβλέπων: Θεόδωρος Τζούρος
Καθηγητής - Πανεπιστήμιο Κρήτης

Αθήνα
3/Φεβ/2021

UNIVERSITY OF CRETE

SCHOOL OF SCIENCES
AND ENGINEERING

DEPARTMENT OF PHYSICS

Investigation of electron capture in swift C^{4+} ($1s2s\,^3S$) collisions with gas targets using a zero-degree Auger projectile spectroscopy apparatus built with the L45 beam line at the "Demokritos" 5.5MV tandem accelerator.

Doctoral Thesis

of

Ioannis Madesis

submitted in partial fulfillment of the requirements for the degree of

Doctor of Philosophy

of the Department of Physics of the University of Crete

Supervisor: T.J.M. Zouros
Professor - University of Crete

Athens
3/Feb/2021

UNIVERSITY OF CRETE

SCHOOL OF SCIENCES
AND ENGINEERING

DEPARTMENT OF PHYSICS

Investigation of electron capture in swift C^{4+} $(1s2s\,{}^3S)$ collisions with gas targets using a zero-degree Auger projectile spectroscopy apparatus built with the L45 beam line at the "Demokritos" 5.5MV tandem accelerator.

Doctoral Thesis

of

Ioannis Madesis

Supervisor: T.J.M. Zouros
Professor - University of Crete

Approved by the seven-member committee

(signature)	(signature)	(signature)
. . . .	. . . .	. . . .
T.J.M. Zouros	E.P. Benis	S. Harissopulos
Professor	Assistant Professor	Director of Research
University of Crete	University of Ioannina	NCSR Demokritos

(signature)	(signature)	(signature)
. . . .	. . . .	. . . .
I. Kominis	T.P. Rakitzis	D. Charalambidis
Assistant Professor	Professor	Professor
University of Crete	University of Crete	University of Crete

(signature)

. . . .
A. Dubois
Professor
Sorbonne Université, CNRS

Athens
3/Feb/2021

Acknowledgments

[...] The examples are numerous, where what he found was quite different from what was expected, but this is also part of *the fun of doing Science*, because sometimes, a bigger surprise was just waiting to be discovered. "Try to anticipate, but never think that you know everything!", in other words, it is not because you imagine numerous obstacles that you should not go and look at unexplored situations. *Science is done by humans*[...] [1].

Support

Contents

List of Figures

List of Tables

xiv

Abstract

This thesis focuses primarily on the investigation of the collision process:

$$C^{4+}(1s2s\ ^3S) + T \rightarrow C^{3+}(1s2s2p\ ^4P,\ ^2P_\pm) + T^+$$
$$\hookrightarrow C^{4+}(1s^2) + e_A\text{'}$$
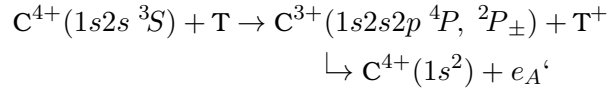
in which a highly-charged (He-like) beam of C^{4+} ions in the long-lived metastable state $(1s2s\ ^3S)$ energetically collide with gas targets (He, H_2). In the collision an electron from the target is captured by the $2p$ orbital of the carbon ion (a process known as electron transfer) in the process giving rise to the production of Li-like doubly-excited states $1s2s2p\ ^4P$ (a spin quartet), $1s(2s2p\ ^3P)\ ^2P_-$ (for short as $^2P_-$) and $1s(2s2p\ ^1P)\ ^2P_+$ (for short as $^2P_+$), both spin doublets, as well as many other levels to be discussed later. This collision process can be readily investigated experimentally since the initial, $1s2s\ ^3S$, ionic core is metastable[1] and therefore naturally found mixed-in with the $1s^2$ ground state ions as provided by accelerators.

One of the main interests in the aforementioned process has to do with the question of whether the similarly configured $1s2s2p\ ^4P$ and $^2P_\pm$ states are populated in the collision according to spin statistics, i.e. in the ratio R of their spin degeneracies of quartets to doublets. The concept of spin statistics is of fundamental interest since most collision processes are assumed to obey spin statistics. In fact, the above process was found not to obey spin statistics as first exposed in 2004 [2,3] for fluorine He-like ions (F^{7+}) leading to controversial claims and results [4–6]. In this thesis, the Single Differential Cross-Section (SDCS), $d\sigma(\theta)/d\Omega$, is determined for each of these $1s2s2p$ produced levels using the high resolution projectile Auger electron spectroscopy technique known as Zero-degree Auger Projectile Spectroscopy (ZAPS), i.e. where the emitted projectile Auger electron e_A is observed at the angle of $\theta = 0°$ with respect to the beam direction.

Towards this purpose, a new, dedicated beam line (L45), together with a unique, state-of-the-art ZAPS experimental setup was built from scratch, at the only heavy ion research accelerator in Greece, the 5.5 MV tandem Van de Graaff accelerator (for short tandem), operated since 1972 by the INPP of the NCSR, in Athens. Furthermore, this new Atomic Physics initiative involved non-trivial changes to the existing hardware and mode of operation of the tandem accelerator itself, used primarily for Nuclear Physics investigations involving mostly proton beams.

Experimental results utilizing the ZAPS technique, regarding relative populations of quartet and doublet states were found to be in agreement with earlier corrected measurements [6]. At the same time, *ab initio* dynamical calculations have been performed by the theory group of Prof. Alain Dubois - UPMC-Sorbone and CNRS Paris, involving for the first time *three* active electrons. These results, presented in Ref. [7], resolve the previously existing disagreement between theory and experiment and draw attention to the limited predictive power of the frozen core approximation as regards to spin statistics in highly correlated dynamical atomic systems.

---

[1] With ms lifetime, a long enough time to make it down to the target chamber

Περίληψη

Η παρούσα διατριβή εστιάζει ως επί το πλείστον στην μελέτη της παρακάτω διεργασίας κρούσης:

$$C^{4+}(1s2s\,{}^3S) + T \rightarrow C^{3+}(1s2s2p\,{}^4P,\,{}^2P_{\pm}) + T^+$$
$$\hookrightarrow C^{4+}(1s^2) + e_A$$
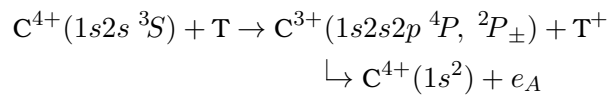
κατά την οποία μια υψηλά φορτισμένη δέσμη ηλιοειδών ιόντων C^{4+} στη μακρόβια, μετασταθή κατάσταση $1s2s\,{}^3S$ συγκρούεται με αέριους στόχους (He, H_2). Κατά τη κρούση αυτή, ένα ηλεκτρόνιο από τον στόχο δεσμεύεται στο $2p$ τροχιακό του ιόντος άνθρακα (ένας μηχανισμός γνωστός ως σύλληψη/ηλεκτρονίου), οδηγώντας στην παραγωγή των διπλά διεγερμένων λιθιοειδών καταστάσεων $1s2s2p\,{}^4P$ (quartet), $1s(2s2p\,{}^3P)\,{}^2P_-$ (εν συντομία $^2P_-$) και $1s(2s2p\,{}^1P)\,{}^2P_+$ (εν συντομία $^2P_+$), (doublets), μεταξύ άλλων που θα συζητηθούν μετέπειτα στο κείμενο. Αυτή η διεργασία κρούσης μπορεί εύκολα να διερευνηθεί πειραματικά, καθώς ο αρχικός $1s2s\,{}^3S$, ιοντικός σχηματισμός είναι μετασταθής[2] και ως εκ τούτου, συνυπάρχει σε διάφορες αναλογίες με τα $1s^2$ ιόντα στη θεμελιώδη κατάσταση κατά τη παραγωγή της δέσμης από τον επιταχυντή.

Το βασικό ενδιαφέρον στη παραπάνω διεργασία έγκειται στο ερώτημα του αν οι καταστάσεις ^4P και $^2P_{\pm}$ με παρόμοια $1s2s2p$ ηλεκτρονιακή διάταξη εποικίζονται κατά την $2p$ σύλληψη σύμφωνα με τη στατιστική των σπιν, δηλαδή κατά τον λόγο R των εκφυλισμών των spin για την quartet προς τις doublets. Η έννοια της εποίκισης σύμφωνα με τη στατιστική των σπιν είναι βασικού ενδιαφέροντος, καθώς οι περισσότεροι μηχανισμοί κατά τη διάρκεια ατομικών κρούσεων θεωρείται ότι ακολουθούν αυτή τη στατιστική. Πιο συγκεκριμένα, έχει βρεθεί ότι στη παραπάνω διεργασία δεν ακολουθεί αυτή τη στατιστική, όπως πρωτοπαρουσιάστηκε το 2004 [2, 3] για ηλιοειδή ιόντα φθορίου (F^{7+}) οδηγώντας σε αμφιλεγόμενα συμπεράσματα [4–6]. Σε αυτή τη διατριβή, οι διαφορικές ενεργείς διατομές $d\sigma(\theta)/d\Omega$ προσδιορίζονται για κάθε ένα από τα παραγόμενα $1s2s2p$ επίπεδα, χρησιμοποιώντας την υψηλής διακριτικής ικανότητας φασματογραφία Auger ηλεκτρονίων ιόντων δέσμης γνωστή ως ZAPS, όπου το παραγώμενο Auger ηλεκτρόνιο e_A μετράται στις $\theta = 0°$ σε σχέση με τη κατεύθυνση της δέσμης.

Προς αυτό το σκοπό, μια νέα πειραματική γραμμη (L45), μαζί με μια μοναδική, υπερσύγχρονη πειραματική εγκατάσταση δημιουργήθηκε από το μηδέν, στον μοναδικό ερευνητικό επιταχυντή βαρέων ιόντων στην Ελλάδα, τον 5.5 MV tandem Van ded Graaff επιταχυντή (για συντομία tandem), που λειτουργεί από το 1972 στο Ινστιτούτο Πυρηνικής και Σωματιδιακής Φυσικής του Εθνικού Κέντρου Έρευνας Φυσικών Επιστημών "ΔΗΜΟΚΡΙΤΟΣ", στην Αθήνα. Επιπλέον, αυτή η νέα πρωτοβουλία ατομικής φυσικής περιλαμβάνει ουσιώδεις αλλαγές στο υπάρχον υλικό και τρόπο λειτουργίας του επιταχυντή tandem, που χρησιμοποιείται κυρίως για πειράματα πυρηνικής φυσικής με τη πλειονότητα των πειραμάτων να αφορά τη χρήση δεσμών πρωτονίων.

---

[2]Έχοντας ms χρόνους ζωής, αρκετά μεγάλους, ώστε η δέσμη να φτάνει στο θάλαμο του στόχου

Τα πειραματικά αποτελέσματα, με τη χρήση της μεθόδου ZAPS, όσον αφορά τους σχετικούς πληθυσμούς των quartet και doublet καταστάσεων, είναι σε συμφωνία με παλιότερες, διορθωμένες μετρήσεις [6]. Ταυτόχρονα, έγιναν υπολογισμοί από *πρώτες αρχές* από την ομάδα θεωρητικών του καθ. Alain Dubois - UPMC-Sorbone και CNRS Paris, οι οποίοι περιλαμβάνουν για πρώτη φορά 3 ενεργά ηλεκτρόνια. Αυτά τα παρουσιασμένα [7] αποτελέσματα, επιλύουν την προϋπάρχουσα διαφωνία μεταξύ θεωρίας και πειράματος και εφιστούν την προσοχή στην περιορισμένη προγνωστική ισχύ της frozen core προσέγγισης όσον αφορά την spin στατιστική σε ιδιαιτέρως συσχετισμένα δυναμικά ατομικά συστήματα.

Λέξεις κλειδιά: ατομική φυσική με επιταχυντές, κρούσεις ιόντων ατόμων, υψηλά φορτισμένα ιόντα, διπλά διεγερμένες καταστάσεις, φασματοσκοπία Auger ηλεκτρονίων, φασματοσκοπία ηλεκτρονίων ιόντων δέσμης,φασματοσκοπία ηλεκτρονίων ιόντων δέσμης στις $0°$, σύλληψη ηλεκτρονίου (μονή μεταφορά ηλεκτρονίου), σπιν στατιστική, ιοντικές δέσμες μεικτών καταστάσεων, ηλιοειδή ιόντα, λιθιοειδή ιόντα, μακρόβιες (μετασταδείς) καταστάσεις, τροφοδοσία αλληλουχίας.

Chapter 1

Introduction

1.1 Ion-atom collisions and accelerator based atomic physics

The investigation of nuclear structure was one of the main goals behind the construction of the first heavy ion accelerators. It wasn't until the early 1960's, when tandem Van de Graaff accelerators were also first introduced to experimental Atomic Physics [8]. Spectroscopy measurements were typically performed on excited states of gaseous targets produced by photon excitation, high-energy electron [9] and light-ion impact excitation [10], restricted primarily by electric dipole selection rules. Alternatively, heavy-ion collisions with gas targets appeared to produce optically inaccessible states, in various degrees of ionization, resulting also in auto-ionizing states [11–13]. To this point in time, target spectroscopy had been limited mostly to gaseous monoatomic species such as noble gases or various self-supporting foil samples. This soon changed when vapour targets were also introduced, such as Mg [14, 15], Li [16] and Na [17]. However, the use of such vapour targets is cumbersome, as they are prone to pollution of vital instrumentation. Ion-induced X-ray and Auger spectroscopy [18] has been just one of the various experimental techniques developed after the introduction of accelerators to Atomic Physics.

It was soon realized that along with the target, the projectile photon and electron [19–23] emissions could also be measured. Compared to target spectroscopy, projectile spectroscopy expands the available options in atomic number, charge state and collision velocity. While the expansion of available ion species is a self-explanatory advantage, charge state selection can benefit in two ways: The first is that control of the number of projectile electrons carried into the collision allows for a more detailed study/isolation of processes such as Single Electron Capture (SEC), Double Electron Capture (DEC) and Transfer-Excitation (TE), amongst others. The second is that Multiply Charged Ions (MCI) stripped to one or two electrons can provide simplified isoelectronic atomic systems. There, the magnitude of Coulomb-governed interactions can be systematically investigated by varying the projectile atomic number Z_p in an isoelectronic series of projectile ions.

Highly-charged ion-atom collision investigations (i.e. ions with just a few electrons) provide a simpler, yet non trivial approach towards the understanding of fundamental atomic physics processes. Their understanding bears great significance towards the study of astrophysical [24, 25] and laboratory [25, 26] plasmas, or even hadron tumor therapy [27]. The ability to reproduce these processes in the lab and measure their cross sections has been invaluable towards the proper understanding of their underlying mechanisms. In particular, state-resolved x-ray [28] and Auger electron [29] measurements can provide the most stringent tests of this understanding.

As described above, there are various fields of research where the investigation of MCI collision processes are applicable. Perhaps the most characteristic area of research for

ion-atom, or in general MCI collisions, is thermonuclear fusion [30]. Within this field, ion atom collisions provide various techniques for the study and characterization of laboratory plasmas. Although the primary ingredients of fusion are most commonly deuterium and tritium, a variety of MCI may emerge within the plasma, due to the plasma - solid surface interaction with the walls of the reactor [30]. There is a variety of ways MCI interfere with the plasma. For example, it has been shown that charge transfer due to the existence of MCI is an important process [31], since it may affect plasma electron densities, thus, preventing break even conditions [32]. Moreover, the existence of high-Z ions within the plasma may affect Ohmic heating [33] required for the preservation of plasma. These effects are just two examples of MCI induced processes that require consideration within plasma modelling and demonstrate the need for experimental data of such processes.

However, ion-atom collisions are not the only field that employs accelerators in Atomic Physics. The incorporation of accelerators in Atomic Physics research has led to many new experimental applications. One of the most interesting is the interaction of high velocity ions with matter [34]. The applications of this experimental approach range from Resonant Coherent Excitation (RCE), a novel ion excitation method [35–37], to cancer tumor therapy using heavy (mostly proton or carbon) ion bombardment [38–40].

More recent applications of accelerator-based Atomic Physics include studying neutral atomic hydrogen collisions with applications in fusion research, for plasma density measurements, through Beam Emission Spectroscopy [41]. Also related to fusion research are collisional cross sections for partially/fully stripped Be ions, since Be is used as the armor material for the components facing the plasma [42]. Due to chemical and physical erosion of these components, an influx of Be ions into the plasma is expected [43]. The effect of erosion on these has been assessed both in simulation [44, 45], but also experimentally by means of Micro Ion Beam Analysis [46]

Another related research initiative, first proposed in 2015 is the Gamma Factory [47, 48] at Conseil Européen pour la Recherche Nucléaire (CERN). The basic setup consists of optical photons that are directed head-on or with a small angle onto a beam of ultra-relativistic ions. In the ion frame of reference, the photon frequency is boosted by the large relativistic γ factor of the ion beam, due to the Doppler effect in the frame of the ion. Considering that for highly-charged hydrogen-like ions with $40 < Z_p < 80$, the $1s - 2p_{3/2}$ transitions require energies >10 keV, this Doppler boost will enable laser spectroscopy of such high-Z_p ions. When these ultra-relativistic ions photon decay, the emitted radiation in the projectile frame is further boosted by an additional γ factor (now γ^2 relative to the initial radiation). Moreover, this photon emission is concentrated into a small solid angle in the direction of the ions' propagation. The two key points of this proposal are: a) the large excitation cross sections for the partially stripped ions will ensure a high flux of secondary photons, b) the energy of the secondary photons can be tuned to energies of up to 400 MeV, thus providing unique experimental advantages both for spectroscopic studies of such H- and Li-like heavy ions, as well as the production of γ-tunable high-energy photon beams.

Another interesting technique regarding accelerator based Atomic Physics is RCE [35–37]. In RCE, a highly charged (non bare) ion beam is channelled through a highly periodic material such as a crystal. As the ion traverses through the crystal lattice, it is periodically affected by the electric and magnetic field fluctuations of the lattice, in its rest frame. The frequency of these fluctuations are a function of the ion velocity, the lattice parameters and the collision angle. If this frequency matches the energy between two electronic energy levels of the channeled ion, then resonant excitation can be observed. This technique has also been used to produce high-Z_p singly excited states [49].

1.2 The 5.5 MV NCSR Demokritos tandem

The first Van der Graaff accelerator was completed in 1933, being the first MV accelerator utilizing the Van der Graaff generator [50]. The simplest description of such an accelerator would be a long insulating glass tube, with its one end placed inside a Van der Graaff generator, a highly charged metal shell (terminal), to which charged particles are accelerated as a result of the potential difference. The 1 MV DTM[1] was an open air accelerator, so the first major improvement was to place the charged terminal inside a pressurized tank with SF_6[2], thus allowing the terminal to reach much higher voltages.

The second major improvement was first proposed in 1936, but only developed in 1960 by the High Voltage Engineering Corporation [51]. This was the development of the "tandem" idea, i.e. a two-stage accelerator, where there are two stages of acceleration, one before and one after the terminal. A beam of initially negatively charged ions, produced in a negatively biased sputter source [52] is guided towards the positively charged terminal. This consists of the first acceleration stage. Once in the terminal, the negative ions are stripped of some of their electrons, thus converting them to positively charged ions which are now further accelerated by the same terminal voltage, in what constitutes the second acceleration stage. This geometry proved advantageous for proton acceleration, since it results in the doubling of the available kinetic energy [50]. This advantage is further extended when using highly-charged, heavier ions, resulting in higher energies for the same terminal voltage.

The result of electron stripping used in the tandem terminal is a complex process that depends on the projectile velocity, its atomic number Z_p and the stripping medium density, amongst others [53, 54]. The resulting ions are not uniformly charged, but their intensity follows a charge distribution that can be approximated by the use of semi-empirical formulas [55, 56], and can be readily calculated [57]. It should be noted that projectiles with higher Z_p usually require higher stripping velocities to obtain a high charge state in sufficient intensities. These variably charged positive ions are then guided through a bending[3], analyzing magnet, where their trajectories can be varied, based on their charge-to-mass ratio. The desired A^{q+} ions can then be selected by setting the analyzing magnetic field so as to allow the proper ions to go through a set of slits and further guided on to the experimental apparatus. An interesting phenomenon during stripping to He-like (two electron) ion beams is that these are not delivered in a pure $1s^2\,^1S$ ground state configuration. Instead, a metastable $1s2s\,^3S$ component, crucial to the measurements described in this thesis, is also produced. This pre-excited beam component can be an invaluable asset, particularly for Auger projectile spectroscopy, since it can lead to the formation of doubly-excited projectile states through direct, single step collision processes such as SEC. Such additional pre-excited, metastable beam components allow for the investigation of ion-atom collision processes where projectile ions now have an initial K-shell vacancy [58]. Benis *et al* [59, 60] were the first to observe that gas (rather than foil) stripping in the tandem accelerator terminal led to a much lower $1s2s\,^3S$ content beam, thus providing with the capability to vary this metastable content.

Towards better control of the He-like beams produced, both in terms of beam intensity and metastable $1s2s\,^3S$ content, three additional ion strippers were added to the INPPs tandem accelerator, at two different stripping points [61]. The first one is the Gas Terminal Stripper (GTS) within the terminal of the accelerator. This addition provides

---

[1]Named after the Department of Terrestial Magnetism of the Carnegie Institution for Science in Washington DC.

[2]A high voltage dielectric in gaseous form.

[3]Usually bent through $90°$.

for better control of the $1s2s\,^3S$ content mostly when sufficient currents can be achieved with the already existing Foil Terminal Stripper (FTS) [58]. In cases when the required charged state ion beam delivered from the terminal is too weak (usually at the lowest collision energies required), an additional stripping point after the analyzing magnet is used known as the post-stripper. Here, the ions have already been accelerated and are now at much higher velocities (than inside the terminal stripping point) and therefore the stripping process is much more effective in producing ions in high-charge states and higher intensities. Both a Foil Post Stripper (FPS) and a Gas Post Stripper (GPS) were constructed and implemented [61].

1.3 The process of electron capture

Charge transfer processes, i.e. the transfer of a target electron to the projectile, occurring in ion-atom and ion-ion collisions (also known as electron capture) belong to one of the most fundamental interactions.

$$A^{q+} + T \rightarrow A^{(q-1)+*}(nl) + T^+ \tag{1.1}$$
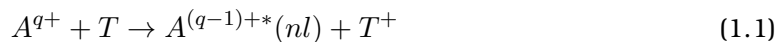
Cross sections in reaction 1.1 can be very large, so these processes play a significant role in Atomic Physics, Astrophysics, Plasma Physics, and Accelerator Physics. The actual cross sections of reaction 1.1 will vary depending on a number of factors. The most characteristic of these factors is the velocity of the projectile ion. At high velocities, beyond the intermediate regime (see next paragraph), the interaction time is short and one may therefore expect the cross sections for SEC to decrease as collision energy increases. This is partially true, and can be roughly described by Schlachter's universal empirical scaling rule for SEC [62]. However, charge transfer is affected by many more factors, including Z_T (the atomic number of the target), Z_p and the charge state q of the incoming ion, among others.

Towards more accurate descriptions of the processes involved, a number of methods/models have been developed. Before their short presentation, a description of the collision velocity regimes is helpful to model classification. Ion-atom collisions are typically divided into three not-so-distinct velocity regimes, characterized by the projectile velocity V_p compared to the classical orbiting velocity v_e of the active electron in its initial or final state. The three regimes are defined as the adiabatic or slow ($V_p \ll v_e$) regime, the intermediate ($V_p \approx v_e$) regime and the high-energy or fast ($V_p \gg v_e$) [63] regime. As a point of reference, the electron velocities of He (or H_2) are 3.73 mm/ns (3.35 mm/ns for H_2), 0.073 MeV/u (or 0.058 MeV/u) and 1.70 au (or 1.53 au) [64], while the projectile velocities of this thesis are in the range of 9.82-15.52 mm/ns (0.5-1.25 MeV/u or 4.49-7.09 au).

One of the first methods developed for charge transfer and ionization calculations was the Classical Trajectory Monte Carlo (CTMC) method [65], applicable in the intermediate energy regime. In CTMC the system under investigation is represented by a macroscopic classical model: The three-body motion Newton's equations for the electron and the protons are solved by numerical integration and examined statistically. Another theory for electron capture is the Classical Overbarrier Model [66–69], again valid mostly for intermediate velocities: The capture of the electron is achieved when the potential energy barrier between projectile and target equals the Stark-shifted ionization energy [70]. Although somehow simplified, it can predict n distributions (i.e. the probabilities for capture to different principal quantum numbers n), also known as "reaction window", for low and intermediate energies [71].

More contemporary approaches include the Two-Centre Basis Generator Method (TC-BGM) [72] and the Atomic Orbital Close Coupling (AOCC) [73], amongst others. The TC implementation of the BGM is similar to the AOCC [74]. In both approaches the Time-Dependent Schrödinger Equation (TDSE) is solved non-perturbatively in a semi-classical description of the collisional process. The trajectories of the cores are calculated classically, whereas the electrons are described in a fully quantum mechanical manner. Their differences lie primarily on the basis states onto which the solutions of the TDSE are projected. The AOCC description is mostly applicable somewhere between intermediate and fast collision velocity regime. It is based on the realization that the initial electron configuration is "fluid" during the collision, and that the electrons move between a certain number of configurations which form the "basis" states of that description [73]. On a final note regarding these type of calculations, the computer processing power they require for the numerical solution of the TDSE limits the number of active electrons carried into the collision. Thus, the inclusion of more than 2 active electrons was considered, until recently (2016), "beyond present capabilities" [75].

For the sake of simplicity, such calculations addressed primarily the simplest case of SEC to a bare projectile forming single-electron states. Experimentally, this type of collision process has been studied extensively by X-ray Spectroscopy [76, 77]. SEC to a bare projectile leads to various $nl\,^2L$ levels as predicted by the above methods, among others. Next, is the case of SEC to single-electron projectiles. Having final states that involve more than one electrons leads to the next level of sophistication for theories under development, that being the total spin $\mathbf{S}$ of the resulting configurations. Measurements of similar electron configurations with different spin $\mathbf{S}$ can determine whether spin statistics are obeyed or not, i.e. whether similar electron configurations are populated according to their spin degeneracies. In the case of single-electron projectiles, spin statistics appear to be obeyed, when considering SEC leading to the formation of two-electron singly excited states [78–80]. For example, SEC production of the similarly configured states of F^{7+} or Ar^{16+} ($1s2p\,^3P$) to ($1s2p\,^1P$) in collisions of F^{8+} and Ar^{17+} with He has been found to obey a 3:1 ratio.

When the projectile carries two or more *unpaired* electrons (also known as an open shell) into the collision, the SEC process becomes much more complex. The $1s2s\,^3S$ metastable state is an example of such a case. In recent TC-BGM calculations [81], this projectile state has been treated in the *frozen core* approximation. Here, due to the very short duration of fast collisions the projectile core electrons are assumed to be frozen, i.e. play a negligible role during the collision. A more recent approach to collisional systems carrying multiple electrons is Ref. [82], introducing a Time Dependent Density Functional Theory (TDDFT) method, where the interacting system may be mapped onto a system of noninteracting particles. Finally, in Ref. [7], where experimental results from this thesis were presented, a novel three electron Atomic Orbital Close-Coupling (3eAOCC) method [83, 84] was used involving, for the first time, three active electrons within a full configuration interaction approach.

As discussed earlier, the C^{4+} is produced in two components, the $1s^2\,^1S$ component, and the pre-excited, long-lived [85] $1s2s\,^3S$ component that exhibits many interesting features [86]. SEC to pre-excited He-like ion beams provide a direct way to create doubly-excited, Auger-decaying states. Moreover, according to the famous book "A Negative Ion Cookbook" by Roy Middleton [87] the inventor of the negative ion sputter source used predominantly in tandem accelerators, carbon is the most intense ion beam produced amongst all available low-Z_p elements. On a final note, as Z_p decreases, *cascade* effects (described in the next sections) complicating the interpretation of the spin statistics ratio R are expected to decrease.

The earliest experimental study of electron capture to the C^{4+} ion found in the literature, was conducted by Zwally *et al* (1970) [88] for collision energies between 400 eV and 40 keV. The decade following, the C^{4+} + gas collision system was studied, in terms of total capture by post-collision charge-state analysis. The most characteristic experimental work is from the group of Crandall (1976-79) [89–92], using magnetic charge state separation. Another interesting experimental technique was used by Goldhar *et al* [93]: the flight time[4] of the ions varied depending on their charge by applying a positive voltage. Along with the experimental work, theoretical models were also developed (1976-78) [94–96] to describe SEC as a function of the collision energy. Almost all of them report results for collision energies less than 50 keV, addressing the slow to intermediate energy regime [97, 98].

Regarding the C^{4+} + gas collision system, the work of Bruch *et al* (1982) [99] contained two novelties. First, by using Extreme Ultra-Violet (EUV) spectroscopy, they were able to determine *state selective nl* electron capture cross sections. Additionally, they report results for 2, 3 and 5 MeV collision energies, far higher than previous studies for C^{4+}. In the low energy regime, other experimental state selective studies for the C^{4+} + gas system are [100–102] (1983-84) using X-ray Spectroscopy. An interesting feature in the work of Dijkkamp *et al* (1984) [102], is that the $1s2s\,^3S$ metastable component was mentioned for the first time and considered to be negligible. Their work, also presented in Refs. [103, 104], provides a wide range of *subshell* state selective cross sections for projectile velocities ranging between 0.1-0.5 a.u. (0.25-6.25 keV/u). Again, theoretical approaches to state selective transfer were also developed (1984) [105, 106] with the C^{4+} + He becoming a benchmark system for such theoretical studies.

Auger projectile electron spectroscopy using a Cylindrical Mirror Analyzer (CMA) was employed by Dillingham *et al* (1984) [107], the second carbon-related reference regarding fast collisions. They recognised the existence of a $1s2s\,^3S$ metastable component in He-like ions, and attributed it to the observed doubly-excited states formed in collisions of He-like fluorine. What is really interesting and complicates further analysis in the presented spectra is the questionable determination of the $1s2s2p\,^4P$ line due to blending with the $1s2s^2\,^2S$ line. Additionally, some lines are attributed to quartets, which is highly improbable in mind of their rather low Auger rates [108]. Reported metastable fractions found in their ion beam seem to agree with similar much later reported measurements [109]. Back to slow collisions, Ref. [110] (1985) also examines the $1s2s\,^3S$ contributions, where the formation of doubly-excited doublets and quartets and their expected behaviour is predicted. They seem to clearly recognize that while the $1s2snl\,^2L$ doublets auto-ionize promptly after formation, the $1s2snl\,^4L$ quartets decay through cascades of fast, allowed optical transitions, thus effectively cascade feeding the lowest doubly-excited quartet state ^4P, a central topic in this thesis. This is very similar to the selective cascade feeding of the $1s2s2p\,^4P$ state also independently identified by Zouros *et al* [5] (2008) as an important mechanism complicating the analysis of spin statistics as expressed in the ratio R of $1s2s2p$ quartets to doublets in He-like fluorine. Finally, Niehaus [111] and Mack [67–69] should be taken into consideration and their CMA Spectroscopy studies regarding the C^{4+} + gas collision system and slow collisions. In these studies, the Classical Over-barrier Model [66] for theoretical calculations is applied.

---

[4]Pulsed beam.

1.4 Projectile electron spectroscopy and ZAPS

Measuring electron emission from a projectile ion introduces a variety of kinematic effects[5]. Such effects as line *broadening* and line *shifting* result from the vector addition of the projectile velocity V_p to the velocity of the emitted electron. Additionally, foil induced projectile Auger electrons suffer additional line broadening due to the straggling of the ion beam in the foil. The ejected electrons come from ions and atoms that do not have a uniquely defined velocity, but follow a normal distribution [112]. This distribution in ion velocities is then transferred to the velocities of the ejected projectile electrons. Moreover, using foil-excitation, multiple charge states are generated [113], resulting in multiple lines observed leading to line blending, making spectra interpretation difficult [114]. This problem was solved with the use of gas targets [93, 115]. By adjusting the gas target pressure *single collision* conditions could be assured. However, the problem of kinematic line broadening remained and occupied various research groups [116, 117]. It was clear that reducing the electron observation angle θ (with respect to the beam direction) to zero, kinematic line broadening effects could be reduced. It should be mentioned that zero degree electron spectroscopy already existed for cusp[6] electrons since 1970 [118], but without the sufficient line resolution, which was not of importance at the time. In fact, the very first ZAPS measurement was taken accidentally by Lucas *et al* [119] while investigating cusp electrons. Concerning projectile spectroscopy, the Aarhus university group achieved the smallest non-zero observation angle of $\theta = 6.4°$ [9], an improvement over their previous $\theta = 15°$ [120, 121], with enough energy resolution to be able to clearly resolve the different $1s2l2l'$ terms. However, at these non-zero observation angles this resolution could only be attained at the cost of much smaller spectrometer acceptance angles $\Delta\theta$. Clearly, placing a spectrometer in-line with the ion beam (i.e. at $\theta = 0°$) would required additional instrumental considerations.
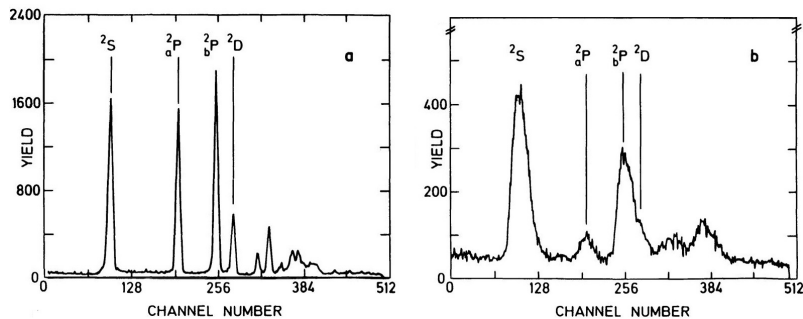
Figure 1.1: Lithium projectile Auger electron spectra for 250 keV Li$^+$ + He collisions, recorded at (a) θ=5° and (b) θ=60°. Line broadening (kinematic broadening) is seen to be substantially reduced as the observation angle θ is decreased from 60° to 5°. The lines designated $_a^2$P and $_b^2$P refer to the lines $^2P_-$ and $^2P_+$ of this thesis. From Bisgaard *et al* [122] (1981).

In Fig. 1.1 [122], the kinematic broadening effect is demonstrated. It presents KLL spectra obtained from 250 keV He-like Li ions on He, similar to the ones studied in the present thesis. Regarding observation at θ=5°, the spectral lines are distinct, maintaining a sufficiently clear structure almost to the end of the spectrum. However, an increase to θ=60° for the observation angle results in extensive overlap. The $_b^2P$ and ^2D lines are now indistinct, while higher energy line structure has been reduced. Assuming normalized

---

[5]The kinematic effects discussed here are presented in Ch. 4.
[6]Electrons isotachic to the beam.

spectra, a comparison can also be made of the intensity of the spectral lines. Comparing the intensities of the ^2S line, it can be assumed that at $\theta=60°$ the measured width of the peak has quadrupled. Between the Auger energies of the ^2S and ^2_aP lines lies the ^4P_J metastable level which is seen to be entirely missing in this spectrum. Since the lifetimes of the various J components for the Li ion are between 0.112 and 6.397 μs [123], such a metastable state decays long after its production in the gas-cell and well outside the observation window of the spectrometer.

It seems, the first who incorporated in-line spectroscopy was Morgenstern in 1976 [124, 125], with the observation angle set to $\theta = 180°$. Although kinematic broadening is minimized, there are other kinematic considerations that limit the spectroscopy at this backward angle. For example, in the measurements of Morgenstern [124], for projectile energies greater than 242 keV (or 60.5 keV/u), electrons can no longer be ejected backwards in the laboratory frame (i.e. at $\theta = 180°$). Even before reaching this limit, the resulting very low energy electrons will be prone to various types of interferences (magnetic fields, power-supply ripple). Although this approach minimized kinematic broadening, it was not universally applicable, and was limited to the keV/u energy regime.

The first ZAPS spectrometer was implemented by Itoh and Stolterfoht in 1983 [126]. They used two consecutive 90° Parallel Plate Analyzers (PPAs) in tandem [114]. The first Parallel Plate Analyzer (PPA), functioned as a deflector, to steer the electrons out of the ion beam path, also suppressing secondary electrons. Additionally, the first PPA had oversized slits for the unobstructed passage of the ion beam. Before entering the second PPA, the electrons were decelerated by a retarding electric field, which further dramatically improved the energy resolution [127]. This was a very nice and important feature of this tandem PPA. Finally, it should be underlined that forward emitted electron observation is only limited by the electrostatic spectrometer's high voltage tolerance (most electrostatic spectrometers are typically rated to $\approx$5 kV).

In 1981, Tanis *et al*, while studying projectile X-rays in coincidence with charged exchanged ions, discovered Resonant Transfer-Excitation (RTE),[7] a new transfer-excitation mechanism. RTE involves the transfer of a target electron to the projectile ion, along with the simultaneous excitation of another projectile electron, resulting in a doubly-excited projectile state [128, 129]. RTE resembles the electron impact phenomenon of dielectronic recombination, only in the case of RTE the impinging electron is lightly bound to the target. Soon after, the theory of RTE as part of the more general TE mechanisms, was formulated [130–132]. Itoh *et al* demonstrated [133] the superiority of ZAPS in such studies, especially in the low-Z_p regime, where the high Auger yields become particularly advantageous over competing X-ray deexcitation. Their ZAPS spectrometer had sufficient resolution to provide the first state-selective observations of TE, attracting considerable attention. Following, Swenson *et al* [134] performed the first state-selective RTE measurements for the O^{5+} + He collision system using the same ZAPS tandem PPA. At this point, the ZAPS technique, promoted by N. Stolterfoht and his group at HMI-Berlin and later by P. Richard and T.J.M. Zouros in Kansas State University, became widely accepted and was adopted by various research groups worldwide. Some indicative work from this era can be found in Refs. [29, 135–150].

ZAPS is the experimental method used in this thesis. In ZAPS, Auger electrons emitted from a moving projectile at $\theta = 0°$ with respect to the ion beam, are analyzed and recorded. The main advantage of the technique is that at this detection angle kinematic line broadening of emitted electrons is minimized. ZAPS is particularly advantageous for low Z_p ions where Auger yields approach unity and can provide *state selective* cross section information about collision mechanisms stringently testing theory. Additionally, at

---

[7]More details in Subsec. 2.2.2.1, on p. 19.

$\theta = 0°$ observation, kinematic *stretching* of the electron spectrum, makes even weaker line structures easier to identify. Regarding applicability, ZAPS has focused primarily on investigations of collision mechanisms involving low-Z_p projectile ions. As Z_p increases, the Auger yield is reduced [151] with x-ray spectroscopy eventually becoming more efficient, and the preferred experimental tool.

Another crucial advantage of the ZAPS technique concerns the detection of various high-spin, metastable states. Such metastable states, instead of Auger decaying promptly[8] within the gas target region, may decay well beyond this region. Depending on the projectile Z_p, the lifetimes of the various J components of these long-lived metastable states can vary. In the case of carbon, the lifetimes of the $1s2s2p\,^4P_J$ states under investigation vary from 2-120 ns [123, 152]. Therefore, considering the projectile velocities in this thesis ($V_p \approx 9 - 17$ mm/ns), for electron spectrometers placed off-axis with respect to the ion beam (i.e. $\theta > 0$), either a very small portion of the ejected ^4P_J electrons will remain within their geometrical observation window,[9] leading to sensitive corrections [78, 107, 153, 154], or in the case of very long lifetimes - electrons may not even be detected at all [155] (e.g. at $\theta = 90°$)[10]. In the earlier ZAPS implementations, typical distances between target gas cell and analyzer entry were 16 cm [114], and 35 cm [126]. Since the metastable ^4P state decays along the path of the ion beam, placing the spectrometer on the beam axis leads to the detection of more Auger decay events, which, however, will also require an important correction for the competing effects of decreasing delayed Auger decay and increasing spectrometer acceptance angle.

Regarding the ZAPS experimental setup stationed in the INPP at the NCSR, there are a few important additions that make it unique. The current setup is based on an older electrostatic Hemispherical Deflector Analyser (HDA) [157–159] ZAPS setup, first tested at the J.R. Macdonald laboratory at Kansas State University [160–162]. It is equipped with a 4-element injection lens for focusing and pre-retardation of the detected electrons. In addition, a two-dimensional Position Sensitive Detector (PSD) is placed at the exit of the HDA, combined with a new much faster Data Acquisition (DAQ) capable of handling rates as high as 100 kHz with minimal dead time. The combination of lens and PSD results in a uniquely powerful state-of-the-art ZAPS setup with about 2 orders of magnitude better efficiency compared to the more traditional Double 90° Parallel-Plate Analyzer (tandem PPA) using only single channel detection [161]. The state selective resolution of this spectrograph allows for the accurate determination of absolute SEC cross sections of the KLL lines of interest, thus providing with the most stringent tests of theoretical calculations and models.

1.5   Spin statistics - experimental and theoretical results

The earliest state-selective Auger measurement involving the ^4P state was by Stolterfoht *et al* [11]. In their experiment, the 200 MeV Xe^{31+} + Ne collision system was examined, acquiring the Ne target KLL spectra. The use of heavy projectile ions, such as Xe, led to a high degree of ionization, which produced an interpretable KLL spectrum, characterized by an enhanced $1s2s2p\,^4P$ line. A suggested explanation was that optical transitions depopulate the higher lying quartets which cascade feed the ^4P state. Similar results presented by Mann *et al* [163] for the ^4P state, supported this cascade feeding. Dumont

---

[8]Typically, these prompt decays occur on a fs to ps time scale [108].

[9]Unlike $\theta = 0°$ observation, where the forwardly emitted electrons remain continuously within the sight of the spectrometer since they travel along the line of sight.

[10]It should be noted that when the projectile velocity V_p is larger than the velocity of the emitted electron, there is a limiting maximum observation angle θ_{max} [156] beyond which observation is no longer possible.

et al [164] described the cascades in detail. This population accumulation in the $1s2s2p\,^4P$ state due to cascades from higher lying states makes the determination of $2p$ SEC to the ^4P state in C^{4+}($1s2s\,^3S$) collisions particularly difficult.

The first to quantify the enhancement of the ^4P line with respect to the similarly configured doublets $^2P_-$ and $^2P_+$, was Anthony *et al* (1987) [153, 154]. Anthony was also one of the first to measure high energy Auger spectra for the C^{4+} + gas collision system between 3 and 8 MeV. Measuring *off* the beam axis, at lab observation angles of $9.6°$ to $10.6°$, the observed metastable ^4P line was rather weak. Never-the-less, Anthony recognized possible cascade feeding. Using fractional parentage coefficients, Anthony estimated the ratio of direct $2p$ SEC onto a $1s2s\,^3S$ ion ending up in the three possible states ^4P, $^2P_-$ and $^2P_+$ to be 4:1:3.

In a more recent study, the ^4P enhancement was highlighted by Tanis *et al* (2004) [2]. The collision system under investigation was 1.1 MeV/u F^{7+} ($1s2s\,^3S$) on He and Ne. After observing the enhanced line, Tanis *et al* defined R, as the ratio of the ^4P over the sum of $^2P_-$ and $^2P_+$ of the formed spectrum. In later publications, where contributions from the two components of the beam could be separated, it was redefined as R_m, the ratio of the corresponding SDCS for SEC strictly to the $1s2s\,^3S$ metastable component. Considering only spin multiplicity, R_m should be 1 $[= 4/(2 + 2)]$, while measured values gave ratios of $2.5 - 2.9 \pm 10\%$. To account for this observed enhancement, a new additional process named *dynamical Pauli exchange interaction* was proposed [2]. Alternatively, Benis *et al* (2004-06) [4, 165], assuming a frozen core approximation and applying spin-recoupling for the three electrons, showed that direct $2p$ electron transfer onto a $1s2s\,^3S$ ion should end up in the three possible states ^4P, $^2P_-$ and $^2P_+$, in the proportions of 8:1:3 and thus resulting in the ratio $R_m = 2$ $[= 8/(1 + 3)]$.

In a follow-up paper, Zouros *et al* (2008) proposed [5] that the enhancement of the ^4P state could be readily explained by transfer into higher nl states, followed by a selective cascade feeding mechanism, without the need to invoke any new additional processes such as the ad hoc dynamical Pauli exchange interaction of Tanis *et al.* [2]. This was supported by theoretical cascade calculations for F^{7+} + He, H$_2$, which were in good agreement with older measurements [145, 146]. Results from Ref. [5] are depicted in Fig. 1.2 (Left). Calculations were presented for both cases of either a) no cascades to the ^4P state, or b) cascades from the $n = 3 - 5$ levels, along with the $2p$ spin statistics prediction. For comparison to the experimental data of Lee *et al* [145, 146], $1s^2\,^1S$ ground state TE contributions to the $^2P_\pm$ states were included in the calculation of R_m ratio shown (in the figured called R_e). In general, this is the expected dependence of R_m on the collision energy: For high collision energies, both calculations converge to the constant $2p$ spin statistics prediction. As the energy decreases, the inclusion of TE contributions reduces R_m values below the $2p$ spin statistics prediction, since the doublet states can be populated by both SEC to the $1s2s\,^3S$ and TE to the $1s^2\,^1S$. This deviation from the value of "2" reaches a local maximum close to 1.2 MeV/u, i.e. in proximity of the RTE resonance. Further decrease in collision energy, results in the further increase of cascade feeding to the ^4P, and therefore, R_m again increases. Differences between the two targets was attributed to different Z_p/Z_t ratio, a parameter explained in Subsection 2.2.1.

In Fig. 1.2 (Right), are shown the measured values of R_m performed for C$^{4,\,5+}$ + He at 0.5-1.0 MeV/u by Strohschein *et al* (2008) [6]. For a more accurate determination of the $1s2s\,^3S$ contributions to the spectrum, they used both a mixed state ($1s^2\,^1S + 1s2s\,^3S$) beam, as well as what was perceived as a purely ground state ($1s^2\,^1S$) C^{4+} ion beam. The Strohschein measurements found R_m values of the order of 6-8, even further away from the frozen-core prediction of 2 by Benis *et al* [4]. They also included cascade feeding calculations based on one-electron TC-BGM calculations of nl SEC to the $1s2s\,^3S$ core
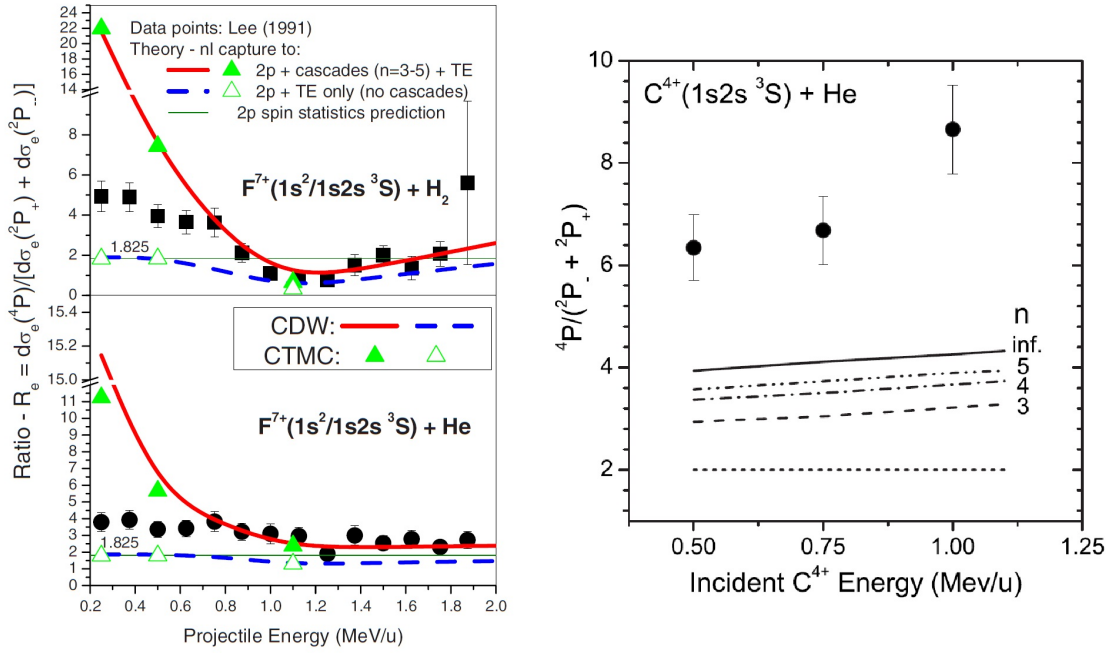
Figure 1.2: Early R_m measurements and theoretical calculations. (*Left*) Figure from Ref. [5] (2008). Ratios R_e ($\approx R_m$ due to differences in Auger yields - see [5] and text for definition) of experimental and theoretical Auger SDCS, for $F^{7+}(1s^2\,{}^1S,\ 1s2s\,{}^3S)$ + H_2/He collisions. Experimental results were obtained from older measurements [145, 146]. Calculations include nl single electron capture with and without cascades. (*Right*) Figure from Ref. [6] (2008). Calculated and measured R_m ratio as a function of the incident projectile energy for single electron capture in $C^{4+}(1s2s\,{}^3S)$ + He collisions. The lower, horizontal short dashed line at R_m=2 represents the value expected from spin statistics. Moving upwards, various lines show calculations including cascades from all relevant states up to $n = 3, 4, 5$ and extrapolation to $n \to \infty$.

applying the frozen core method, to provide initial population cross sections. However, when cascade feeding was also included they found the ratio R_m only increased to about 4, still quite a bit smaller than their observed value of 6-8. They concluded, that only half of the observed ${}^4P$ enhancement originated from such cascades, thus still allowing room for the originally proposed dynamical Pauli exchange interaction.

In a follow-up to Ref. [6], more elaborate cascade calculations for the same system, Röhrbein *et al* (2010) [81] now also included in their cascade analysis, Auger transitions, not included in the previous Strohschein treatment. They showed that the resulting R_m ratio could be further increased to a value of about 5, still leaving room for additional enhancement mechanisms. Without cascades though, just from $2p$ SEC, the ratio $R_m = 2$ was found, showing cascade enhancement to be about a factor of 2.5.

1.6   Dissertation goals

The goal of this thesis is the investigation of SEC to the $1s2s\,{}^3S$ metastable component of the ion beam, and the study of population mechanisms. This is accomplished by building from scratch a complete beam line (L45) with a ZAPS setup composed of a novel, high-efficiency HDA [166] in the NCSR at the INPP. The entire setup constitutes a dedicated Atomic Physics beam line at the INPP, to further complement the nuclear physics research

already pursued there to date. The apparatus, along with all its parts has been tested and characterized.

Along with the measurements for this thesis, a series of *ab initio* dynamical calculations have been performed involving for the first time *three* active electrons within a full configuration interaction approach, presented in Ref. [7]. These state-of-the-art calculations were performed and supplied by the group of Prof. Alain Dubois in Paris. In this 3eAOCC treatment, the time-dependent Schrödinger equation is solved nonperturbatively, with the inclusion of all couplings related to the static and dynamic interelectronic repulsions and effects originating from the Pauli exclusion principle. By doing so, the C^{4+} and C^{3+} electronic structures and dynamics can be accurately modelled, inducing, among others, excitation and capture to doubly-excited states on the carbon center. The 3eAOCC treatment therefore goes much beyond the frozen core model advocated in the past [6, 81], where only one active electron is considered in the dynamics.

The theoretical results presented in Ref. [7] with the inclusion of cascades [167] were found to be in excellent agreement with the experimental results on the ratio R_m measured and presented in this thesis. This agreement gives a first indication that the spin statistical frozen core approach does not seem to be applicable to multielectron multi-open-shell atomic systems. The complexity of this type of collision, where the projectile configuration involves multi-open-shell configurations, required the more sophisticated 3eAOCC treatment with the use of three active electrons (for the first time - only two had ever been used before) plus configuration interaction. The contribution of the 3eAOCC results was crucial to the overall understanding of the measured R_m values, since the enhancement of the ^4P line due to the cascades distorts the result of pure $2p$ capture.

1.7 Dissertation outline

The content of this thesis is divided into two sections: The first one is the implementation of the ZAPS experimental station in the INPP of the NCSR. The second focuses on the experimental study of the dynamics of the ^4P state produced in collisions of He-like pre-excited carbon atoms with gas targets in the MeV/u energies regime. A brief outline of the thesis is given below.

In Ch. 2, the formation of doubly-excited projectiles is described in detail. Methods for varying the $1s2s\,^3S$ pre-excited component in He-like ion beams are reviewed. The mechanisms for populating the $1s2l2l'\,^{2,4}L_J$ states such as SEC, TE are presented, along with previously published calculations. The role of the quartet/doublet configuration of populated states is presented, along with their expected behaviour, and possible deviations from that scheme. Pure $2p$ transfer is discussed, complemented by the definition of the R_m ratio, used to quantify the enhanced ^4P line in the KLL spectrum formed in energetic ion-atom collisions. Previous approaches for the estimation of the R_m are presented, along with the novel 3eAOCC approach

In Ch. 3, the ZAPS experimental station at the tandem laboratory of the INPP of the NCSR is presented. Vacuum considerations, the implementation of a doubly differentially pumped target gas cell, the spectrograph consisting of the HDA, the focusing/decelerating lens and the two-dimensional PSD are presented in detail. The experimental work, along with Monte Carlo simulations using SIMION for the optimal operation of the focusing lens is also presented. The electronics scheme, along with the optimization of the High-Voltage Power Supply (HVPS)s operation is described. The measurements for defining the Dead Time Correction (DTC) of the apparatus are presented. Finally, the implementation of various ion beam stripping points for varying the $1s2s\,^3S$ metastable content of the ions is shown.

In Ch. 4 kinematic considerations for the ZAPS acquired spectra is reviewed, along with the Auger electron energy calibration scheme used. Known considerations for the transformation to Double Differential Cross-Section (DDCS) are described, along with the experimental determination of the efficiency of the overall setup. Moreover, the experimental determination of the G_τ correction factor required for the correct "normalization" of the ^4P state to the rest of the KLL lines is discussed, along with the acquired spectra. The analysis scheme is presented in detail. Finally, the two-spectra equations for the determination of metastable beam fractions, line ratios and SDCSs from each ion beam component are reviewed, along with the respective uncertainty analysis.

In Ch. 5 the results of the study are presented. The collision system under investigation is 6-15 MeV C^{4+} + H$_2$, He, Ne and Ar, measured using varied $1s2s\,^3S$ content of the C^{4+} ion beam. First, are shown the results of $1s2s\,^3S$ content determination, using a technique based on the acquisition of two spectra of different $1s2s\,^3S$ content [168]. Next, the production cross section ratios R_m and r_m describing ratios of lines produced by transfer to the metastable are presented. They are compared to the spin recoupling theory, and electron transfer ratio $R_{m_{T2p}}$ to $2p$ is examined. Finally, the SDCSs for transfer to the $1s2s\,^3S$ component are presented.

In Ch. 6 the contributions of TE mechanisms to the spectra are discussed and evaluated. A description of the Resonant Transfer-Excitation with Auger emission (RTEA) within the Impulse Approximation (IA) treatment is presented. Analytical expressions for the various Compton profiles for Ne and Ar are calculated. The RTEA contributions are calculated and compared to the $1s^2\,^1S$ contributions from the measured spectra. Finally, theory is compared to measured ratios R_g and r_g[11] involving ground state contributions, and discussed.

In Ch. 7 a summary of all results is given. Also there is discussion about the future prospects of the high efficiency spectrograph implemented at the INPP.

In the appendices, various technical details and useful information on various energy levels, selection rules among others are included. Also included are the tabulated results of Ref. [108], as a complete set of energies of $1s2lnl'$ configurations.

Finally, the recently accepted (PRL) publication [7] from the APAPES group is included. In Ref. [7] the results of this thesis regarding the He target are presented, along with the 3eAOCC computational/theoretical approach regarding SEC. The main attribute of this publication is that for the first time there is an agreement between theory and experiment. More papers on these new results are expected to follow.

---

[11]See Ch. 6 for the definitions.

Chapter 2

1s2l2l' states: Production and Properties

2.1 Mixed-state beams

He-like and Be-like ionic beams, are typically delivered in mixed states due to the long life-time of certain excited ionic states. The amount of metastable fraction in the ion beam is determined by the stripping energy, the stripping medium's effective areal density, and its distance from the target [59, 60, 109]. "Pre-excited" states, such as $1s2s\,^3S$ and $1s^2 2s2p\,^3P$ are ideal candidates for the formation of doubly excited auto-ionizing states. This can be achieved by either capture to $1s2s\,^3S$ or $1s$ needle ionization [137] of the $1s^2 2s2p\,^3P$ component (i.e. the removal of a K-shell electron without affecting the surrounding electrons). He-like beams, in particular, are delivered in a mixture of $1s^2\,^1S$ ground state and $1s2s\,^1S$ and $1s2s\,^3S$ metastable states [59, 109]. The metastable components are expected to be produced statistically, in a ratio of 1:3. This means that 25% of the stripped $1s2s$ ions will result in $1s2s\,^1S$, whereas 75% will result in $1s2s\,^3S$. In the case of carbon, lifetimes for these states are $\tau_{1s2s\,^3S} = 2.1 \times 10^{-2}$ s and $\tau_{1s2s\,^1S} = 3.0 \times 10^{-6}$ s [58]. As stated earlier, there are two stripping locations for the ion beam, the terminal ($\approx$26.35$\pm$0.5 m from target), and the post-stripper ($\approx$12.1$\pm$0.5 m from target). For current energy range and distance combinations, the $1s2s\,^3S$ survives practically unaffected (0.004-0.012% loss).

Table 2.1: $1s2s\,^1S$ surviving percentage of original population from both stripping points. for all the projectile energies in this work. Bold percentages represent the respective distances of the strippers used for each energy in the present work.

		MeV/u			
Stripper	Distance (m)	0.50	0.75	1.00	1.25
Post-stripper	12	**66**%	**71**%	74%	77%
Terminal	25	42%	50%	**54**%	**58**%

However, the $1s2s\,^1S$ component is expected to experience significant losses. In Table 2.1, the surviving percentage of original population is calculated for various cases. Combining with the 3:1 ratio and the calculated $1s2s$ fractions in all cases[1], the final $1s2s\,^1S$ surviving fraction at the target gas cell is found to be $\leq 4\%$ of the beam. Moreover, the $1s2s\,^1S$ component is expected to contribute primarily to the ^2S, $^2P_-$ and $^2P_+$ lines of the spectrum. Electron capture to the $1s2s\,^1S$ does not populate the ^4P, and population by RTE of the $1s2p^2\,^2D$ is energetically forbidden. Therefore it is not considered further

---

[1]Maximum metastable fraction of the beam was $\leq 25\%$

in the present work. The two spectra technique, described in Sec. 4.5, considers only the $1s^2\,^1S$ and the $1s2s\,^3S$ components of the beam, neglecting the $1s2s\,^1S$ component. This results in a $\leq 3\%$ over-estimation of the respective fractions. Other expected states such as $1s2p\,^3P$ and $1s2p\,^1P$ have ns lifetimes [169], therefore are not studied.

2.2   Population of the 1s2l2l' states

The observed KLL Auger spectrum originates from the lower-lying doubly-excited C^{3+} states involving a K-vacancy. The five Auger lines that comprise it are shown in the analyzed ZAPS spectrum of Fig. 2.1. These states are identified in the spectrum as ^2S, ^4P, $^2P_-$, $^2P_+$ and ^2D. In general, the reaction is:

$$\text{C}^{4+}\left(1s^2, 1s2s\,^3S\right) + \text{He} \rightarrow \text{C}^{3+**}\left(1s2l2l'\,^{2,4}L_J\right) + \text{He}^+ \rightarrow \text{C}^{4+}\left(1s^2\right) + e_A + \text{He}^+ \quad (2.1)$$
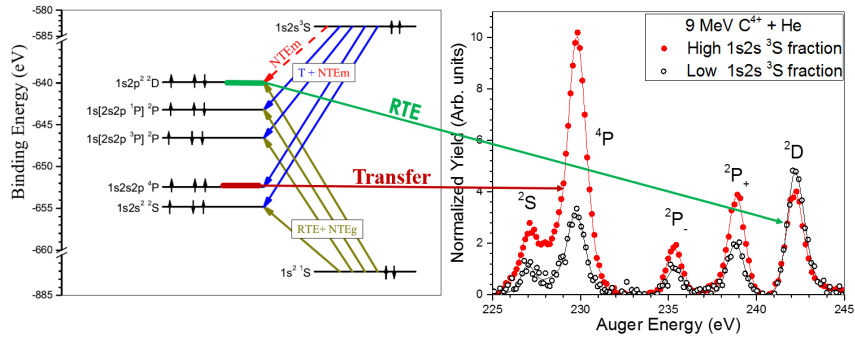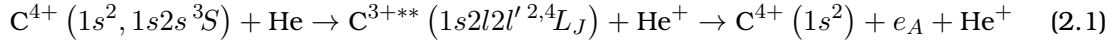
Figure 2.1: Carbon Auger KLL lines: [Left] Energy level diagram and corresponding production mechanisms. [Right] Two ZAPS KLL spectra for 9 MeV mixed-state C^{4+} collision with He, each with different metastable content. The intensity of the ^4P lines formed by direct 2p transfer to the $1s2s\,^3S$ state is proportional to the metastable beam fraction.

For these KLL states, the main production mechanisms are shown in Fig. 2.1. These are Transfer, RTE, Non-Resonant Transfer-Excitation from the ground state (NTEg) and Non-Resonant Transfer-Excitation from the metastable state (NTEm) (See subsections 2.2.1 and 2.2.2 for more details.).

- The ^4P is assumed to be formed primarily by capture to the $1s2s\,^3S$ component of the beam. Formation by RTE from the $1s^2\,^1S$ component is in principle possible. However, RTE strength depends on the Auger rate, which in the case of the ^4P is five orders of magnitude smaller compared to the doublet states [108]. Another possible channel is NTEg from the $1s^2\,^1S$ component. Contributions from this channel, for the collision energies utilized in these experiments, can be minimized with the use of light targets such as H$_2$ or He [170, 171]. This applies also to contributions from the $1s2s\,^3S$ component through NTEm. Therefore, the ^4P production cross section from the $1s^2\,^1S$ component can safely be assumed zero.

- The ^2D state is assumed to be formed primarily from the $1s^2\,^1S$ by RTE. Capture to the $1s^2\,^1S$ component leads to $1s^2nl\,^2L$ singly excited states that are not autoionizing and therefore not observed. Production by RTE from the $1s2s\,^3S$ is forbidden energetically. NTEm contributions are similarly minimized. NTEg contributions are considered $1s^2\,^1S$ contributions. Therefore, the ^2D production cross section from
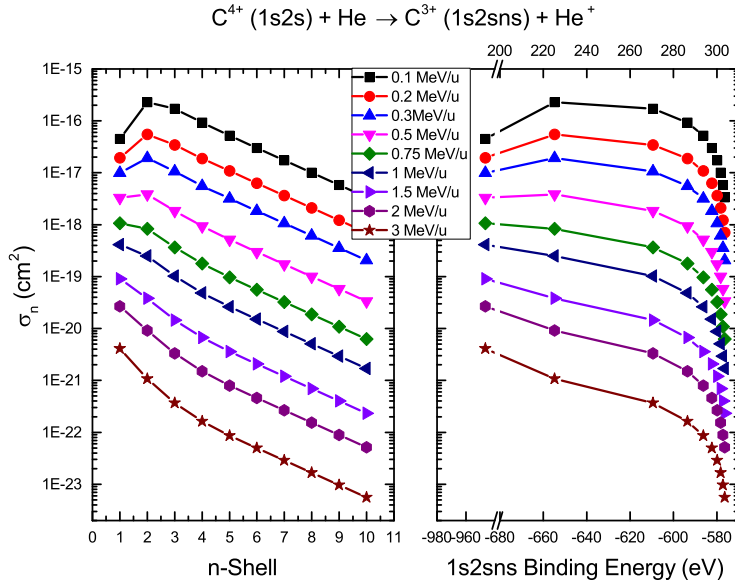
Figure 2.2: *(Left:)* Calculations for the σ_n partial capture cross section for the C^{4+}+He system, deduced from the Be^{4+}+He results. Results from Ref. [172]. *(Right:)* Same data as left, but the x-axis is transformed to the corresponding binding energies for the respective $1s2sns\,^2S$ states. Binding energies calculated by Sakho *et al* [173].

the $1s2s\,^3S$ component, for the present collision energy range, can be assumed negligible.

- Finally, the ^2S, the $^2P_-$ and the $^2P_+$ states can be populated from both components of the beam. In particular, by transfer to the $1s2s\,^3S$, and by RTE from the $1s^2\,^1S$ component. As explained in Subsection 2.2.2.2, NTEm contributions are considered negligible for light targets, whereas NTEg contributions are considered $1s^2\,^1S$ contributions. Finally, these states can be also populated from the $1s2s\,^1S$ component, however, this contribution is negligible due to low $1s2s\,^1S$ fractions arriving to the target gas cell.

2.2.1 Transfer

In SEC, an electron is captured/transferred from the target to the projectile ion. Although transfer can occur to the $1s^2\,^1S$ ground state ions, the resulting $1s^2nl$ $(n \geq 2)$ states are not autoionizing and therefore not observed by Auger electron spectroscopy. Alternatively, transfer to the pre-excited $1s2s\,^3S$ component of the beam leads to the formation of various doubly-excited, autoionizing $1s2snl'\,^{2,4}L_J$ states. Electron transfer to projectile ions for low collision energies[2] is *state selective*, with intermediate shells ($n \approx 4$, depending on the collision system under consideration) accounting for most of the transfer. The basic parameters describing electron transfer are the projectile charge q, the ionization potentials of the target and the collision velocity. Based on these parameters, a distribution around a central value n_{max} is formed, known as "reaction window" [69]. Fig. 2.2 shows calculations from Ref. [172]. Values for $n \geq 6$ were extracted with the use of the $1/n^3$ scaling law. The calculations regard the Be^{4+}+He $\rightarrow$ Be^{3+}+He$^+$ collision system, with the energy reduced to MeV/u. In similar reports [175], Belkić presents capture cross sections for C^{4+}+H (1s) by correcting the corresponding energies of the calculated Be^{4+}+H (1s)collision system. Since the results are presented in MeV/u, it is similarly assumed that the Be^{4+}+He correspond also to the C^{4+}+He results. Moreover, He-like ions show the same one-electron capture cross section and the same range of binding energies of preferentially populated states "reaction window" irrespective of whether the configuration is $1s^2\,^1S$ or $1s2s\,^3S$ [69, 176]. As seen in Fig. 2.2, for the lower energy, the

---

[2] " $\approx$KeV/u"
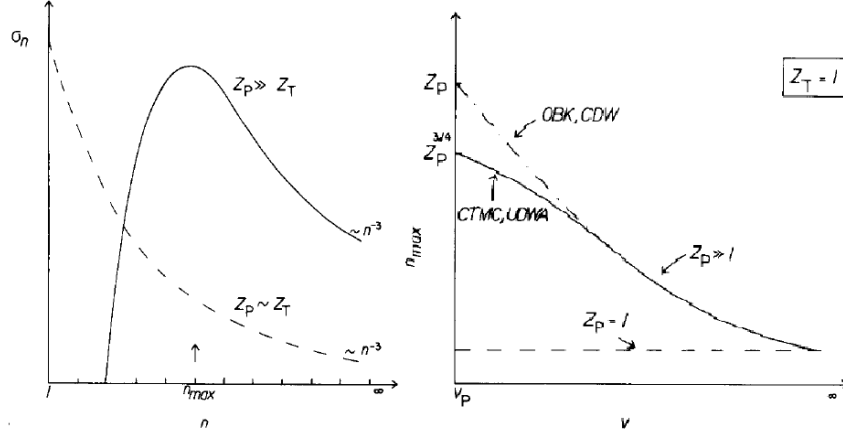
Figure 2.3: Asymmetry and velocity effects on the σ_n distributions. *(Left:)* Qualitative n distribution of the capture cross section, σ_n, for different values of the asymmetry parameter Z_P/Z_T. *(Right:)* Dependence of n_{max} on the projectile velocity for different values of the asymmetry parameter Z_P/Z_T. Figures from [174].

reaction window already results in $n_{max} = 2$. For lower collision energies [69], or more asymmetrical systems [174] this window can be even narrower.

Increasing the projectile energy, two effects take place: First of all, the distribution broadens [69]. At the same time, as seen in Fig. 2.2, at the center of the distribution, n_{max} decreases. This is also illustrated in Fig. 2.3 from Ref. [174]. In Fig. 2.3 the asymmetry parameter is introduced. As it can be seen, high Z_P/Z_T corresponds to high state selectivity. For more symmetrical systems, lower n_{max} values are favoured. Also can be seen in Fig. 2.3, on the right, is the dependence of n_{max} on the ion velocity. As velocity or MeV/u increases, capture to lower shells is preferred.

As a final example, Fig. 2.4 is presented. For these two collision systems, the respective
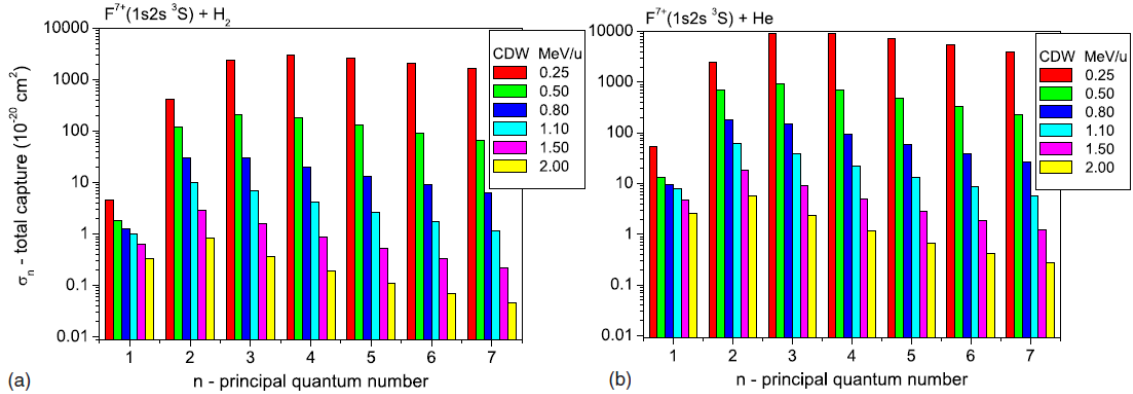
Figure 2.4: Calculation results for the n-distribution of the capture cross sections σ_n in the reaction $F^{7+} + H_2$, He. Figure from Ref. [5].

n_{max} for each energy appear to be the same, considering the asymmetry parameters. It is interesting to point out that for these calculations, $n = 1$ does not become the dominant channel. This trend still applies to calculations from Newport *et al* [177] (Fig. 8). However, according to Shevelko [178] and also the data from Ref. [172], presented in Fig. 2.2, for sufficiently high velocities, $n = 1$ can become the dominant capture shell.

18

2.2.2 Transfer Excitation

Introduction

Amongst the interactions that take place during an ion-atom collision there is a particular class that strongly influences the fundamental processes such as excitation or ionization. These interactions are attributed either to $e - n$ interactions or to $e - e$ Coulomb interactions, between the target atom and the ionized projectile nucleus/electrons [179, 180]. In the following sections, a brief description of these processes will be given.

Figure 2.5: Schematic diagram of two known TE processes that can lead to the same doubly excited states and thus, interfere. Figure from Ref. [180].

2.2.2.1 Resonant Transfer and Excitation

In RTE [129, 130, 181], a target electron is transferred to the ion, while a projectile electron is excited to a higher-lying level during the same collision, through the electron-electron interaction, in a correlated two-electron process analogous to the time reversed Auger decay [182, 183]. As such, RTE is a resonant process with all the attributes of an Auger transition. Since the $1s2s\,^3S$ state lies energetically above the respective $(1s2s\,^3S)nl^{2,4}L$ states, these cannot be populated by RTE, since an Auger decay from these states to the $1s2s\,^3S$ state is not energetically possible. Thus, RTE can only energetically occur from the $1s^2\,^1S$ ground state component of the ion beam for the KLL lines under consideration.

2.2.2.2 Non-Resonant Transfer and Excitation

Non-Resonant Transfer-Excitation (NTE) is allowed from both $1s^2\,^1S$ ground and $1s2s\,^3S$ metastable state. NTE from the ground state and NTE from the metastable state are denoted respectively NTEg and NTEm [145]. NTE [131, 134, 184] differs from RTE in that both excitation and transfer happen independently in the same collision. Excitation is attributed to a target nucleus-projectile electron interaction, while transfer due to a projectile nucleus-target electron interaction, both treated as independent single electron processes, as shown in Fig.2.5. Thus, NTE does not exhibit a resonant behavior similar to RTE. Instead, the NTE process is stronger, for lower projectile energies energies. In the measurements of this thesis, the lowest energy measurements were taken for 6 MeV C^{4+}. For this energy, the RTE contributions are expected to be dominant. Furthermore, for light H_2 or He targets NTEm contributions are negligible [170, 171]. For heavier targets such as Ne or Ar larger NTE cross sections are expected. This is attributed to both higher Z numbers, and the fact that more electrons are carried into the collision.

2.3 The *1s2s2p* ^4P state

Quartet states can be populated by capture to the $1s2s\,^3S$ component. The lowest quartet state is the $1s2s2p\,^4P_{1/2,3/2,5/2}$, a state that is metastable with respect to both auto-ionisation and radiative decay [185–187], due to the $\Delta S = 0$ selection rule. However, the $1s2s2p\,^4P_{1/2,3/2}$ fine-structure components are connected to the $1s^2kp$ continuum states by spin-orbit interactions via intermediate states such as $^2P_{1/2,3/2}$ more commonly known as Configuration Interaction (CI) [186, 188]. The lifetimes for these two components, in the case of carbon, are 2.94 and 7.10 ns, respectively [123]. The $^4P_{5/2}$ component has a longer lifetime than the other two [189]. This is because it is coupled to the adjacent $1s^2kf$ continuum states through the spin-spin interaction [187, 188]. That, again in the case of carbon, results in a lifetime of 121.36 ns [123]. The other, higher quartet states are metastable with respect to auto-ionization in a similar way, but they can all $E1$ decay to the next lower lying opposite parity $1s2snl\,^4L$ state leading to a cascade sequence that accumulates on the (lowest) ^4P level. See next section for more details.

2.4 Doublets/Quartets and Cascades
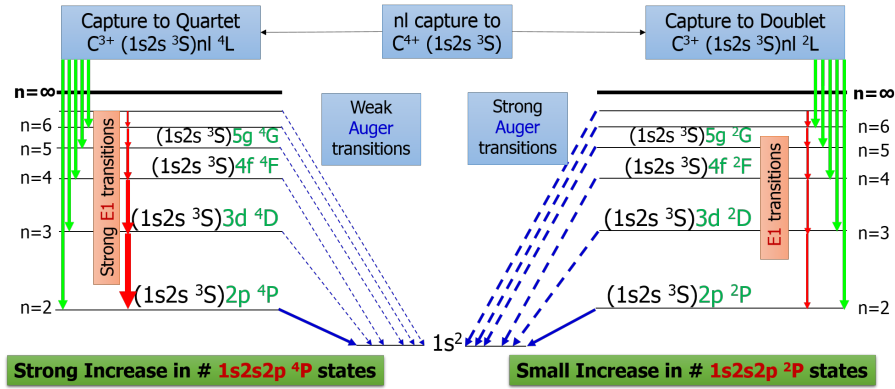
Figure 2.6: Cascade feeding of states populated by capture to the $1s2s\,^3S$ component. (*Left*:) The higher-lying quartets decay radiatively by strong $E1$ transitions since competing Auger decays are weak due to spin conservation considerations. Therefore, higher-n quartet systems tend to accumulate to energetically lower states, eventually leading to a preferential enhancement of the ^4P population. (*Right*:) In contrast, for the doublets, Auger decay is stronger than the competing E1 transitions. Electrons from higher-n ($n > 2$) doublet states have been measured [190], providing evidence for capture to higher-n $(1s2s^3S)nl^2L$ states.

As already mentioned, capture to the $1s2s\,^3S$ metastable state of the projectile can also populate a variety of $(1s2s\,^3S)nl\,^{2,4}L$ configurations with $n > 2$. Depending on the total spin of their electronic configuration, these higher-lying doubly-excited levels can be divided into two distinct spin types: doublets and quartets. For the quartets, Auger decay to the ground state is very weak, as it implies a violation of the spin conservation rule requiring a spin-orbit/-other-orbit interaction with orders of magnitude smaller relative transition rates ($\sim\alpha^4$) [67, 164, 187, 191]. Competing radiative $E1$ transitions [192], for low-Z ions, between quartets (red arrows in Fig. 2.6) are much stronger and prevail. More recent calculations by Zouros *et al* [5] are in agreement with the above reasoning.

For the doublets, however, the Auger decay channel is much stronger than the competing radiative channels, at least for low-Z_p elements, such as carbon [29, 108, 181].

FIG. 3. Term diagram of the quartet system of C IV.
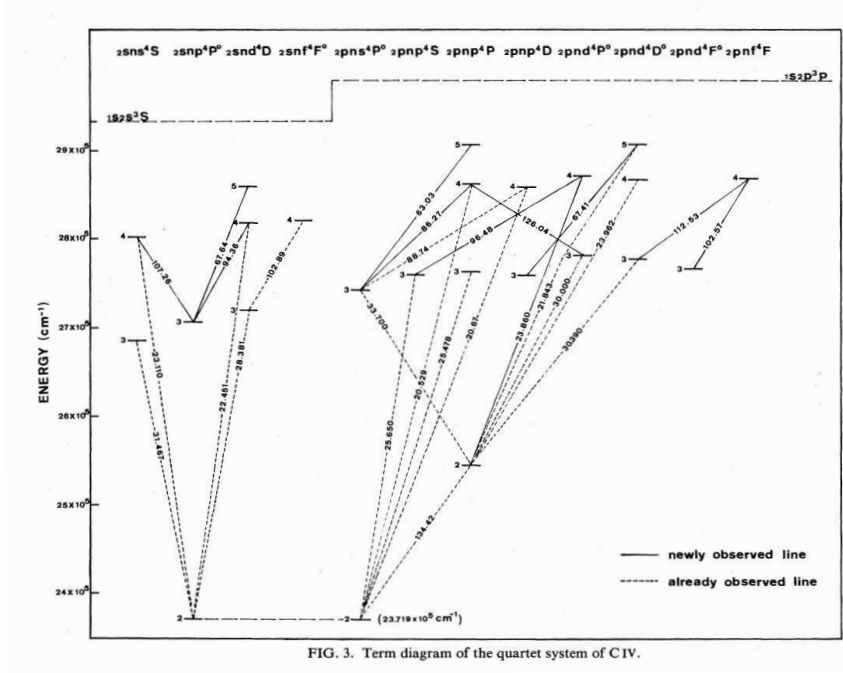
Figure 2.7: Term diagram of the quartet system of C IV. Fig. from Ref. [164]. As seen, few states appear to not transition directly to the $^4P^o$ and $1s2p^2\,{}^4P^e$ states. See text for more details.

All the doublets, described in Ref. [108], where checked for possible cascade feeding. This was achieved by checking which states had low ξ_A also low sum of Probability of a Radiative decay Directly to Final (PRDF) values. These are presented in Table 2.2:

Table 2.2: Selected doublet states with cascading characteristics. See text for more details.

Configuration	State	Auger Energy (eV)	ξ_A	ΣPRDF
$1s2p(^3P)3p$	$^2P_{\frac{3}{2}}$	276.4 eV	0.000	0.93
$1s2p(^3P)3d$	$^2F_{\frac{5}{2}}$	279.3 eV	0.089	0.86
	$^2D_{\frac{5}{2}}$	277.9 eV	0.000	0.29
	$^2D_{\frac{3}{2}}$	277.9 eV	0.004	0.28
$1s2s(^1S)3d$	$^2D_{\frac{3}{2}}$	277.3 eV	0.048	0.76
	$^2D_{\frac{5}{2}}$	277.3 eV	0.012	0.77
$1s2s(^3S)3p$	$^2P_{\frac{3}{2}}$	270.9 eV	0.609	0.88
	$^2P_{\frac{1}{2}}$	270.9 eV	0.601	0.85

The first two configurations, cannot be formed by single capture. It would require an additional $2s-2p$ excitation from the $1s2s\,{}^3S$ component, that translates to a more complex mechanism. The $1s2s(^1S)3d$ configurations are the most dubious, due to ξ_A and PRDF values. They appear to be formed by capture to the $1s2s\,{}^1S$ component, however, the LS-coupling scheme used by Chen, cannot lead to safe estimations. Should they be formed, the only states that the may cascade to are the $^2P_{\pm}$. Finally, the $1s2s(^3S)3p$. This state can be formed by $3p$ capture to the $1s2s\,{}^3S$ component. However, the only cascade

21

path is to the ^2S state, therefore, it is not expected to interfere with the results of this study. Bliman *et al* [193] report measurements for the radiative decay of the $1s2s(^3S)3p$ $^{2,4}P$ to ground transition, He-like carbon colliding with H_2. Therefore, the higher-lying doublet states, will mostly Auger decay with minimal cascade feeding of the lowest ^2P states [81] with Auger energies between 270 and 298 eV [108], already observed in the spectra.

2.5 R_m

The R_m ratio is defined by Eq. 2.2. It is defined as the ratio of the total Cross Section (CS)s for capture to the $1s2s\,^3S$ component forming the ^4P over the sum of $^2P_-$ and $^2P_+$.

$$R_m = \frac{\sigma_m\left(^4P\right)}{\sigma_m\left(^2P_-\right) + \sigma_m\left(^2P_+\right)} \tag{2.2}$$

It was first defined in Ref. [194], as a test to investigate the enhancement of the ^4P population, presented in the F^{7+}+He, Ne collision system. However, experimentally, the numerator includes contributions from $1s2snl\,^4L$ quartet states, formed by the same mechanism, with capture to higher n values. One way to understand the approaches for determining the R_m experimental ratio is to reduce R_m to the product of 2 different contributions:

- The first one is R_{mT2p}. Its definition is similar to Eq. 2.2. The difference is that it involves the CSs for strictly $2p$ SEC to the ^4P over the $^2P_-$ and $^2P_+$.

- The second is R_{cc}. It's defined in Eq. 2.6. This term stands for the cascade contributions to the measured ^4P state, enhancing the R_m ratio. Although intuitively, the cascades have an additive effect, a multiplicative term was chosen, for reasons explained later in the text.

2.5.1 Spin statistics with frozen core

The first attempt to predict R_{mT2p} was by Anthony *et al* (1987) [153, 154]. Using fractional parentage coefficients, he estimated the ratios of direct $2p$ electron capture onto a $1s2s\,^3S$ ion ending up in the three possible states ^4P, $^2P_-$ and $^2P_+$ to be 4:1:3. This results in an estimation of $R_{mT2p} = 1$.

After that, Benis *et al* [4, 165] exhibited how the capture of a $2p$ electron to a $1s2s\,^3S$ ion results in a 8:1:3 ratio of probabilities to the respective states. To achieve that, they construct an initial $|1s2s\left(^3S\right)\rangle$ state with spin quantum numbers $s_{12} = 1$ and m_{12}. After adding the captured $2p$ electron with $s_3 = 1/2$, the available s values for the resulting $\left|\left[1s2s\left(^3S\right)\right]2p\left(^{2s+1}P\right)\right\rangle$ state, are 1/2 and 3/2. Averaging the probabilities for all the possible $(2s_{12}+1)(2s_3+1)(=6)$ states to end up in a state with final spin s provides with Eq. 2.3:

$$P(s) = \frac{2s+1}{6} = \begin{cases} 4/6 & \text{for the } \left[1s2s(^3S)\right]2p(^4P) \text{ state} \\ 2/6 & \text{for the } \left[1s2s(^3S)\right]2p(^2P) \text{ state} \end{cases} \tag{2.3}$$

It can be seen in Eq. 2.3, that the expected capture ratio is $R_{mT2p} = 4/2 = 2$.

In order to examine the doublet states, recoupling from a $\{[(s_1, s_2)s_{12}], s_3\}s$ coupling scheme to a $\{s_1, [(s_2, s_3)s_{23}]\}s$ one is required. In this coupling scheme $s_{23} = 1$ for the $1s[2s2p(^3P)](^2P_-)$ state and $s_{23} = 0$ for the $1s[2s2p(^1P)](^2P_+)$ state. For these states, the

probability of populating each s_{23} value is given by Eq. 2.4

$$P(s_{23}) = 3(2s_{23} + 1)\begin{Bmatrix} 1/2 & 1/2 & 1 \\ 1/2 & 1/2 & s_{23} \end{Bmatrix}^2 = \begin{cases} 1/4 & \text{for the } 1s[2s2p(^3P)](^2P) \text{ state}(s_{23} = 1) \\ 3/4 & \text{for the } 1s[2s2p(^1P)](^2P) \text{ state}(s_{23} = 0) \end{cases}$$
(2.4)

It should be noted here that the results regarding the relative capture between the doublet states is equal to the one predicted by Anthony [153, 154]. Other than that, these methods describe either a "pure spin statistics" or a "frozen $1s2s\,^3S$ spin statistics" approach. They are purely statistical approaches on the coupling of a free electron to an existing $1s2s\,^3S$ state.

2.5.2   Röhrbein approach

In 2008, R_m was measured for C^{4+} by Strohschein *et al* [6]. In their measurements, spanning between 6 and 12 MeV (0.5-1 MeV/u) the obtained results, with He as target, which were approximately 6-8. Their calculations, although limited to include strictly radiative cascades, provided with R_m values in the vicinity of 4, including the pure capture ratio being $R_{m_{T2p}} = 2$.

Röhrbein *et al* [81] treated this problem with a complete calculation of electron capture, state populations, energy level, Auger and radiative rate calculations. They divide the calculation into 4 distinctive steps:

1. Calculation of the electron transfer probabilities.

2. Calculation of the three-electron projectile states and their decay rates.

3. Calculation of the three-electron initial populations.

4. Solution of the rate equations.

2.5.2.1   Calculation of the electron transfer probabilities

This step focuses to the solution of the time-dependent Schrödinger equation for the active electrons in the collision. They address the problem using the TC-BGM [195]. In the single-particle Hamiltonian to be solved, other than the kinematic term, there are three potential terms, regarding the target nucleus, target electrons and the projectile electrons. For the target electrons, only the exchange term is used, an approximation by the optimized potential method. Regarding the projectile electron potential, the effective potential depends on the classical projectile coordinate $\mathbf{R}(t) = (b, 0, V_p t)$. The potential from the projectile electrons is also obtained by the optimized potential method. What is of importance here are the asymptotic properties on the potential where $u_{eff}^P(r_P) = -6/r_P$ for $r_P \to 0$, and $u_{eff}^P(r_P) = -4/r_P$ for $r_P \to \infty$. This means that for small r_P values, the target electron is affected only from the projectile nucleus, while for larger values, the projectile nucleus is shielded. This fixed potential assumes that the projectile electrons do not contribute to the collision, thus termed frozen core approximation. That means that only initial target electrons are propagated, making SEC the main focus of the calculation.

For the TC-BGM calculation, the basis of the target electron consisted of 20 states, the basis of the projectile 35 states, and 51 pseudo states to account for coupling to the continuum, giving rise to a total of 106 states. The collision energy of their calculation is well within the energy regime of this thesis.

2.5.2.2 Calculation of the three-electron projectile states and their decay rates

A crucial step of the the process was to calculate the radiative and Auger decay rates. Regarding photon de-excitations of the $(1s2s\,{}^3S)nl\,{}^{2,4}L$ states, the transition rates were calculated by utilizing a multiconfiguration Dirac-Fock (MCDF) method. All electric-dipole ($E1$) as well as magnetic-dipole ($M1$) and electric-quadrupole ($E2$) transitions were taken into account. The inclusion of the Auger channel in Ref. [81] is the major difference compared to the calculations of Ref. [6]. For their calculations of the Auger rates and their coupling to the continuum, the primary and sufficient coupling mechanism is the Coulomb repulsion. It should be noted, however, that said inclusion, although it didn't affect quartet populations, it resulted to a renormalization of the radiative branching ratios of the doublets [7], resulting to a 25% increase of the R_m calculation, compared to Ref. [6].

2.5.2.3 Calculation of the three-electron initial populations

The next step is to determine the initial populations of three-electron $(1s2s\,{}^3S)nl\,{}^{2,4}L$ projectile states. This is directly connected with the estimation of the $R_{m_{T2p}}$, that is the ratio for $2p$ capture. There are a few distinctive steps, in order to translate the TC-BGM results to $(1s2s\,{}^3S)nl\,{}^{2,4}L$ projectile states. The first step is to combine the result of TC-BGM with a $1s2s\,{}^3S$ core. This is achieved by formulating the $|\Psi(t_1)\rangle$ states:

$$|\Psi(t_1)\rangle = \frac{1}{\sqrt{3}} \left(\hat{1} - \sum_{j=2}^{3} \hat{P}_{1j} \right) |\psi(1, t_1)\rangle \, |1s2s\,{}^3S(2,3)\rangle. \qquad (2.5)$$

The $|\Psi(t_1)\rangle$ states are products of the C^{4+} ($1s2s\,{}^3S$) and a spin orbital obtained from the TC-BGM calculation. Again, the use of the $1s2s\,{}^3S$ state implies that the two projectile electron remain unaffected during the capture process, thus frozen. The next step is to calculate the transition amplitudes. These are the A_{if} ($= \langle \Phi_f | \Psi(t_1) \rangle$) overlaps between the calculated (MCDF) three electron projectiles states and the propagated states. The three-electron $(1s2s\,{}^3S)nl$ states are a group of six initial states, as described by Eq. 2.3, as a result of the coupling of the captured electron to the state. This means the initial populations of the states formed have a quartets over doublets ratio equal to 2.

Having the initial populations set, Röhrbein *et al* feed them to standard rate equations [196] along with the respective ratiative and Auger rates, the latter not considered in Ref. [6]. In these equations, the rate of change for each population is equal to summed radiative contributions from higher levels, minus losses from either radiative decay to lower levels or Auger decay.

The results of Rörhbein provide with a value of "5" for the R_m with a slight increase for the higher collision energies. This consists of an increase approximately 25% compared to the results of Strohschein [6], just by including the Auger transitions. One way to interpret their results, is again to consider R_m to be the product of two numbers, $R_{m_{T2p}}$ and R_{cc}. Considering that their calculation includes $R_{m_{T2p}} = 2$, it is safe to assume that the R_{cc} cascade contributions have led to an increase of ≈ 2.5 according to their results.

2.5.3 The 3eAOCC approach

In Ref. [7] a new approach was introduced. It focuses on the determination of $R_{m_{T2p}}$, the initial populations produced during the collision. It is based on a semiclassical atomic orbital close-coupling approach (referred to as 3eAOCC in the following), with asymptotic descriptions of both target and projectile [83]. Under the consideration of all the couplings

related to interelectronic repulsions and effects resulting from the Pauli exclusion principle, the time-dependent Schrödinger equation is solved non-perturbatively. However, as implied by the name, and contrast to previous calculations, this approach includes three active electrons. Doing so, the electronic structures of the C^{4+} and C^{3+} configurations, along with the dynamics of their spin and spatial components, are modelled in detail. These dynamics induce, among others, excitation and capture to doubly excited states on the carbon center, thus this approach goes beyond the independent electron and frozen core approximations applied in the past [6,81]. Regarding He, it is described by a single electron attached to He^+ through a model potential expressed as: $V(r) = \sum_{i=1}^{13} -\frac{c_i}{r} e^{-\alpha_i r^2}$ where the coefficients and exponents are optimized to get ground state with binding energy close to the first ionization energy (24.6 eV), the first excitation energies and correct Coulombic limits at $r \to 0$ and $+\infty$. This results to a He^+ ion with a passive electron.

For the atomic states centred on He, C^{4+} and C^{3+}, the electronic structures are described by sets of Gaussian-type orbitals (GTO), and antisymmetrized products of these GTOs in order to obtain the states under investigation for all (singlet/triplet, doublet/quartet) possible spin symmetries. For doublet spin symmetry, 1794 (1807) states and pseudo states for C^{4+} + He (C^{4+} + H) collisions were used, while for quartet spin symmetry, respectively 802 (812). Special emphasis was given on the optimization of the GTO sets and the description of the C^{3+} ($1s2\ell n\ell'$) states for $n =$2, 3 and ℓ, ℓ' =0, 1. Total cross sections were calculated, for the complete basis set, including and a multiplication by a factor of 2, to account for the two electrons in the He target. Convergence of the results was checked by varying the size of the basis set, and the model potential of He. These variances led to $\leq 15\%$ differences for the cross section, and much smaller deviations $\approx 5\%$ in the ratio R. The ratio $R_{m_{T2p}}$ is evaluated, for the three P states under consideration, using partial (M_L=0) cross sections, in accordance with known ZAPS sensitivity [180] to the component parallel to the impact velocity direction (defining the z-axis in the calculations).

In total, three cases were considered for the evaluation of R_m: The first is simply to use the $2p$ SEC cross sections provided from the 3eAOCC calculations. Since the basis included states above the C^{3+} ($1s2s2p\,^{2,4}P$) levels, it was possible to evaluate R_m including radiative cascade feeding from higher C^{3+} ($1s2snp\,^4L$) levels [5,6,81], as discussed earlier. The other two cases include radiative cascade contributions, as described in the previous sections. In order to conduct the cascade calculations, radiative branching ratios (RBR)s were calculated with the COWAN [197] code along with nl SEC cross sections to higher-lying ^4L states provided by the 3eAOCC treatment. The calculated cross sections and RBRs were then fed into a cascade matrix algorithm, described in detail in a recently accepted publication [167]. The second case for the evaluation of R included cascades from SEC populating only the $n = 3$ and $n = 4$ quartet levels and the third was also extrapolated to include all higher quartets based on an $\frac{1}{n^3}$ population model. The results of the calculations are presented in Table 2.3.

2.5.4 An R_{cc} approximation

However, such detailed cross sections are not always available, therefore an additional approach for estimating the R_{cc} is presented, developed at an earlier stage of the thesis. Using the calculations from Ref. [172], presented in Fig. 2.2 an *estimate* can be provided

Table 2.3: 3eAOCC results on the R_m ratio for the He target. First column is the energy of the carbon projectile. The second column is the corresponding $R_{m_{T2p}}$ values, calculated from the corresponding partial cross sections. The third column is the R_m value enhanced with cascades from the $\mathrm{C}^{3+}(1s2snp\ ^4L)$ levels, with $n \to \infty$. $n =3$, 4 values where directly from the 3eAOCC calculation. Higher n values were extrapolated on a n^{-3} model, also used in Ref. [81]. Finally, an estimation of the R_{cc} based on the previous columns is provided in the fourth column.

Projectile Energy (MeV)	$R_{m_{T2p}}$ (M_L=0)	R_m ($n \to \infty$)	R_{cc}
2.00	0.95	2.01	2.12
4.00	1.18	1.97	1.67
6.00	1.29	2.00	1.55
9.00	1.37	2.16	1.58
12.00	1.44	2.35	1.63
15.00	1.46	2.38	1.63

for the said enhancement. This estimation is described by Eq. 2.6:

$$\frac{\sum_{l=0}^{(n+1)-1} \sigma\left([1s2s\ ^3S](n+1)l\ ^4L\right)}{\sum_{l=0}^{n-1} \sigma\left([1s2s\ ^3S]nl\ ^4L\right)} = \frac{\sigma_{n+1}}{\sigma_n} \tag{2.6}$$

This equation assumes that the relative populations of quartets between two shells are proportional to relative total capture cross sections of these shells. This is a rough estimation that bypasses radiative and Auger yields, but can provide an upper limit for the expected enhancement of R_m and ^4P, that is given by Eq. 2.7:

$$R_{cc} = \frac{\sum_{n=2}^{n_{lim}} \sigma_n}{\sigma_{n=2}} \tag{2.7}$$

Therefore, the cascading contributions are added for all shells up to n_{lim}, and then normalized to capture to shell $n = 2$. This ensures that for $n_{lim} = 2$, the enhancement is unity. This explains the necessity for the R_{cc} to be a multiplicative term. For it to be additive, it requires absolute cross sections, where when normalized to shell $n = 2$ is less prone to induce errors.

As it can be seen, it follows a descending pattern, similar to the calculations in Ref. [5]. The small slope may be attributed to the smaller Z_P/Z_T ratio, compared to Ref. [5]. The descending pattern is due to the fact that for lower collision energies/velocities, electrons are captured to higher n shells, as depicted in Fig. 2.3. This leads to strong enhancement of the ^4P state. As the energy increases, capture to $n = 2$ is getting relatively stronger, thus the expected cascade contribution becomes weaker. In the energy range of this study, R_{cc} enhancement is limited to a factor 1.76 to 2.03 for $n_{lim} = 10$.

Commenting on the differences with the 3eAOCC results, seen in Table 2.3:

1. Qualitatively, both the calculation and the approximation exhibit stronger enhancement for the lower collision energy regime.

2. However, in collision energies closer to the ones under investigation, the approximation described by Eq. 2.6 provides with stronger enhancement. This is not
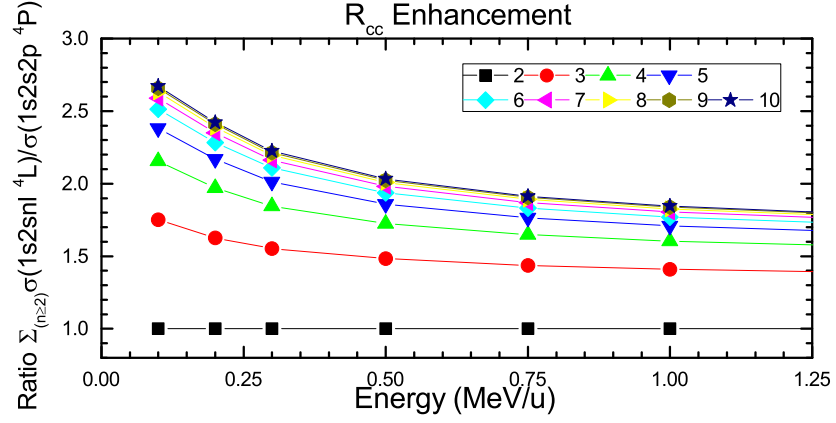
Figure 2.8: Cumulative R_{cc} enhancement for various n_{lim} values. See text for more details.

unexpected. The data for C^{4+}+He from Ref. [172], presented in Fig. 2.2, are calculations for bare Be on He. According to, Ref. [175], this calculation can describe the C^{4+}+He, when collision energy is reduced to MeV/u. That can be translated a different effective Z_P/Z_T, in a frozen core-wise manner. It should be noted that a similarly stronger enhancement is present also in Ref. [81] (2-2.5).

Chapter 3

Experimental Arrangement

Introduction

In this chapter there will be a brief description of the experimental arrangements. Both the beamline and the experimental apparatus were built as part of this thesis, based on the design of the apparatus in KSU [166]. Compared to the KSU installation, there are
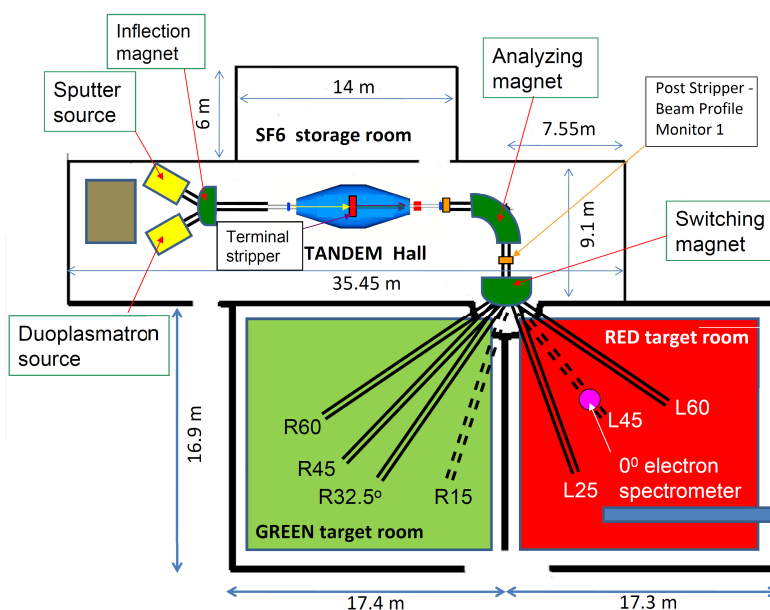
Figure 3.1: Top view of the Tandem laboratory. The experimental station is located at the Red target room, at the L45 line (See purple circle).

2 major upgrades. A new, doubly-differentially pumped gas cell is used. This allows for both higher-pressures in the target area, along with a cleaner electron path. The DAQ and the DAC electronics were also upgraded. Regarding the DAQ, a custom system was bought, designed specifically for the Multi-Channel Plates (MCP) used. The DAC was provided by Fasmatech™. It includes 10 individual DACs along with 4 low-ripple HVPSs. Also, the voltage equations for the spectrograph, along with the various lens schemes are programmed within.

The installation, setup and testing of the equipment is described in detail. Also, beyond the spectrograph and the beamline, the implementation of a GTS and a Gas/Foil Post-Stripper is summarized. The new GTS, GPS and FPS, will give access to both beams of highly charged states, along with beams of varying $1s2s\,^3S$ metastable content.

3.1 Tandem accelerator

The experimental setup was constructed and assembled in the INPP in the NCSR, Athens. The ion beams used in the experiment are produced by a Tandem Van de Graaff 5.5 MV electrostatic accelerator.

In Fig. 3.1, an overview of the Tandem laboratory is presented. Construction of the beamline began shortly after the arrival of the initial equipment in July 2013 and the first spectra were obtained by July 28, 2014.

3.2 Beamline L45

Beamline L45 is located at $45°$ left after the switching magnet with respect to beam direction, inside the Red target room. Beamline components include beam transport tubing, the various support stands, the optically aligned focusing elements, the gate valves, pumping ports, and vacuum gauges amongst others. In Fig. 3.1, the position of the switching magnet exit ports, including the L45 port exit in the Red Target room, along with various transmission elements, can be seen.
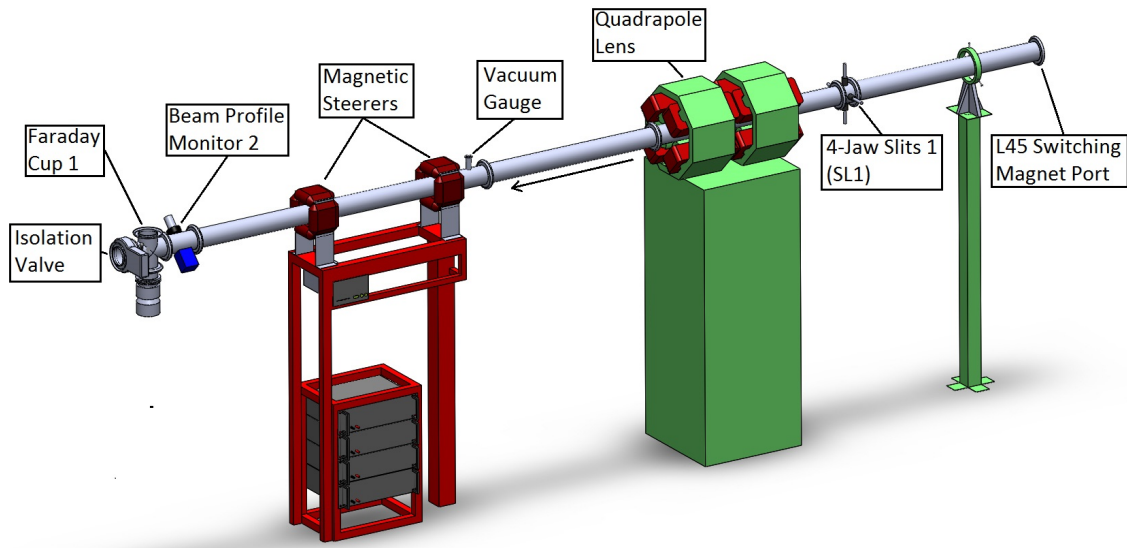

Figure 3.2: Schematic view of the beamline design from the exit of the L45 switching magnet exit port up to the isolation valve.

During the construction, a precise Computer Aided Design (CAD) schematic view of the beamline design was made with the use of Solidworks™ software, shown in Fig. 3.2. These components, with respect to the direction of the beam, are: the upstream 4-jaw slits, referred as Slits No1 (SL1), the Electromagnetic Quadrupole lens, the vacuum gauge (Leybold ITR 90 [198]), the magnetic parallel steerers, Beam Profile Monitor 2 (BPM2), the 400 lt/s turbo pump (Leybold 361C), and the pneumatic Faraday Cup 1 (FC1).

Slits The setup contains two 4-jaw slits, SL1 and Slits No2 (SL2), for beam alignment and manipulation. The distance between SL1 and SL2 is estimated $\approx$4.45 m. Between the two slits, is the beamline quadrupole, and a pair of XY electromagnetic steerers, as shown in Fig. 3.2. The first slit is placed after the L45 port exit and the second before the target 6-way cross chamber. SL1 is considered the upstream stable point. It is the preferred calibration option for the alignment telescope for two reasons: It is located on

the L45 switching magnet port, which was initially used for the telescope placement. Also, since it is located at the furthest from the telescope it minimizes possible errors in the telescope calibration.
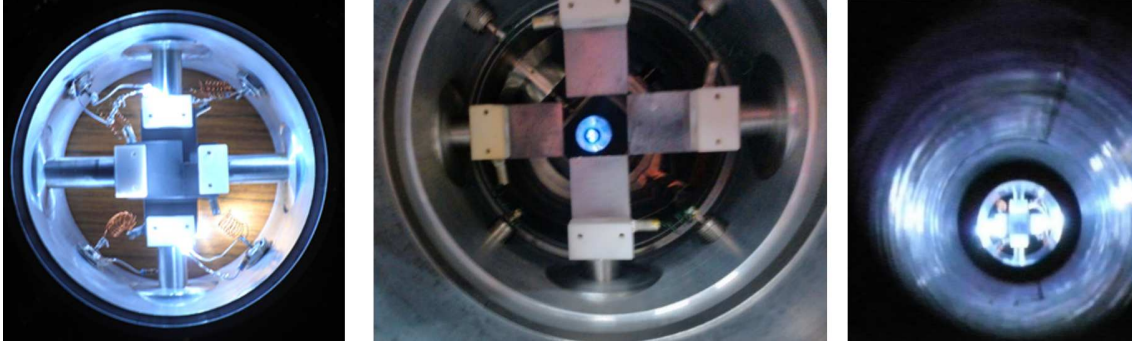

Figure 3.3: 4-jaw slits. From left to right: (Left) Connectivity tests for proper LED operation. (Middle) Both slits in place, and the SL1 powered on. (Right) Zoom to the lit SL1.

Slit central positions in mm				
Slit position	Up	Left	Right	Down
SL1	4.00	3.50	2.64	3.60
SL2	6.40	12.20	8.95	8.55

Table 3.1: Slit center settings. This setting are used for the telescope alignment and for setting well-defined apertures for the ion beam.

Typical collimation values for SL1 were 6×8 mm^2, where the 2nd value corresponds to the horizontal axis. These values were selected due to the focal properties of the closely located switching magnet. For SL2, typical values were $1.5\text{-}2.5 \times 1.5\text{-}2.5$ mm^2 depending on the transmitted current and the levels of background in the spectra. It should be noted here that the smallest aperture of the gas-cell (first) has a diameter of 2 mm. Therefore, the setting of 2.5×2.5 mm^2 was the largest used, and was used mostly for current maximization.

3.3 Vacuum

3.3.1 Vacuum measurement

Vacuum monitoring is required to ensure low background, eliminate beam collisions with air particles and optimize the passing of the ion beam. For all three vacuum gauges the selected controller model was Oerlikon Ionivac^{TM} ITR 90, in variations depending on the connection valve. It incorporates both a Bayard Alpert hot-cathode ionization measurement system for pressures $< 2.0 \times 10^{-2}$ mbar and a Pirani measurement system for pressures $> 5.5 \times 10^{-3}$ mbar [198]. In the overlapping pressure range of $2.0 \times 10^{-2} > \cdots > 5.5 \times 10^{-3}$ a mixed signal of the two measurements is displayed, thus providing a continuous scale from atmospheric pressure to high vacuum, to ultra-high vacuum. Another critical feature of these gauges is the absence of any permanent magnets. The leaked field within the apparatus would affect the trajectories of low-energy electrons.

Vacuum gauges are placed at:

1. **Analyser Chamber** The value of the pressure inside the chamber is the criterion for the activation of the MCP, since it is operated on high voltages[1]. Typical operating values of this chamber *without* any target gas load are $\approx 1 - 3 \times 10^{-7}$ Torr. Low vacuum pressure is also important for maintaining low background in the electron spectra.

2. **Gas Cell Cross** A low pressure at this part of the beamline provides a good estimation of the efficiency of the doubly differentially pumping of the target gas-cell.

3. **Beamline** The 3rd vacuum gauge was installed between the quadrupole and the target gas cell. Future modifications include the connection between the vacuum gauge controller and the isolation valve of the L45 beamline for the safe operation of the accelerator.

3.3.2 Vacuum pumping

- Chamber. The chamber is pumped with the use of a TurboVac TMP600C™ [199][2], installed at the lower CF160 flange. It is backed by a SC15D™ oil-free pump [200]. Both the chamber and the gas target require the use of oil-free pumps to avoid any contaminations.

- Gas Cell area. The gas cell area is pumped with the use of a TurboVac TMP600C™, installed at the lower CF160 flange. Additionally, an SL80H™ [201][3] is installed on the top of the 6-way cross for the doubly differentially pumping of the target gas cell, see Fig. 3.10. Both turbo pumps are backed by one SC30D™. Both backing pumps are placed on styrofoam blocks for vibration absorption.

- Beamline. The setup is similar to other beamlines in the Tandem Laboratory. It consists of a TurboVac TMP361C™ [199][4] backed by a Trivac D16B™.

After roughly two days of pumping the system attained a vacuum of about 10^{-7} Torr, with the specific pressure recorded as follows: Collision chamber: 1.3×10^{-7} Torr, Target 6-way cross: 2.5×10^{-7} Torr, L45 beamline: 1.2×10^{-7} Torr, as shown in Fig. 3.5.

3.3.3 Vacuum testing

After the installation of the Baratron unit (see Subsection 3.4.3 for details) for the gas target, and baking of the beamline, the apparatus was tested for a range of H_2 and He target gas pressures. Light gas targets are considered the best candidates for ion-atom collision experiments due to their simple atomic structure. They are also used for benchmarking, since they present the lowest pumping speeds [199, 201]. The gas cell pressure ranged between 0 and 50 mTorr. Beamline valve was closed, to avoid contamination from the accelerator's vacuum systems support. At the end of each measurement, the gas supply is turned off. The deviation from the initial value is set to be the measurement uncertainty for all. For each measurement, a 10 second period was set as stabilization time. The MKS pressure transducer was pre-heated for a period of 24 hours. No spectrometer was present in the spectrograph chamber, due to maintenance. The results are presented in Fig. 3.4.

---

[1]The typical value of voltages across the MCP ranges from 1.8 kV to about 2.2 kV.
[2]N_2 pumping speed for the TMP600C™ is 560 l·s^{-1}
[3]N_2 pumping speed for the SL80H™ is 65 l·s^{-1}
[4]N_2 pumping speed for the TMP361C™ is 345 l·s^{-1}
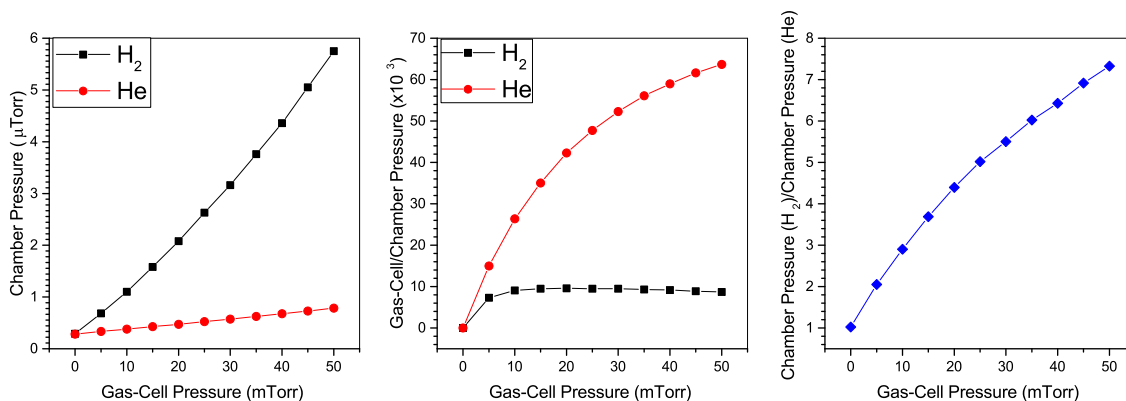
Figure 3.4: Chamber pressure as a function of the gas cell pressure. [*Left*] Chamber pressure as a function of the gas load in the gas cell for H_2 and He. [*Center*] Ratio of chamber pressure over to gas cell pressure for both gases. For H_2, a plateau in the ratio is appearing for gas cell pressures higher than 10 mTorr gas load. For He, higher gas-cell over chamber pressure ratios are achievable. [*Right*] Ratio of the chamber pressure with H_2 over chamber pressure with He as a function of gas cell load.
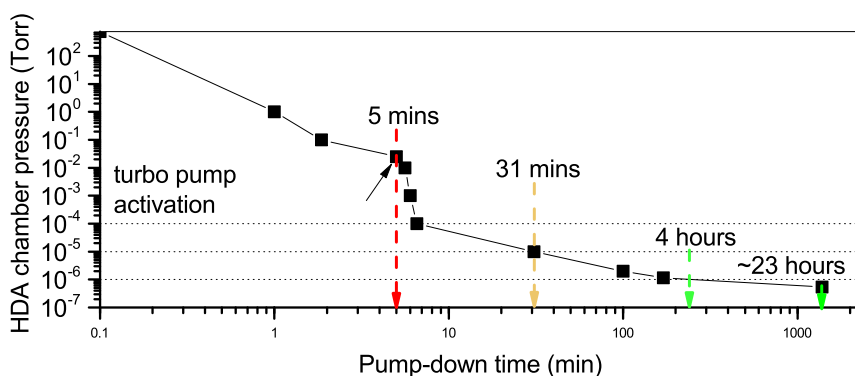

Figure 3.5: Chamber vacuum as a function of time during pump down.

The results showing higher chamber pressures for H_2 can be initially attributed to the lower pumping speeds relatively to He [199]. Additionally, the vacuum gauges are calibrated for either air, O_2, CO or N_2 [198]. Use of H_2 or He requires a correction factor of 2.4 or 5.9, respectively. Therefore, regarding the comparison of the two gases, a proper comparison would require the multiplication of the He results (or the respective division of the H_2 results) by a factor of 2.458. The MKS Baratron pressure transducer, used for measuring target gas pressure inside the gas-cell, does not depend on the gas.

3.4 Target Gas-cell

3.4.1 Doubly Differentially pumped gas cell

A low (2-4$\times 10^{-7}$ Torr or better) chamber pressure with a fully loaded (5-40 mTorr He or H_2) target gas cell is crucial for obtaining high quality, low background electron spectra. This is accomplished through the use of a doubly differentially pumped gas cell with its own independent pumping system, a concept first tried out in KSU ([166, 202]). The concept of the doubly differentially pumped gas cell is the combination of an inner gas

33
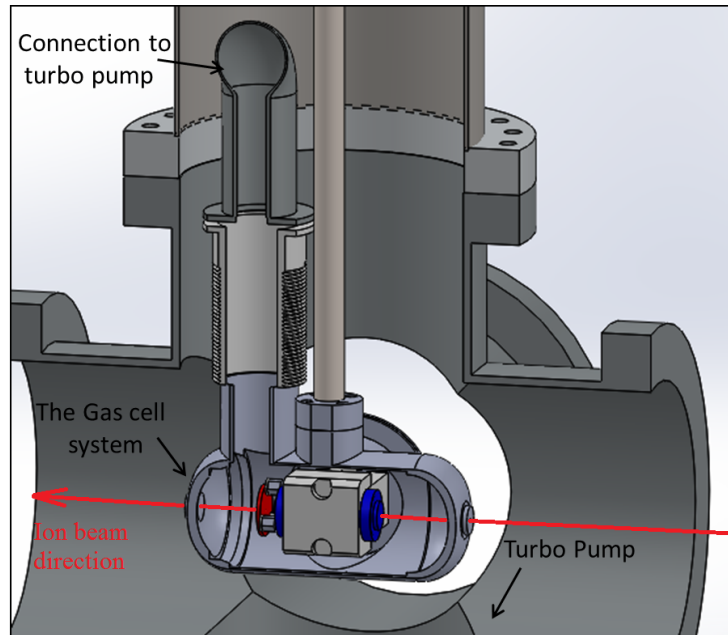
Figure 3.6: 3-D Schematic of the doubly differentially pumped gas cell [61].

cell for the target gas and a second outer gas cell that encompasses it. This outer gas cell is connected with a small turbo pump that pumps the volume inside it. This is done to avoid any contamination of the beamline by the target gas. The system is supported by a XYZ translation stage [61] and is placed inside the target 6-way cross. This translation stage was constructed in the machine shop, on August 2014, for the APAPES beamline. At the bottom flange of the 6-way cross a TurboVac TMP600C™ turbo pump is installed for this area, as mentioned in Subsection. 3.3.2.

3.4.2 Aperture dimensions

The initial dimensions of the target gas cell aperture are presented in Table. 3.2. In order to improve the beam transmission though the gas cell while maintaining the differential pumping conditions, we increased the aperture values as presented in Table 3.2. The vacuum conditions achieved with the larger openings in comparison to the initially smaller are presented in Fig. 3.7

3.4.3 Gas feed through and pressure stabilization unit

A MKS Baratron pressure transducer and a control gas supply valve are used in the experiment for the control and stabilization of the pressure. The system consists of an MKS 390H pressure transducer, an MKS 248 control valve[5], an MKS 250E pressure controller and an MKS 270D signal conditioner [203–206]. The purpose of this setup is a controlled gas-target pressure in the mTorr regime. The gas pressure is measured at specific time intervals set by the unit and a feedback is provided to the signal conditioner unit that communicates with the valve control unit. The valve control unit then, responds to the information from the pressure controller unit and increases or decreases the flow of gas in order to stabilize the pressure. The complete system has a supply of four target gases (H_2, He, Ne and Ar).

---

[5]Model 0248A with a flow range of 100 sccm≡1.27 torr·l/s^{-1}.

Table 3.2: Characteristic dimensions of the target gas cell.

| Gas cell dimensions		
Apertures (circular)	New Diameter (mm)	Old Diameter (mm)
A1 outer cell entrance	2.0	1.8
A2 inner cell entrance	2.5	1.7
A3 inner cell exit	2.5	1.8
A4 extra aperture	2.5	1.8
A5 outer cell exit	2.5	2.5
Inner cell length (outside dimension)	49.8	
Outer cell length (outside dimension)	140	
Inner cell diameter (outside dimension)	25	
Outer cell diameter (outside dimension)	63	
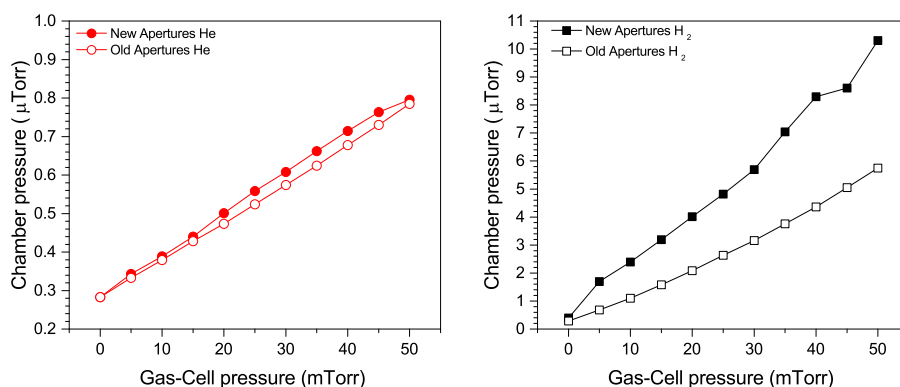
Figure 3.7: Comparison of old and new gas cell apertures. [*Left*] In the case of He, there is a minor slope increase. Correction was applied for different base pressure. No drastic changes are expected for the new apertures. [*Right*] However, in the case of H_2 a substantial increase in the slope of the data points is present. This indicates that for the lower molecular weight gas target, the change in aperture size has led to a loss in pumping capability.

3.4.4 Electrical connections

There are two electrodes, connected to two different points of the inner gas cell. The first electrode is connected to the inner gas cell, and is used for controlling the kinetic energy of the electrons generated inside it by applying a biasing voltage to it. This is useful for separation and identification of metastable from prompt states [207]. The second electrode is connected to an aperture 7.5 mm away from the exit of the inner gas cell and is typically used at ground potential. When the inner cell is biased this aperture limits the electric field to just the space between aperture and gas cell exit. It should be noted that by applying voltage to the gas cell, it may function as a lens, since the external gas cell is grounded by default. This means that this technique is mostly used for trouble-shooting, rather than accurate cross-section measurements. The inner gas cell is supported by an acetal resin (Delrin™) base which is an insulator. This way the inner gas cell remains electrically isolated from the outer gas cell. In order to avoid charge up of the Delrin™ base it had to be covered with graphite spray.
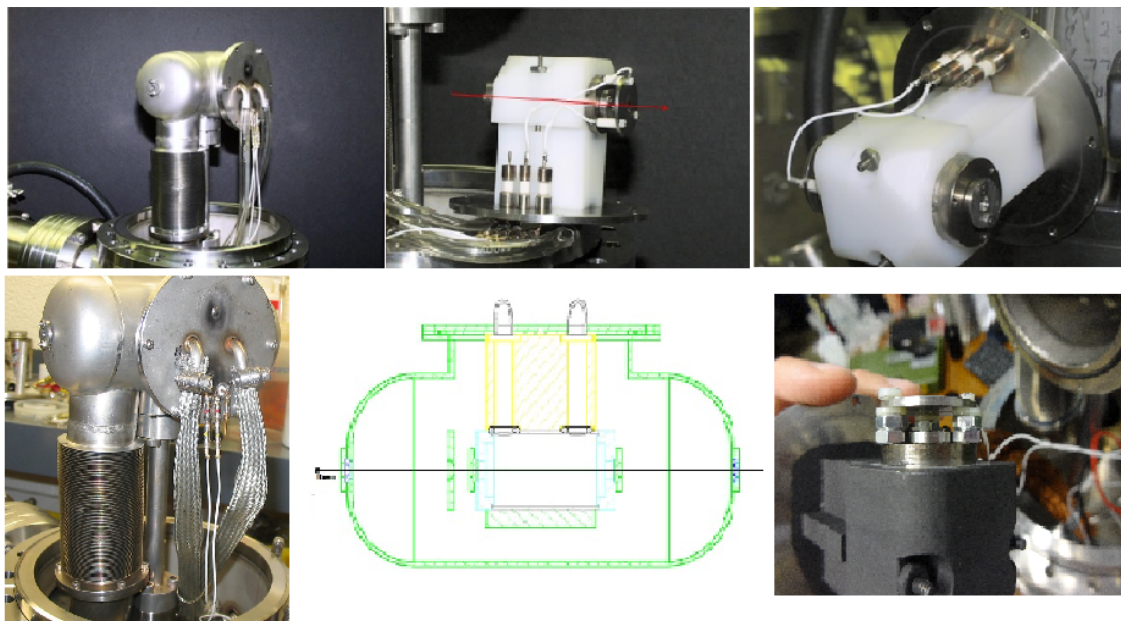
Figure 3.8: The target gas cell.

Figure 3.9: Gas delivery system. From left to right: MKS 390H pressure transducer, MKS 250E pressure controller and MKS 270D signal conditioner and last, the gas manifold.

3.5 The Hemispherical Deflector Analyzer

The spectrograph under investigation is a *paracentric* HDA. The term *paracentric* derives from the fact that the entrance aperture is asymmetrical to the hemispherical electrodes of the analyzer. More particular, the entrance radius[6] is smaller the the mean radius of electrodes of the HDA (see Table 3.5). It has been shown [157, 160, 208, 209] that this configuration results to improved energy resolution. This is accomplished by taking advantage of the strong intrinsic lensing properties of the existing HDA fringing fields.

The spectrograph consists of the HDA, the 4-element focusing lens and the PSD. In this section, the HDA is described. The HDA consists of two hemispherical shells with inner R_1 and outer R_2 radii of 72.4 mm (2.85″) and 130.8 mm (5.15″) respectively. This corresponds to a mean radius of $\overline{R} = \frac{R_1+R_2}{2} = 101.6$ mm, while the paracentric entry is at $R_0 =$82.6 mm. In Table 3.5, all necessary dimensions are tabulated. The spectrograph is depicted in Fig. 3.10.

The four-element lens is also supported on this plate where the exit lens element and plate are on the same potential $V_p = V_{L2}$. Finally, there is a support plate, on which

---

[6]Distance from the center of the hemispheres
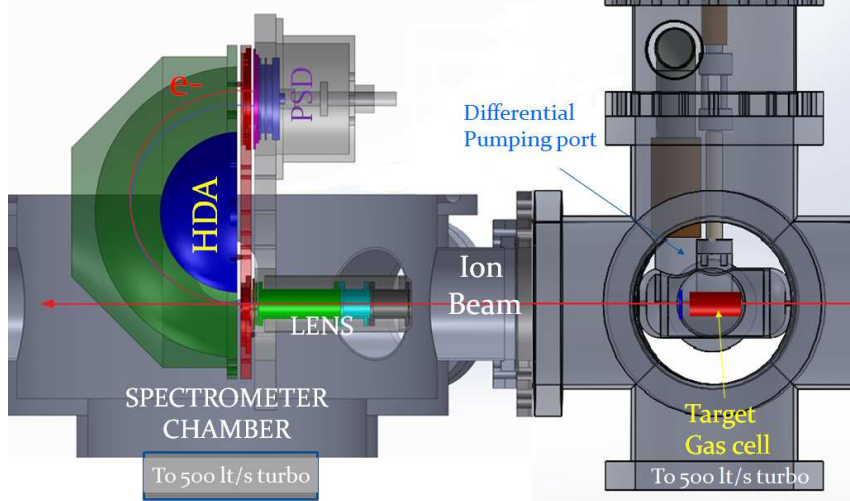
Figure 3.10: The experimental apparatus. The red arrow shows the beam alignment along with the (forward) emitted electrons. It consists of a doubly differentially pumped target gas cell, along with paracentric HDA with 4-element injection lens and 2-D PSD. Each color denotes a different electrode voltage. The length of the gas cell is 49.8 mm and the distance of its center to the lens entry is 286 mm [61]. Ions go through the spectrometer and are collected by Faraday Cup 2 (FC2). Schematics of the collision chamber and gas cell are from Ref. [210].

the relative ground plate and the housing of the PSD are placed. The basic geometrical parameters of the setup are given in Table 3.5 on p. 56.

On the relative ground plate a pair of 90.0% transmission copper [211] grids is placed. It's purpose is to shield the analyser from external fields and to correct fringing fields produced from large openings. The latter is achieved by setting it also on V_p potential. After the grid pair, a 3rd 90.0% grid is placed, electrically isolated from the pair. This grid is set at a slightly more negative voltage than the V_p, usually V_p - 9-38 V. It serves as a filter for background electrons generated from inside the spectrograph [166], which are much more evident in the high resolution mode of the spectrograph. The combination of these grids leads to a $1 - 0.90^3 = 1 - 0.729 = 27.1\%$ loss in transmission, which is treated in the data analysis.

3.5.1 Analyser Voltages

The HDA has been studied extensively in the literature [157–160, 212–216]. From the analysis of the general trajectory equation, of an ideal HDA, the voltages of the inner and outer hemispheres must satisfy the following equation for a central electron trajectory of energy W [216]:

$$qV_{R_i} = \frac{W}{F} \left\{ F - \gamma \left(\frac{R_0}{R_\pi} \right) \left[\frac{R_0 + R_\pi}{R_i} - 1 \right] \right\} \qquad (i = 1, 2) \qquad (3.1)$$

where F is the deceleration factor and q is the electron charge $q = -|e|$. W is the undecelerated tuning energy of the spectrograph. R_0 and R_π are entry and exit radii respectively. Parameter γ is an independent variable which sets the entry bias $V(R_0)$ [157]. It is defined as $\gamma \equiv 1 - \frac{qV_0}{E_0}$ with $V_0 \equiv V(R_0)$ being the value of the potential at R_0 [217]. The plate electrode V_p determines final electron deceleration. By biasing V_p to particular values, related to the tuning energy W according to Eq. 3.2, passing energy $w \left(= \frac{W}{F} \right)$ is

set to smaller values, depending on deceleration factor F.

$$V_p = w - W = \frac{W}{F} - W = W\left(\frac{1}{F} - 1\right) \leq 0 \tag{3.2}$$

3.5.2 Deceleration mode

The concept behind the HDA's deceleration mode is the improvement of the spectrograph's resolution. The resolution of every electron spectrograph is a function of its geometrical parameters. For the ideal HDA the *base* energy resolution is given by the following formula [215]:

$$\mathcal{R}_B \equiv \frac{\Delta E_B}{E_0} = \frac{\Delta r_0 + \Delta r_\pi}{D_\gamma} + \alpha_{max}^{*2} \tag{3.3}$$

where

Δr_0 is the the diameter of the entry aperture or slit (real or virtual). The particular spectrograph does not have an actual entry slit. For the needs of the ZAPS technique, the ion beam has to pass through the spectrometer, therefore the actual diameter of the entrance is 6 mm. The functional diameter is defined by the focusing of the lens. Therefore, this is referred to this as a *virtual* slit.

Δr_π is the exit slit of the electron analyzer. If a PSD is used, then this quantity corresponds to spacial resolution of the PSD.

D_γ is the dispersion length. It is defined [159, 215, 216] as the magnitude of image displacement caused by a small change in the reduced pass energy, divided by the relative energy change, for the same initial pass energy:

$$D \equiv \tau \left[\frac{\partial r_\pi}{\partial \tau}\right]_{r_\pi, \tau} \tag{3.4}$$

whereas for the *ideal* HDA is given by [215]:

$$D_\gamma = \left(\frac{R_\pi + R_0}{\gamma}\right)\frac{R_\pi}{R_0} \tag{3.5}$$

α_{max}^* is the maximum angle of incidence at the HDA entry.

Reduced pass energy τ is defined by Eq. 3.6, where T and t are the initial and post-deceleration kinetic energy of the electron:

$$\tau \equiv \frac{t}{w} = F\left(\frac{T}{W} - 1\right) + 1 \tag{3.6}$$

Base energy resolution $\mathcal{R}_B$ is a constant, to first order. As mentioned above, it depends only on the geometrical parameters of the analyzer. In systems with a deceleration mode, it is the *overall* base resolution $\Re_B$ of the spectrograph that is of primary importance [159]. In most high-resolution applications, deceleration is typically used to improve the energy resolution of the HDA by decelerating the electron beam prior to HDA entry. This is accomplished by negatively biasing the last input lens element at the potential $V_{L2} = -(E_{s0} - E_0) = -(W - w) = w - W$ (The same potential V_p used on the base plate of the HDA, as described in Eq. 3.2). In this case the *overall* base resolution $\Re_B$ of the HDA is improved by the deceleration factor F, and given by Eq. 3.7 [215]:

$$\Re_B = \frac{\Delta E_B}{E_{s0}(=W)} = \frac{1}{F}\left(\frac{\Delta E_B}{E_0(=w)}\right) = \frac{1}{F} \times \mathcal{R}_B \qquad (\textit{Overall base resolution}) \tag{3.7}$$

3.5.3 Energy Acceptance Window

The energy range which can be *simultaneously* detected with linear energy dispersion in the focal plane is defined as the energy window of the analyzer [218]. For an exit slit spectrometer the energy acceptance window is the base energy width [159]. In the case of a PSD-equipped spectrograph, with d_{PSD} effective diameter, the energy acceptance window ΔT_{window} is defined as below.

The reduced pass energy is related to the position according to Eq. 3.8

$$\tau = \frac{r_\pi(\gamma + \xi) - R_\pi(\gamma - 1)}{R_\pi + r_\pi \xi} \tag{3.8}$$

with r_π being the exit radius and ξ being the HDA paracetricity defined as $\xi = \frac{R_\pi}{R_0}$ [4]. The limits of the PSD are at $R_\pi \pm \frac{d_{PSD}}{2}$ obtained at the energy acceptance limits τ_{max} and τ_{min}. Then, the reduced energy acceptance window $\Delta\tau_{window} = \tau_{max} - \tau_{min}$ is obtained by Eq. 3.8 [4]:

$$\Delta\tau_{window} = \frac{\left[\frac{d_{PSD}}{R_\pi(1+\xi)}\right]\gamma}{1 - \left(\frac{\xi}{2}\right)^2 \left[\frac{d_{PSD}}{R_\pi(1+\xi)}\right]^2} \approx \frac{\gamma}{1+\xi}\frac{d_{PSD}}{R_\pi} \tag{3.9}$$

In systems with a deceleration stage, it is the quantity $\Delta T_{window} = T_{max} - T_{min}$ that is of importance, since it depends on the deceleration factor F. ΔT_{window} can be written as [4]:

$$\Delta T_{window} = \Delta\tau_{window}\frac{W}{F} \tag{3.10}$$

The energy acceptance window ΔT_{window} is inversely proportional to the deceleration factor F. For $F = 1$, with a non-decelerated electron beam, the energy acceptance window of the current spectrograph is estimated approximately $W \pm 15\%$. For higher values of the deceleration factor F, this percentage decreases accordingly to Eq. 3.10.

3.6 Lens Voltages Optimization

A major factor on the acquisition of Auger spectra is the determination of the optimal lens voltages. In slit or aperture type HDAs, the size of their entry and exit slits/apertures primarily determines their energy resolution (Eq. 3.3). The lens's purpose is primarily to provide the highest possible transmission and resolution. Within the framework of APAPES, electron trajectory simulations, based on the experimental setup were ran by various groups [216, 219, 220]. A Monte Carlo brute-force search was applied on all possible combinations of lens voltages V_{L4} and V_{L5} [220] to obtain the optimal energy resolution for the ZAPS [181, 221] experimental setup under question.

3.6.1 Trajectory simulation data

In the ZAPS technique, electrons are measured in the direction of the ion beam. Therefore, the HDA entry aperture must be large (6 mm here) to allow the unobstructed passage of the ion beam itself. This reduces the background originating from secondary electrons produced from the ions colliding with various HDA components. The ion beam goes through the lens and the HDA itself, exiting from a hole in the back of the HDA and eventually stopped by FC2, used for ion beam normalization. The physical size of the HDA entry aperture, as a ZAPS prerequisite, however, reduces the capabilities of the spectrometer, as seen in the energy resolution formula (Eq. 3.3). Consequently, the lens system is vital

in regulating the energy resolution of the HDA. This is because, through the focusing of the electron beam, a much smaller, virtual HDA entry aperture can be defined [214]. The necessity of a focusing element can be demonstrated through direct comparison between spectra acquired with the lens activated and deactivated. Such comparison is shown in Fig.3.11: In Fig. 3.12, the elements of the focusing lens are shown. Lenses of this type use
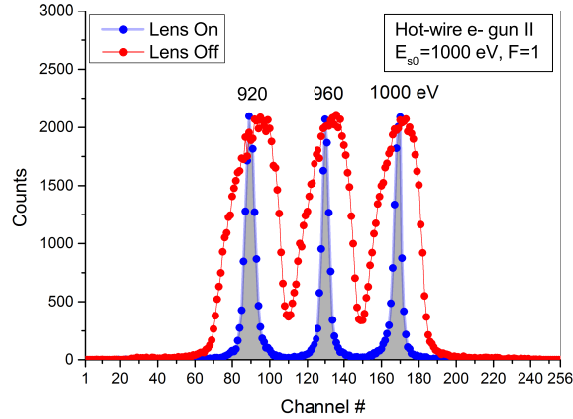

Figure 3.11: Comparison between activated and deactivated spectrograph lens. Energy spectrum produced by the hot-filament e-gun recorded on the spectrograph, without pre-retardation ($F = 1$). Resulting line profiles with the injection lens on values from Table 3.3) or off (all lens electrode voltages zero, i.e. $V_{L4} = V_{L5} = 0$), are shown as detected along the HDA dispersion direction on the PSD. The physical size of the HDA entry aperture $d_a = 6$ mm is very large, but with lens focusing, the HDA entry diameter can be made close to 10 times smaller, and amounts to an effective virtual HDA entry aperture of this size.

four or more cylindrical electrodes in order to provide both focusing and pre-retardation of electrons, to improve performance. Although these components can be studied individ-
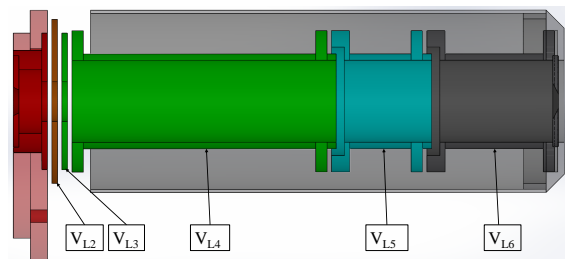
Figure 3.12: The 4-element electrostatic focusing and decelerating lens. V_{L6} is typically set to ground. V_{L5} and V_{L4} were investigated in various combinations. V_{L3} is electrically connected to V_{L4} with the use of stainless steel $1/16$ in. balls between lens elements. V_{L2} is electrically connected to V_p. Around the lens is a protective cylinder that along with the base plate of the HDA minimizes possible target gas contaminations. The outer cylinder is electrically connected to V_{L6}.

ually, the combination of such lens with an HDA and a PSD is not trivial. This required the investigation of the properties of the complete spectrograph, performed in Ref. [220]. There, the two intermediate adjustable lens electrode voltages, V_{L4} and V_{L5}, were varied over the available voltage space in a brute-force approach. Lens voltages exhibiting optimal energy resolution for the combined lens/HDA/PSD spectrograph system were sought with and without pre-retardation. In this approach all voltage polarity combinations (pos-

itive/negative) for the two electrodes were tested. However, only the combination of both negative polarities was considered practical, since it exhibited the lowest potential difference between neighbouring electrodes. This is experimentally critical for the avoidance of sparks between electrodes. The results of this approach are presented in Table 3.3.

Table 3.3: Optimal lens voltages for the both negative V_{L4} and V_{L5} case, and for various pre-retardation factors $F = 1$–10. The SIMION® [222] methods used are SIM2Dul and SIM3Dud, using the terminology from Ref. [220]. SIM2Dul is a 2D approach in which electron emission points and trajectories are on the HDA symmetry plane. In the SIM3Dud approach, the trajectories are uniformly emitted from a parallel to the beam disk, placed in the center of the gas cell. For the resolution value presented here, there are two additional aspects. These are the inclusion of a source intrinsic FWHM energy distribution of 0.25 eV and use of a PSD position resolution of 0.2 mm which approximates a 256×256 binning. The experimental resolutions are also listed on the last line with their uncertainties. Results for FWHM comparisons also shown in Fig. 3.15. Table from Ref. [220]

F	1	2	4	6	8	10	Method
Sim.							
V_p(V)	0.00	-500.00	-750.00	-833.33	-875.00	-900.00	$-E_{s0}(1 - \frac{1}{F})$
V_{L4}(V)	-695.3	-805.5	-243.4	-492.0	-633.3	-730.9	SIM2Dul
V_{L5}(V)	-663.1	-490.6	-652.9	-687.4	-697.1	-689.2	SIM2Dul
$\Delta\chi_{1/2}$ (mm)	0.330	0.440	0.505	0.577	0.649	0.732	SIM3Dud
$R_{1/2}$ (%)	0.334	0.204	0.114	0.0858	0.0714	0.0638	FWHM
Exp.							
$R_{\frac{1}{2}}$ (%)	0.474	0.235	0.108	0.0794	0.0665	0.0573	Fil. e-gun
$\Delta R_{1/2}$ (%)	±0.069	±0.008	±0.013	±0.0047	±0.0057	±0.0038	Meas.

3.6.2 Experimental approach

During the installation of the DAQ, a hot-filament e(lectron)-gun was constructed for testing. First version of the e-gun was a simple light bulb circuit with two AA (2×1.5 V) batteries in series, with glass removed from the bulb. The circuit is floated to the desired potential $V_{e-gun} = \frac{W(eV)}{e}$ V, to control the energy of the emitted electrons. The first version can be seen in Fig. 3.13.

The structure is placed on a teflon base, and supported under the target gas cell. The potentiometer is for adjusting current flow, and subsequently the electron emission. Filament current required attenuation for two reasons: First, there is an excessive electron production when driving the filament with high currents. This leads to increased space-charge for the electron beam, emission of secondary electrons, etc. Moreover, even at medium currents, filament temperature tends to spread the energy of emitted electrons. Therefore, the electron beam is not monoenergetic, but velocities follow a Maxwell{Boltzmann distribution, which can affect resolution measurements.

For the second version of the e-gun, e-gun II, a copper casing was constructed. It also included an ≈ 1.5 mm $\varnothing$ aperture in front of the filament. This version can be seen in Fig. 3.14. SIMION® [222] qualitative simulations were used to define a better geometry for the design. These simulations showed that the use of an outer grounded
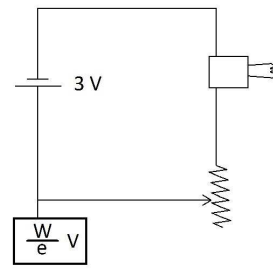
Figure 3.13: *Left:* First version of the hot-filament e-gun. The bulb is placed on a teflon isolating base. *Right:* Electric diagram. A variable resistor is placed in series with the filament, controlling current flow, and thus, electron production. See text for more information.

shell improves transmission. Moreover, it also improved electron beam focus, which in turn made the gun less sensitive to current fluctuations. Finally, a grounded shell minimizes the possibility of sparks.

Figure 3.14: Hot-filament e-gun MKII. *Left:* The bulb and the socket are placed within an aluminium cylinder. An aperture is placed in front of the filament. The filament, along with the socket and the aluminium casing are floated at the desired potential, usually around -1000 V. A teflon base was constructed with a lathe, with the necessary holes for vacuum pump down. *Middle:* A copper casing with a corresponding aperture surrounds the filament casing. This casing is on ground potential. *Right:* The e-gun assembled. All casings were constructed on the lathe, to ensure proper alignment.

In Fig. 3.15 (taken from Ref. [220]) the results on resolution measurements using the calculated voltages with the aforementioned e-gun are shown. For every pre-retardation factor used, a set of three peaks is acquired. With these, the energy axis of the spectra is calibrated, the peak widths are measured and overall achieved resolution is calculated. The intensity of the electron beam was monitored with the use of the DAQ (count rate), and controlled with the intensity potentiometer. Minimizing intensity provided with almost a monoenergetic beam. As it can be seen, resolution measurements are in very good agreement with the trajectory simulations.

3.7   The 2D-Position Sensitive Detector

The 2-dimensional PSD is a sensor provided by Quantar™, model 3394A [223]. It consists of a pair of MCP's with a diameter of 40 mm that act as electron multipliers and a Resistive Anode Encoder (RAE). The MCP is an array of closely spaced small holes in a highly resistive material. Application of a high voltage produces a large electric field across the typically thin 2 mm thickness of the MCP. Incident charged particles, or photon-
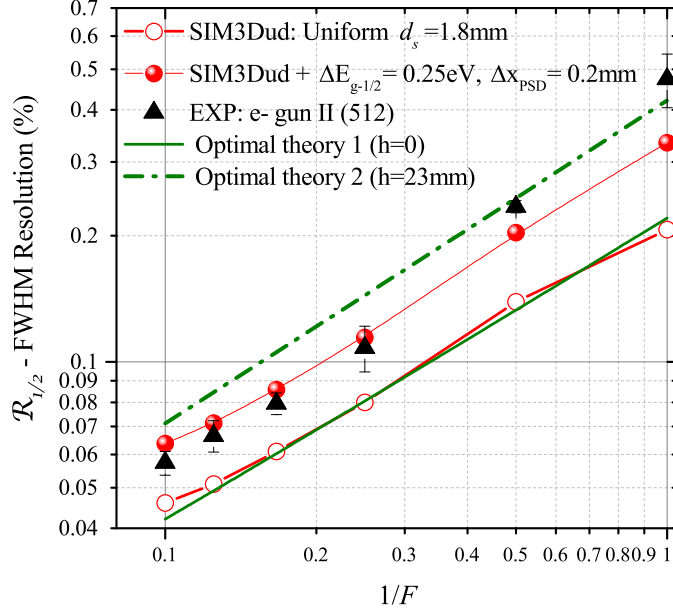
Figure 3.15: $R_{\frac{1}{2}}$ FWHM energy resolution is plotted as a function of $1/F$ for pre-retardation factor F, from Ref. [220]. Comparison between simulation and experiment for the lens voltages obtained and listed in Table 3.3. (Black triangles) Hot-filament electron gun results. (Open red circles) SIMION® [222] results for a uniform distribution of a disk source with diameter $d_s = 1.8$ mm (method SIM3Dud, see Ref. [220] for details). (Red spheres) SIM3Dud results also including effects of a source intrinsic FWHM energy distribution $\Delta E_{g-1/2} = 0.25$ eV and a PSD position resolution $\Delta\chi_{PSD} = 0.2$ mm. Lines: Ideal HDA optimal theory computed assuming i) source diameter $d_s = 1.8$ mm, ii) two values for PSD distance h from HDA plane.

induced secondary electrons inside the microchannels, lead to an electron cascade in the microchannel. Typical dimensions of microchannels are holes with a diameter of 10 µm, whereas the center-to-center distance is 15 µm. The holes through the MCP's are often set at 8° from the surface normal. When two or more MCP′s are used, the 2nd MCP is rotated by 180°, so that the holes of the 1st and the holes of the 2nd MCP form a *chevron* shape. This arrangement allows the electrons to exit the 1st MCP, and continue the electron cascade in the 2nd. This also reduces the ion feedback, where positive ions produced by electrons colliding with residual gas molecules[7] or gas molecules desorbed from the channel drift back onto the channel input. In certain cases, these ions can produce additional secondary electrons, resulting in a regenerative feedback situation [224]. In Fig. 3.16 a schematic for the operation of the MCP′s is presented.

Secondary electron production depends on the overall V_{MCP}. This voltage is divided into three voltage fractions. To obtain stable voltage ratios between the stages of the PSD, a resistor chain/voltage divider was used, and can be seen in Fig. 3.18. The two first are equal in amplitude (≈45%) and they are used to control the gain of the MCP. As a result, V_{MCP} acts partially as a gain factor for the MCP's. The last ≈10% of overall V_{MCP} is used as an extraction voltage for the collection of secondary electrons on the RAE surface. The correct value for the V_{MCP} depends on the output of the MCP's and depends on their condition. It should be noted that higher values can lead to quicker "wear out" of the MCP's. However, a dependence between V_{MCP} and spectrum line resolution has

---

[7]At ambient pressures greater than 1.0^{-6} Torr
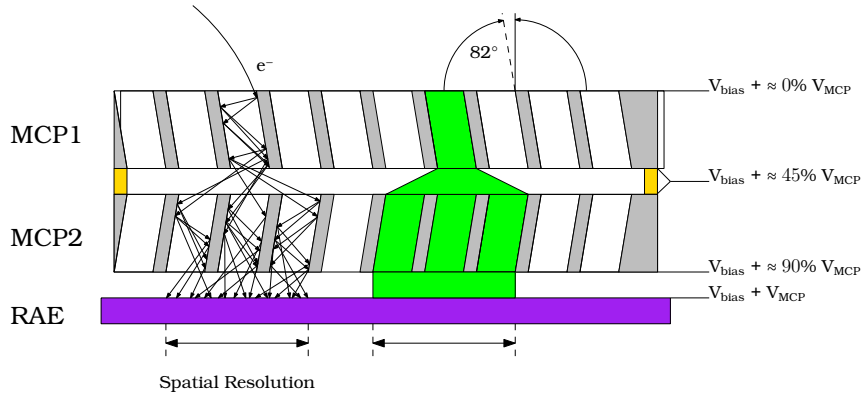
Figure 3.16: The operation of the Chevron arranged MCP of use in the PSD. The green areas denote the uncertainty in the position of the incoming electron over the RAE. V_{bias} is a voltage applied to the entry MCP to ensure that the impact energy of electrons, and therefore the MCP efficiency, is always the same, independent of the initial kinetic energy of the emitted electron.

been observed. In order to find the optimal V_{MCP}, the widths of monoenergetic electron produced by the hot-filament e-gun were measured as a function of the V_{MCP}. Results are presented in Fig. 3.17. For every set of measurements, the spectrograph was run in high resolution mode, where deceleration ratio (F) was set to F=4. The tuning energy W of the analyser was 1000 eV. The electron beams produced were set at 980, 990 and 1000 eV, for energy calibration of the analyser. Plotted data include both best width and average width of the three peaks. E-gun current was set to lowest value, since a connection between intensity and line peak width was observed. Lens voltages used were computed by a Monte Carlo method in SIMION® [222] [220]. Fig. 3.17 shows a 3D depiction of one of the measurements.
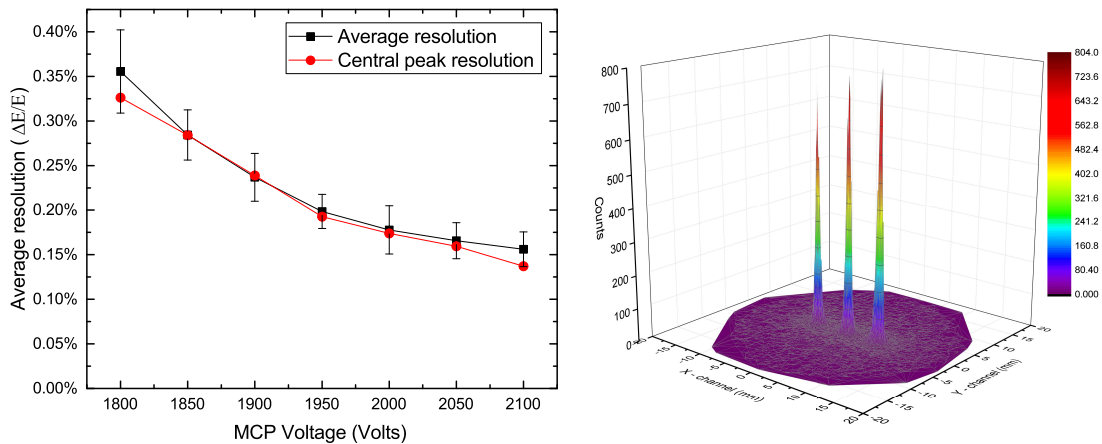
Figure 3.17: *Left*: Resolution as a function of MCP voltage. The trend of the measurements indicate that higher V_{MCP} values are preferable. However, the value of +2050 V was used to avoid "wear out" of the MCP's. *Right*: 3D plotting of hot-filament e-gun measurements. Co-ordinates in pixels were converted to mm. MCP voltage is set to +2050 V.

3.8 Electronics

The complete electronic setup is presented in Fig. 3.18. In general, the electronics of the setup are divided into two categories. The control of the various voltages of the spectrograph, mostly precision HVPS's, and the DAQ.
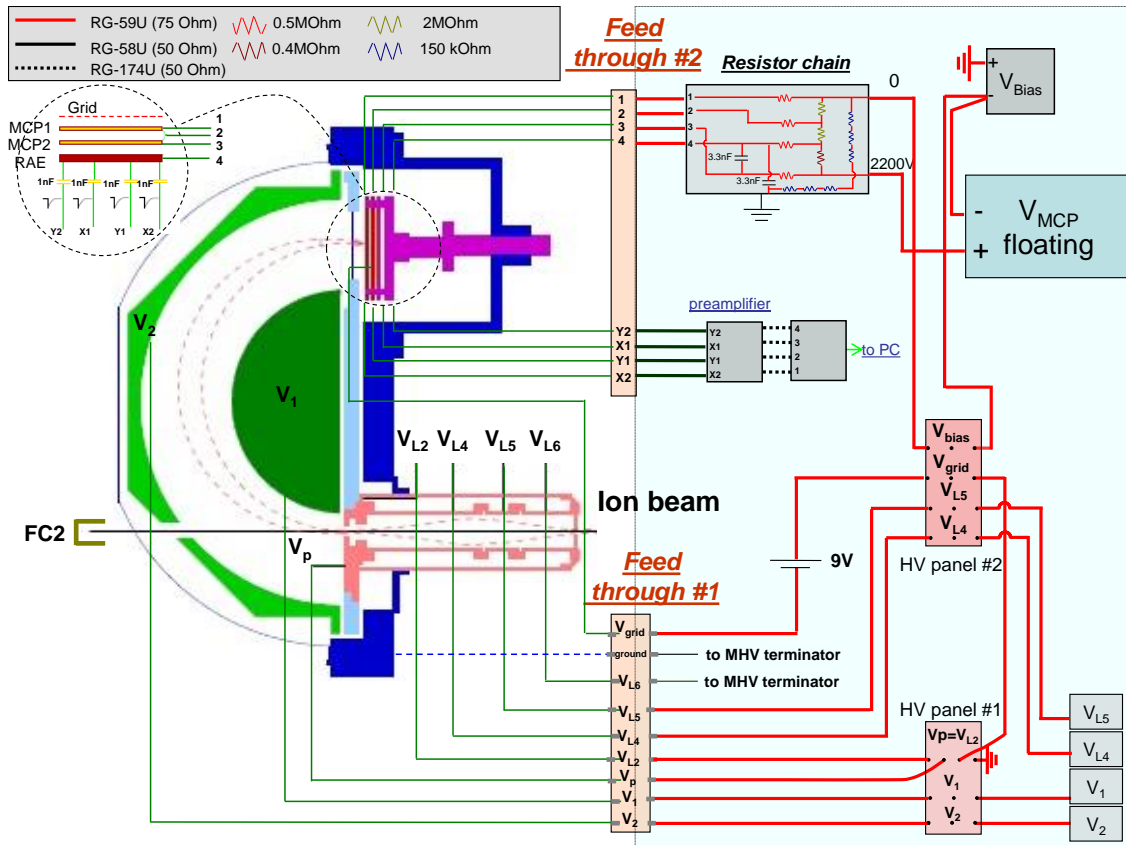
Figure 3.18: The complete setup of HDA and PSD electronics. All HVPS are computer controlled through the Fasmatech™ control unit.

3.8.1 Power supplies

The are three categories of HVPS:

1. **HMI** The HMIs are high precision HVPS provided by the Hahn-Meitner-Institut [225] with fixed predefined polarity and the lowest ripple[8] even at higher voltages amongst the three types of HVPS used.

2. **Tennelec** The Tennelec HVPS [226] have invertible polarity, however, they need to shut down before any polarity change. Although not comparable to the HMI's, they exhibit sufficient stability for the high resolution spectroscopy and were placed on electrodes that rarely require polarity changes.

3. **Applied Kilovolts** The Applied KiloVolts HVPSs can digitally reverse their polarity but at the cost of 1 bit. This drops their internal DAC's resolution to 15 bits. Taking

---

[8]Absolute error 0.2% and additionally 0.1%/kV.
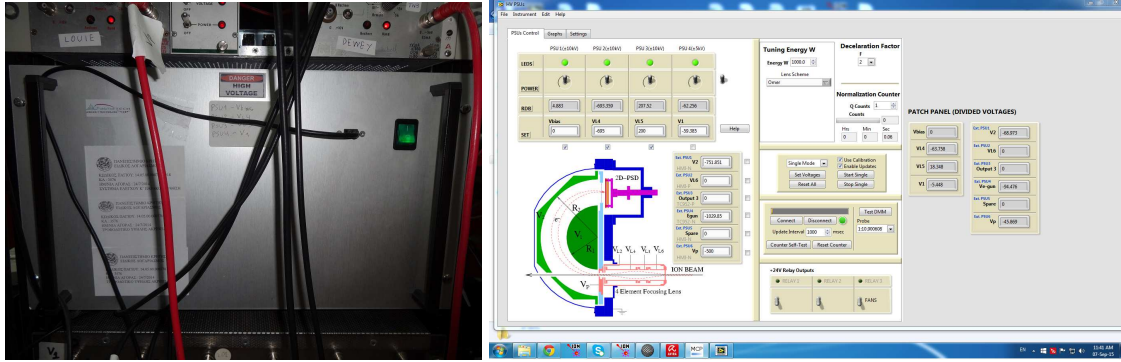
Figure 3.19: *Left*: Fasmatech Rack-mount Unit. It consists of a custom made DAC, 4 HVPS and a USB connection. On the back, there are 6 pairs of DAC output to control up to six HVPS through *fine* and *coarse* inputs. *Right*: The Fasmatech Labview™. The voltages deriving from the equations of motion of a charged particle inside a HDA were coded in the program. The user selects the W - Tuning Energy of the spectrograph, the Deceleration Ratio (F) for high-resolution spectra, the position of the central ray, the impact energy of analysed electrons and the voltage scheme for the focusing lens. With the use of the DAC, an additional external HVPS was used to control the energy of the hot filament e-gun.

all that into consideration they were connected to specific voltages of the apparatus. They are integrated inside the rack mountable unit provided by Fasmatech. Specifically, inside the Fasmatech unit there are:

(a) 3 Applied KiloVolts model HP010RAA025 [227] with a ±10 kV range.

(b) 1 Applied KiloVolts model LS005RIP010 [228] with a ±5 kV range.

To provide the V_{bias} for the MCP the 3 kV floating HP 6515A unit was chosen which had also been used with success in KSU.

3.8.2 Correction to voltage calibration

In principle, a HVPS is a voltage amplifier. A voltage is used as input, which is accordingly amplified by a gain factor. Both Tennelec and HMI HVPS exhibit a "coarse" and a "fine" voltage input. The purpose of the dual input is to increase the precision of the HVPS. Both inputs accept 0-10 V DAC signals. The difference between the 2 channels is the gain factor. In the case of the HMI HVPS, gain factor for the coarse channel is set at 500 V/V, while for fine is set at 10 V/V. Therefore, regarding DAQ outputs with similar bit depth, the use of a second, lower-gain fine channel can provide with a 50-fold[9] improved HVPS accuracy. However, in order to achieve this accuracy, proper implementation is required.

The first implementation of this scheme is presented in Fig. 3.20. Under this scheme, each assigned voltage is partitioned into two numbers:

- A multiple of 100 V, which is assigned to the coarse channel (Ust=100*div(voltage,100)).

- The remaining required volts, assigned to the fine channel (Uhand=mod(voltage,100)).

For an example value of 345.45 V, Ust is assigned 300 V and Uhand is assigned 45.45 V. After the voltage distribution, voltages are calibrated according to the scheme presented in Fig. 3.21. At this point, it should be reminded that the calibrated values are the values

---

[9]Actual improvement depends on the ratio of coarse over fine gain factors.
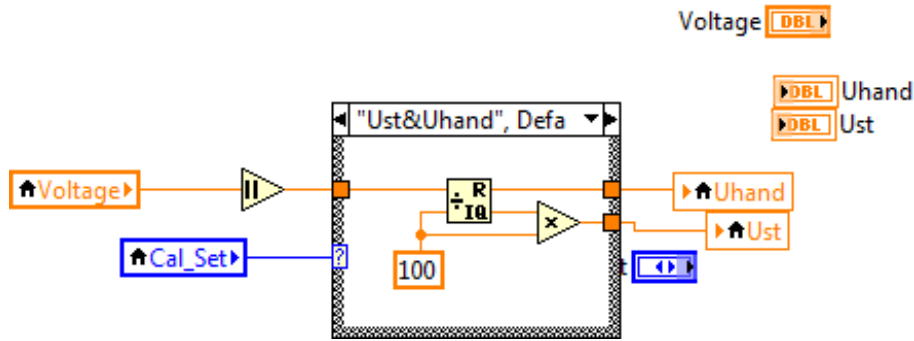
Figure 3.20: Voltage distribution to "coarse" and "fine" channels. Coarse channel is set to (required) multiples of 100 V, and fine channel handles the remaining volts required. See text for detailed explanation.
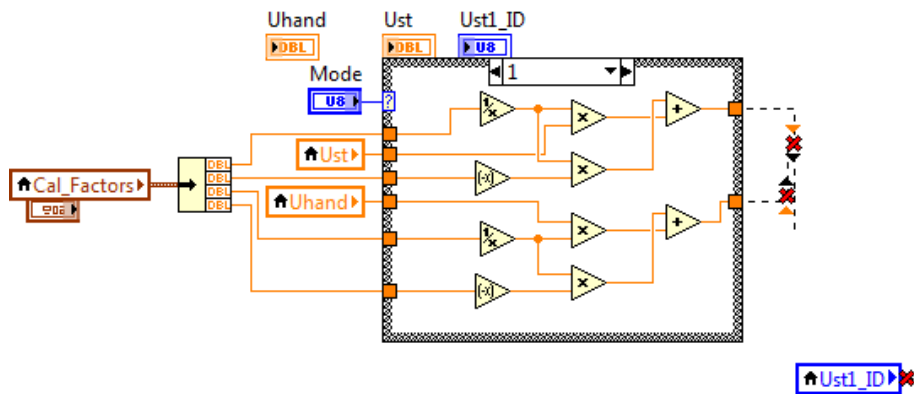
Figure 3.21: Voltage calibration.

that the DAC outputs in order to achieve the requested voltages. The acquired DAC has a 16 bit depth, and provides voltages over a region of -10 V to 10 V. However, since the HVPS have fixed polarity, only half values are used which results in the loss of one bit of resolution. The working range of data is from 32768 to 65535. The next step, is to output the required DAC value. Considering the aforementioned bit loss, the procedure is depicted in Fig. 3.22:
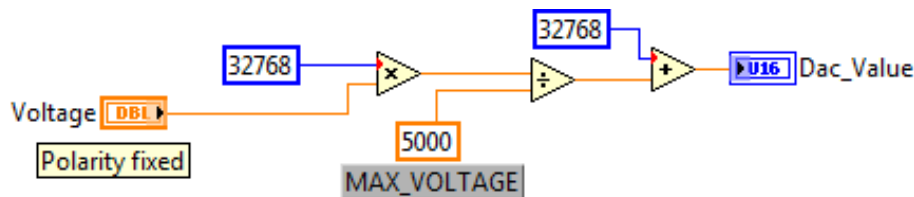
Figure 3.22: Digitization of requested voltage. The voltage value is converted to the 32768 - 65535 range in use.

The problem is actually located between the calibration, and the DAC value. Here is an example: Assuming that the requested voltage is 2254 V. Then, the Ust is calculated and calibrated to be 2200 V, and the VI assigns the following DAC value:(2200*32768/5000)+32768= 42185.92. At this point, it is clear that the use of a lower gain, "fine" channel is not enough. Since the DAC value is an integer, it is unclear how the VI handles the .92 result of the calculation. In every case, there is a $\pm 1/2$ bit uncertainty. For a 5 kV HVPS, with

47

15 bits of precision, this corresponds to 150 mV, which should be corrected.

The proposed solution to this problem is the following: Instead of blindly assigning the coarse DAC value, an intermediate algorithm is inserted. The algorithm calculates the rounded down (floor) bit integer that corresponds to the requested voltage value, and assigns it for the coarse channel.

After that, it calculates the voltage loss for the coarse channel, and adds this loss to the voltage assigned for the fine channel. This procedure is described in Fig. 3.23: After proper testing, it was decided that the algorithm should be inserted after calibra-
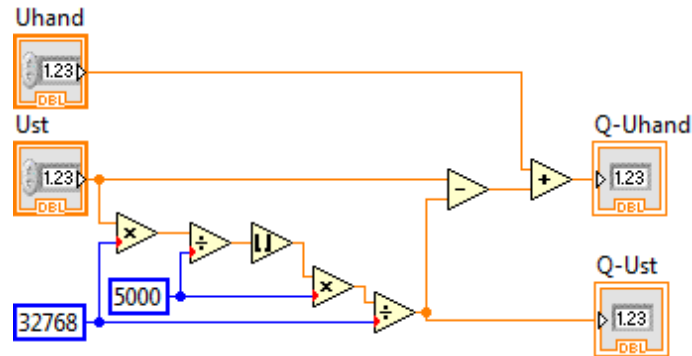
Figure 3.23: A schematic algorithm for voltage correction. The requested voltage is transformed to bit value by multiplying with 32768/5000. The *calculated* bit value is rounded down to integer. Then, this is transformed back to voltage range. Adding and subtracting the value of "32768" makes no difference to rounding down, and therefore, was omitted. The difference between initial and coarse voltage is then added to requested fine voltage. This way the coarse channel always request a voltage that is described by a bit value with little to no uncertainty.

tion. Positioning the algorithm before the calibration step is in vain, as the calibration itself cancels out whatever improvement it may bring. Therefore, the algorithm is placed between calibration and digitization. By doing so, the coarse uncertainty is minimized. Whatever uncertainty remains for the coarse channel comes from the calibration constants, and is expected to be much less than 150 mV. The fine channel, with a gain factor of 10 V/V has a 3 mV precision. By transferring the coarse channel uncertainty to the fine channel, and considering the deviations of the calibration constants, it is safe to assume that total uncertainty for the supplied voltages is ≤ 10 mV.

3.8.3 Data acquisition

The four signals from the PSD are sent first to the preamplifier unit, and then to the Digital Signal Processor (DSP) unit, which includes an Analogue - to - Digital Converter (ADC). Each cascade of electrons, produced by the MCP's is collected by the RAE. The RAE encodes the event's location by distributing the collected charge signal to four outputs. For every output, the distributed charge signal is decoupled by 1 nF capacitors giving rise to small negative pulses of the order 1 mV. These pulses are then driven to the preamplifier unit, and then to the DSP. There, the position of each event is decoded with the use of

Eqs. 3.11a and 3.11b [229], and binned to a 2-D array.

$$X = \frac{X_1 + Y_1}{X_1 + Y_1 + X_2 + Y_2} \tag{3.11a}$$

$$Y = \frac{X_2 + Y_1}{X_1 + Y_1 + X_2 + Y_2} \tag{3.11b}$$

The dimension of the 2-D array that contains the position information was chosen to be 256×256. A selection of a 128×128 array would result in poorer quality spectra since it means that a peak would be detected in less channels. An array of 512×512 has been seen to result not only in larger disk capacity consumption, but also in a doubling in acquisition time. The accompanying software [230] of the DAQ included a subroutine where the position information (X,Y) can be rotated around the center of the PSD. Therefore, there was no need to adjust the inherent X and Y PSD axes to the spectrograph. This subroutine includes the advantage that if an area of the PSD, near the edges, performs less than ideally, it is easy to rotate the PSD by hand, and then correct through the software.
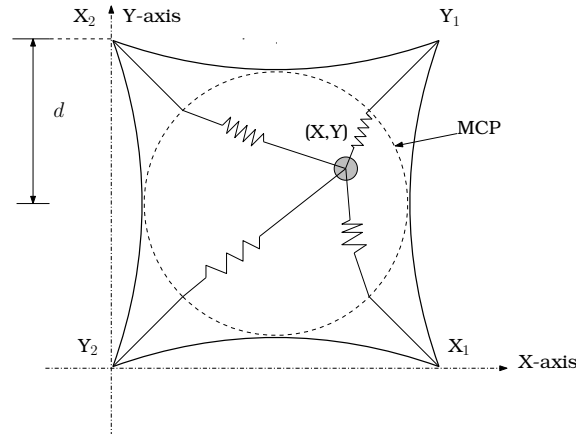
Figure 3.24: Schematic of the RAE. The signals from the four corners of the RAE are transformed to XY coordinates with the use of Eq. 3.11a and 3.11b [229]. The difference between MCP radius and d corresponds to the "dead" area at the edges of the PSD.

After the events are distributed on the 2-D array, a gate is applied. As seen in Fig. 3.25, two projection windows are placed in the form of rectangles. The red rectangle indicates the area over the PSD that the data with same X-coordinate are summed. Provided that the digital rotation of the data is correct, the X-coordinate corresponds to the energy of the analysed electrons (dispersion axis). Although it does not include information about the electron spectrum, it does include information useful in troubleshooting.

3.8.4 Data Normalization

Normalization the spectra acquired to the number of ions collected by the final Faraday Cup (FC2) is necessary for absolute cross section measurements.This was achieved by considering three facts:

- Beam Current Integrator (BCI) provides a series of digital output pulses whose number is proportional to the accumulated quantity of charge on the FC2, with a 100 Hz
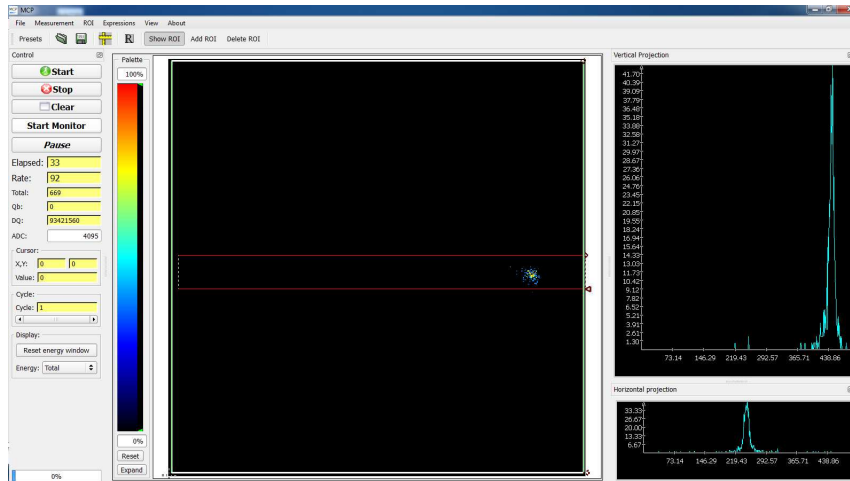
Figure 3.25: The DSP software view while in operation. The red rectangle indicates the area over the PSD that the data with same X-coordinate, and therefore energy, are summed and plotted as a function of the X-coordinate, leading to the spectrum on the top-right corner.

Figure 3.26: The preamplifier module: (Left) BNC Inputs, (Right) Lemo outputs

rate at full scale reading. This provides an accurate measurement[10] of the charge collected.

- The DSP, acquired from ATOMKI[11], has 4+1 inputs. The first four are the four signals that come from the preamplifier. The 5th independent input is an analogue trigger input with a resolution of 12 bits.

- There are five modes of operation of the MCP2 [230] program that was supplied along with the preamplifier and DSP unit. The one selected is the "Trigger Mode" in which a set of data is recorded every time the analogue input exceeds a certain, user-programmed threshold.

A connection has been established between the BCI of the laboratory and the DAQ, with the use of a NI USB-6211 counter [231]. The digital output of the BCI unit was connected to the counter [231] which recorded the pulses. As long as the collected pulses are less than the number set by the user, the counter keeps sending a 5 V trigger to the DAQ. This is interpreted by the DAQ as a command to keep recording data. After the

---

[10]BCI presents a 1% error

[11]Debrecen, Bem tér 18/c, 4026 Hungary. The purchase was a result of the collaboration with Dr. Béla Sulik and Dr. Iván Valastyán

Table 3.4: DAQ specifications

Preamplifier		DSP Unit	
Input:	BNC connectors	Input:	Lemo connectors
Output:	Lemo connectors	INTERFACE (I/O):	Standard RJ45
Consumption:	350 mA	Consumption	600 mA
Dimensions:	110x130x40 mm	Dimensions:	200x100x50 mm
Weight:	200 gr	Weight:	400 gr

desired number of pulses is collected, the signal drops below a certain threshold and the data recording is stopped. In Table 3.4 are the specifications of the DAQ:

3.8.5 Dead Time Correction

The DTC is defined as the ratio of total number of counts sent to the DAQ over the number of counts recorded by the DAQ. DTC is the correction needed to account for the fact that during the digitization of the analogue input signal for the next level of acquisition, other incoming pulses will be ignored. In order to measure DTC, the setup, as presented in Fig. 3.27 on the left, was applied. The goal was to feed the four channels of the preamplifier with negative pulses, emulating the recording of events. This was accomplished with the use of a pulser. The same signal was fed to an oscilloscope, in order to accurately monitor the frequency of the incoming pulses. The recorded rate of events was monitored on the computer screen. For a range of frequencies, extending from 2.5 kHz, up to 150 kHz, the ratio of generated pulses over the recording rate (DTC) is plotted in Fig. 3.27 on the right. The fact that the same pulse was fed to all four X_1, X_2, Y_1 and Y_2, combined with Eq. 3.11a and 3.11b led to the recording of a single pixel in the center of the PSD. For pulse frequencies up to 112 kHz, DTC remained unitary. However,
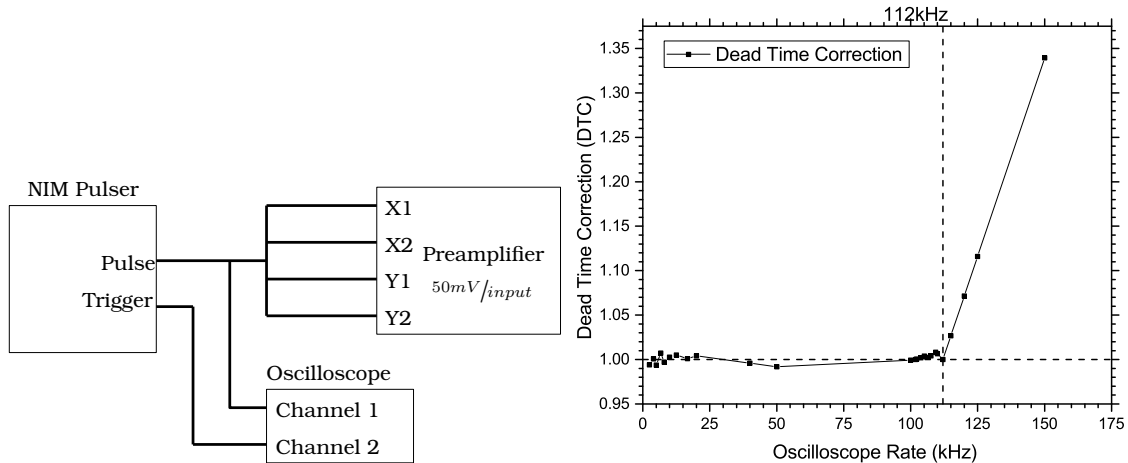
Figure 3.27: *Left*: DTC measurement connection diagram. The signal from the pulser was fed to the four inputs of the preamplifier and to the oscilloscope. *Right*: DTC factor was calculated for a range of pulse frequencies extending from 2.5 kHz, up to 150 kHz. While presenting unitary dead-time correction in lower rates, approximately at 112 kHz the DTC factor started increasing.

for higher frequencies, the recorded rate remained at 112 kHz. This resulted in a linear increase of the DTC, for pulse frequencies higher than 112 kHz. During the experiments,

the observed rate values never exceeded 25-30 kHz, depending on the beam current, or the gas target pressure. Therefore, the DTC for all measurements is assumed to be "1". The ability of the DAC to handle such rates is considered a great improvement, compared to the previous implementation of the spectrograph [166], since no correction is needed.

3.9 Ion electron strippers

Depending on the energy of the ion beam during the stripping process, a particular Gaussian-like charge state distribution results, centered around the mean charge state. Higher stripping energy leads to a higher mean charge state [54, 56, 61]. Thus, to produce more intense few-electron or even bare ion beams, additional stripping points after acceleration, known as post(-acceleration)-strippers, are used.

As a part of APAPES, three new ion strippers have been installed in the NCSR 5.5 MV TANDEM Van de Graaff accelerator [61]. The additional strippers serve two purposes: For the production of He-like ion beams, gas or foil terminal or post stripping is used to vary the content of the $1s2s\,^3S$ metastable beam fraction [6, 109, 166, 232, 233]. Also, post-stripping at higher energies can produce highly charged states in sufficient beam currents [55, 56].

One of the new strippers is an additional GTS to complement the already existing foil stripping system inside the accelerator's terminal. A post stripping point containing both a GPS and a FPS was also installed in the beamline section between the analysing and switching magnet, after Beam Profile Monitor 1 (BPM1). The FPS had been previously used in KSU, while the GPS was redesigned and then built in the laboratory's machine shop. The accelerator facility along with the position of the post stripper system can be seen in Fig. 3.28.
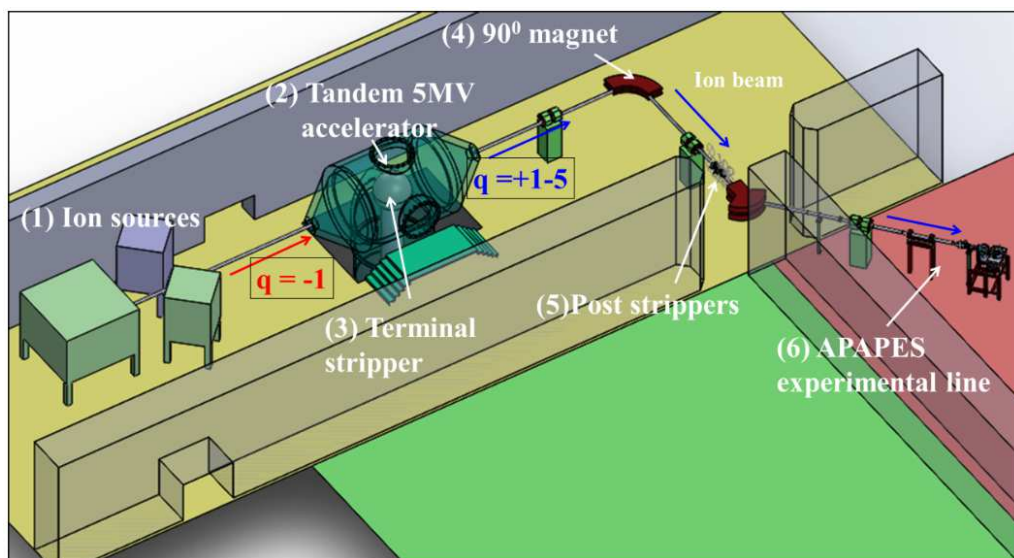
Figure 3.28: Schematic of the "Demokritos" TANDEM accelerator facility showing accelerator tank, ion sources, ion strippers (terminal and post) and L45 APAPES experimental line. Image from [61].
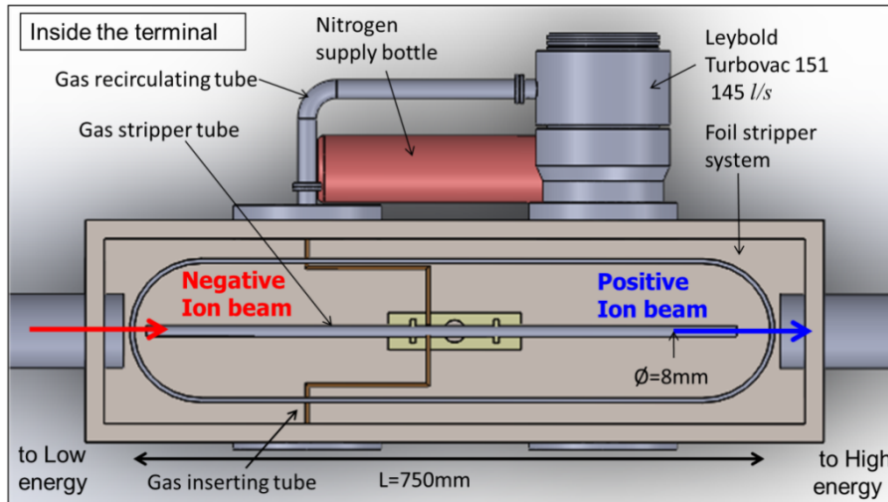
Figure 3.29: Schematics of the strippers system inside the terminal of "Demokritos" TANDEM Van de Graaff accelerator. Image from [61].

3.9.1 Gas Terminal Stripper

There are several differences between gas and foil-stripping which are related to the fact that foils have a much higher density than gas.

1. Foils tend to gradually get worn out and break because of the interaction with the ion beam.

2. For the same ion beam energy, different charge state distributions are produced, that can be calculated theoretically [55, 56, 234].

3. The gas enables the experimenter to vary the density of the gas, affecting the final charge state distribution.

The problem using a GTS is the contamination of the beamline with stripping gas. For this reason a gas recirculating system was installed with a 145 $l \cdot s^{-1}$ turbo pump (Leybold 151), to better confine the stripper gas inside the terminal. Gas collected from the turbo pump is recirculated, and sent back to the GTS. In Figure 3.29 there is a schematic of the tandem accelerator's terminal along with both stripping systems.

A difficulty encountered during the installation of the GTS was the operation of the turbo pump. The turbo pump had to be powered using voltage produced by the electric generator of the accelerator. This is because the controller of the pump cannot be placed inside the accelerator. The optimal operating conditions for the turbo is three-phase AC 17.5 V power with 833 Hz frequency. Therefore, an alternative high-frequency, 3-phase power supply had to be found. Since the accelerator motor generates 125 V, single phase, 400 Hz, an electric circuit was constructed[12]. This is the Steinmetz circuit shown schematically in Figure 3.30 and the toroidal transformer used is shown in Figure 3.31 with which the accelerator generator power was transformed to the one needed for turbo pump operation.

---

[12]Many thanks to Dr. Béla Sulik for the design.
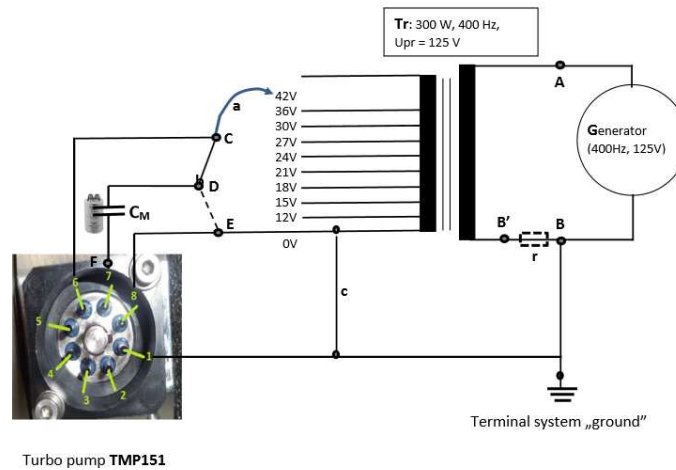
Figure 3.30: Diagram of the electric connections between the generator of the accelerator and the turbo pump.
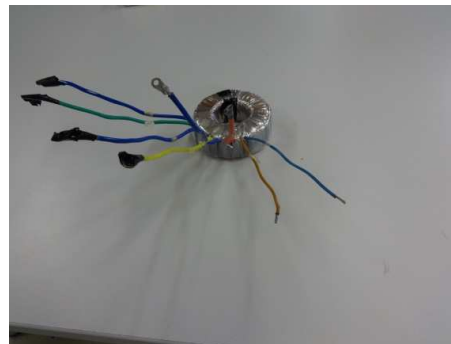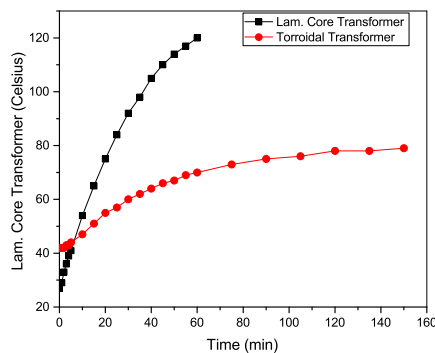
Figure 3.31: *[Left]*: Testing two different transformers for the GTS installation. The first transformer that was tested appeared to overheat during operation, and was replaced with a toroidal transformer. *[Right]*: Photo of the 400 Hz 125 V to 17.5 V toroidal transformer used to power the recirculating gas turbo.

3.9.2 Post Strippers

Maximum energy during stripping at a tandem accelerator is equal to maximum voltage of the terminal $\times$ the ion charge. The semi-empirical formulas that have been developed [55, 56] show that sufficient beam intensity of highly charged states cannot be achieved through collisions in this energy regime. Higher collision energies are needed for the dominant production of the highly charged states with sufficient intensity. These can be achieved after the second stage of acceleration. An appropriate place for this second stripping to occur is between the analysing and switching magnets. This way, the switching magnet operates also as a further analysing magnet to select the required charge state following post stripping. The complete 3D schematic of the post strippers can be seen in Figure 3.32

3.9.2.1 The foil stripper

It consists of a metal rod with 12 available slots for foil mounting. To move or rotate the foils, a system of concentric plastic rings including magnets is used. A connection with
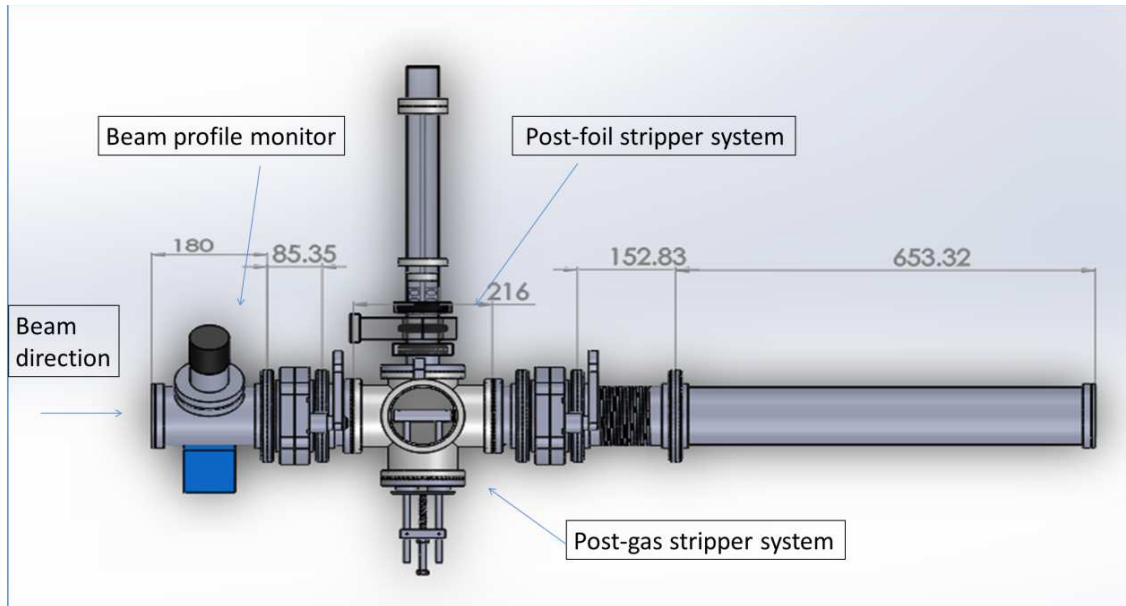
Figure 3.32: Complete 3-D schematics of the post stripper system. Top view. It contains both a GPS and a FPS. Image from [61].

the fore-pump was established. This allowed for the removal, and replacement of the foils while avoiding breaking the vacuum of the accelerator or damaging foils from sudden pressure changes.

3.9.2.2 The gas stripper

The construction of the gas stripper was based on an older KSU design. For the confinement of the stripping gas inside the post stripping 6-way cross a 400 l·s^{-1} turbo pump (Leybold 361C) was installed right underneath the gas stripper. In addition, a pair of removable baffles were installed before and after the gas stripper. The baffles consist of two isolation valves in which holes of 7 mm diameter were drilled to allow for ion passage while restricting to some extent the flow of gas. An additional advantage of the baffles is the improvement of beam transmission, since they provided additional bounds to the aligned passage of the beam.

Table 3.5: Basic geometrical parameters of the ZAPS setup.

	Quantity	Symbol	Value
HDA	Inner Shell Radius	R_1	72.4 mm
	Outer Shell Radius	R_2	130.8 mm
	Central Ray Radius	R_{mean}	101.6 mm
	Paracentric entry	R_0	82.6 mm
	Exit radius	R_π	101.6 mm
	PSD diameter	d_{PSD}	40 mm
Target gas-cell	Gas-cell length	L_{gc}	49.89 mm
	Gas-cell aperture diameters (Ion beam entry-to-exit)		2.0, 2.5, 2.5, 2.5, 2.5 mm See Table 3.2
	Gas cell center to entry distance	s_0	289.48 mm
Beam passage	Lens entry aperture diameter	d_{LE}	4 mm
	Lens exit aperture diameter		6 mm
	Beam exit aperture diameter		9 mm
Acceptance	Full angular acceptance	$\Delta\theta$	0.793º
	Full acceptance solid angle	$\Delta\Omega_0$	1.499×10^{-4} sr
	Integrated full acceptance solid angle	$\overline{\Delta\Omega_0}$	1.510×10^{-4} sr

Chapter 4

Data Analysis

Introduction

The task of data analysis is the transformation of the raw data to double differential cross sections DDCS($\equiv \frac{d^2\sigma_i}{d\Omega d\varepsilon_i}$). This process includes:

1. Kinematic transformations regarding the energy calibration of the raw data to the projectile rest frame.

2. The electron yield normalization with respect to the experimental parameters.

3. An additional solid angle correction, required due to the metastability of the $1s2s2p\,^4P_J$ state.

4. Determination of the separate contributions from the $1s2s\,^3S$ and $1s^2\,^1S$ states of the ion beam [168].

5. Determination of the overall detection efficiency.

4.1 Kinematic Considerations

4.1.1 General Kinematics
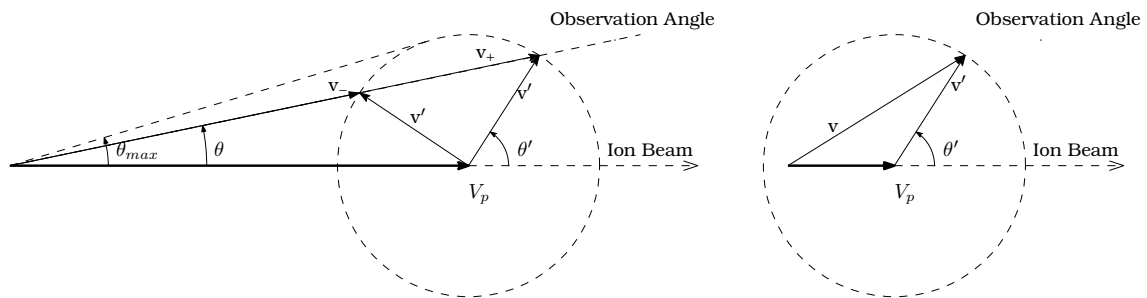
Figure 4.1: Velocity addition diagrams. The electron velocity $\mathbf{v}'$ in the projectile rest frame is transformed to the laboratory frame according to the vector addition rule $\mathbf{v} = \mathbf{V_p} + \mathbf{v}'$, where $\mathbf{V_p}$ is the velocity of the projectile emitter. *[Left]* $\mathbf{V_p} > \mathbf{v}'$ leading to a maximum possible laboratory frame emission angle θ. *[Right]* $\mathbf{V_p} < \mathbf{v}'$ where all angles θ are possible.

A brief summary of electron kinematic transformations for electrons emitted from moving ions is presented. The special relativistic considerations are also included in

this approach resulting in the shift of few meV in the position of the Auger lines in typical MeV/u ion beams. Auger electrons emitted from scattered projectiles are kinematically influenced. A detailed analysis of the general electron kinematic effects can be quite complicated [29, 181]. However, for the case of energetic collisions of a few MeV/u or larger, projectile ions are scattered through very small angles (~mrads), resulting in negligible effects both on the energy loss and on the projectile electron trajectories. In this case, a simple velocity vector addition model is sufficient for the determination of the kinematic effects. Thus, the velocity $\mathbf{v}$ of the Auger electron in the laboratory frame is obtained by adding the projectile velocity $\mathbf{V_p}$ to the velocity $\mathbf{v'}$ of the electron in the projectile rest frame [156]. Denoting with prime, quantities in the projectile rest frame, the electron kinetic energy ε in the laboratory frame can be related to the corresponding rest frame electron kinetic energy ε' as:

$$\varepsilon = \frac{1}{2} m \mathbf{v} \cdot \mathbf{v} = \varepsilon' + t_p + 2\sqrt{\varepsilon' t_p} \cos \theta', \tag{4.1a}$$

or its more accurate relativistic counterpart

$$\varepsilon = \gamma_p \varepsilon' + t_p + \sqrt{(1 + \gamma')(1 + \gamma_p)\varepsilon' t_p} \cos \theta', \tag{4.1b}$$

where $t_p = \frac{m}{M_p} E_p$ is the reduced projectile energy known also as the *cusp* electron energy (electrons isotachic to the projectile ion). E_p and M_p are the kinetic energy and mass of the projectile, respectively, while m is the electron mass and γ_p ($= 1 + \frac{t_p}{mc^2}$) and γ' ($= 1 + \frac{\varepsilon'}{mc^2}$) are the relativistic γ-parameters for speeds V_p and v', respectively. Clearly, Eq. 4.1b can be seen to go to its classical limit Eq. 4.1a, when γ_p and γ' go to 1.

At strictly zero degree observation ($\theta = 0°$) the rest frame emission angle is either $\theta' = 0°$ or $180°$. Thus, as applicable to the ZAPS technique the relation between the electron kinetic energies in the laboratory ε and and rest frame ε' can be written directly from Eq. 4.1b as [156]:

$$\varepsilon(t_p, \varepsilon') = \gamma_p \varepsilon' + t_p \pm \sqrt{(1 + \gamma')\varepsilon'(1 + \gamma_p)t_p} \tag{4.2}$$

The $\pm$ symbol represents the solution for either forward ($+, \theta' = 0°$) or backward ($-, \theta' = 180°$) emission from the ion. All measurements in this thesis correspond to the forward emitted electrons which in the laboratory frame appear about 1 keV higher in energy than the backward emitted electrons and are well separated in the Auger energy spectrum. The inverse of Eq. 4.2 is given by:

$$\varepsilon'(t_p, \varepsilon) = \gamma_p \varepsilon + t_p - \sqrt{(1 + \gamma)\varepsilon(1 + \gamma_p)t_p} \tag{4.3}$$

Table 4.1: Parameters for kinematic transformations.

Parameter	Description	Units
ε	Electron energy in laboratory frame	eV
ε'	Electron energy in rest frame	eV
E_p	Ion kinetic energy	eV
M_p	Ion mass	amu
$t_p = \frac{m}{M_p} E_p$	Cusp Energy	eV

4.1.2 Frame transformation effects

The transformation of rest energy to laboratory energy is one of the various kinematic effects due to emittance from a projectile. The most obvious transformation is known as *shifting* [166]. Forward emission of Auger electrons yields a larger laboratory value, whereas backwards emission leads to smaller laboratory energies depending on the value of t_p. Detecting Auger lines at energies larger than their rest-frame value is useful in measuring electron emissions with small Auger energies. As the energy of Auger electron drops below a certain threshold, their detection becomes difficult. The lower their energy is, the more they are affected by small magnetic and electric fields. Another known effect is *doubling*, an immediate result of the double ($\pm$) result of Eq. 4.2, depending on forward or backwards electron emission from the projectile.

Other than *shifting* and *doubling*, there are another two transformation effects that contribute to an overall enhancement or reduction of the spectrum intensity in the laboratory frame, and need to be treated for an accurate conversion to the rest frame. These are *stretching* and *angular compression*, both contributing to the enhancement or reduction of the intensity of the Auger lines. For the study of these effects, it is convenient to adopt the universal dimensionless parameter ζ:

$$\zeta \equiv \sqrt{\frac{t_p}{\varepsilon'}} = \frac{V_p}{\mathbf{v'}} \tag{4.4}$$

- **Stretching:** Stretching is caused due to the transformation of the energy axis between the frames. If an arbitrary number of channels[1] corresponds to a $\Delta\varepsilon$ in the laboratory frame, after the transformation, it will correspond to $\Delta\varepsilon' \neq \Delta\varepsilon$. Depending on the emission of the electron, and the ζ value, stretching ($\Delta\varepsilon' < \Delta\varepsilon$) or compression ($\Delta\varepsilon' > \Delta\varepsilon$) is established. It should be noted, that as it is a transformation of the energy axis, there are no qualitative differences in the spectrum. It does not increase the overlap of two neighbouring Auger lines nor does it affect the overall image. It does, however, affect the resolution $\left(= \frac{\Delta\varepsilon^{(\prime)}}{\varepsilon^{(\prime)}}\right)$ of the Auger lines. For small $\Delta\varepsilon$ it can be shown that:

$$\frac{\Delta\varepsilon}{\Delta\varepsilon'} \approx \frac{d\varepsilon}{d\varepsilon'} = \sqrt{\frac{\varepsilon}{\varepsilon'}} = |1 \pm \zeta| \qquad (\theta = 0°) \tag{4.5}$$

from which the following is derived:

$$\frac{\Delta\varepsilon}{\varepsilon} = \sqrt{\frac{\varepsilon'}{\varepsilon}} \frac{\Delta\varepsilon'}{\varepsilon'} \tag{4.6}$$

During integration of an Auger line yield determination stretching significantly changes the width of the line, and therefore the calculated yield.

- **Angular Compression:** Angular compression is presented in Fig. 4.2. Electrons emitted isotropically in the projectile rest frame are detected in narrow solid angle in the forward direction in the laboratory frame for fast projectile ions. As seen in the figure, for fast emitters the projectile frame solid angle $\Delta\Omega'$ ($\Delta\Omega'_-$ and $\Delta\Omega'_+$) is always larger than the laboratory frame solid angle $\Delta\Omega$ defined geometrically. For zero degree observation angle ($\theta = 0°$) it has been shown [29, 166] that:

$$\frac{\Delta\Omega}{\Delta\Omega'} \approx \frac{d\Omega}{d\Omega'} = \frac{\varepsilon'}{\varepsilon} = \frac{1}{(1 \pm \zeta)^2} \qquad (\theta = 0°) \tag{4.7}$$

---

[1] For example the width of an Auger line.
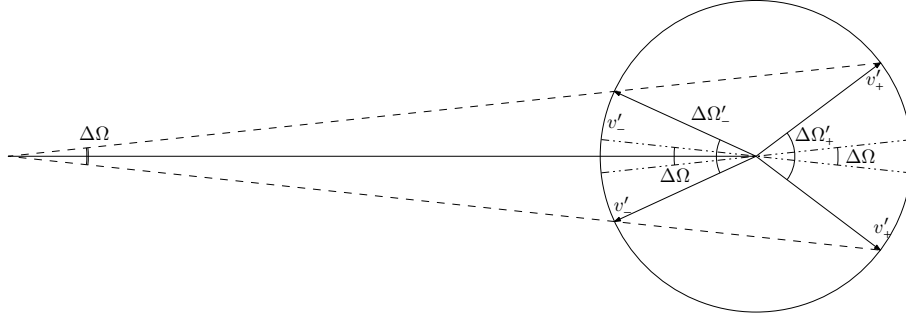
Figure 4.2: Angular compression of electrons emitted from fast projectiles. Figure from Ref. [166]

The aforementioned frame effects result in an enhancement of the recorded electron spectra in the laboratory frame [29, 166]. Thus, the intensities laboratory and rest frame spectra are Eq. 4.8:

$$\frac{d^2\sigma}{d\Omega' d\varepsilon'} = \sqrt{\frac{\varepsilon'}{\varepsilon}} \frac{d^2\sigma}{d\Omega d\varepsilon} = \frac{1}{|1 \pm \zeta|} \frac{d^2\sigma}{d\Omega d\varepsilon} \tag{4.8}$$

4.1.3 Energy Calibration

Since the measured electrons are emitted from a moving projectile, their detection energy depends on the projectile energy. Although the energies of the KLL Auger electrons are known and can be used for calibration, the projectile energy at each beam pass[2] is not known precisely. For example, a 1% uncertainty in beam energy leads to an uncertainty of 0.6%, or about 9 eV in the case of ^2D for a 12 MeV carbon beam. However, typical beam energy uncertainty is around 0.1% which leads to electron laboratory energy uncertainty less than 1 eV. In order to simplify the energy calibration procedure, nominal beam energy E_p is assumed to be correct. By combining the data that resulted from the fitting procedure of the known peaks (x_c =center) measured in the lab frame, an Excel™ file has been programmed to calculate the necessary three a, b, c calibration constants [166] by a Least Squares method.

It has been shown that a 2$^{\text{nd}}$ degree polynomial is sufficient to describe the relation between PSD channel and electron laboratory energy [166]:

$$T(i) = a + b \cdot i + c \cdot i^2. \tag{4.9}$$

This is a direct quadratic function that assigns a value for lab frame electron energy T to every "X" channel number i. Since the Auger energies and the projectile energy are known, the first step is to transform the known Auger (rest frame) energies to the lab frame. Using projectile energy t_p and Eq. 4.2, the expected laboratory energies $\varepsilon[j]$ are calculated. The center channel $i_c[j]$ for each Auger calibration peak j in the laboratory frame is measured, directly from the raw spectrum. Then, the three optimal calibration constants of Eq. 4.9 can be found applying a least squares fit solution for the $T(i_c[j], a, b, c) = \varepsilon[j]$ system:

$$T(i_c[j], a, b, c) = a + b \cdot i_c[j] + c \cdot i_c[j]^2 \qquad (j = 1 \ldots j_{max}) \tag{4.10a}$$

$$S(a, b, c) = \sum_{j=1}^{j_{max}} \left[T(i_c[j], a, b, c) - \varepsilon[j] \right]^2 \tag{4.10b}$$

---

[2]Day-to-day variations

60

Table 4.2: Example KLL Auger lines of carbon used for calibration [235].The laboratory energies are computed according to Eq. 4.2 for a C^{4+} projectile energy of $E_p = 18$ MeV $(t_p = 822.87$ eV $\equiv 1.5$ MeV/u).

j	Auger line	Auger energy - E_A (eV)	Lab energy - ε (eV)
1	$1s2s^2\,^2S$	227.23	1915.56
2	$1s2s2p\,^4P$	229.64	1922.73
3	$1s(2s2p\,^3P)\,^2P_-$	235.55	1939.45
4	$1s(2s2p\,^1P)\,^2P_+$	238.86	1949.26
5	$1s2p^2\,^2D$	242.15	1958.64

Thus, calibration parameters a, b, c are adjusted for fixed t_p until the sum S of the squares of the differences between the computed $\varepsilon[j]$ and the experimental energies $T(i_c[j], a, b, c)$ has been minimized. With this information available, the axis of the acquired spectrum can be transformed from channels i to laboratory energy in eV. Typically, this is done for the 5 ($j_{max} = 5$) main well known KLL Auger lines of carbon given in Table 4.2. It should be noted that the application of this method requires at least 3 known Auger lines in the spectrum. This is because a quadratic function as Eq. 4.9 has 3 separate parameters. Therefore, at least 3 pairs of $(i_c[j], \varepsilon[j])$ are needed to provide an correct triplet of (a, b, c). Spectral regions with less known lines, cannot be resolved with this method, unless:

- A linear form of Eq. 4.9 is used, without the quadratic term, or

- the aforementioned regions' lie close to resolvable regions. Then, with the use of passing energy W and the pre-retardation factor F, the (a, b, c) can be reduced to their universal form (A, B, C) [166] with the use of Eqs. 4.11. With the universal form, spectral regions, in proximity to the resolved region can also be calibrated with the use of the respective W and F.

$$A = \frac{a}{W}F - F + 1 \tag{4.11a}$$

$$B = \frac{b}{W}F \tag{4.11b}$$

$$C = \frac{c}{W}F \tag{4.11c}$$

Table 4.3: Average values of universal energy calibration factors and their respective uncertainties for $F = 4$.

Energy (MeV)	C	$\sigma_{\bar{C}}$	B	$\sigma_{\bar{B}}$	A	$\sigma_{\bar{A}}$
6	1.9E-06	3.9E-07	6.2E-04	1.0E-04	8.9E-01	7.4E-03
9	1.6E-06	2.2E-07	6.9E-04	5.9E-05	8.9E-01	2.4E-02
12	1.7E-06	5.6E-07	6.7E-04	1.5E-04	8.8E-01	7.0E-03
15	2.3E-06	5.3E-07	5.2E-04	1.5E-04	8.9E-01	9.3E-03
Avg.	1.9E-06	2.4E-07	6.2E-04	6.1E-05	8.9E-01	6.9E-03

Combining Eq. 4.9 and Eqs. 4.11 results to Eq. 4.12:

$$T(i) = W\left(\frac{A - 1 - F}{F}\right) + \frac{W}{F}B \cdot i + \frac{W}{F}c \cdot i^2 \tag{4.12}$$

Using Eq. 4.12, and the found constants from Table 4.3, any spectra can be calibrated for every possible combination of W and F.

The previous procedures for calibration are not the only ones available. Within the ZAPS method, energy calibration of the beam can be achieved with the use of cusp (isotachic to the ion beam) electrons [236]. This approach, however, requires a spectrograph of higher precision in measuring exact energies, such as the tandem PPA. The HDA, equipped with a PSD, although advantageous in many ways, has a large acceptance window that cannot deliver this type of precision. Therefore, the aforementioned method was considered to be the most efficient one for this work.

4.2 Absolute normalized yields

All previous procedures transform the x-axis of the spectrum, the energy axis. The following section describes the normalization needed on the measured electron spectra for conversion to laboratory DDCS, given by the following equation [166]:

$$DDCS_i \equiv \frac{d^2\sigma_i}{d\Omega dE_i} = \frac{N_{e_i}\, DTC}{N_I\, L_{eff}\, n\, \overline{\Delta\Omega}\, \Delta E_i\, T\, \eta_i} \tag{4.13}$$

where i refers to the channel number of the PSD X projection. With the use of Eqs. 4.8 and the inverse of 4.3 it is transformed to the rest frame. Although N_I refers to total number of ions, the He-like beams used here contain two components. These are $1s^2\,{}^1S$ and $1s2s\,{}^3S$, each one with its own distinct contributions in almost each KLL line. For this reason, Eq. 4.13 strictly speaking results in normalized yields rather than DDCS. Once the fraction of metastable ions is determined an absolute DDCS integrated in energy SDCS can be obtained from the normalized yields. In case a KLL line has contribution only from one component of the beam (e.g. the ^4P state that is populated only from the $1s2s\,{}^3S$ state) then and absolute DDCS can be obtained.

Number of electrons recorded in channel i - $\mathbf{N_{e_i}}$

This is the measurement taken from the DAQ, which is the number of counted electrons in every channel i. The statistical uncertainty is $\delta N_{e_i} = \sqrt{N_{e_i}}$.

Dead-time correction - DTC

The DTC is defined as the ratio of total number of counts recorded by a scaler over the total number of counts recorded by the ADC. Basically it is an average correction for the case of an increased count rate that the DAQ cannot handle. As seen in Fig. 3.27 on page 51, DTC=1, below 112 kHz, so there is no need for correction even at 20 kHz, which is a typical counting rate during the experiment.

Number of ions - $\mathbf{N_I}$

N_I is the number of ions collected by the FC2 during each spectrum measurement. It is given by the following formula:

$$N_I = \frac{Q(nC)}{q \cdot 1.6 \times 10^{-10}} \tag{4.14}$$

where q is the ion charge state, and $Q(nC)$ is the total charge recorded by FC2 and is calculated by the following formula:

$$Q(nC) = \frac{Q_{cnt} I_{FS}(nA)}{C_{nts}} \tag{4.15}$$

where Q_{cnt} is the number of counts set by the experimentalists, and equals the number of pulses generated from the BCI, and received by the DAQ. Once the requested number of pulses have been received, the measurement stops. I_{FS} is the maximum of the scale the BCI operates, typically measured in nA (usually 2, 6, 20 or 60 nA). Finally, C_{nts} is the rate of pulses generated by the BCI per second. For the Brookhaven BCI used for all measurements to date this is fixed at $C_{nts} = 100$ Hz. The determination of N_I is based on the assumption that the beam current is not affected by collisions in the target. Expected uncertainty for Model 1000 used is 0.02%

Effective length of the gas-cell - L_{eff}

Typically, for a gas cell with actual length L_{gc}, with aperture openings of diameter D_1 and D_2 the effective length is given by $L_{eff} = L_{gc} + \frac{D_1 + D_2}{2}$. The effective length is given by $L = 50$ mm, $D_{entrance} = 1.5$ mm and $D_{exit} = 2.0$ mm for a total of $L_{eff} = 51.75$ mm. After the widening, the new values became: $D_{entrance} = 2.5$ mm and $D_{exit} = 2.5$ mm for a total of $L_{eff} = 52.50$ mm= 5.250 cm. According to Ref. [166], the average of the entrance and exit apertures can be accepted as uncertainty. That results to $\delta L = 2.5 mm$ and uncertainty $\delta L / L =$ 5%.

Target gas density - n

n is the number of molecules per cm^3. Using the state equation, applicable to this range of pressures, and assuming that the gas temperature is at room temperature (300 °K), the density can be calculated by the following formula [166]:

$$n \, (\# \, \text{molecules}/cm^3) = 3.222 \times 10^{13} \, P(\text{mTorr}) \tag{4.16}$$

where P is the target gas pressure determined by the MKS Baratron capacitive manometer used. Uncertainty of measure pressure is less than 0.12% according to the manufacturer [203]

$\overline{\Delta\Omega}$

$\Delta\Omega_0$ is the *point source* solid angle defined by the opening of the lens entrance ($d_{LE} = 4.0$ mm) and the distance to the center of the gas cell ($s_0 = 289.48$ mm). Eq. 4.17 provides the solid angle of a cone with apex angle $2\theta_0$:

$$\Delta\Omega_0 = \int_0^{2\pi} \int_0^{\theta_0} \sin\theta \, d\theta d\phi$$

$$= 2\pi \left[1 - \frac{s_0}{\sqrt{s_0^2 + \left[\frac{d_{LE}}{2} \right]^2}} \right] \tag{4.17}$$

$$= 1.50 \times 10^{-4} \text{ Sr}$$

Regarding prompt states, Equation. 4.17 can be integrated along the length of the gas cell L_{gc} (=52.50mm) with the following form:

$$\overline{\Delta\Omega_0} = \frac{2\pi}{L_{gc}} \int_{s_0 - \frac{L_{gc}}{2}}^{s_0 + \frac{L_{gc}}{2}} \left[1 - \frac{s}{\sqrt{s^2 + \left[\frac{d_{LE}}{2} \right]^2}} \right] ds \tag{4.18}$$

$$= 1.51 \times 10^{-4} \text{ Sr}$$

thus, yielding a 0.8% correction to the initial $\Delta\Omega_0$ value. The uncertainty in this quantity arises from any uncertainties in s_0, since it is rather difficult to measure. Assuming a 5 mm uncertainty in s_0, which corresponds to 10% of the gas cell length, integrated solid angle uncertainty reads $\delta(\overline{\Delta\Omega})/(\overline{\Delta\Omega})$=1.65%.

ΔE

ΔE is the energy step of the spectrum per channel and is obtained from the first derivative of Eq. 4.9 with respect to the channel number leading to:

$$\Delta E_i = b + 2\,c \cdot i \tag{4.19}$$

It is the only correction that has a non-uniform effect across the PSD as it increases with i.

Analyser transmission - T

T is defined as the transmission of the spectrograph assumed here to be independent of channel number. It is defined as the ratio of the number of particles reaching the detector to the number of particles entering the spectrograph (i.e. the entry lens). This can also depend on the specific transmission of the lens and therefore depend on the lens voltages and also the retardation factor F [214]. However, as already shown for the same HDA in Ref. [166] (Fig. 46), for F values up to 8 this was found to be a constant and therefore independent of the lens voltages. Thus, the transmission was determined by the three grids of 90% transmission leading to a total of $T = 0.90^3 = 0.729\%$ transmission. The active area of the PSD appears to be from channel 40 up to 220, in the case of a 256×256 DAQ counts matrix.

MCP efficiency - η

η is actually the overall efficiency of the measurement. However, since all the experimental parameters are accurately determined for our ZAPS setup, the efficiency η is primarily the absolute efficiency of the MCP. η is the absolute MCP efficiency. It is the probability that an electron that reaches the surface of the MCP will create a measurable signal. The
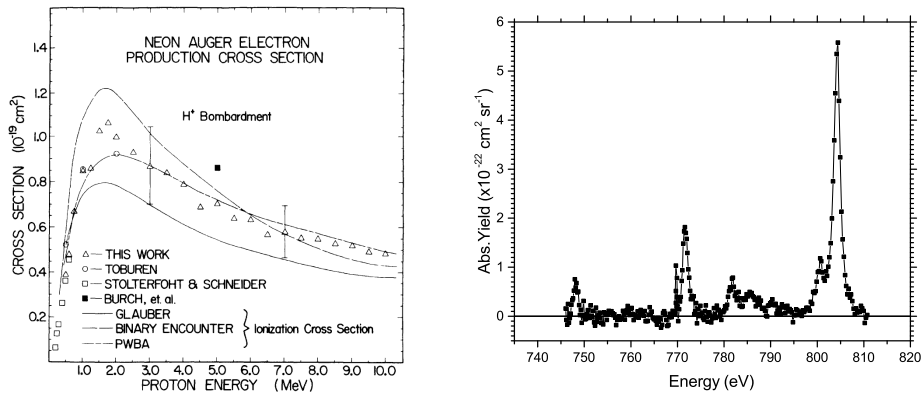
Figure 4.3: (Left): Ne K-shell Auger-electron production cross sections for H⁺ bombardment as a function of H+ energy. Figure from Ref. [237]. (Right): Target KLL Auger normalized spectrum, obtained from collisions of 3 MeV protons on Ne. See text for details.

efficiency of the MCP's depends on the active area of the MCP, the V_{MCP} setting, and the

energy of the electrons, presenting its maximum efficiency at around 300 to 350 eV. To ensure an effective efficiency over the active PSD area, the whole MCP system is biased appropriately so that the central trajectory electrons always imping on the front MCP at an energy of 1000 eV as described in detail in Ref. [166]. Determination of the efficiency η can be done either by comparison to Binary Encounter electron measurements [181] or using known cross sections [237] for the production of target Auger electrons. The latter method is used in this work.

To apply this method, the H$^+$ + Ne collisional system was used, similar to Ref. [237]. The Ne gas target was bombarded with 3 MeV protons. After BKG subtraction, the acquired spectrum was normalized to the aforementioned factors, according to Eq. 4.13, except efficiency. Then, the spectrum was integrated, to acquire total experimental yield, and compared to data from Ref. [237], In Fig. 4.3, (Left) these data are presented, where for 3 MeV protons, yield a value of $8.7 \cdot 10^{-20}$ cm^2. It should be noted that our results using Eq. 4.13 are DDCSs. Therefore, after the integration which removes the dE factor, the result is multiplied by 4π to account for the angular distribution. Comparison of the measured yield with the known cross section leads to evaluation of the MCP's efficiency. Thus, the efficiency was found to be η = 0.50 or 50%.

4.3 Effective solid angle corrections

Table 4.4: Lifetimes τ_J and Auger yields ξ for the J-components of $1s2s2p\,^4P_J$. Values obtained from Ref. [123] and from Ref. [238] respectively.

Ion	J	Ref. [123]		Ref. [238]	
		τ_J (ns)	ξ_J	τ_J (ns)	ξ_J
C^{3+}	$1/2$	2.94	1.00	3.70	0.99
	$3/2$	7.10	1.00	13.19	0.94
	$5/2$	121.36	1.00	117.20	1.00
O^{5+}	$1/2$	0.90	0.97	1.09	0.96
	$3/2$	2.50	0.77	4.40	0.58
	$5/2$	29.57	0.99	28.30	0.99

In ZAPS, electrons are measured with high energy resolution at 0° with respect to the beam direction and state-selective cross sections can be determined. The accurate evaluation of the $1s2s2p\,^{2,4}P$ electron yields produced by capture to the metastable $1s2s\,^3S$ beam component, and the ratios of their cross sections is one of the goals of this thesis. In the framework of ZAPS prompt states are the doubly-excited projectile states for which $\frac{V_p\tau}{L_c} \ll 1$. V_p is the projectile velocity, τ the total lifetime of the state, and L_c the length of the target gas cell. Under this condition, the emission of the respective prompt Auger electrons takes place within the limits of the target gas cell. For the HDA of this experiment, the $\Delta\Omega_0(s_0)$ solid detection angle for point source emission was given by Eq. 4.18. However, zero-degree Auger electrons originating from long-lived projectile states such as $1s2s2p\,^4P_J$ [191, 239, 240] are characterized by lifetimes ranging from ns to ms depending on atomic number Z_p and total angular momentum J of the state. Therefore, the long-lived projectile states can Auger decay all along the path of the ion towards, inside and even beyond the spectrometer. On the same time, their effective detection solid angle $\overline{\Delta\Omega}$ increases as the emitting ion approaches the spectrometer entry. This results for a correction to the measured electron yield and the resulting cross section determination [156, 241].

In order to compensate for the increase in the solid angle due to emission as the projectile approaches the spectrometer, as well as the decrease due to the decay of the population, the G_τ correction factor was introduced. The idea is to apply a multiplicative term to the $\Delta\Omega_0$, as defined in Eq. D.1, and result to an effective solid angle that is proportional to the point source solid angle $\Delta\Omega_0$ of prompt Auger electrons. Such correction

factors exist already in the literature [6, 147]. In App. D a detailed theoretical explanation is given on how this correction factor is calculated [156]. Below, the experimental work conducted towards the G_τ determination and theoretical calculation validation, as part of the measurements for this thesis are presented.

4.3.1 Experimental approach for the determination of the solid angle correction factor G_τ

This method is partly based on earlier work by Lee *et al.* [147]. Be-like ions produced in tandem Van de Graaff accelerators are delivered in various excited ionic states, i.e. the ground state $1s^2 2s^2\,^1S$ and the metastable state $1s^2 2s2p\,^3P$. Their lifetimes are in the µs to s range, depending on Z_p and total angular momentum J [242, 243]. This is because although $(1s^2 2s2p)^3P_{0,1} \leftrightarrow (1s^2 2s^2)^1S_0$ are E1 transitions [244], the $(1s^2 2s2p)^3P_2 \leftrightarrow (1s^2 2s^2)^1S_0$ transition is M2 [245]. Therefore it is characterized by longer lifetimes, and therefore metastable. During collisions with H_2 gas targets, needle ionization[3] of the $1s$ electron of the $1s^2 2s2p\,^3P$ state results in the production of $1s2l2l'\,^{2,4}L_J$ configurations. These, in the LS coupling scheme, should give rise to the ^4P and $^2P_-$ states. In Ref. [147], the $1s(2s2p\,^1P)\,^2P_+$ state was also included. However, in the LS coupling scheme, the $2s$ and $2p$ electrons interact strongly as parts of the same shell and are less affected by the K-shell configuration [241]. Thus, even after the $1s$ ionization, the L-shell electrons should maintain their ^3P coupling. Therefore, the only observable states are the ^4P and the $^2P_-$, while $^2P_+$ would require a rearrangement of the L-shell spins through higher order processes [241].

The production of these states by $1s$ ionization of the $1s^2 2s2p\,^3P$ beam component, has an advantage for the determination of the G_τ correction factor. Capture to higher nl-states is known to be strong for He-like ions [5, 191]. This can lead to cascade feeding of these states [81], which, considering the existing setup, could alter their measured spin statistical population ratio [4]. Cascades are expected in collisions of He-like ion beams where the ^4P state is produced by electron capture to the $1s2s\,^3S$ long-lived component of the beam. Since capture can occur in various nl states, there is high probability for the formation of various $1s2s(^3S)nl\,^4L$ quartet states. Quartet states tend to accumulate to the ^4P since their Auger rates are orders of magnitude lower than the corresponding radiative de-excitations [5, 6, 81, 238].

The production population statistics of the ^4P and $^2P_-$ states results in the ratios $\sigma(^4P) : \sigma(^2P_-) = 2 : 1$, as implied from the multiplicities of these states. A measurement of this ratio also includes the correction factor G_τ, due to the metastability of the ^4P. The combination of the above results in:

$$\frac{\sigma(^4P)}{\sigma(^2P_-)} = 2 = \frac{\frac{Z(^4P)}{\xi_{4P} G_\tau}}{\frac{Z(^2P_-)}{\xi_{2P_-}}} \tag{4.20}$$

and therefore

$$G_\tau = \frac{1}{2} \frac{Z(^4P)}{Z(^2P_-)} \frac{\xi_{2P_-}}{\xi_{4P}} \tag{4.21}$$

where Z denotes the measured normalized electron yields obtained from the fitted areas, while ξ is the Auger yield of each state whose values are adopted from Ref. [238]. Within this method, G_τ is experimentally determined in a cascade-free environment, thus providing additional tests of the theoretical models used to calculate G_τ to date [123, 156, 246].

---

[3]Low-Z particles can selectively ionize the inner shell of projectiles without substantially disturbing the outer shells, in a procedure named "needle ionization" [114, 137].

Table 4.5: Experimental Auger line energies for O^{4+} and C^{2+} collisions with light targets. Intermediate states are presented along with their respective production mechanism, and the corresponding Auger yields ξ_A and final state.

Initial state	Intermediate state	Mechanisms	Final state	Oxygen		Carbon	
				Energy (eV)[a]	ξ^{c}	Energy (eV)	ξ
$1s^2 2s^2\,^1S$	$1s 2s^2\,^2S$	K-ioniz.	$1s^2\,^1S$	412.7	1	227.15[b]	0.99[d]
$1s^2 2s 2p\,^3P$	$1s 2s 2p\,^4P$	K-ioniz.	$1s^2\,^1S$	416.0	0.895	229.64[b]	0.98[e]
$1s^2 2s^2\,^1S$	$1s 2s^2 2p\,^3P$	$1s \to 2p$	$1s^2 2p$	423.7		235.7[a]	
$1s^2 2s 2p\,^3P$	$1s(2s 2p\,^3P)\,^2P_-$	K-ioniz.	$1s^2\,^1S$	424.9	0.739	235.44[b]	0.92[f]
$1s^2 2s^2\,^1S$	$1s 2s^2 2p\,^1P$	$1s \to 2p$	$1s^2 2p$	428.4		238.3[a]	
$1s^2 2s 2p\,^3P$	$1s 2s 2p^2\,^3P_-$	$1s \to 2p$	$1s^2 2p$	436.4		243.6[a]	
$1s^2 2s 2p\,^3P$	$1s 2s 2p^2\,^3D$	$1s \to 2p$	$1s^2 2s$	448.2	0.899	251.9[a]	

[a]Experimental values from Lee *et al.* [147]
[b]Ref. [235]
[c]Mean Auger yield, as defined by Eq. D.6d
[d]Calculated from Ref. [108]
[e]Ref. [241]
[f]Ref. [238]

The $1s^2 2s 2p\,^3P$ metastable fraction component, although not required for the determination of the G_τ, can be experimentally determined. Typical fraction values of this component are $\gtrsim 50\%$ for low Z_p ions. $1s$ ionization of the $1s^2 2s^2\,^1S$ ground state results in the also known Li-like ^2S intermediate state. Since the $1s$ needle ionization process is not expected to depend strongly on the L-shell configuration, the production cross sections from the ground state and the metastable state can be expected to be equal. Thus, $1s$-ionization cross sections should be equal, i.e. $\sigma_{1s}(1s^2 2s^2\,^1S) = \sigma_{1s}(1s^2 2s 2p\,^3P)$ [147]. Consequently, the following ratios of the production cross sections should be valid: $\sigma(^2S) : \sigma(^4P) : \sigma(^2P_-) = 3 : 2 : 1$. This result is different from the corresponding result $\sigma(^2S) : \sigma(^4P) : \sigma(^2P_-) : \sigma(^2P_+) = 8 : 4 : 3 : 1$ reached in Ref. [147], due to the inclusion of the $^2P_+$ state. Using these $1s$-ionization cross sections, the $1s^2 2s 2p\,^3P$ metastable fraction component can be calculated. Regarding the approximation assumed by Lee *et al.* [147] the f_m metastable fraction is given by[4]:

$$ f_m \equiv \left[1 + \frac{\frac{Z(^2S)}{\xi_{2S}}}{\frac{Z(^4P)}{\xi_{4P}} + \frac{Z(^2P_-)}{\xi_{2P_-}} + \frac{Z(^2P_+)}{\xi_{2P_+}}} \right]^{-1} = \left[1 + \frac{3}{8} \frac{Z(^2S)}{Z(^2P_-)} \frac{\xi_{2P_-}}{\xi_{2S}} \right]^{-1} \quad (4.22) $$

while the present formulation, omitting the $^2P_+$ state leads to:

$$ f_m \equiv \left[1 + \frac{\frac{Z(^2S)}{\xi_{2S}}}{\frac{Z(^4P)}{\xi_{4P}} + \frac{Z(^2P_-)}{\xi_{2P_-}})} \right]^{-1} = \left[1 + \frac{1}{3} \frac{Z(^2S)}{Z(^2P_-)} \frac{\xi_{2P_-}}{\xi_{2S}} \right]^{-1} \quad (4.23) $$

---

[4]It should be noted that in Ref. [147] ξ's are included in the definition of $Z(\texttt{AugerState})$, whereas in the present thesis $Z(\texttt{AugerState})$ refers to the measured normalized electron yields obtained from the fitted areas.

This correction amounts to only a small increase of a few percent in the value of the previously reported metastable fraction (at least for the systems studied here), well within the experimental uncertainty. The new (corrected) values f_m of the $1s^2 2s2p\,^3P$ metastable fraction are reported in Table 4.6. As mentioned earlier, the $1s^2 2s2p\,^3P$ lifetimes are in the μs to s range, depending on Z_p and total angular momentum J [242, 243]. This means that at current velocities ($\approx$10 mm/ns) they require disproportionately long distances to observe a decrease in their population. Therefore, it is not illogical to compare fractions produced in different accelerator facilities. It should be reminded that fraction results do not affect G_τ results.

4.3.2 Results

Electron spectra

In Fig. 4.4 the recorded spectra from the 17.5 MeV O^{4+} with H$_2$, and 6.6 MeV C^{2+} with H$_2$ collisional systems are presented. In the case of oxygen, two different pre-retardation factors $F = 8$ (middle) and $F = 4$ (bottom) were used. Single collision conditions were ensured by properly adjusting the target gas pressure[5]. Reproducibility was ensured by recording multiple sets of spectra under identical conditions which were compared and then added, provided there were no inconsistencies amongst them.
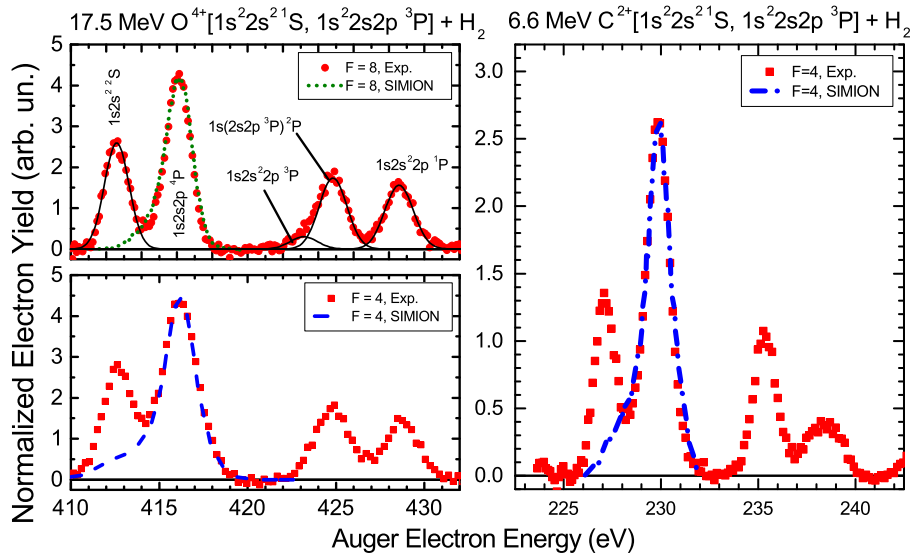
Figure 4.4: *Left:* Oxygen Auger KLL spectra obtained in collisions of 17.5 MeV O^{4+} with H$_2$. Line assignment for each peak is also given. SIMION simulations [156] of the ^4P spectral distributions are shown by the dotted (Left-Top) and dashed (Left-Bottom) lines, in excellent agreement with the measurements. The solid lines for the higher resolution mode (Left-Top) correspond to Voigt profile least square fits [247] of the peaks. The small peak at the low energy shoulder of the $1s(2s2p\,^3P)\,^2P_-$ peak, was identified as arising from the $1s2s^2 2p\,^3P$ intermediate state. Its contribution was carefully accounted for and separated from that of the $1s(2s2p\,^3P)\,^2P_-$ peak of primary interest (see text). *Right:* Carbon Auger KLL spectra obtained in collisions of 6.6 MeV C^{2+} with H$_2$. Line assignment as in left, but with lower resolution. The $1s2s^2 2p\,^3P$ line could not be resolved.

In Fig. 4.4, in the higher resolution $F = 8$ mode (left - top), the small asymmetry of $1s(2s2p\,^3P)\,^2P_-$ is due to the additional low intensity $1s2s^2 2p\,^3P$ Auger line. This state can

---

[5]P = 20 mTorr.

be formed from the $1s^2 2s^2\,{}^1S$ ground state via $1s \rightarrow 2p$ excitation and decays promptly to the $1s^2 2p$ final state. To precisely determine G_τ, the contribution of $1s2s^2 2p\,{}^3P$ is needed. For this reason, the spectrograph was set to a higher ($F = 8$) than the usual ($F = 4$) resolution mode to improve its resolution. The $1s2s^2 2p\,{}^3P$ contribution was found to be about 17% of the total area of both peaks near 424 eV.

To obtain accurate peak areas, the line spectra were fitted with Voigt profiles. These account for the convolution of the narrow intrinsic Lorentzian distribution of the Auger decay and the broader (Full Width at Half Maximum (FWHM)≈ 2 eV in the projectile rest frame) Gaussian distribution of the HDA's response function. The measured lines FWHMs are characterized primarily by the instrumental resolution. The same constant FWHM (determined by fitting the prompt ^2S peak) was used for all prompt lines, except for the ^4P peak whose profile is slightly different due to its metastability.

Metastable fraction f_m

For the determination of each $1s^2 2s 2p\,{}^3P$ beam fraction, Eq. 4.23 was used. Although not required for the G_τ determination, it serves as a check. Results presented in Table 4.6 show that the present determined metastable fractions f_m measured by the HDA spectrometer are within the experimental uncertainty. This result can be expected since all ion beams were delivered by the same type of accelerator utilizing the same stripping method, i.e. foil stripping inside the tandem accelerator tank.

G_τ **for the HDA**

Table 4.6: Metastable $1s^2 2s 2p\,{}^3P$ fraction f_m and effective solid angle correction factor G_τ determined experimentally (Exp. - using Eq. 4.21) and by SIMION [241] Monte Carlo simulations. For the simulations, two different sets of lifetimes were used, one from Ref. [123] and one from Ref. [238]. Both lifetime sets are in Table 4.4. For the calculations regarding the energies of the current study see Table D.1 in p. 130.

Ion	E_p (MeV)	Mode	f_m	G_τ	
				Exp.	SIMION
C^{2+}	6.6	$F = 4$	0.70 ± 0.05	2.0 ± 0.4	1.92^a
					2.41^b
O^{4+}		$F = 4$	0.70 ± 0.05	1.9 ± 0.4	2.47^a
					2.80^b
O^{4+}		$F = 8$	0.67 ± 0.05	1.5 ± 0.4	2.08^a
					2.33^b

[a]Ref. [123]
[b]Ref. [238]

For the case of oxygen, the SIMION [241] obtained G_τ values are within estimated experimental uncertainty of the measured values, for the lifetimes reported in Ref. [246], while they deviate by an additional $\approx$20% for the lifetimes reported in Ref. [238]. However, in the case of carbon, SIMION [241] results are well within the experimental uncertainties. Even though the carbon analysis includes an extra experimental uncertainty due to the unresolved $1s2s^2 2p\,{}^3P$ peak. A variation of it's contribution from 10% up to 30% results in experimental values that remain within the SIMION range of results. From Table 4.6 it is seen that G_τ depends sensitively on the lifetimes and the corresponding Auger yields

involved, as evident from the $\approx$15% differences in the estimated values of G_τ using the lifetimes reported in Refs. [123, 238], both for oxygen as well as for carbon.

4.4 Data analysis outline

The apparatus includes a 2-D PSD which along with the DAQ software, generates files that have the information of every pixel in the 2-D matrix representing the PSD information. As described earlier, the PSD information can be digitally rotated. The common practice is to digitally align the dispersion plane of the analyzer with the X-axis of the monitor. Two gates are applied on the PSD online image, one for X-projections and one for Y-projections. Careful and consistent placement of these rectangular projection filters unwanted background. Further filtering is applied on the pulse height distribution of incoming signals. All collected data with same X-coordinate[6] and Y-coordinate are summed to a three column "projection file". This file consists of three columns: 1) channel number, 2) total counts summed for the same "Y" channels within the "Y" window, 3) total counts summed for the same "X" channels (energy) within the "X" window.

The basic analysis of the acquired spectrum requires the following distinctive steps:

1. **Background subtraction**. The data analysis require only the values of the areas of the peaks in the electron spectra. Therefore no need for an additional background measurement is needed but rather a background subtraction through an appropriate fitting.

2. **Energy Calibration**. A quadratic function of the "X" channel of the detector was assigned to the laboratory electron energy in eV. Assignment of electron energy to each channel is described by Eq. 4.9.

3. **Lab-to-rest frame transformation**. The lab electron energies were transformed to the rest frame of the projectile ion using the relativistic transformation formula, Eq. 4.3.

4. **Normalization**. The final step for every spectrum is to be normalized with respect to experimental parameters, in order to obtain normalized yields.

For the needs of the APAPES initiative, an Excel™ file was developed, that performs all the above tasks. The main advantage of this file is that it requires only three specific inputs: The spectrum, the experimental parameters and the constants of the fitted functions[7] on the raw data. The implemented analysis scheme is presented.

All spectra were acquired in multiple, low-count runs. This allowed for in-between comparisons to ensure reproducibility throughout the measurement. This accounts for possible DAQ freezing problem, experienced in the past, along with unwanted changes in the metastable fraction to the beam. The latter can be a result of either the FTS foil being worn out, or the GTS pressure variations. After completion of the measurement, all the reproducible low-count runs were summed to a final raw data file. This spectrum is then fitted [247] with Voigt/SplitVoigt functions and a cubic background, in order to obtain the centres of the peaks. This step is required for the spectrum self calibration, described in subsection 4.1.3.

Experimental parameters are divided into two categories, variable and fixed. Variable parameters are target pressure, ion beam energy, charge state, retardation factor F,

---

[6]bins of same energy
[7]Peak centers and BKG constants

tuning energy W, total counts and scale of BCI. Fixed parameters are solid angle, length of gas cell, DTC, transmission and MCP efficiency. Channels are converted to laboratory frame energy with the use of Eq. 4.9, and then transformed to the rest frame with the use of Eq. 4.3. The Y-axis of the spectrum is normalized with the use of Eq. 4.13 to DDCS lab frame, and then converted to rest frame with the use of Eq. 4.8. After that, the spectrum is ready for analysis.

For the analysis various schemes were evaluated, on a consistency basis. The analysis scheme finally implemented is, on a large extend, automated. This ensured a consistent approach to the analysed data. The analysis scheme, implemented within the FitYK™ software [247], is presented below.

1. **BKG** Although trivial, in the case of higher collision energies and/or low-Z targets, consistent selection of background between the various metastable fraction measurements, is of significant importance. This also applies for the integrations to evaluate the SDCS's on the final, processed spectra. To ensure consistency between the fits of the raw and the final spectra, the initial background is reproduced also for the rest-frame fit. Due to the rest frame transformation, a 4th degree polynomial is required. The Excel™ file produces automatically the FitYK command to replicate the initial background. To avoid absolutely locked parameters, all background parameters had a $\pm 0.1\%$ parameter window (domain) for the fits.

2. **^{2}S** All Auger lines that originate from prompt states are fitted with a Voigt profile. This corresponds to a Lorentzian line shape of natural width folded with the Gaussian-like response function of the HDA [133, 141, 170, 216]. Therefore, a Voigt profile was selected for ^2S. However, since the ^2S line blends with the ^4P line, the parameter that defines the ratio of Lorentzian and Gaussian widths was locked to zero. This corresponds to a strictly Gaussian line shape. The goal was to avoid the extended wings of the Loretzian distribution, that could interfere with the ^4P line. This was cross-checked by running independent fits and considering everything else a background (including the ^4P). Finally, the actual function used is a variation of the Voigt function called VoigtA. This variation has the area as a parameter and provides the uncertainty of the area.

3. **^{4}P** The long-lived ^4P components may Auger decay near the entrance of the HDA lens. This results in a low-energy shoulder for the ^4P (at 229.64 eV rest frame energy) that blends with the ^2S (at 227.17 eV rest frame energy). To treat this problem, the following procedure was implemented:

   The C^{4+} + Neon spectra present significantly large yields regarding the ^4P state. For every projectile energy, at rest frame, the spectra with high metastable fractions were selected. Then, the ^4P state was profiled with the use of two SplitVoigt functions with equal center parameters. For all other spectra, all the fitting parameters except the center and total peak height were fixed to this Ne standardized reference profile, within the FitYK [247] program.

4. **^{2}P$_-$ and ^{2}P$_+$** For these states, the same procedures with the ^2S line were followed. An additional restriction was to set the *gwidth* parameter equal in both peaks. *gwidth* is a parameter proportional to the Gaussian width. This limitation is based on the assumption that since these lines are close energetically, they should exhibit same characteristics in terms of resolution.

5. **1s2p^2 ^{2}D** No particular restrictions in this case. ^2D is expected to be produced dominantly by TE from the ground state. Therefore, it is expected to have a Fano-like

profile [180]. For this reason, the line was fitted with with a SplitVoigt asymmetric profile.

The areas of the above lines are then the so called normalized yields. In the next section the SDCS analysis is described.

4.5 Single Differential Cross Sections - Contribution analysis - Ratio Calculations

In order to transform normalized state production yields to SDCS, the $1s2s\,^3S$ metastable fraction of the beam must be taken into consideration. Depending on the energy and the stripping method used, the $1s2s\,^3S$ content of the beam can be varied [59, 109]. In particular, a GTS is known to produce beams with significantly lower metastable content (<5%) [59, 60, 109]. This allowed for the early developments of the two-measurements technique, in which the low, but non-zero, metastable fraction was assumed negligible, with small error. The high metastable content measurement is typically performed with a foil stripper, while the second, much lower metastable content measurement, with a gas stripper. The two KLL spectra were then normalized at the ^2D line and subsequently subtracted resulting in just the $1s2s\,^3S$ contributions [6, 59].

Benis *et al* [168] developed a method where the condition of a zero metastable fraction in the low fraction second measurement can be relaxed, as long as the two fractions are appreciably different. This is particularly helpful in cases where the production of a low enough metastable fraction is not always possible [168, 246]. This method was used for the data analysis of this work and will be presented.

4.5.1 Basic principles

The KLL spectrum under consideration is comprised by the five $1s2l2l'\,^{2,4}L_J$ states described in Sec. 4.4. These are ^2S, ^4P, $^2P_-$, $^2P_+$ and ^2D [144, 202]. Considering a spectrum, originating from an ion beam with two distinct components, there are, in principle, eleven variables, and five data points (measured yields):

- Five SDCS from the $1s^2\,^1S$ component of the beam, for every one of the five $1s2l2l'\,^{2,4}L_J$ states.

- Five SDCS from the $1s2s\,^3S$ component of the beam, for every one of the five $1s2l2l'\,^{2,4}L_J$ states.

- The metastable content ($1s2s\,^3S$) of the delivered ion beam, defined as f_{3S}.

- The five normalized yields.

Metastable fraction f_{3S} is defined by Eq. 4.24:

$$f_m \equiv \frac{N_m}{N_m + N_g} = \frac{N_m}{N_I},\qquad(4.24)$$

where N_m is the number of initial ions in the $1s2s\,^3S$ state, N_g is the number of initial ions in the $1s^2\,^1S$ state and N_I is the total number of ions. Even by acquiring two different spectra with appreciably different metastable content leads to twelve variables (two fractions) with ten data points. However, examination of the production mechanisms of the ^4P and the ^2D states can remove some of the variables. As described in detail in

Ch. 2, the ^4P is populated primarily from the $1s2s\,^3S$ component of the beam, while the ^2D state is populated solely from the $1s^2\,^1S$ component of the beam. Under these assumptions, valid for low-Z gas targets, there are only ten variables left, along with ten data points, leading to an exact solution.

Before proceeding, the notation used in the following section is explained.

- $N_i^e[x]$. It defines the integrated number of electrons for line x. Typically it refers to integration of raw data, unless stated otherwise.

- κ_i. It is the normalization parameter for every spectra ($\equiv N_I n L_c T \eta \Delta\Omega_0$). It includes all the normalization parameters included in Sec. 4.2.

- $\xi[x]$. It is the Auger yield for line x.

- $\dfrac{d\sigma_i[x]}{d\Omega'}$. It defines the production cross section $\left(\equiv \dfrac{N_i^e[x]}{\kappa_i \cdot \xi[x]}\right)$ of line x in spectrum i. Often used is the short hand writing, $d\sigma_i[x] \equiv \dfrac{d\sigma_i[x]}{d\Omega'}$.

- $\dfrac{d\sigma_{m,g}[x]}{d\Omega'}$. It defines the SDCS contribution of the respective (g - ground, m - metastable) beam component for line x. Often used is the short hand writing, $d\sigma_{m,g}[x] \equiv \dfrac{d\sigma_{m,g}[x]}{d\Omega'}$.

4.5.2   Ratios determination

There are four line ratios under investigation for the KLL spectrum. They are described in detail in Ref. [168]. It should be noted that the formalization in Ref. [168] is written treating the raw data acquired. This is one of the main advantages of this method, with the only limitation that the two spectra are relatively normalized, as stated in the previous section. By doing so, the line ratios under consideration can be estimated *in-situ*, during the acquisition of the spectra. However, small deviations can be expected, originating primarily to the ΔE factor (See Eq. 4.19), the only non-uniform transformation of the spectra. Here, they are briefly presented:

R_m: The main ratio of interest to this work. It is the ratio of the ^4P to the sum of the $^2P_-$ and $^2P_+$ contributions representing together the total ^2P production from the $1s2s\,^3S$ metastable component of the beam.

r_m: It is the ratio of the $1s(2s2p\,^1P)\,^2P_+$ to $1s(2s2p\,^3P)\,^2P_-$ contributions from the $1s2s\,^3S$ component. It serves as an additional test of the spin-statistics predicted value [4, 165] of 3. Additionally, upwards deviations from the predicted value, may indicate the production of the $1s2p^2\,^4P^e$ line, the second lower quartet state that can be formed.

Additionally to the contributions from $1s2s\,^3S$, information on two similar ratios can be extracted, regarding contributions from $1s^2\,^1S$. The contributions to these ground states ratios arise from TE, which theory is expected to be able to calculate within about 20% when the process is resonant RTE.

R_g: It is the ratio of ^2D to $^2P_\pm$ from the $1s^2\,^1S$ component.

r_g: It is the ratio of the $1s(2s2p\,^1P)\,^2P_+$ to $1s(2s2p\,^3P)\,^2P_-$ contributions from the $1s^2\,^1S$ component.

Regarding the ratios delivered from the $1s^2\ {}^1S$ component: These ratios are not constant over the energy range examined here. However, as shown in Ch. 6, an average value can be obtained. Moreover, the variation of calculated values for the collision energies under consideration can provide with a standard deviation estimation. Impulse Approximation - Resonant Transfer-Excitation with Auger emission (IA-RTEA) calculations result in a value of $R_g = 4.93$ with a standard deviation of $\sigma_{\bar{R}_g} = 0.22$, in the case of He. The deviation from a single value is due to the different energies, and therefore resonances, of the ${}^2P_-$, ${}^2P_+$ and ${}^2D$ lines. Similarly, $r_g = 2.84$ with a standard deviation of $\sigma_{\bar{r}_g} = 0.11$. The smaller deviation is the result of comparing only two lines, whose energies are in proximity. In the case of H_2, $R_g = 4.81$ with a standard deviation of $\sigma_{\bar{R}_g} = 0.38$, and $r_g = 2.78$ with a standard deviation of $\sigma_{\bar{r}_g} = 0.18$. For both ratios, the change compared to He can be attributed to different ionization potential. The increase of the standard deviations is attributed to the narrower Compton profile, making the disparities between the resonances more pronounced.

$$R_m \equiv \frac{\dfrac{d\sigma_m[{}^4P]}{d\Omega'}}{\dfrac{d\sigma_m[{}^2P_+]}{d\Omega'} + \dfrac{d\sigma_m[{}^2P_-]}{d\Omega'}} \qquad (4.25a)$$

$$r_m \equiv \frac{\dfrac{d\sigma_m[{}^2P_+]}{d\Omega'}}{\dfrac{d\sigma_m[{}^2P_-]}{d\Omega'}} \qquad (4.25b)$$

$$R_g \equiv \frac{\dfrac{d\sigma_g[{}^2D]}{d\Omega'}}{\dfrac{d\sigma_g[{}^2P_+]}{d\Omega'} + \dfrac{d\sigma_g[{}^2P_-]}{d\Omega'}} \qquad (4.25c)$$

$$r_g \equiv \frac{\dfrac{d\sigma_g[{}^2P_+]}{d\Omega'}}{\dfrac{d\sigma_g[{}^2P_-]}{d\Omega'}} \qquad (4.25d)$$

For convenient expression of the line ratio formulas, a shorthand function was defined [168]. This is Eq.4.26:

$$N[x,y] \equiv \left(\frac{N_1^e[x]}{N_1^e[y]} - \frac{N_2^e[x]}{N_2^e[y]} \right) \qquad (4.26)$$

where x, y denote a specific line, subscript denotes which spectrum of the dual spectrum technique is used, and N^e is the integral of the line. The most useful aspect of this function is that it is free of any normalization parameters. Each of the two fractions within the formula is the ratio of the two lines within the same spectrum. Therefore, the application of the formulas can be performed at all analysis stages. That is either the raw data acquired or the final normalized spectra. Also not required is the knowledge of the

metastable fraction in each measurement $i = 1, 2$.

$$R_m = \frac{\dfrac{N[^4P,^2D]}{G_\tau \xi[^4P]}}{\dfrac{N[^2P_+,^2D]}{\xi[^2P_+]} + \dfrac{N[^2P_-,^2D]}{\xi[^2P_-]}} \quad \text{(4.27a)} \qquad r_m = \frac{\xi[^2P_-]}{\xi[^2P_+]}\frac{N[^2P_+,^2D]}{N[^2P_-,^2D]} \quad \text{(4.27b)}$$

$$R_g = \frac{\dfrac{N[^2D,^4P]}{\xi[^2D]}}{\dfrac{N[^2P_+,^4P]}{\xi[^2P_+]} + \dfrac{N[^2P_-,^4P]}{\xi[^2P_-]}} \quad \text{(4.27c)} \qquad r_g = \frac{\xi[^2P_-]}{\xi[^2P_+]}\frac{N[^2P_+,^4P]}{N[^2P_-,^4P]} \quad \text{(4.27d)}$$

4.5.3 Fraction calculations

For each spectrum, the ^4P and ^2D lines are proportional to the f_m and $(1-f_m)$ quantities, respectively. Applying this to Eq. 4.13 results in Eqs. 4.28a and 4.28b:

$$d\sigma_m[^2D] = \frac{N_e(^2D)}{N_g nl\Delta\Omega T\eta}\frac{N_g}{N_I} = \frac{d\sigma(^2D)}{d\Omega}\frac{N_g}{N_I} \tag{4.28a}$$

$$d\sigma_g[^4P] = \frac{N_e(^4P)}{N_g nl\Delta\Omega T\eta}\frac{N_m}{G_\tau N_I} = \frac{d\sigma(^4P)}{d\Omega}\frac{N_m}{G_\tau N_I} \tag{4.28b}$$

$N_e(x)$ is the integral of line "x" after transformation to the rest frame. Eqs. 4.28a and 4.28b practically define the SDCS for the respective lines. Equation 4.28b includes also a lifetime correction factor that the ^4P state requires since it is a metastable state that decays from the gas target, throughout the exit of the HDA.

$$d\sigma_1[^2D] = \frac{d\sigma_g(^2D)}{d\Omega}(1 - f_1) \quad \text{(4.29a)} \qquad d\sigma_2[^2D] = \frac{d\sigma_g(^2D)}{d\Omega}(1 - f_2) \quad \text{(4.29b)}$$

$$d\sigma_1[^4P] = \frac{d\sigma_m(^4P)}{d\Omega}\frac{1}{G_\tau}f_1 \quad \text{(4.29c)} \qquad d\sigma_2[^4P] = \frac{d\sigma_m(^4P)}{d\Omega}\frac{1}{G_\tau}f_2 \quad \text{(4.29d)}$$

This system can be solved exactly for the values of f_1 and f_2 of the two different metastable fractions.

$$f_1 = d\sigma_1[^4P]\left[\frac{d\sigma_1[^2D] - d\sigma_2[^2D]}{d\sigma_1[^2D]d\sigma_2[^4P] - d\sigma_2[^2D]d\sigma_1[^4P]}\right] \tag{4.30a}$$

$$f_2 = d\sigma_2[^4P]\left[\frac{d\sigma_1[^2D] - d\sigma_2[^2D]}{d\sigma_1[^2D]d\sigma_2[^4P] - d\sigma_2[^2D]d\sigma_1[^4P]}\right] \tag{4.30b}$$

By using the same projectile energy, gas pressure and BCI counts, the normalization factors are kept the same, thus they are cancelled out in (4.30a) and (4.30b).

The major advantage of this method is that it also cancels out factors such as the ^4P lifetime correction factor G_τ, minimizing the possible uncertainties that might occur. The only limitation is that the spectra need to be acquired under the same conditions. For

the more general case of non-normalized, raw spectra, metastable fractions are given by Eq. 4.31:

$$f_{3S}^{[i]} = \frac{N_i^e[^4P]}{\kappa_i} \left[\frac{\kappa_1 N_2^e[^2D] - \kappa_2 N_1^e[^2D]}{N_2^e[^2D]N_1^e[^4P] - N_1^e[^2D]N_2^e[^4P]} \right] \text{ for } i=1,2 \tag{4.31}$$

4.5.4 Beam component contributions

At this point, with the metastable fractions calculated, production cross sections for the ^4P and ^2D from the $1s2s\,^3S$ and $1s^2\,^1S$ respectively, can be calculated. However, the $1s^2\,^1S$, $1s(2s2p\,^3P)\,^2P_-$ and the $1s(2s2p\,^1P)\,^2P_+$ require a different approach, since they have contributions from both beam components. For each one of these states, the solution is in a matrix equation system as in Eq. 4.32:

$$\begin{bmatrix} f_1 & (1-f_1) \\ f_2 & (1-f_2) \end{bmatrix} \times \begin{bmatrix} d\sigma_m[x] \\ d\sigma_g[x] \end{bmatrix} = \begin{bmatrix} d\sigma_1[x] \\ d\sigma_2[x] \end{bmatrix} \tag{4.32}$$

Utilizing the restrictions regarding the production of ^4P and ^2D, the formulas for all lines for the separate $1s^2\,^1S$ and $1s2s\,^3S$ contributions are given below [168]

$$\frac{d\sigma_m[x]}{d\Omega'} = S[^2D]H[x,^2D] \tag{4.33a}$$

$$\frac{d\sigma_g[x]}{d\Omega'} = S[^4P]H[x,^4P] \tag{4.33b}$$

with

$$S[x] \equiv \frac{d\sigma_1[x]d\sigma_2[x]}{d\sigma_2[x] - d\sigma_1[x]} \tag{4.34a}$$

$$H[x,y] \equiv \left(\frac{d\sigma_1[x]}{d\sigma_1[y]} - \frac{d\sigma_2[x]}{d\sigma_2[y]} \right) \tag{4.34b}$$

4.6 Error propagation

The primary uncertainty of the calculated results arises from the analysis formulas, described in Ch. 2. These formulas make use of the aforementioned normalized yields. Their uncertainties were calculated using the following method. The statistical uncertainty σ_i for each channel i is given by $\sigma_i = \sqrt{N_i}$, where N_i is the number of counts. For each of the spectra, the uncertainties were processed similarly to the data points, and processed within the FitYK [247] fitting program . Each data point is then weighted accordingly ($w_i = \frac{1}{\sigma_i}$), and the standard error of the fitting parameters is calculated. For the lines where Area was a fitting parameter, it straight forwardly provides the yield uncertainty. The rest were assumed to have a similar $\frac{\Delta\text{Area}}{\text{Area}}$ ratio.

To calculate the resulting uncertainty for each of the formulas $F(x_1, x_2, \cdots, x_n)$, the following function was implemented:

$$\Delta F(x_1, x_2, \cdots, x_n, \Delta x_1, \Delta x_2, \cdots, \Delta x_n,) = \sqrt{\left(\frac{\partial F}{\partial x_1}\Delta x_1\right)^2 + \left(\frac{\partial F}{\partial x_2}\Delta x_2\right)^2 + \cdots, \left(\frac{\partial F}{\partial x_n}\Delta x_n\right)^2} \tag{4.35}$$

For the calculation of these functions, Mathematica™ was used. Eq. 4.36 is an example of the computed error functions.

$$
\begin{aligned}
dRm =& (\mathrm{dn12d}^2\mathrm{n22d}^2(\mathrm{n14p}(\mathrm{n22pm} + \mathrm{n22pp}) - \mathrm{n24p}(\mathrm{n12pm} + \mathrm{n12pp}))^2 \\
&+ \mathrm{dn12pm}^2\mathrm{n22d}^2(\mathrm{n14pn22d} - \mathrm{n12dn24p})^2 + \mathrm{dn12pp}^2\mathrm{n22d}^2(\mathrm{n14pn22d} - \mathrm{n12dn24p})^2 \\
&+ \mathrm{dn14p}^2\mathrm{n22d}^2(-\mathrm{n12d}(\mathrm{n22pm} + \mathrm{n22pp}) + \mathrm{n12pmn22d} + \mathrm{n12ppn22d})^2 \\
&+ \mathrm{dn22d}^2\mathrm{n12d}^2(\mathrm{n14p}(\mathrm{n22pm} + \mathrm{n22pp}) - \mathrm{n24p}(\mathrm{n12pm} + \mathrm{n12pp}))^2 \\
&+ \mathrm{dn22pm}^2\mathrm{n12d}^2(\mathrm{n14pn22d} - \mathrm{n12dn24p})^2 + \mathrm{dn22pp}^2\mathrm{n12d}^2(\mathrm{n14pn22d} - \mathrm{n12dn24p})^2 \\
&+ \mathrm{dn24p}^2\mathrm{n12d}^2(-\mathrm{n12d}(\mathrm{n22pm} + \mathrm{n22pp}) + \mathrm{n12pmn22d} + \mathrm{n12ppn22d})^2)^{\frac{1}{2}} \\
&\times \frac{1}{(-\mathrm{n12d}(\mathrm{n22pm} + \mathrm{n22pp}) + \mathrm{n12pmn22d} + \mathrm{n12ppn22d})^2}
\end{aligned}
$$

$$(4.36)$$

Terms beginning with "nX" denote yields from either spectrum "1" or "2" acquired. Spectrum "1" is the spectrum with the high $1s2s\,^3S$ content. "nX" is followed by state name, for example "n22pm" is the measure yield of the $1s(2s2p\,^3P)\,^2P_-$ from the low metastable content spectrum. Terms beginning with "dnX" denote their respective uncertainties.

$$
R_m = \frac{\dfrac{N[^4P,^2D]}{G_\tau}}{N[^2P_+,^2D] + N[^2P_-,^2D]}
$$

$$(4.37)$$

Chapter 5

Results on metastable state contributions - Single Electron Capture

Introduction

The collision system under investigation is the mixed state ($1s^2\,{}^1S$, $1s2s\,{}^3S$) carbon ions colliding with various gas targets. The carbon ions were accelerated to 6, 9, 12 and 15 MeV (0.50, 0.75, 1.00 and 1.25 MeV/u). The gas targets used were H_2, He, Ne and Ar. For each of the above combinations, two measurements were performed, each with different metastable $1s2s\,{}^3S$ content, as required by the contribution separation technique [168] applied here[1]. Single collision conditions were ensured, by proper adjustment of the gas target pressure. Between measurements with different gas targets, the gas distribution tubes were carefully flushed. Considering the requirements of the dual spectra technique [168], the production of certain states must be limited to a single component individually. This can be achieved with the use of low-Z targets, such as H_2 and He, with respectively low number of electrons. Moreover, these being simple atomic systems, they are easier to approach theoretically. Therefore, primary results are obtained from the H_2 and He spectra, while Ne and Ar serve as complementary measurements. In the following sections, results are presented, discussed. At the same time, the TC-BGM [81] and 3eAOCC [7, 248] theoretical approaches are discussed and compared to the experimental results.

5.1   Results on determined fractions

5.1.1   Metastable fraction results from H_2 and He spectra

The production method for every projectile energy is presented in Table 5.1. For 6 and 9 MeV, the FTS produced ion beam, the stripping energy results in rather small beam currents for the desired charge state (4+) [61]. Consequently, post-stripping was applied. For these energies, C^{3+} ions were accelerated and post-stripped to C^{4+} at the GPS.

In Fig. 5.1, the $1s2s\,{}^3S$ fractions are presented for the H_2 and He spectra. The calculation is based on Eqs. 4.30a and 4.30b. In almost all cases, the margins between the two targets overlap. Comparing the results of H_2 and He, there are two major qualitative differences:

---

[1]See Sec.4.5

Table 5.1: Production methods applied for varying $1s2s\,^3S$ metastable content. For higher collision energies, content variation was sufficient, with the use of the Gas/Foil Terminal Stripper (GTS/FTS). For lower collision energies, a C^{3+} $(1s^22s)$ ion beam, accelerated to the requested energy, was stripped at the Gas Post-Stripper (GPS), just before the beamline selection magnet.

$1s2s\,^3S$ content	Energy (MeV)			
	6	9	12	15
High	$C^{3+}\rightarrow$ GPS	$C^{3+}\rightarrow$ GPS	FTS	FTS
Low	GTS	GTS	GTS	GTS
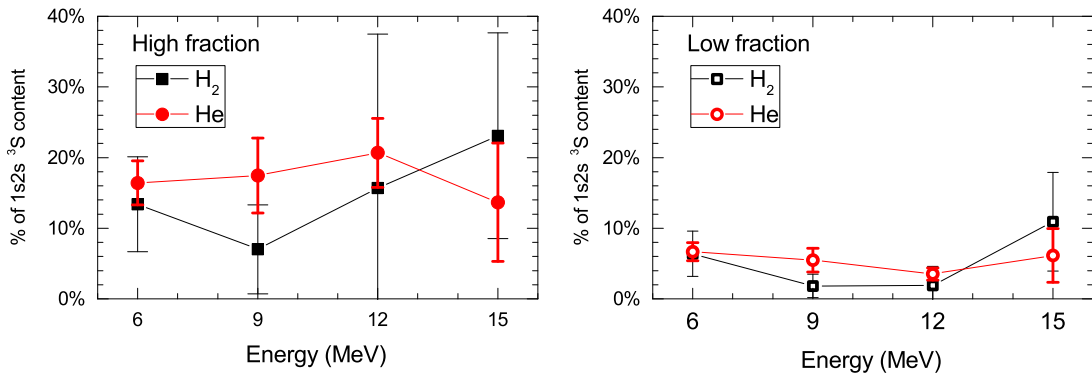
Figure 5.1: Determined $1s2s\,^3S$ metastable fractions with the use of the H_2 and He spectra. On the left are the results for the high metastable content spectra, and on the right for the low metastable content. Only statistical uncertainties depicted.

- For the high metastable content spectra, the results for all energies have an average fraction of 17% with a standard deviation of 2.5%. Considering that two distinct production methods were used, results for the full energy range seem consistent. This is further emphasized in the case of the low metastable content. In this set, the full energy range was acquired with the GTS. The results for all energies have an average of 5.5% with a standard deviation of 1.2%.

- Moreover, it is clear that for the H_2 spectra, uncertainty is significantly larger, a result of the $C^{4+}+H_2$ collision system having lower cross sections.

In this context, the experimental data of He for the determination of the $1s2s\,^3S$ metastable fraction are considered the most accurate. It should be emphasized that the above fractions are not necessary for the determination of the various ratios or the cross sections when using the two measurement technique. Regarding ratios determination, as seen in Eq. 4.26, 4.37, 4.27b, 4.27c and 4.27b, and stated before, each ratio, results from ratios of lines within the same spectrum. Therefore, these results are free from both metastable fraction determinations, and normalization parameters. We include the fraction determination in this study for completeness purposes as well as and because they can be used in cross section determination of heavier targets, e.g. Ne and Ar.
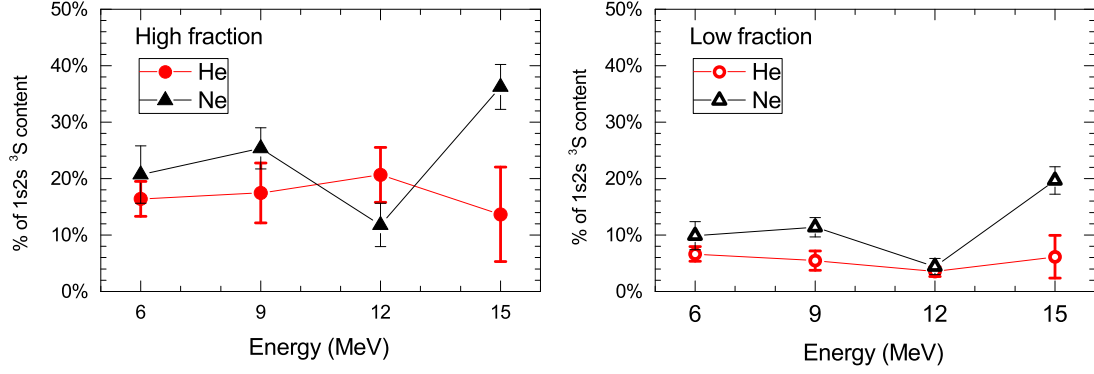
Figure 5.2: Determined $1s2s\,{}^3S$ metastable fractions with the use of the Ne and He spectra. On the left are the results for the high metastable content spectra, and on the right for the low metastable content. Only statistical uncertainties depicted.

5.1.2 Metastable fraction results from He and Ne spectra

For completeness, the comparison of the determined fractions from the spectra of Ne and He is also included. In Fig. 5.2, the corresponding $1s2s\,{}^3S$ fractions are presented. Examination of the results yields two major observations:

- First, with the exception of the 12 MeV point, there is an increasing trend for the determined fractions, as the energy increases.

- Again, with the exception of the 9 MeV point, there is fair agreement with the results from the He spectra.

The interpretation of these results requires proper understanding of the underlying TE mechanisms. There are in total three TE mechanisms that contribute to the formation of the ^2D line. These are RTE, NTEg and NTEm, described in Subsec. 2.2.2, p. 19. The resonance energy for RTE is around 6 MeV and is the dominant production mechanism at this collision energy. From this point, as the collision energy increases, all TE contributions decrease. However, due to its resonant behaviour, RTE decreases at a faster rate, compared to NTEg and NTEm. Although NTEg does not affect this method, any NTEm contributions to the ^2D would violate the assumption that the ^2D is produced primarily from the $1s^2\,{}^1S$ fraction of the beam. Such NTEm contributions are expected relatively close to the low energy wing of the ^2D resonance, and also 8for much higher projectile energies regarding the high energy wing. Bearing this under consideration, and the results on the fraction determination, we can see that there is fair agreement within the vicinity of the ^2D resonance energy.

Finally, the metastable fraction results from Ar are omitted. Comparing fraction results of Ar with the corresponding results of He, or even with the Ne, highlights the inappropriateness of this gas target regarding the method's aforementioned restrictions. Being the "heaviest" target, Ar exhibits both high nuclear charge and a large number of active electrons carried into the collisions. Therefore, although the production of ^4P is increased due to the many more electrons to be captured, NTEm contributions to the ^2D configuration are relatively more significant, thus the method for determining the metastable fraction is no longer applicable.

81

5.2 Results on production ratios

In this section, the results on capture ratios R_m and r_m, defined in Ch. 4 are presented. Regarding the H_2 and He targets, experimental results are obtained with the use of the equations described in Ch. 4. In the case of Ne and Ar, the state contributions from each component were obtained using the He fractions and Eqs. 4.32. The solution of Eqs. 4.32 provides with cross sections for all KLL states being produced from both ($1s^2\,^1S$ and $1s2s\,^3S$) beam components.

Regarding the ^2D state produced from collisions with Ne and Ar targets, it can be assumed to be populated also from the $1s2s\,^3S$ component of the ion beam. Ne and Ar being heavier targets, carry a larger number of electrons into the collision. For that reason, NTEm contributions to the ^2D state are no longer considered negligible. However, in the case of ^4P, production from the $1s^2\,^1S$ component it is highly improbable through the TE mechanisms, due to required spin-flip. In most cases, ^4P (^2D) production from the $1s^2\,^1S$ ($1s2s\,^3S$) component was found to be 1.5-2 orders of magnitude smaller than production from the $1s2s\,^3S$ ($1s^2\,^1S$) component, respectively, when extraction of separate contributions using the He fractions was applied.

Before presenting the results on the R_m ratios, it should be also noted that the latter approach regarding the Ne and Ar results bears the additional uncertainties of the fractions. Therefore, although the measurements have lower statistical uncertainty as a result of the stronger cross sections, the final results have higher uncertainties compared to the H_2 and He results. Due to increased uncertainties, some Ne and Ar results may be omitted.

5.2.1 The R_m ratio

As a reminder, R_m is defined as the ratio of the ^4P to $^2P_\pm$ contributions from the $1s2s\,^3S$ metastable component of the beam (See Eq 4.25a).

In Fig. 5.3, both experimental and theoretical results (in black lines and squares) on the ratio R_m for He and H_2 are presented. Also included in Fig. 5.3 are results both theoretical and experimental from previous studies (in blue/red lines and circles) for the He target [6, 81], highlighting the existing disagreement. As described in Ch. 2, regarding the present calculations, three limiting cases were examined. First, the directo $2p$ SEC case of $R_{m_{T2p}}$, calculated from the corresponding partial cross sections for direct $2p$ capture (dotted lines). The second case includes radiative cascade contributions from the $1s2snl\,^4L$ $n = 3, 4$. The radiative branching ratios were calculated with the COWAN code [197], while the nl SEC cross sections within the 3eAOCC calculation (dashed lines). Finally, the third case expands the second case, adding an extrapolation for capture to higher n levels, based on a $^1/n^3$ population model, similarly used in Ref. [81].

Regarding the comparison between theory and experiment, it can be seen that there is very good agreement between measured and calculated R_m values, for both the H_2 and He targets. The only exception is the 6 MeV point for H_2, where the experimental value is found to be larger than the theoretical. However, it exhibits the trend of increasing R_m with decreasing impact energy, in qualitative agreement with present calculations and the results reported in Ref. [5] for F^{7+} +H_2 collisions. The result for the H_2 at 15 MeV is omitted, due to the extremely high uncertainties, as a consequence of the low statistics. Comparing the theoretical results of the H_2 and He targets, there are two observations:

- First, in the no-cascade case, where the cross-sections of SEC to the ^4P over the $^2P_\pm$ are compared ($R_{m_{T2p}}$), the results are similar. For the lower collision energies, the $R_{m_{T2p}}$ is close to the pure spin statistics value of 1. As the energy increases, the
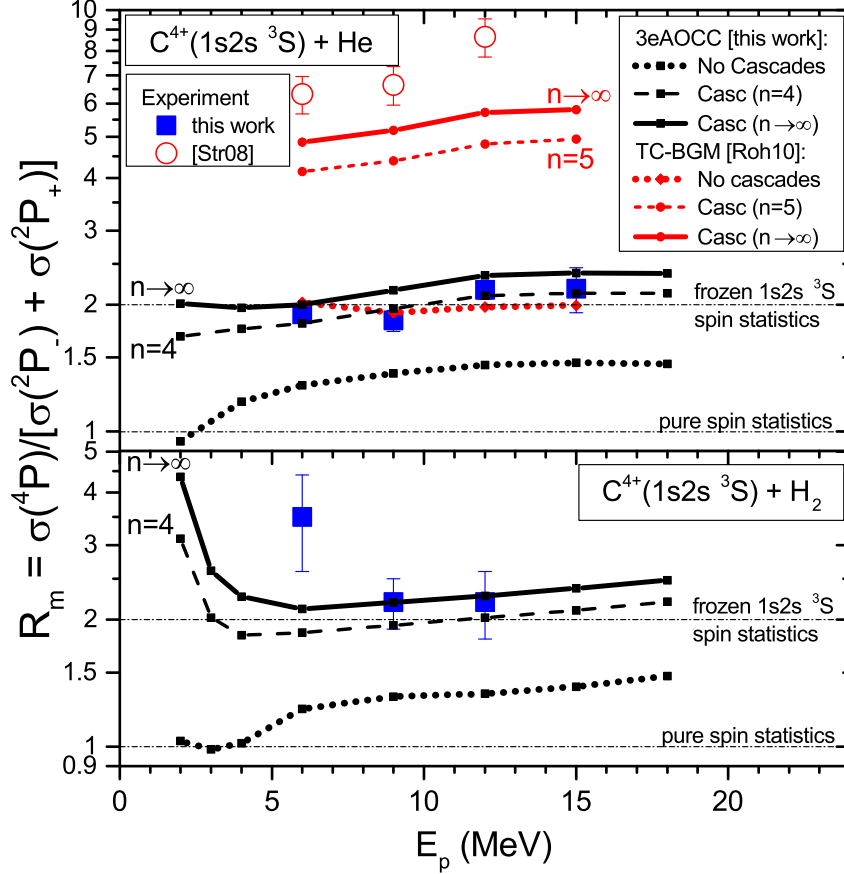
Figure 5.3: Results on the R_m ratio. Experimental results for H_2 and He are obtained from the use of Eq. 4.37. Ratio R_m, for $C^{4+}(1s2s\,^3S)$ collisions with He (top) and H_2 (bottom) as a function of projectile energy. Experiment (ZAPS): Squares (this work), circles [6]. Theory: Black lines (3eAOCC - this work), red lines [81]. Results *without* (dotted) and *with* radiative cascades from $1s2snl\,^4L$ states up to the indicated n (dashed) and extrapolated to $n \to \infty$ (solid) are shown. The *frozen* $1s2s\,^3S$ core spin statistics and *pure* spin statistics values are also indicated. Only statistical uncertainties depicted. Figure from Ref. [7]. See text for more details.

---

calculated $R_{m_{T2p}}$ value gradually shifts to 1.5[2]. As it can be seen, the calculations clearly depart from the frozen core value of 2, at least for this energy regime.

- The second observation regards the addition of the cascade contributions. It is clearly seen in Fig. 5.3 that, in the case of He, the inclusion of just the $1s2snl\,^4L$ ($n = 3, 4$) quartets selectively enhances the ratio R_m by a factor of $\approx 1.40 - 1.78$, the latter attributed to the lower collision energies. Extrapolating the cascade contributions to $n \to \infty$ with the $1/n^3$ scaling law there is further increase by a factor of $\approx 1.12 - 1.20$. In the case of H_2, the results are qualitatively similar. However, for the H_2 target, the effect of cascades is far more intense. The addition of the $1s2snl\,^4L$ ($n = 3, 4$) quartets leads to an enhancement of a factor of $\approx 1.50 - 2.00$. Again, extrapolating the cascade contributions to $n \to \infty$, results in a further increase by a factor of $\approx 1.12 - 1.40$. It can be seen that for the $C^{4+}+H_2$ system, the cascade contributions are stronger, relative to the $C^{4+}+$He case. This, also observed in Ref. [5], can be

---

[2]Especially in the case of He, the 1.5 value appears to be reached asymptotically, as an upper limit.

attributed to the different asymmetry parameter Z_P/Z_T for these two systems. For both cases, as the collision energy lowers, n_{max}, the shell where SEC is maximum, tends to increase. However, due to the different asymmetry parameters, for the $C^{4+}+H_2$ case, this increase takes place at higher, compared to the $C^{4+}+He$ case, energies. As already described, increasing n_{max} leads to stronger population by SEC of higher $1s2snl\,^4L$ quartets, and therefore, stronger cascade contributions to the ^4P state.

These results demonstrate the effect of the cascade contribution over the measured ratio R_m. Along with the experimental and theoretical results of this thesis, Fig. 5.3 also includes previous independent R_m measurements (open red circles). These measurements have been critically re-evaluated by proper $\overline{G_\tau}$ corrections in Ref. [241], a correction presented in p.85. Regarding the TC-BGM calculations [81] (red lines in Fig. 5.3), and the difference in the results presented in this thesis, it can be most likely attributed to the use of the multiple active electrons approach, instead of the more limited one-electron treatment within the $1s2s\,^3S$ frozen core approximation. There are few more comments for the results of the TC-BGM [81] calculation: Regarding the cascade contributions, the results for R_m from Ref. [81] are 2 to 2.5 times larger compared to present results [7]. This may be partially attributed to the $1s2s\,^3S$ frozen core approximation, in which quartets and doublets are populated in fixed proportions. This applies not only to the initial population ratio $R_{m_{T2p}}$ but also to SEC to higher nl states. Finally, regarding the comparison of the two R_m calculations, it can be seen that both calculations show an increasing trend in their common range between 0.5 to 1 MeV. What is interesting is that for the calculations presented in this thesis [7, 248] this trend originates in the $2p$ SEC $R_{m_{T2p}}$, whereas for the data from Ref. [81] it appears to originate in the cascades.

Complimentary to the above measurements, are measurements at higher Auger energies, closer to the $1s2s\,^3S$ series limit, at 298.96 eV [235]. During these measurements, it was realized that the spectrum up to the series limit exhibited various Auger lines. In Ref. [190], this study is presented. The main argument in this study is the existence of various $(1s2s\,^3S)nl\,^2L$ states. Their observation in the Auger spectra indicates capture to higher n. Therefore, $(1s2s\,^3S)nl\,^4L$ quartet states are expected to be similarly populated, since there are no selection rules or other symmetries blocking such a process. However, as discussed, they are not observable since their Auger decays is very weak due to spin conservation.

As can be seen, various $(1s2s\,^3S)nl\,^2L$ ($n = 3, 4$) are populated. Hatched lines are the $2s2p\,^{3,1}P$ lines, populated by excitation mechanisms. Unlabelled lines are Auger states that are expected to be populated from the $1s^2\,^1S$ ground state by TE mechanisms, see Ref. [190] for more details. Also, regarding the intensities of the various $(1s2s\,^3S)nl\,^2L$ ($n = 3, 4$) formed lines, an R_{cc} of approximately 1.5 up to 2 as an upper limit, is suggested [190].

Previous isoelectronic measurements [59, 109], analyzed with the two spectra method by Benis et al [168], provided some similar values with the ones presented here. For the sake of simplicity MeV/u will be used. For the $B^{3+} + H_2$ collision system they report $R_m = 3.5 \pm 0.4$ at 0.41 MeV/u and $R_m = 2.9 \pm 0.2$ at 0.36 MeV/u,, where all are within uncertainty of the results of this thesis for the H_2 target yielding $R_m = 3.54 \pm 0.90$ at 0.50 MeV/u. Regarding the He target, the results do not overlap. For the $F^{7+} + H_2$ case they report $R_m = 1.8 \pm 0.3$ at 1.33 MeV/u, in good agreement with the He target [168]. Due to the high asymmetry parameter parameter of the $F^{7+} + H_2$, one would expect a higher R_m value, even at this collision velocity. Therefore, a 3eAOCC calculation could provide more information on the $R_{m_{T2p}}$, and how this is affected varying Z_p.
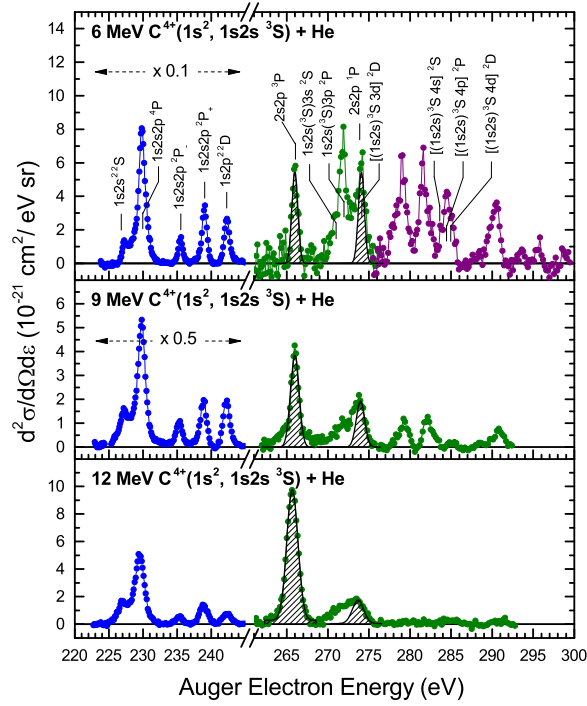
Figure 5.4: Higher energy Auger lines. Figure from Ref. [190].

5.2.1.1 Comparison to previous measurements

A similar measurement was conducted by Strohschein *et al* [6]. In their publication, they study the $C^{4,5+}$+He, Ne system, in the 0.5-1 MeV/u velocity range. Before discussing the respective results on the R_m ratio, there are two major differences regarding their experimental approach:

- Regarding the apparatus, there is one major difference. As described in detail in Ref. [249],the gas cell is placed much closer, right in front of the analyzer (tandem PPA). This gives rise to two issues:

  1. The different geometry of the apparatus leads to the calculation of a different solid angle correction factor. They define their correction factor $\zeta = \frac{N_{TRUE}(x)}{N_{OBS}(x)}$ [249]. This correction factor acts as a multiplier to the measured ^4P yield, contrast to our own G_τ(i.e. G_τ = 1/ζ) [156, 241]. Reported ζ values for 6, 9 and 12 MeV C^{4+} collisions with He are 7.3, 8.8, and 10.2 as shown in Ref. [6]. These values correspond to G_τ correction factors of 0.137, 0.114 and 0.098, respectively. Benis *et al* [241] reported a different J-averaging scheme than the one Strohschein used, similar to the one used in Ref. [147], that results to G_τ values of 0.496, 0.449 and 0.415 for the respective energies.

  2. The velocities of the ion beams used here is $V_p \approx 10 - 16$ mm/ns range. The C^{3+} ^4P, lifetimes range between 3 to $\approx$120 ns [123], depending on the $J-$level (see Table. 4.4 on page 65). Therefore, for setups where the gas cell is quite close to the analyzer (57 mm) the expected ^4P signal is rather low. For example, for such velocities, and low $1s2s\,^3S$ fraction ion beams, an even smaller percentage of the populated $^4P_{\frac{5}{2}}$ sub-level, auto-ionizes before the analyser. Although this, along with the mid-flight varying acceptance angle, is treated

with the use of a correction factor [249], the low ^4P signal for their low fraction[3] measurement may lead to the erroneous conclusion that there is no metastable beam component present.
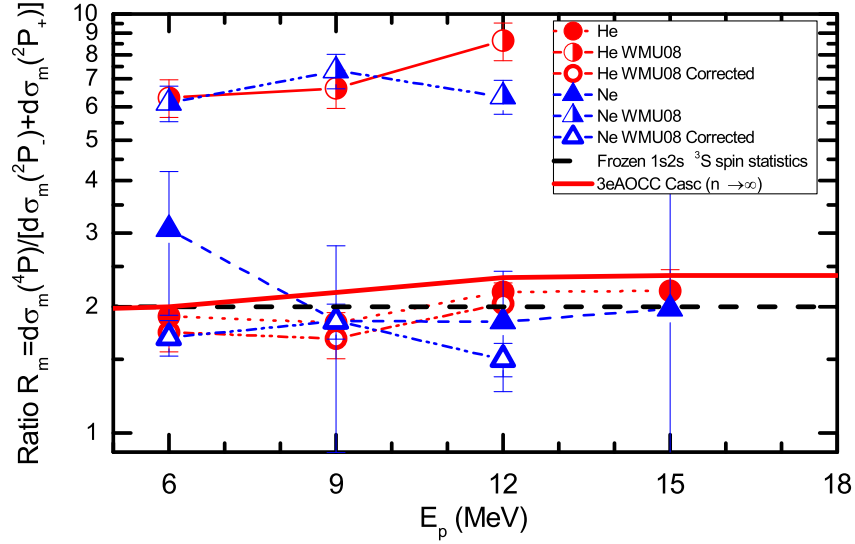
Figure 5.5: Results on the R_m ratio. Comparison for He and Ne between present work and Ref. [6] with and without corrections. Only statistical uncertainties depicted. See text for more details.

- The method for separating $1s^2\,{}^1S$ and $1s2s\,{}^3S$ contributions in Ref. [250] also requires two measurements of variable metastable content, as it is fashioned after the method of Benis *et al* [168]. The major difference is that the low-fraction measurement is considered to have zero metastable content ($<3\%$), therefore termed "ground state". This method requires the normalization of the ground-state spectra ^2D intensity to the corresponding mixed-state ^2D intensity. By doing so, the line intensities of the generated spectrum correspond to the ground state contributions of the mixed-state spectrum. Then, the normalized ground-state spectrum is subtracted from the mixed-state spectrum. This procedure assumes that all of the ^2D intensity in the mixed-state beam is due to the ground-state component, and therefore the resulting normalization factor gives an upper limit to the ground-state fraction present in the mixed state beam and a corresponding lower limit to the metastable fraction [6]. After the subtraction, what is left is considered contributions from just the $1s2s\,{}^3S$ component of the ion beam. From the $1s2s\,{}^3S$ spectrum, the strength of each line, and subsequently the ratio under question, can be determined.

In Fig. 5.5 the comparison for the R_m ratio is shown. In their publication, Strohschein *et al* [6] obtain R_m values between 6 and 8 for the collision energies reported. However, after applying our own new corrections to their correction factor, their results appear to be much closer to the results of this thesis: Regarding He, results appear to have a small offset, well within uncertainty. Regarding Ne, results are within uncertainty. Thus, the two experiments, after applying our corrections to their measured ratio, are in agreement, with R_m being in the vicinity of 2, in agreement with the 3eAOCC calculations, including the cascades.

---

[3]Termed "ground state" within Ref. [6].

5.2.1.2 Partial R_m ratios

To further explore the situation, two auxiliary ratios were defined. These are R_{m+} and R_{m-}, corresponding to the production by $2p$ capture to the $1s2s\,^3S$ ratio of the ^4P over $^2P_+$ and $^2P_-$, respectively.

As can be seen in Fig. 5.6, R_{m+} seemingly shows good agreement with the statistical approach. However, since there is cascading feeding to the ^4P state the experimental values should be higher. Moreover, for the case of R_{m-}, the overall ratio is smaller than the statistical value of 8, even though in the frozen core picture cascade feeding requires values higher than 8.
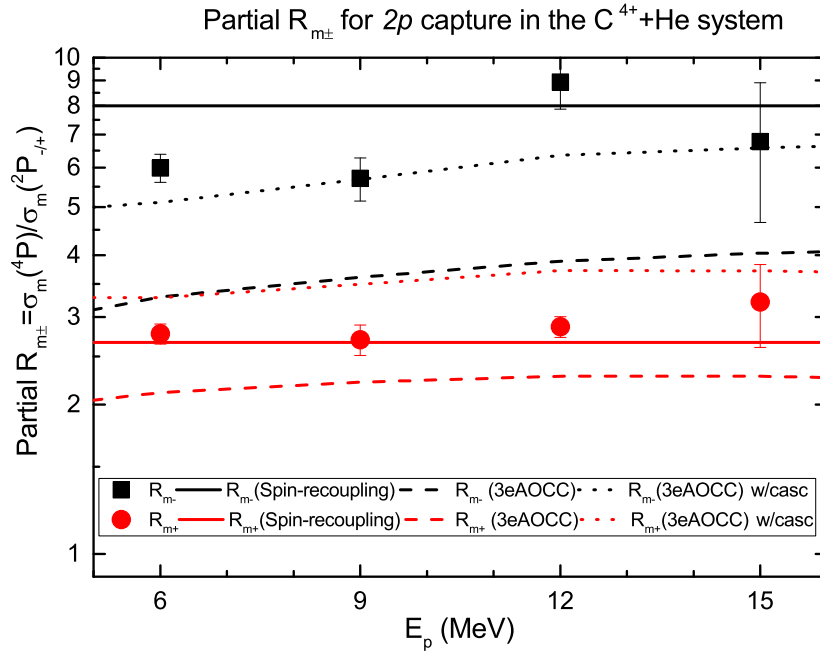
Figure 5.6: Results on the partial $R_{m\pm}$ ratios, for He. The frozen core spin recoupling calculations for these partial ratios are also presented, along with the 3eAOCC results for both simple $2p$ SEC and the full quartets cascade calculation. Only statistical uncertainties depicted. See text for more details.

This is further indication that the frozen core approximation does not predict the SEC production populations of the $1s2s2p$ states. While experimental values near or over[4] the predicted values would be acceptable, values below indicate that frozen core spin recoupling is not valid. Instead, in the case of the 3eAOCC, the experimental values are above the 3eAOCC $2p$ SEC values, and close to the calculated cascade enhanced $R_{m\pm}$ values. The fact that for both ratios, the experimental values are higher that the calculated values is in accordance with the expected cascades that enhance their numerators. This is shown clearly regarding the experimental results in the case of R_{m-}, while for the case of the R_{m+} the results are slightly lower that the calculated ratio.

In a simplified approach, Eqs. 5.1 form a representation of the spins of the $1s$, $2s$ and

---

[4]due to cascades

$2p$ atomic orbitals for the three $1s2s2p\ {}^4P,\ {}^2P_\pm$ states:

$$|{}^4P\rangle \equiv |\uparrow\uparrow\uparrow| \tag{5.1a}$$

$$|{}^2P_-\rangle \equiv \frac{1}{\sqrt{2}}(|\uparrow\downarrow\uparrow| - |\downarrow\uparrow\uparrow|) \tag{5.1b}$$

$$|{}^2P_+\rangle \equiv \frac{1}{\sqrt{6}}(|\uparrow\downarrow\uparrow| + |\downarrow\uparrow\uparrow| - 2|\uparrow\uparrow\downarrow|) \tag{5.1c}$$

The $C^{3+}(1s2s2p)\ {}^4P,\ {}^2P_-$ and ${}^2P_+$ states are expressed by linear combinations of Slater determinants in order to be eigenfunctions of the total spin $\mathbf{S}^2$ operator, for the components of largest M_S value $(+3/2$ for ${}^4P$ and $+1/2$ for ${}^2P_\pm)$. Describing the capture process, the initial $1s2s\ {}^3S$ state is described by $\equiv |\uparrow\uparrow\rangle$. Then, a spin-up or -down electron from He can be captured by the projectile to produce respectively, the ${}^4P$ state (Eq. 5.1a) or the ${}^2P_+$ state (through the third term in Eq. 5.1c). As it can be be seen, the ${}^2P_-$ state cannot be produced by direct capture, but requires additionally a spin exchange between a projectile electron and the active target electron. This involves a second-order process, which is expected to have lower cross section, compared to direct SEC mechanism populating the ${}^4P$ and ${}^2P_+$ states.

In Ref. [7] a more quantitative approach is also included for this concept, applying the Oppenheimer-Brinkman-Kramers (OBK) approximation [251]. In this approximation, SEC to the ${}^4P$ and ${}^2P_+$ levels is primarily described by the projectile nucleus-electron attraction matrix element I^P that couples the $1s$ atomic orbital of the He to the $2p$ atomic orbital of the projectile nucleus, and is proportional to the charge of the projectile nucleus $Z_P = 6$. More specific, the relative strengths are I^P for the ${}^4P$ and $\sqrt{\frac{2}{3}}I^P$ for the ${}^2P_+$. However, capture to the ${}^2P_-$ level is exclusively driven by exchange electron-electron couplings, that are independent of the projectile charge, therefore is comparatively a factor $Z_P = 6$ weaker. This approximation, which also excludes bielectronic, direct and exchange, matrix elements, then provides with a reasonable upper[5] limit for the ratio R_{T2p} equal to 3/2, in agreement with the 3eAOCC [7, 248] calculations. Moreover, even in this approximation, it is shown that the R_{T2p} is not static as implied by frozen core spin statistics, but dynamic, exhibiting dependence on collision velocity and Z_P, amongst others. However, only configuration interaction and close-coupling, included in 3eAOCC can provide a quantitative description of the C^{3+} doubly excited states populated during the collision.

5.2.2 The r_m ratio

r_m is another production $2p$ capture ratio studied in this thesis. Since it is the ratio of the two ${}^2P_\pm$ states it is not affected by cascade effects. In Fig. 5.7, the results for r_m are presented. For almost all He measurements a clear deviation from the spin recoupling value of 3 is present. For the H_2 measurements, the values show larger deviations, although values close to the frozen core value exhibit large uncertainties. As seen, Ne and Ar measurements are well within uncertainty, except at 6 MeV. In the case of Ar, r_m is in general lower than the other targets, with an ascending trend. It should be noted that Ne and Ar, being heavier targets, cannot provide safely interpretable results. However, contribution analysis using the fractions determined using the He target produced similar and consistent results. It is noteworthy that Ne results lie within the values calculated with He, although no direct comparison should be attempted.

---

[5]Neglecting the weak ${}^2P_-$ capture contribution
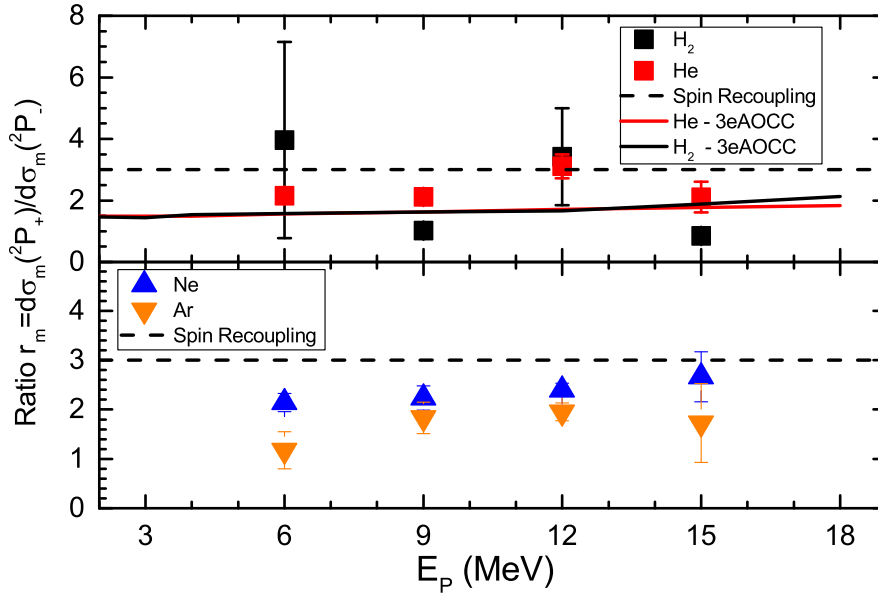
Figure 5.7: Results on the r_m ratio, for H_2, He, Ne and Ar. Only statistical uncertainties depicted. See text for more details.

5.3 Cross section determination for the 1s2s ^{3}S contributions

In Fig. 5.8 the results for the SDCS's by transfer to the $1s2s\,^3S$ component for the production of doublet states are presented. When Auger electrons are detected at $\theta = 0°$ with respect to the beam direction, and the final ionic state[6] is characterised by $L_f = 0$, then only transitions from the $M_L = 0$ substates can be observed [180]. Therefore, all experimental data are compared with capture to the $M_L = 0$. The following equations are used for the conversion of total and partial SEC CS to SDCS:

$$\sigma_{M_L=0} : SDCS_{Rest}(\theta = 0°) = (2L_d + 1)\frac{\sigma_{M_L=0}}{4\pi} \tag{5.2a}$$

$$\sigma : SDCS_{Rest}(\theta = 0°) = \frac{\sigma}{4\pi} \tag{5.2b}$$

For all the doublet states, the TC-BGM [81] calculation appears to be 1.5 orders of magnitude smaller than the 3eAOCC [248] calculation, however energy dependence is similar. This difference is partially attributed to the $(2L_d + 1)$ factor in Eq. 5.2a, since the TC-BGM calculation is for total capture.

SDCS results for H$_2$
For the ^2S line, the 15 MeV data point was not obtained with a reasonable uncertainty due to low value cross sections and the related poor statistics. Lying on the low energy wing of the metastable ^4P, the ^2S SDCS is expected it general to present higher uncertainties. In the case of the $^2P_+$, the cross sections appear to decrease exponentially [7]. For all doublet state experimental results, comparison with $\sigma_{M_L=0}$ results would require a scaling by a factor of 0.5. The $^2P_-$ line presents a less smooth descending trend, with higher uncertainties, which can be expected due to the lower SDCS [248].

---

[6]After the emission of the Auger electron.
[7]All cross sections are presented on logarithmic scale.
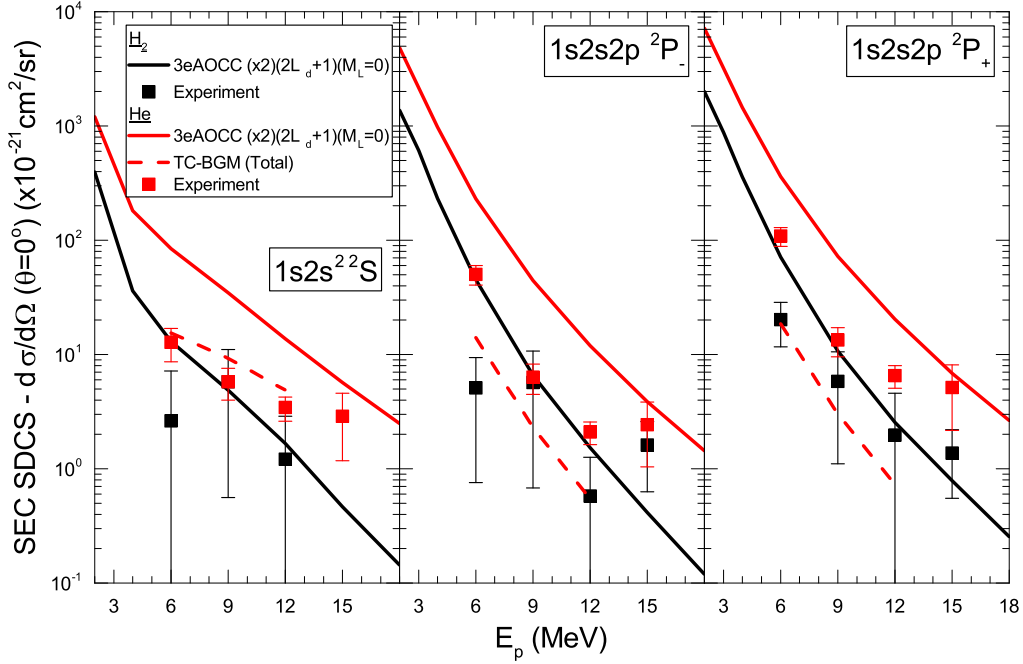
Figure 5.8: SEC SDCS for the production of the KLL doublet states for the $C^{4+}(1s2s\,^3S)$ + T$\rightarrow$ $C^{3+}(1s2s2l\,^2L)$ + T$^+$ reaction for the He (Red) and H_2 (Black) targets. Presented 3eAOCC [248] calculations are for partial ($M_L = 0$) capture. The calculated cross sections were transformed to SDCS with the use of Eq. 5.2a, and multiplied by 2 to account for the two electrons/target. Additionally, TC-BGM [81] calculations for the He target, for total capture are included, and also transformed as described in Eq. 5.2b. Only statistical uncertainties are shown. See text for more details.

SDCS results for He

For this target, the discrepancy between the measured values and 3eAOCC theory requires a scaling factor of 0.25. However, simultaneous comparison with TC-BGM theory can bring forward some finer details. For the ^2S state, experimental results show agreement with the TC-BGM theory for total capture. It should be noted that the ^2S state has only the $M_L = 0$ component. The experimental results for $^2P_\pm$ states however, lie in between the TC-BGM and the 3eAOCC. It could be argued that the TC-BGM calculations regard total SDCSs, and the SDCS for $M_L = 0$ is higher. However, comparison of total (Not shown) and partial SDCSs in the case of the 3eAOCC, shows that the SDCS for $M_L = 0$ is greater[8] only by a factor of 1.5 to 2 compared to SDCS for total capture. Therefore, it may be assumed that such TC-BGM calculation would not be in agreement. The $^2P_-$, at 12 MeV, presents a slight decrease. This decrease appears to be the reason behind the increase of R_m, r_m and R_{m-} for this energy. On a final note, regarding the TC-BGM calculation, and the doublets P states, the calculated r_m ratio value is around 1.32 ($\approx 4/3$), and it is not the one predicted by frozen core spin statistics (3), also predicted by Anthony *et al* [153, 154] using fractional parentage coefficients.

In Fig. 5.9 is the comparison between the experimentally measured ^4P SDCS, and the 3eAOCC and TC-BGM calculations for the He target, including the cascade contributions from higher lying states. For both targets, the aforementioned scaling factors appear to be applicable for the comparison of the 3eAOCC and the experimental results. In the case of He, experimentally measured values lie within the two calculations. Regarding

---

[8]Due to the $(2L_d + 1)$ term, as shown in Eq. 5.2a.
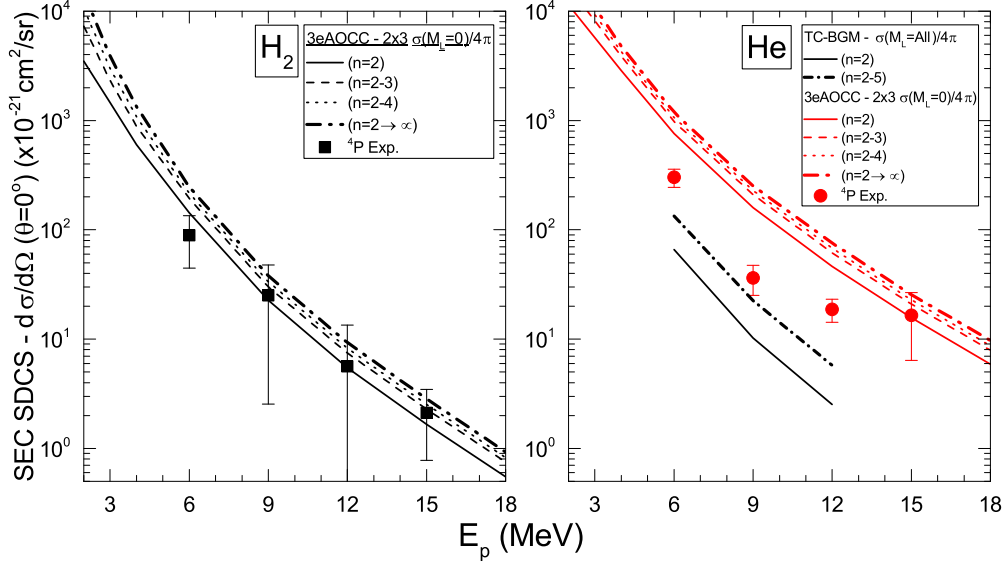
Figure 5.9: SDCS for the production of the ^4P for the C$^{4+}(1s2s\,^3S)$ + T→ C$^{3+}(1s2s2l\,^2L)$ + T$^+$ reaction along with cascade contributions. Experimental results are presented. The 3eAOCC results are presented for $2p$ SEC along with cascade feeding contributions from higher n quartets for the partial SDCS($M_L = 0$) component. In the case of the He target, additional TC-BGM calculations for total capture are included for the $n = 2$ and $n = 2 - 5$ cases. Only statistical uncertainties are shown. See text for more details.

comparison between calculations, the same discrepancy with the doublets is shown here, with the TC-BGM [81] results being an order of magnitude smaller than 3eAOCC. What is interesting in this comparison between the TC-BGM and 3eAOCC calculations for the quartets, is that the cascade enhancement in the case of the TC-BGM is visibly larger, compared to the 3eAOCC. Their calculations [81] indicate an increase in the ^4P due to the cascades of a factor about $R_{cc} \approx 2.03 - 2.12$, whereas the 3eAOCC calculation, in the case of He, presented a $R_{cc} \approx 1.40 - 1.78$ factor. This can be linked to a previously stated assumption for the Ref. [81] results for the cascade enhancement: That in the $1s2s\,^3S$ frozen core approximation, quartets and doublets are populated in fixed proportions [4]. The reasoning in Ref. [4][9] applies not only to the initial population ratio $R_{m_{T2p}}$ but also to SEC to higher nl states. This can explain the stronger enhancement of the ^4P state in the calculations of Ref. [81].

Finally, the obtained experimental cross sections for the Ne and Ar target are presented, in Fig. 5.10.

SDCS results for Ne

As a reminder, the Ne and Ar data are processed using the fractions obtained with He. In general, all the KLL cross sections follow the same trend, decreasing as the collision energy increases. A slightly elevated cross section for the ^4P at 6 MeV is the reason for the increased R_m value in Fig. 5.5, the only incompatibility with the data from Ref. [6]. A noticeable difference, is the fact that for 15 MeV collision energy the cross sections appear to increase. An assumption for this increase can be based on the following reasoning:

---

[9]Regarding only the ratio between quartets and doublets.
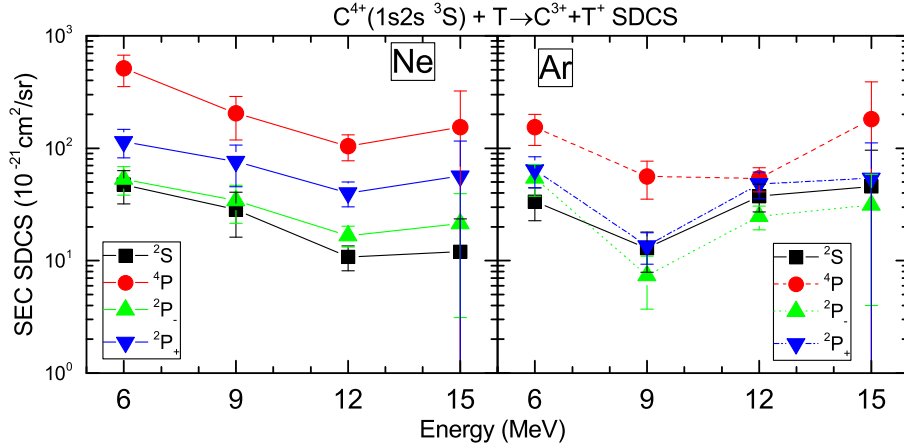
Figure 5.10: SEC SDCS for the production of KLL states in the $C^{4+}(1s2s\,^3S)$ + T$\to$ $C^{3+}(1s2s2l\,^{2,4}L)$ + T$^+$ reaction for the Ne and Ar targets. Experimental results for the ^4P state have been corrected by dividing by the solid angle correction factor G_τ (See Sec. 4.3 and App. D for more details.). Only statistical uncertainties are shown. See text for more details.

In his dissertation Zamkov [252] applies a velocity matching model. The idea, presented in a simple manner, is that capture probability is analogous to the overlap of the Compton profiles of the target and the projectile, the latter being shifted/increased by the ion velocity. This idea had been proposed earlier [253, 254] regarding intermediate collision velocities. However, it is considered to date, but requires variation regarding the energy regime under study [255, 256]. Considering that inner electrons have much higher velocities, increase of the collision velocity may implement the matching velocity conditions with them. This explains reason the electron-capture cross sections in collisions with light targets (H$_2$, He) decrease much faster than with heavy ones (Ne, Ar) having several electron shells [255] as seen in the present data. Unfortunately, no Compton profiles for the C^{3+} $1s2s2p$ configurations were available to perform calculations for this thesis. The closest calculation found is for the $1s2s$ configuration [257]. However, in Fig. 6.1, in Ch. 6, the ratio of $\eta = \frac{V_P}{u_e}$ is presented, for all the sub-shells of Ne and Ar. For Ne, at 15 MeV, this ratio is 0.73, indicating that the ion velocity and the electron velocity for the $1s^2$ electrons are comparable. This may explain the increase of the cross section.

SDCS results for Ar

Observations for the measured cross sections are similar to the ones for Ne, regarding the almost constant cross sections, and the rise at higher energies. As seen in Fig. 6.1, similar proximity to the Ar $2s$ and $2p$ electrons is observed from 9 MeV. However, also at 9 MeV, a discrepancy is observed, where all but the ^4P state present a drop.

Chapter 6

Results on ground state contributions - Transfer Excitation

Introduction

Complementary to the $1s2s\,^3S$ contributions results, this chapter, although apart from the main topic of this dissertation, adds the experimental results from the $1s^2\,^1S$ contributions, along with the necessary RTE theory.

In 1981, Tanis *et al* had encountered a new mechanism that resembled dielectronic recombination. It involved both transfer of an electron from the target to the ion, along with the excitation of another (projectile) electron, resulting in a doubly excited state [128, 129]. This mechanism is termed RTE [130, 131], and belongs to a larger family of TE processes. The simplest way to be described is by describing a time-reversed Auger decay. These processes lead to population of the states examined in this thesis from the $1s^2\,^1S$ component of the ion beam. Therefore, the need to isolate each component contribution, firstly introduced in Ch. 2. In this chapter, the experimental contributions from the $1s^2\,^1S$ component, are compared to theory.

6.1 RTEA theory

6.1.1 Description of RTEA

RTE is the ion-atom collision analogue of Radiationless Capture (RC) in electron-ion collisions . In RC, a free electron with momentum p, mass m and kinetic energy $\varepsilon = p^2/m$ collides with a positive ion of charge state q and is captured into an intermediate resonance state. RC is a resonant process that will only take place if the energy ε of the electron in the rest frame of the ion matches the energy level difference of the resonant and initial state. The energy which becomes available during the capture process is carried away by the promotion of a bound electron to another bound orbit. Assuming that capture occurs to an excited state, a doubly-excited intermediate state occurs. There are two decay channels for this state. The first is by photon decay, in which case the process is termed Dielectronic Recombination (DR). The second is by Auger electron emission [130], particularly strong for low-Z ions. In this case, the process is called Resonant Elastic Scattering (RES) [166].

$$e^- + Z^{q+} \rightarrow Z^{(q-1)**} \rightarrow \begin{cases} Z^{(q-1)+} + \gamma & \text{DR} \\ Z^{(q)+} + e_A^- & \text{RES} \end{cases} \tag{6.1}$$
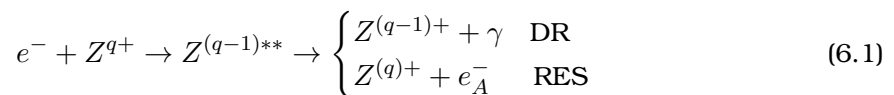
In RTE the captured electron in not a free electron, but a bound electron from the target atom. RTE has been theoretically described within the impulse approximation as resonant quasi-free electron scattering. The target electron, assumed to be lightly bound and therefore quasi-free is not characterized by distinct momentum p but rather by a continuous momentum distribution. The excited states are relaxed either by photon emission or Auger electron emission and are therefore investigated by x-ray - ion coincidences (RTEX), x-ray - x-ray coincidences (RTEXX), or by high resolution Auger electron spectroscopy RTEA measurements respectively. For low-Z ions because of the high Auger yield and the better resolution and efficiency of Auger measurements RTEA experiments have been the dominant mode of investigation since they can resolve the different levels, not possible in older x-ray measurements.

6.1.2   The Impulse Approximation (IA)

The theory of RTEA has been described within the IA [130], in collisions where the velocity u_e of the target electron is much smaller than the velocity V_p of the projectile, or simply $\eta = \frac{V_p}{u_e} >> 1$. When this condition is true, the interaction time between projectile and electron is short compared to the orbiting time of the perturbing electron [171]. This means that in the projectile frame the target electron can be considered to interact as a free particle. This assumption simplifies the ion-atom interaction since the problem is treated as an electron impact problem, in which the target electron has a collision energy ε, broadened by its momentum distribution due to the additional orbital motion around the target carried into the collision [171].

Within the IA it has been shown that RTE can be considered to be analogues to the time-reversed Auger decay process. The captured electron in the projectile frame is a "quasi-free" particle with the velocity of the projectile, in which the "quasi-free" electrons interact, essentially with the ground state ($1s^2\,^1S$) fraction of the ion beam, in this energy range. This interaction leads also to doubly excited states, identical to those generated by direct capture (^2P) to the metastable fraction of the beam ($1s2s\,^3S$) and decay by Auger electron emission.

Within the IA treatment the RTEA contributions to the SDCS at $\theta = 0°$ is given by [166]:

$$
\begin{aligned}
\frac{d\sigma_{RTEA}}{d\Omega'}\left(\theta = 0°\right) &= \frac{\Omega_{RC}}{\epsilon_0} \cdot \frac{J(p_z')}{V_p + p_z'} \cdot \frac{\hat{W}\left(\theta' = 180°\right)}{4\pi} \cdot \xi \qquad (L_i = 0, L_f = 0) \\
&= \frac{2.475 \times 10^{-30}}{4\pi\epsilon_0} \cdot \frac{J(p_z')}{\sqrt{2\left(E_R + E_I\right)}} \cdot \frac{(2L_d + 1)^2(2S_d + 1)}{(2L_i + 1)(2S_i + 1)} \cdot \frac{A_\alpha^{d\to i}}{E_R}\xi
\end{aligned}
$$

(6.2)

where $A_\alpha^{d\to i}$ and E_R are the transition rate in s^{-1} and the resonance energy of the Auger state under consideration, respectively. E_I is the ionization energy for the targets subshell. p_z' is the z-momentum component, given by [166]:

$$
p_{z'_{(i)}} = \sqrt{2}\left(\sqrt{E_R + E_{I_{(i)}}} - \sqrt{t_p}\right)
$$

(6.3)

The statistical weights for the intermediate states (d) and initial states (i) are given by:

$$
\omega_d = (2L_d + 1)(2S_d + 1), \quad \omega_i = (2L_i + 1)(2S_i + 1)
$$

(6.4)

For the present calculations, the initial state is the $1s^2\,^1S$ ground state, therefore, $L_i = S_i = 0$. For the intermediate states ^2S, $^2P_\pm$ and ^2D we have $L_d = 0, 1, 2$, respectively, while $S_d = 0$, for all.

6.1.3 Impulse Approximation criterion

It should be noted that comparison to experimental data requires certain weighting of the sub-shell contributions. The validity criterion for the IA requires that the velocity of the participating target electrons u must be much smaller than the projectile velocity V_p ($\eta = V_p/u_i \gg 1$). For some collision systems, the target inner shells will not always fulfill this criterion. The experimental DDCS's for Binary Encounter electron (BEe) production, which is similarly described within the IA show that in the case of Ne and Ar, K-shell electrons should not be taken into account [64]. In Table 6.1 a few basic parameters are presented. The ionization energy of these shells is required for the calculation of RTEA SDCS calculations. Kinetic energies of electrons in each sub-shell are required for the evaluation of the validity of the IA. Using the kinetic energies for every target, for

Table 6.1: Binding (I) and kinetic energies (K) of the various target electrons, used for the calculations are listed below in eV. Binding energies are experimental data, while kinetic energies are calculated from non-relativistic Hartree-Fock wave functions. Data from Ref. [64].

	H$_2$		He		Ne		Ar	
Sub-shell	I	K	I	K	I	K	I	K
$(1\sigma_g)^2$	15.43	31.96						
$1s^2$			24.59	39.51	866.9	1259.1	3203.0	4192.9
$2s^2$					48.47	141.88	320.0	683.1
$2p^6$					21.60	116.02	245.9	651.4
$3s^2$							29.24	103.5
$3p^6$							15.82	78.07

every subshell from Table 6.1 the validity of the IA can be evaluated. For electrons in H$_2$ and He, whose kinetic energies are 31.96 and 39.51 eV respectively, carbon projectiles require kinetic energies of less than 1 MeV for target electron and projectiles velocities to be comparable, for the energy range in this thesis. In the case of Ne and Ar this is somehow different. In Fig. 6.1, the applicability of the IA is examined. In the case of Ne, the
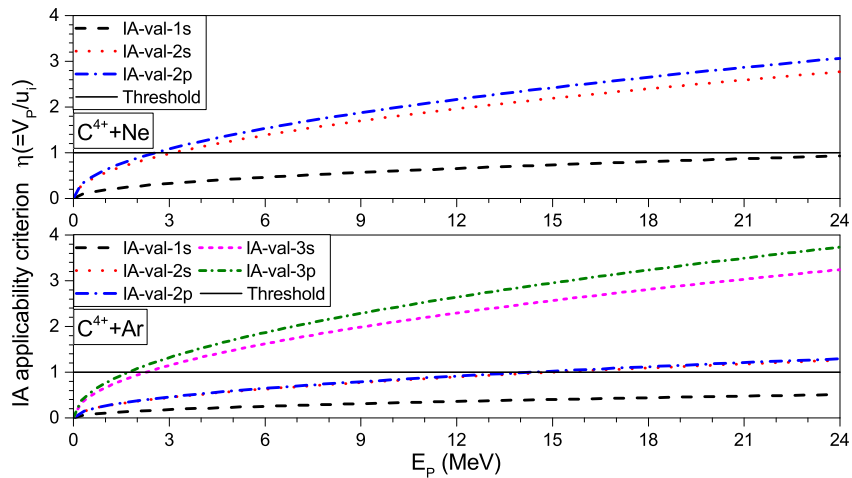
Figure 6.1: η applicability criterion for every sub-shell of Ne (Top) and Ar (Bottom) as a function of projectile energy for a carbon beam.

IA applicability criterion is not satisfied for the K-shell electrons even for 24 MeV carbon beams. In the case of Ar, K-shell electrons also do not satisfy it. L-shell electrons satisfy it but only marginally and for carbon beam energies higher than 15 MeV, or 1.25 MeV/u.

6.2 RTEA SDCS results

6.2.1 KLL formation for the $C^{4+}(1s^2)$+H_2, He collision system

In the case of H_2 and He gas targets, RTEA calculations can be considered somehow simplified, since these targets include a single sub-shell. Therefore, the calculation is straightforward, without any weighting factors. For this section, calculation for the ^2S, $^2P_-$, $^2P_+$ and the ^2D lines were performed, with the use of Eq. 6.2. Along with the calculations, are presented the experimental $1s^2\,^1S$ ground state contributions, determined with the use of Eqs. 4.33b. Some additional parameters required in the calculations are presented in Table 6.2: It should be reminded that the L_d weighting factor in Eq. 6.2

Table 6.2: Atomic structure parameters used in computing RTEA contributions.

State	$(2L_d + 1)$	$(2S_d + 1)$	E_R (eV)	$A_\alpha^{d \to i}$ (s^{-1})	ξ
$1s2s^2\,^2S$	1		227.23	7.48E+13	1.00
$1s(2s2p\,^3P)\,^2P_-$	3	2	235.55	1.47E+13	0.92
$1s(2s2p\,^1P)\,^2P_+$	3		238.86	3.86E+13	1.00
$1s2p^2\,^2D$	5		242.15	9.31E+13	1.00

is squared indicating its dependence on relative production strength [166]. In Fig. 6.2, calculations and DDCS results are presented for the RTEA produced KLL lines. A factor
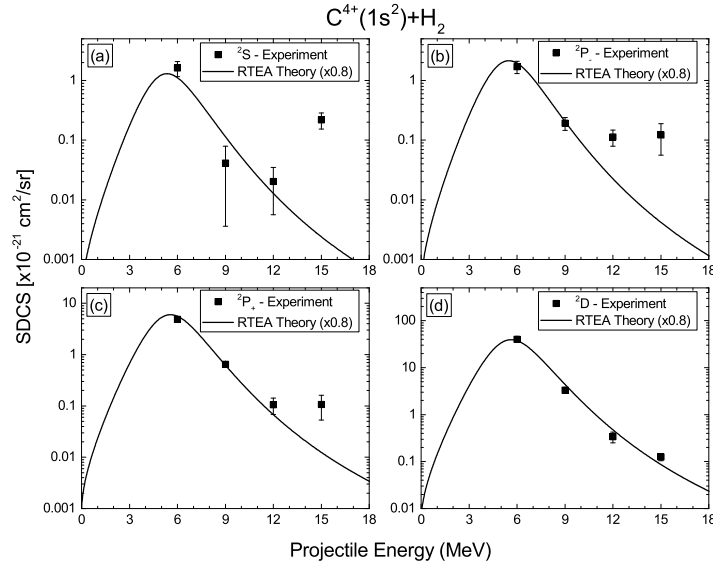
Figure 6.2: RTEA calculations and experimental $1s^2\,^1S$ contributions of KLL lines for the C^{4+}+H_2 collision system. Only statistical uncertainty is shown.

of $\times 0.8$ was applied to all H_2 calculations. Compared to the other lines, ^2D is at least an order of magnitude larger, due to its Auger rate and the weighting factor L_d. Due to the strength of the ^2D line, it appears to replicate the folding of the Compton profile relatively well. However, in the case of the $^2P_-$ and $^2P_+$ lines, at graphs (b) and (c) of Fig. 6.2, that

is not the case. For the case of the $^2P_+$ (c) there is a deviation at 15 MeV, whereas in the case of the weaker $^2P_-$ (b), the deviation begins at 12 MeV. For both the $^2P_\pm$ lines, the experimental measurements appear to converge to a similar value. These deviations can possibly be attributed to NTEg contributions, as described below.

Measurements, regarding RTEA by Lee *et al.* [146] for the $F^{7+}+H_2$, He collision system present a similar behaviour on the high energy wing of the resonance. In Fig. 6.3 are their results on the production of said lines, obtained from Ref. [146].
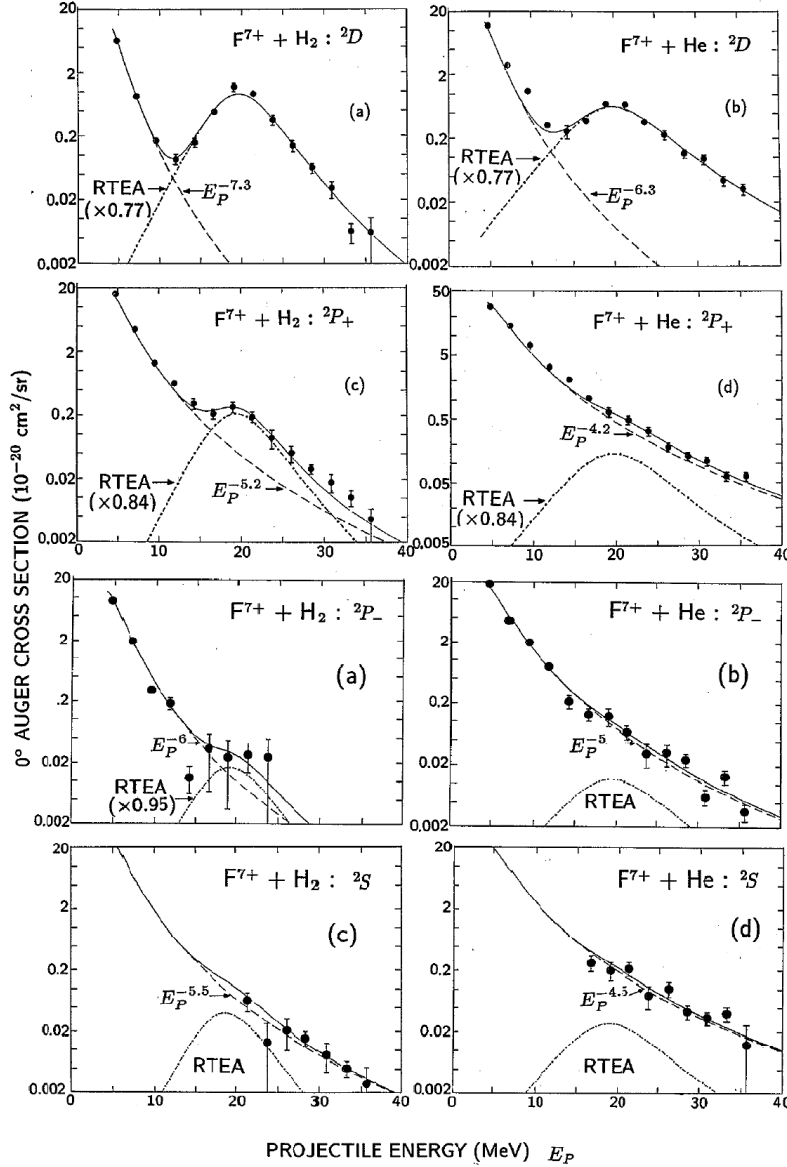
Figure 6.3: Figs. 4 and 5 from Lee *et al*, PRA, 1991 [146]. Data points represent the experimental absolute Auger electron production cross section from ^2D, $^2P_+$, $^2P_-$ and ^2S states produced in $F^{7+}(1s^2\,^1S$, $1s2s\,^3S)+H_2$ and He collisions versus projectile energy. In the case of the ^2D line, solid lines are the sums of RTEA-IA (dot-dashed lines) and NTEm (broken line) contributions. For the rest of the lines, solid lines are the sums of RTEA-IA (dot-dashed lines) and Transfer and/or NTEm (broken line) contributions.

In their analysis, they combine results of RTEA-IA calculations with an exponential dependency to the projectile energy that is attributed to Transfer and/or NTEm contributions, to fit experimental absolute Auger electron production cross sections. However, their analysis refers to NTEm contributions, since NTEg contributions are considered negligible. This is based on the assumption that the $1s \rightarrow 2p$ excitation cross section is much smaller than the $2s \rightarrow 2p$ cross section [146]. This is further supported by measurements from Ref. [258], where NTEg cross sections were found to be $\approx 5 - 10\%$ of the maximum RTEA cross sections for $1s2s2p^2\,^3D$ production in $F^{6+}(1s^22s)+H_2$, which involves a $1s \rightarrow 2p$ excitation.

It should be stressed that for the line under consideration $L_d = 2$, and therefore strong RTEA signal is expected. Indeed, comparison to current figures, regarding the $1s^2\,^1S$ contributions to the ^2D does not indicate any deviation from the expected calculation, as shown in Figs. 6.2 (d) and 6.4 (d). The $^2P_\pm$ lines, for which $L_d = 1$, present a much weaker signal, and therefore any NTEg contributions can be expected to have a larger effect. This can be seen in older measurements, in Fig. 6.3 from Lee *et al* [146]. To clearly identify such contributions requires measurements at the low energy wing of the resonance. Such measurements are currently unattainable for carbon at the Demokritos 5.5 MV accelerator. Considering the above, these high-energy wings can be an indication of NTEg contributions to the $^2P_\pm$ lines. This is further supported by the fact that the same
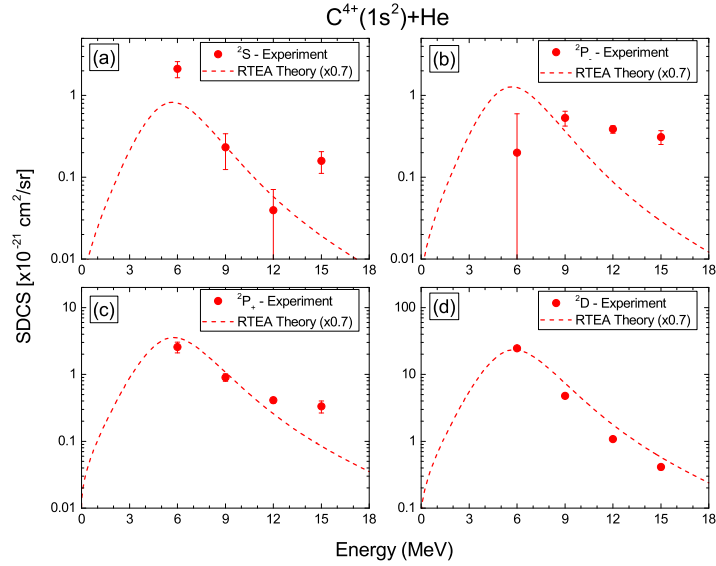
Figure 6.4: RTEA calculations and experimental $1s^2\,^1S$ contributions of KLL lines for the C^{4+}+He collision system. Only statistical uncertainty is shown.

behaviour is observed for the He target. In Fig. 6.4 are the results the C^{4+}+He collision system, respectively. A factor of $\times 0.7$ was applied to all He calculations. As seen, the results for He are qualitatively comparable to H_2 results, with a single exception the $^2P_-$ SDCS at 6 MeV, which was measured with higher uncertainty. Similarly to C^{4+}+H_2, the $^2P_\pm$ lines seem to follow an asymptotic trend, converging to similar values, and the ^2D line profile is well represented.

Finally, in Figs 6.2-(a) and 6.4-(a) results for the ^2S line are presented. Compared to the other lines, the measurements for the ^2S line exhibit higher uncertainty. This is attributed to the fact that the ^2S line lies over the low-energy wing of the ^4P line. Although $L_d = 0$ for the ^2S line, its higher Auger rate (See Table 6.2) compensates for it, casting it's strength comparable to the $^2P_-$ line.

Experimental results, for both gas targets, exhibit similar trends: Good agreement to RTEA calculations in the 6 to 12 MeV regime, along with a rise at 15 MeV. This rise at 15 MeV is rather difficult to interpret. Should it be attributed to NTEg contributions of approximately the same magnitude as at the $^2P_\pm$ lines, then, measured SDCS at 12 MeV appear to be rather low. In every case, the fact that both gas targets exhibit same trends to the ^2S SDCS indicates that this is systematic. It should be reminded that the extraction of the $1s^2\,^1S$ and $1s2s\,^3S$ contributions for these targets was achieved with the use of the self-consistent formulas, and not with the use of pre-defined fractions. The uniform trend of the ^2D over the measured energy range for both targets eliminate possible normalization

errors.

6.2.2 Results for the ^2D formation for the $\mathbf{C^{4+}(1s^2)}$+Ne, Ar collision system

In this section, calculations and experimental results for the C^{4+} ($1s^2\,^1S$) + Ne, Ar$\rightarrow\,^2D$ collision system are presented. For this section, only contributions to the ^2D will be examined. Both Ne and Ar calculations contain contributions from various sub-shells. Even by eliminating some through the validity criterion of the IA (See Fig. 6.1), still, further weighting of the contributions of each sub-shell is required. Considering the increased NTEg contributions, the number of variables is comparable to the number of experimental points, therefore lines with relatively weak RTEA signature are more complex to approach. Thus, only ^2D is presented due to its strong RTEA signature.
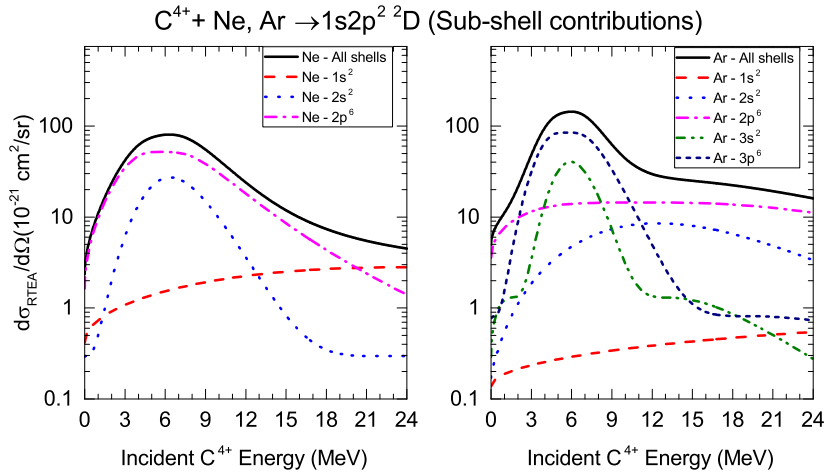
Figure 6.5: Zero-degree RTEA contribution calculations for the ^2D line from all the sub-shells of Ne (Left) and Ar (Right). All calculations performed using Eq. 6.2, with the parameters presented in Tables E.2, E.3 and 6.1. Total SDCS as a function of the energy also plotted.

In Fig. 6.5 are the calculations for each sub-shell RTEA contribution to the $C^{3+}\,^2D$ line. Each sub-shell calculation is multiplied with the respective number of electrons. Inner sub-shells, which are characterized by higher ionization energies present significant shift to their respective resonance energy. However, not all sub-shells contribute to each respective line. As presented earlier, in Fig. 6.1, for both Ne and Ar, only $n = 2$ and $n = 3$ respectively contribute to the formation of ^2D.

In Fig. 6.6 are presented the experimental SDCS for the C^{4+} ($1s^2\,^1S$) + Ne, Ar collision system. Again, it is reminded that $1s^2\,^1S$ contributions for the case of Ne are extracted with the use of fractions obtained from He. Similarly to the previous cases, for higher collision energies, an increased deviation is observed. However, it is not possible to evaluate if this is a result of the increased NTEg contributions. Especially in the case of Ar, as seen in Fig. 6.1, there is a threshold at 15 MeV. Although no sudden rise of RTEA produced lines is expected, this serves as an example regarding the complexity of these targets.
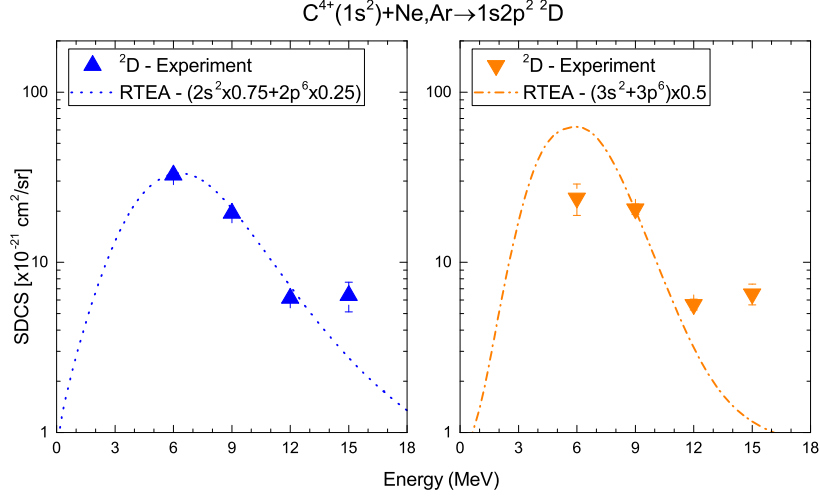
Figure 6.6: Zero-degree RTEA contribution calculations for the ^2D line from valence electrons of Ne (Left) and Ar (Right), and experimental SDCS.

6.3 RTEA production ratios R_g and r_g

6.3.1 Theoretical values of R_g and r_g

Expected values for the R_g and r_g ratios can be readily calculated with the use of Eq. 6.2, along with Eqs. 4.25c and 4.25d.

$$R_g = \frac{\frac{d\sigma_g[^2D]}{d\Omega'}}{\frac{d\sigma_g[^2P_-]}{d\Omega'} + \frac{d\sigma_g[^2P_+]}{d\Omega'}}$$

$$= \frac{(2L_{d_{[^2D]}}+1)^2}{(2L_{d_{[^2P]}}+1)^2} \frac{\frac{J(p'_{z_{[^2D]}})}{\sqrt{2\left(E_{R_{[^2D]}}+E_I\right)}} \frac{A^{d\to i}_{\alpha_{[^2D]}}\xi_{[^2D]}}{E_{R_{[^2D]}}}}{\frac{J(p'_{z_{[^2P_-]}})}{\sqrt{2\left(E_{R_{[^2P_-]}}+E_I\right)}} \frac{A^{d\to i}_{\alpha_{[^2P_-]}}\xi_{[^2P_-]}}{E_{R_{[^2P_-]}}} + \frac{J(p'_{z_{[^2P_+]}})}{\sqrt{2\left(E_{R_{[^2P_+]}}+E_I\right)}} \frac{A^{d\to i}_{\alpha_{[^2P_+]}}\xi_{[^2P_+]}}{E_{R_{[^2P_+]}}}} \tag{6.5}$$

Since all states in question are doublets, and they all Auger decay to the same final state ($1s^2 {}^1S$), all S_d, S_i and L_i terms have been cancelled to simplify the expressions. The $(2L_d + 1)$ term (squared) is crucial in determining fractions like R_g, where the strength of various states is compared. To further simplify the given equation, a few characteristic quantities from Table 6.2 are required.

As seen in Table 6.2, the resonance energies although not identical, differ by a factor of less than 3%. Therefore, the E_R terms can be cancelled out without much loss to accuracy. Finally, regarding the $J(p'_{z_{[state]}})$ terms: The argument of the Compton profile function is a combination of ion velocity, target ionization energy and state resonance energy. Since the only difference is the resonance energy, these result in *almost* identical foldings of the Compton profile, varying only in the exact resonance energy[1]. These mismatches result in a small variation over the projectile energy region of the order of 4%, and for the sake of simplicity can be omitted. Applying these, Eq. 6.5 can be approximately

---

[1]Resonance energies for the particular states lie within 5.676 and 5.823 MeV.

simplified to:

$$R_g \approx \frac{(2L_{d_{[^2D]}}+1)^2}{(2L_{d_{[^2P]}}+1)^2} \frac{A_{\alpha_{[^2D]}}^{d\rightarrow i}\, \xi_{[^2D]}}{A_{\alpha_{[^2P_-]}}^{d\rightarrow i}\, \xi_{[^2P_-]} + A_{\alpha_{[^2P_+]}}^{d\rightarrow i}\, \xi_{[^2P_+]}} = 4.96 \qquad (6.6)$$

Applying the same approximations to the r_g production ratio, we obtain:

$$r_g \approx \frac{A_{\alpha_{[^2P_+]}}^{d\rightarrow i}\, \xi_{[^2P_+]}}{A_{\alpha_{[^2P_-]}}^{d\rightarrow i}\, \xi_{[^2P_-]}} = 2.85 \qquad (6.7)$$

where in the case of r_g, the weighting terms are also simplified since they are both P states, therefore $L_{d_{[^2P_+]}} = L_{d_{[^2P_-]}}$. Eqs. 6.6 and 6.7 represent a simplification for the R_g and r_g production ratios for the $C^{4+}+H_2$,He systems. Without the simplification, there is a minor dependence on the projectile energy, which is depicted in Figs. 6.7 and 6.8.

It should be mentioned that the above formulas are valid only for targets with a single sub-shell, such as H_2 and He. Heavier targets such as Ne and Ar, require weighted averaging over the individual sub-shells, taking into consideration the IA applicability criterion, presented in Fig. 6.1.

6.3.2 Experimental values of R_g and r_g
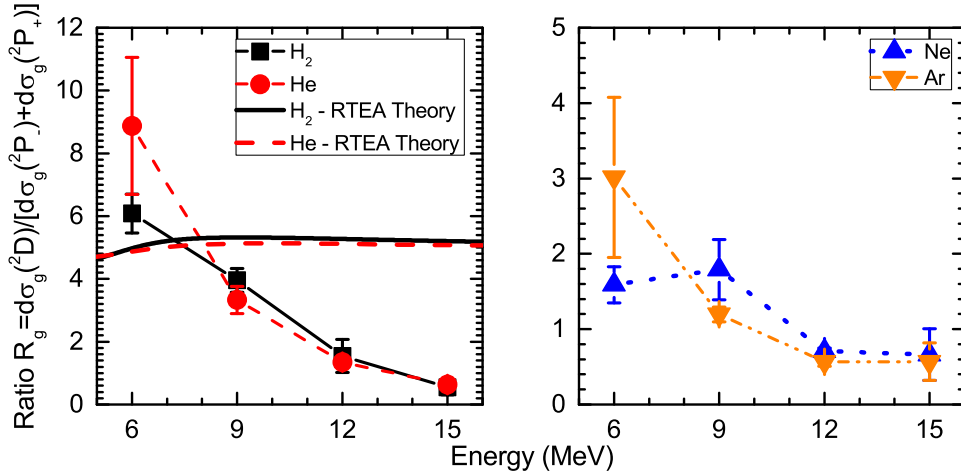
Figure 6.7: Experimental results for the R_g ratio. (*Left:*) Results for H_2 and He along with the respective calculations. Contrary to the calculations, experimental results indicate some type of asymptotic drop as a function of projectile energy. (*Right:*) Results for Ne and Ar.

In Fig 6.7 the experimental results for the R_g ratio are presented. On the left are the results regarding the H_2 and He, along with the calculated expected value based on the RTEA theory [130, 166]. On the right are the results regarding the Ne and Ar, for which the separate component contributions were calculated with the use of the He fractions.

Regarding the results for H_2 and He, there is an evident deviation from pure RTEA theory. However, this is partially explained by the SDCS results presented in the previous section. As seen in Figs. 6.2 and 6.4 both $^2P_\pm$ lines deviate from their expected values, with the $^2P_-$ deviation being more apparent. This is assumed to be due to the relative strength of the NTEg contributions, compared to the RTEA contributions.

All experimentally measured lines are a mixture of RTEA and NTEg contributions, both originating from $1s^2\, ^1S$. This means that as the projectile energy departs from the
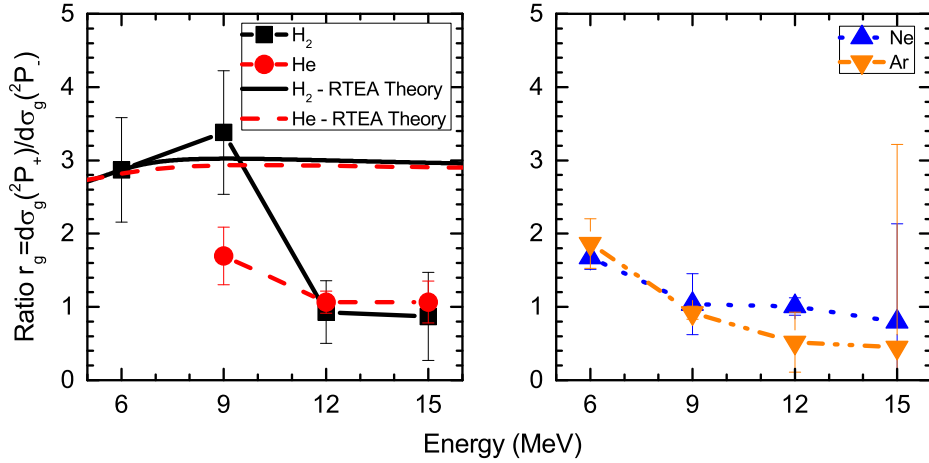
Figure 6.8: Experimental results for the r_g ratio. Result for 6 MeV C^{4+}+He omitted due to high uncertainty ($\approx 200\%$)

RTE resonance energy and the states are expected to diminish in a resonant type manner, the experimentally measured values remain stronger than expected. Weaker lines result to being more susceptible to NTEg contributions, and therefore deviate from RTE theory. To better understand this, an example can be made in Fig.6.3, where the $^2P_-$ experimental measurements are mostly described by NTEg contributions. Both the RTEA calculated values for R_g and r_g are larger that "1", as shown in Eqs.6.6 and 6.7. This means that for both ratios, lines in the denominator are RTEA weaker than those at the numerator. Therefore, the denominators drift from their RTEA expected values in a more pronounced manner than the numerators, as collision energy increases. As a result, the experimentally measured R_g and r_g ratio decreases as collision energy increases.

In Fig. 6.8 the results regarding r_g ratio are presented. As seen, experimentally measured values present a similar to the R_g trend, as a function of energy. Since the denominator of r_g is a weaker line compared to the numerator, the same reasoning of R_g applies also here regarding the behaviour of r_g experimentally measured values.

Chapter 7

Summary and conclusions

The basic purpose of this work is twofold. The first is to describe in detail the setting up of a completely new beamline L45 at the Demokritos 5.5 MV tandem to conduct atomic physics collision experiments, implementing the ZAPS HDA. This consists of a high efficiency hemispherical spectrograph, that combines a doubly-differentially pumped gas cell, a 4-element retarding lens, and a PSD. It has been installed and running smoothly [221]. All components were tested, characterized and assembled into a high efficiency [166] atomic physics experimental station. All the details regarding the installation, operation and optimization were presented. The optimization included among others the testing of the results of numerical simulations for the lens operation, and the improvement of the resolution of the spectrograph [220, 259]. In addition, a custom e-gun was constructed, that allowed for the testing of numerical simulations and the optimization of the retarding lens voltages, in order to improve the spectrographs resolution. Good agreement was found between simulation and experiment. Additional correction factors (G_τ) were determined both experimentally using Be-like states of C^{2+} and O^{4+} and numerically [156]. By producing the $1s2s2p\,^4P$ in a cascade free environment, it was possible to experimentally estimate the required correction factors required.

The second was to investigate one electron transfer to $1s2s\,^3S$ pre-excited carbon ions and the relative populations of the $1s2lnl'$ formed states. The utilization of the ZAPS technique allowed for the execution of the experiment in the relatively high collision energy regime of 0.5-1.5 MeV/u that is difficult to measure due to the small cross sections involved and therefore rarely found in the literature. Experimental results on the determined metastable fractions, with the use of the two spectra technique [246] were presented. Fraction results obtained with H_2 are characterized by relatively higher uncertainties. This can be attributed to the following reasoning. First, the lower cross sections compared to He can result inherently in higher uncertainty. Secondly, the narrower Compton profile of H_2, results in a much quicker drop, as collision energy increases, in the production of the $1s2p^2\,^2D$ state used for the accurate fraction determination. Fraction results with He, in agreement within uncertainties with the respective H_2 results, were found to be more consistent, with fewer uncertainty. Therefore, they were used for a more appropriate determination of contributions from the Ne and Ar spectra.

The results on the experimentally measured production ratios R_m and r_m were presented. The measured R_m values are found to be nearly constant with collision energy and close to 2, in contrast to previous findings. The excellent agreement found between theory and experiment provide valuable insight on SEC dynamics. Initially, results for $2p$ SEC depart significantly from the spin statistics value, and lie between 0.9 and 1.5 for both targets. Also, the calculations in Ref. [7] exhibit how the $R_{m_{T2p}}$ is not a static term, but varies depending on collision velocity, amongst others. This also shows, that

even in this velocity regime (Collision time of the order of 10^{-17} s), the $1s2s$ projectile core electrons *cannot* be considered frozen, and dynamically contribute to the states populated through SEC.

Moreover, the R_m ratio measurements with He and Ne are in agreement with older, corrected measurements [6, 241]. It should be reminded at this point that production ratios are calculated by comparing ratios of lines within the same spectrum. That means that they are free from any normalization parameters, and in principle could be deduced directly from the spectra themselves. Finally, the $2p$ SEC SDCSs to the $1s2s\,^3S$ for the $C^{4+}+H_2$, He, Ne and Ar collisional system for energies ranging from 6 to 15 MeV were presented. For the case of $1s2s2p\,^4P$ the experimental measurements, although corrected for solid angle effects, still remain affected by cascades from higher lying quartets.

7.1   Future Plans

- Expanding the R_m measurements to the isoelectronic sequence for $3 \leq Z_p \leq 9$, or even Si. As originally proposed by the APAPES initiative [221], a systematic isoelectronic approach is planned, to also investigate the role of cascades in the formation of the excited three-electron states by electron capture. Moreover, as Z_p increases, the low energy wing of the RTEA resonance peak is going to be accessible, which also includes NTE contributions. Finally, the use of heavier targets, both experimentally and in calculations, introduces an increase of the asymmetry parameter Z_P/Z_T, that will further explore cascade feeding.

- Upgrade the experimental setup by integrating an existing larger collision chamber. The collision chamber that is currently in use is small and suitable only for gas targets confined to a cell. The new chamber has a much larger volume (600 mm diameter) that allows for a convenient integration of components that are planned to be installed. These include a jet target that will allow for the localization of the electron emission volume. This will allow for more accurate measurements where the exact emission point is required, such as lifetime measurements, or Time-of-Flight (TOF).

- Studies on the production of metastable ion beams as a function of the GTS pressure, the foil stripper, the collision energy and the ion in use. Also under consideration is the varying of the atomic number of the FPS foils, or even the stripping gas used at the GPS. Possible candidates are aluminum foils to investigate the varianceof the C^{4+} metastable fraction. This will allow for maximazing the difference of metastable content produced by the two different stripping media. Thus, the accuracy of the two spectra method will be improved.

Appendix A

Normalized spectra

In this appendix, the measured, normalized with the use of Eq. 4.13 spectra are presented. In Fig. A.1 the normalized spectra with varied $1s2s\,^3S$ content are presented. The $1s2s\,^3S$
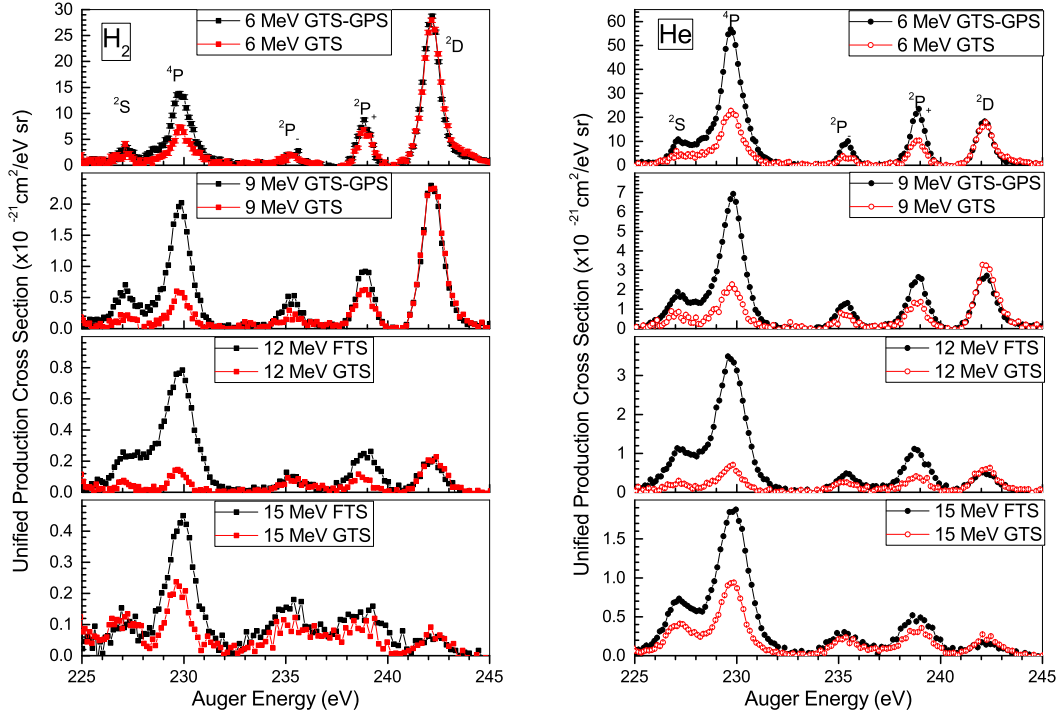
Figure A.1: *(Left:)* Normalized H_2 spectra.*(Right:) Normalized He spectra. See text for details.*

variation is identified by the varying intensity of the ^4P line. Another crucial observation regards the variation of the ^2D populated solely from the $1s^2\,^1S$ component of the ion beam. As can be seen there is very little variation, indicating the low $1s2s\,^3S$ component. Other than that, both gas target results appear quite similar. An interesting aspect in these spectra is that for 12 MeV collisional energy, the metastable content exhibits maximum variation.
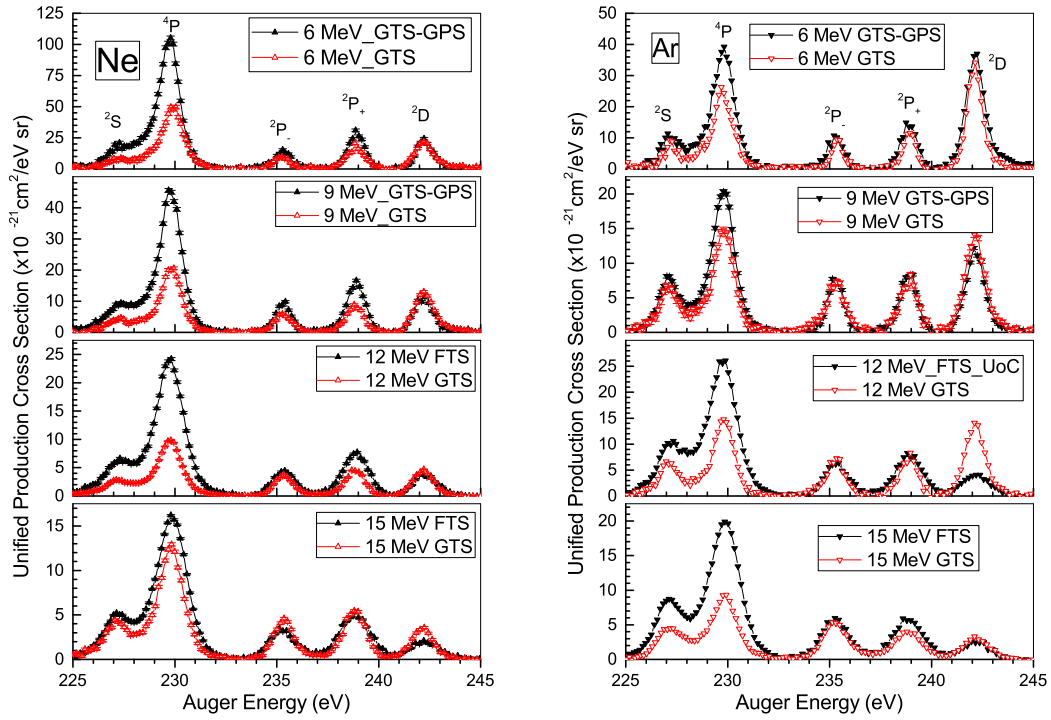
Figure A.2: *(Left:)* Normalized Ne spectra.*(Right:) Normalized Ar spectra. See text for details.*

For the sake of completeness, spectra with Ne and Ar targets are also presented, in Fig. A.2. Regarding these measurements, it should be considered that due to the targets higher nuclear charge, and the increased number of electrons carried into the collision, it is difficult to isolate populating mechanisms. This is augmented by the fact that the metastable fraction is not obvious optically. However, there are some interesting observations to be pointed out. First of all, although Ne presents higher yields for lower energies that drop as the energies increases, in the case of Ar, yields appear more stabilised. Also, Ne presents the strongest ^4P yields. This is the reason it was selected to model the ^4P line for the fitting procedure. Other than that, the Ar measurement at 12 MeV exhibits major variation for both beam contents, unsimilar to all other measurements. No explanation can be given for this set of measurements.

Appendix B

Tabulated SDCS results

In this appendix, we present the tabulated, experimentally measured results. These include normalized yields (NY#) of the two measured spectra for high (#→1) and low (#→2) metastable content, used in the analysis of the two measurement technique to determine the individual contributions of the ground and metastable component, as described in Ref. [168]. Using Eqs. (4.33a) and (4.33b), from Subsection 4.5.4, the contributions to the ^2S, $^2P_-$ and $^2P_+$ states from the $1s^2\,^1S$ and the $1s2s\,^3S$ components of the ion beam were separated and presented. It is reminded again that the ^2D and ^4P states are assumed to be populated exclusively from the $1s^2\,^1S$ and $1s2s\,^3S$ components of the beam, respectively, so no separation is required. In the case of the ^4P, the calculated G_τ solid angle correction, presented in Table D.1 for each collision energy respectively has already been applied.

B.1 Single Differential Cross Sections for collisions with H_2

Table B.1: Normalized yields and beam component contributions for the $C^{4+} + H_2 \rightarrow C^{3+}$ $(1s2s^2\,^2S)$ reaction. Collision velocity V_p and energies are defined in au, Mev and MeV/u. Normalized yields NY1 and NY2 are calculated for the two spectra utilizing Eq. 4.13. $d\sigma_{g/m}/d\Omega$ denote SDCSs for either the g(round) $1s^2\,^1S$ or the m(etastable) beam component contribution, respectively. ΔNY1, ΔNY2, $\Delta d\sigma_g$ and $\Delta d\sigma_m$ denote the uncertainties in the corresponding quantities.

$C^{4+} + H_2 \rightarrow C^{3+}$ $(1s2s^2\,^2S)$										
V_p	E_p		NY1	ΔNY1	NY2	ΔNY2	$d\sigma_g/d\Omega$	$\Delta d\sigma_g/d\Omega$	$d\sigma_m/d\Omega$	$\Delta d\sigma_m/d\Omega$
au	MeV	MeV/u	cm^2/sr	cm^2/sr	cm^2/sr	cm^2/sr	cm^2/sr	cm^2/sr	cm^2/sr	cm^2/sr
4.4700	6.00	0.50	1.75E-21	2.83E-22	1.68E-21	2.00E-22	1.62E-21	4.60E-22	2.63E-21	4.54E-21
5.4770	9.00	0.75	4.44E-22	3.55E-23	1.47E-22	2.56E-23	4.12E-23	3.76E-23	5.79E-21	5.23E-21
6.3246	12.00	1.00	2.08E-22	2.21E-23	4.32E-23	1.24E-23	2.03E-23	1.47E-23	1.22E-21	1.67E-21
7.0710	15.00	1.25	4.65E-23	1.24E-23	1.38E-22	3.34E-23	2.19E-22	6.54E-23	-5.29E-22	5.24E-22

Table B.2: Normalized yields and beam component contributions for the C^{4+} + $H_2 \rightarrow C^{3+}$ $(1s2s2p\,^4P)$ reaction. Same notation as in Table B.1. Calculated G_τ solid angle correction, presented in Table D.1 for each collision energy respectively has already been applied.

C^{4+} + $H_2 \rightarrow C^{3+}$ $(1s2s2p\,^4P)$									
V_p	E_p		NY1	ΔNY1	NY2	ΔNY2	$d\sigma_g/d\Omega$	$\Delta d\sigma_g/d\Omega$	$d\sigma_m/d\Omega$	$\Delta d\sigma_m/d\Omega$
au	MeV	MeV/u	cm^2/sr	cm^2/sr	cm^2/sr	cm^2/sr	cm^2/sr	cm^2/sr	cm^2/sr	cm^2/sr
4.4700	6.00	0.50	1.20E-20	2.10E-22	5.70E-21	1.56E-22	0.00E+00	5.01E-22	8.95E-20	4.49E-20
5.4770	9.00	0.75	1.77E-21	2.70E-23	4.62E-22	2.24E-23	0.00E+00	4.51E-23	2.52E-20	2.26E-20
6.3246	12.00	1.00	8.83E-22	1.20E-23	1.08E-22	1.03E-23	0.00E+00	1.68E-23	5.63E-21	7.83E-21
7.0710	15.00	1.25	4.89E-22	1.37E-23	2.31E-22	1.63E-23	0.00E+00	4.71E-23	2.12E-21	1.34E-21

Table B.3: Normalized yields and beam component contributions for the C^{4+} + $H_2 \rightarrow C^{3+}$ $(1s2s2p\,^2P_-)$ reaction. Same notation as in Table B.1.

C^{4+} + $H_2 \rightarrow C^{3+}$ $(1s2s2p\,^2P_-)$									
V_p	E_p		NY1	ΔNY1	NY2	ΔNY2	$d\sigma_g/d\Omega$	$\Delta d\sigma_g/d\Omega$	$d\sigma_m/d\Omega$	$\Delta d\sigma_m/d\Omega$
au	MeV	MeV/u	cm^2/sr	cm^2/sr	cm^2/sr	cm^2/sr	cm^2/sr	cm^2/sr	cm^2/sr	cm^2/sr
4.4700	6.00	0.50	2.16E-21	2.52E-22	1.92E-21	1.73E-22	1.70E-21	4.02E-22	5.09E-21	4.34E-21
5.4770	9.00	0.75	5.78E-22	3.02E-23	2.93E-22	3.30E-23	1.92E-22	4.64E-23	5.69E-21	5.01E-21
6.3246	12.00	1.00	1.86E-22	1.93E-23	1.22E-22	2.97E-23	1.13E-22	3.40E-23	5.76E-22	6.82E-22
7.0710	15.00	1.25	4.67E-22	3.17E-23	2.85E-22	2.90E-23	1.22E-22	6.62E-23	1.61E-21	9.82E-22

Table B.4: Normalized yields and beam component contributions for the C^{4+} + $H_2 \rightarrow C^{3+}$ $(1s2s2p\,^2P_+)$ reaction. Same notation as in Table B.1.

C^{4+} + $H_2 \rightarrow C^{3+}$ $(1s2s2p\,^2P_+)$									
V_p	E_p		NY1	ΔNY1	NY2	ΔNY2	$d\sigma_g/d\Omega$	$\Delta d\sigma_g/d\Omega$	$d\sigma_m/d\Omega$	$\Delta d\sigma_m/d\Omega$
au	MeV	MeV/u	cm^2/sr	cm^2/sr	cm^2/sr	cm^2/sr	cm^2/sr	cm^2/sr	cm^2/sr	cm^2/sr
4.4700	6.00	0.50	6.93E-21	2.32E-22	5.86E-21	1.61E-22	4.89E-21	3.77E-22	2.02E-20	8.49E-21
5.4770	9.00	0.75	1.01E-21	2.87E-23	7.45E-22	3.16E-23	6.50E-22	4.45E-23	5.84E-21	4.73E-21
6.3246	12.00	1.00	3.98E-22	1.75E-23	1.41E-22	3.20E-23	1.05E-22	3.68E-23	1.97E-21	2.60E-21
7.0710	15.00	1.25	4.00E-22	1.91E-23	2.45E-22	2.47E-23	1.07E-22	5.38E-23	1.38E-21	8.26E-22

Table B.5: Normalized yields and beam component contributions for the C^{4+} + $H_2 \rightarrow C^{3+}$ $(1s2p^2\,^2D)$ reaction. Same notation as in Table B.1.

C^{4+} + $H_2 \rightarrow C^{3+}$ $(1s2p^2\,^2D)$									
V_p	E_p		NY1	ΔNY1	NY2	ΔNY2	$d\sigma_g/d\Omega$	$\Delta d\sigma_g/d\Omega$	$d\sigma_m/d\Omega$	$\Delta d\sigma_m/d\Omega$
au	MeV	MeV/u	cm^2/sr	cm^2/sr	cm^2/sr	cm^2/sr	cm^2/sr	cm^2/sr	cm^2/sr	cm^2/sr
4.4700	6.00	0.50	3.47E-20	1.16E-21	3.75E-20	1.03E-21	4.01E-20	2.24E-21	0.00E+00	2.84E-20
5.4770	9.00	0.75	3.10E-21	8.78E-23	3.27E-21	1.39E-22	3.33E-21	1.91E-22	0.00E+00	4.24E-21
6.3246	12.00	1.00	2.85E-22	1.25E-23	3.32E-22	7.53E-23	3.38E-22	8.58E-23	0.00E+00	6.64E-22
7.0710	15.00	1.25	9.68E-23	4.62E-24	1.12E-22	1.13E-23	1.26E-22	2.19E-23	0.00E+00	1.12E-22

B.2 Single Differential Cross Sections for collisions with He

Table B.6: Normalized yields and beam component contributions for the $C^{4+} + He \rightarrow C^{3+}$ ($1s2s^2\,^2S$) reaction. Same notation as in Table B.1.

$\mathbf{V_p}$	$\mathbf{E_p}$		NY1	$\mathbf{\Delta NY1}$	NY2	$\mathbf{\Delta NY2}$	$d\sigma_g/d\Omega$	$\mathbf{\Delta d\sigma_g/d\Omega}$	$d\sigma_m/d\Omega$	$\mathbf{\Delta d\sigma_m/d\Omega}$
au	MeV	MeV/u	cm^2/sr	cm^2/sr	cm^2/sr	cm^2/sr	cm^2/sr	cm^2/sr	cm^2/sr	cm^2/sr
4.4700	6.00	0.50	3.87E-21	3.04E-22	2.83E-21	2.52E-22	2.12E-21	4.73E-22	1.28E-20	4.14E-21
5.4770	9.00	0.75	1.20E-21	5.03E-23	5.37E-22	7.15E-23	2.33E-22	1.09E-22	5.78E-21	1.79E-21
6.3246	12.00	1.00	7.40E-22	3.16E-23	1.59E-22	2.45E-23	3.95E-23	3.12E-23	3.43E-21	8.26E-22
7.0710	15.00	1.25	5.31E-22	2.43E-23	3.26E-22	2.16E-23	1.59E-22	4.72E-23	2.88E-21	1.71E-21

Table B.7: Normalized yields and beam component contributions for the $C^{4+} + He \rightarrow C^{3+}$ ($1s2s2p\,^4P$) reaction. Same notation as in Table B.1. Calculated G_τ solid angle correction, presented in Table D.1 for each collision energy respectively has already been applied.

$\mathbf{V_p}$	$\mathbf{E_p}$		NY1	$\mathbf{\Delta NY1}$	NY2	$\mathbf{\Delta NY2}$	$d\sigma_g/d\Omega$	$\mathbf{\Delta d\sigma_g/d\Omega}$	$d\sigma_m/d\Omega$	$\mathbf{\Delta d\sigma_m/d\Omega}$
au	MeV	MeV/u	cm^2/sr	cm^2/sr	cm^2/sr	cm^2/sr	cm^2/sr	cm^2/sr	cm^2/sr	cm^2/sr
4.4700	6.00	0.50	4.96E-20	5.15E-22	2.01E-20	4.26E-22	0.00E+00	1.13E-21	3.02E-19	5.73E-20
5.4770	9.00	0.75	6.33E-21	1.01E-22	1.98E-21	8.66E-23	0.00E+00	1.90E-22	3.62E-20	1.10E-20
6.3246	12.00	1.00	3.87E-21	7.50E-23	6.59E-22	3.23E-23	0.00E+00	5.92E-23	1.87E-20	4.43E-21
7.0710	15.00	1.25	2.26E-21	6.44E-23	1.02E-21	4.99E-23	0.00E+00	1.48E-22	1.65E-20	1.01E-20

Table B.8: Normalized yields and beam component contributions for the $C^{4+} + He \rightarrow C^{3+}$ ($1s2s2p\,^2P_-$) reaction. Same notation as in Table B.1.

$\mathbf{V_p}$	$\mathbf{E_p}$		NY1	$\mathbf{\Delta NY1}$	NY2	$\mathbf{\Delta NY2}$	$d\sigma_g/d\Omega$	$\mathbf{\Delta d\sigma_g/d\Omega}$	$d\sigma_m/d\Omega$	$\mathbf{\Delta d\sigma_m/d\Omega}$
au	MeV	MeV/u	cm^2/sr	cm^2/sr	cm^2/sr	cm^2/sr	cm^2/sr	cm^2/sr	cm^2/sr	cm^2/sr
4.4700	6.00	0.50	8.44E-21	2.07E-22	3.54E-21	2.06E-22	2.00E-22	3.97E-22	5.04E-20	9.83E-21
5.4770	9.00	0.75	1.55E-21	5.03E-23	8.51E-22	7.20E-23	5.33E-22	1.10E-22	6.34E-21	1.87E-21
6.3246	12.00	1.00	7.40E-22	3.33E-23	4.47E-22	3.31E-23	3.87E-22	4.06E-23	2.10E-21	4.70E-22
7.0710	15.00	1.25	6.02E-22	3.15E-23	4.42E-22	2.91E-23	3.11E-22	6.03E-23	2.44E-21	1.40E-21

Table B.9: Normalized yields and beam component contributions for the $C^{4+} + He \rightarrow C^{3+}$ ($1s2s2p\,^2P_+$) reaction. Same notation as in Table B.1.

$\mathbf{V_p}$	$\mathbf{E_p}$		NY1	$\mathbf{\Delta NY1}$	NY2	$\mathbf{\Delta NY2}$	$d\sigma_g/d\Omega$	$\mathbf{\Delta d\sigma_g/d\Omega}$	$d\sigma_m/d\Omega$	$\mathbf{\Delta d\sigma_m/d\Omega}$
au	MeV	MeV/u	cm^2/sr	cm^2/sr	cm^2/sr	cm^2/sr	cm^2/sr	cm^2/sr	cm^2/sr	cm^2/sr
4.4700	6.00	0.50	2.00E-20	2.08E-22	9.64E-21	2.04E-22	2.57E-21	4.66E-22	1.09E-19	2.02E-20
5.4770	9.00	0.75	3.09E-21	4.94E-23	1.59E-21	6.94E-23	9.04E-22	1.13E-22	1.34E-20	3.83E-21
6.3246	12.00	1.00	1.67E-21	3.25E-23	6.27E-22	3.08E-23	4.12E-22	4.01E-23	6.52E-21	1.46E-21
7.0710	15.00	1.25	9.90E-22	2.82E-23	6.28E-22	3.08E-23	3.32E-22	6.77E-23	5.14E-21	2.98E-21

Table B.10: Normalized yields and beam component contributions for the $C^{4+} + He \rightarrow C^{3+}$ ($1s2p^2\,^2D$) reaction. Same notation as in Table B.1.

$\mathbf{V_p}$	$\mathbf{E_p}$		NY1	$\mathbf{\Delta NY1}$	NY2	$\mathbf{\Delta NY2}$	$d\sigma_g/d\Omega$	$\mathbf{\Delta d\sigma_g/d\Omega}$	$d\sigma_m/d\Omega$	$\mathbf{\Delta d\sigma_m/d\Omega}$
au	MeV	MeV/u	cm^2/sr	cm^2/sr	cm^2/sr	cm^2/sr	cm^2/sr	cm^2/sr	cm^2/sr	cm^2/sr
4.4700	6.00	0.50	2.05E-20	2.13E-22	2.29E-20	4.85E-22	2.45E-20	8.31E-22	0.00E+00	6.54E-21
5.4770	9.00	0.75	3.95E-21	6.32E-23	4.53E-21	1.98E-22	4.79E-21	2.90E-22	0.00E+00	2.05E-21
6.3246	12.00	1.00	8.54E-22	1.65E-23	1.04E-21	5.09E-23	1.08E-21	6.15E-23	0.00E+00	3.58E-22
7.0710	15.00	1.25	3.55E-22	1.01E-23	3.86E-22	1.89E-23	4.12E-22	3.55E-23	0.00E+00	3.55E-22

B.3 Single Differential Cross Sections for collisions with Ne

The contributions from each beam component were obtained with Eq. 4.32, and the metastable fraction values f_1 and f_2 obtained by the He measurements, utilizing Eq. 4.31.

Table B.11: Normalized yields and beam component contributions for the $C^{4+} + Ne \rightarrow C^{3+}$ $(1s2s^2\,^2S)$ reaction. Same notation as in Table B.1.

$C^{4+} + Ne \rightarrow C^{3+}$ $(1s2s^2\,^2S)$										
V_p	E_p		NY1	ΔNY1	NY2	ΔNY2	$d\sigma_g/d\Omega$	$\Delta d\sigma_g/d\Omega$	$d\sigma_m/d\Omega$	$\Delta d\sigma_m/d\Omega$
au	MeV	MeV/u	cm^2/sr	cm^2/sr	cm^2/sr	cm^2/sr	cm^2/sr	cm^2/sr	cm^2/sr	cm^2/sr
4.4700	6.00	0.50	8.89E-21	4.44E-22	4.37E-21	3.52E-22	1.30E-21	1.33E-21	4.75E-20	1.55E-20
5.4770	9.00	0.75	5.52E-21	2.09E-22	2.20E-21	1.78E-22	6.84E-22	8.83E-22	2.84E-20	1.22E-20
6.3246	12.00	1.00	3.29E-21	8.23E-23	1.67E-21	7.22E-23	1.34E-21	1.49E-22	1.08E-20	2.68E-21
7.0710	15.00	1.25	3.26E-21	1.02E-22	2.50E-21	9.41E-23	1.88E-21	8.67E-22	1.20E-20	1.16E-20

Table B.12: Normalized yields and beam component contributions for the $C^{4+} + Ne \rightarrow C^{3+}$ $(1s2s2p\,^4P)$ reaction. Same notation as in Table B.1. Calculated G_τ solid angle correction, presented in Table D.1 for each collision energy respectively has already been applied.

$C^{4+} + Ne \rightarrow C^{3+}$ $(1s2s2p\,^4P)$										
V_p	E_p		NY1	ΔNY1	NY2	ΔNY2	$d\sigma_g/d\Omega$	$\Delta d\sigma_g/d\Omega$	$d\sigma_m/d\Omega$	$\Delta d\sigma_m/d\Omega$
au	MeV	MeV/u	cm^2/sr	cm^2/sr	cm^2/sr	cm^2/sr	cm^2/sr	cm^2/sr	cm^2/sr	cm^2/sr
4.4700	6.00	0.50	9.37E-20	1.06E-21	4.47E-20	7.98E-22	1.13E-20	1.33E-20	5.13E-19	1.59E-19
5.4770	9.00	0.75	4.19E-20	4.38E-22	1.84E-20	3.74E-22	7.61E-21	6.07E-21	2.04E-19	8.52E-20
6.3246	12.00	1.00	2.68E-20	2.23E-22	1.00E-20	7.60E-23	6.58E-21	1.32E-21	1.05E-19	2.72E-20
7.0710	15.00	1.25	1.41E-20	1.87E-22	7.65E-21	1.12E-22	2.39E-21	7.23E-21	8.80E-20	9.68E-20

Table B.13: Normalized yields and beam component contributions for the $C^{4+} + Ne \rightarrow C^{3+}$ $(1s2s2p\,^2P_-)$ reaction. Same notation as in Table B.1.

$C^{4+} + Ne \rightarrow C^{3+}$ $(1s2s2p\,^2P_-)$										
V_p	E_p		NY1	ΔNY1	NY2	ΔNY2	$d\sigma_g/d\Omega$	$\Delta d\sigma_g/d\Omega$	$d\sigma_m/d\Omega$	$\Delta d\sigma_m/d\Omega$
au	MeV	MeV/u	cm^2/sr	cm^2/sr	cm^2/sr	cm^2/sr	cm^2/sr	cm^2/sr	cm^2/sr	cm^2/sr
4.4700	6.00	0.50	1.52E-20	3.46E-22	1.07E-20	3.46E-22	7.66E-21	1.30E-21	5.34E-20	1.51E-20
5.4770	9.00	0.75	1.04E-20	1.80E-22	6.90E-21	1.79E-22	5.33E-21	9.14E-22	3.41E-20	1.26E-20
6.3246	12.00	1.00	6.89E-21	9.18E-23	4.77E-21	8.02E-23	4.33E-21	1.87E-22	1.67E-20	3.48E-21
7.0710	15.00	1.25	7.54E-21	1.60E-22	6.35E-21	1.17E-22	5.37E-21	1.36E-21	2.13E-20	1.82E-20

Table B.14: Normalized yields and beam component contributions for the $C^{4+} + Ne \rightarrow C^{3+}$ $(1s2s2p\,^2P_+)$ reaction. Same notation as in Table B.1.

$C^{4+} + Ne \rightarrow C^{3+}$ $(1s2s2p\,^2P_+)$										
V_p	E_p		NY1	ΔNY1	NY2	ΔNY2	$d\sigma_g/d\Omega$	$\Delta d\sigma_g/d\Omega$	$d\sigma_m/d\Omega$	$\Delta d\sigma_m/d\Omega$
au	MeV	MeV/u	cm^2/sr	cm^2/sr	cm^2/sr	cm^2/sr	cm^2/sr	cm^2/sr	cm^2/sr	cm^2/sr
4.4700	6.00	0.50	2.95E-20	3.32E-22	1.96E-20	3.49E-22	1.28E-20	2.72E-21	1.14E-19	3.24E-20
5.4770	9.00	0.75	1.79E-20	1.87E-22	9.39E-21	1.91E-22	5.52E-21	2.19E-21	7.62E-20	3.07E-20
6.3246	12.00	1.00	1.17E-20	9.74E-23	5.61E-21	7.86E-23	4.35E-21	4.87E-22	4.00E-20	9.90E-21
7.0710	15.00	1.25	1.14E-20	1.52E-22	7.50E-21	1.10E-22	4.28E-21	4.43E-21	5.67E-20	5.93E-20

Table B.15: Normalized yields and beam component contributions for the C^{4+} + Ne → C^{3+} ($1s2p^2\,^2D$) reaction. Same notation as in Table B.1.

C⁴⁺ + Ne → C³⁺ ($1s2p^2\,^2D$)										
V_p	**E_p**		**NY1**	**ΔNY1**	**NY2**	**ΔNY2**	**$d\sigma_g/d\Omega$**	**$\Delta d\sigma_g/d\Omega$**	**$d\sigma_m/d\Omega$**	**$\Delta d\sigma_m/d\Omega$**
au	MeV	MeV/u	cm²/sr	cm²/sr	cm²/sr	cm²/sr	cm²/sr	cm²/sr	cm²/sr	cm²/sr
4.4700	6.00	0.50	2.64E-20	2.98E-22	3.01E-20	5.36E-22	3.25E-20	1.20E-21	-4.48E-21	1.29E-20
5.4770	9.00	0.75	1.47E-20	1.54E-22	1.79E-20	3.65E-22	1.94E-20	9.39E-22	-7.81E-21	1.21E-20
6.3246	12.00	1.00	5.58E-21	4.63E-23	6.04E-21	8.47E-23	6.14E-21	9.67E-23	3.42E-21	8.88E-22
7.0710	15.00	1.25	2.48E-21	3.29E-23	3.12E-21	4.57E-23	3.65E-21	7.25E-22	-4.91E-21	9.69E-21

B.4 Single Differential Cross Sections for collisions with Ar

For the Ar target, the contributions from each component of the beam were obtained similarly to the Ne target.

Table B.16: Normalized yields and beam component contributions for the C^{4+} + Ar → C^{3+} ($1s2s^2\,^2S$) reaction. Same notation as in Table B.1.

C⁴⁺ + Ar → C³⁺ ($1s2s^2\,^2S$)										
V_p	**E_p**		**NY1**	**ΔNY1**	**NY2**	**ΔNY2**	**$d\sigma_g/d\Omega$**	**$\Delta d\sigma_g/d\Omega$**	**$d\sigma_m/d\Omega$**	**$\Delta d\sigma_m/d\Omega$**
au	MeV	MeV/u	cm²/sr	cm²/sr	cm²/sr	cm²/sr	cm²/sr	cm²/sr	cm²/sr	cm²/sr
4.4700	6.00	0.50	7.18E-21	1.27E-22	4.11E-21	4.85E-22	2.01E-21	1.03E-21	3.35E-20	1.09E-20
5.4770	9.00	0.75	6.60E-21	3.09E-22	5.68E-21	4.19E-22	5.26E-21	5.48E-22	1.29E-20	5.03E-21
6.3246	12.00	1.00	9.21E-21	4.81E-22	3.10E-21	2.53E-22	1.85E-21	5.57E-22	3.75E-20	1.03E-20
7.0710	15.00	1.25	7.53E-21	2.43E-22	4.19E-21	3.32E-22	1.46E-21	3.78E-21	4.58E-20	5.04E-20

Table B.17: Normalized yields and beam component contributions for the C^{4+} + Ar → C^{3+} ($1s2s2p\,^4P$) reaction. Same notation as in Table B.1. Calculated G_τ solid angle correction, presented in Table D.1 for each collision energy respectively has already been applied.

C⁴⁺ + Ar → C³⁺ ($1s2s2p\,^4P$)										
V_p	**E_p**		**NY1**	**ΔNY1**	**NY2**	**ΔNY2**	**$d\sigma_g/d\Omega$**	**$\Delta d\sigma_g/d\Omega$**	**$d\sigma_m/d\Omega$**	**$\Delta d\sigma_m/d\Omega$**
au	MeV	MeV/u	cm²/sr	cm²/sr	cm²/sr	cm²/sr	cm²/sr	cm²/sr	cm²/sr	cm²/sr
4.4700	6.00	0.50	3.49E-20	1.25E-21	2.11E-20	1.05E-21	1.17E-20	4.05E-21	1.53E-19	4.73E-20
5.4770	9.00	0.75	1.83E-20	5.44E-22	1.29E-20	6.15E-22	1.04E-20	1.59E-21	5.60E-20	2.07E-20
6.3246	12.00	1.00	2.96E-20	1.34E-21	2.44E-20	1.42E-21	2.33E-20	1.57E-21	5.40E-20	1.31E-20
7.0710	15.00	1.25	2.38E-20	6.43E-22	1.00E-20	8.54E-22	-1.26E-21	1.55E-20	1.82E-19	2.08E-19

Table B.18: Normalized yields and beam component contributions for the C^{4+} + Ar → C^{3+} ($1s2s2p\,^2P_-$) reaction. Same notation as in Table B.1.

C⁴⁺ + Ar → C³⁺ ($1s2s2p\,^2P_-$)										
V_p	**E_p**		**NY1**	**ΔNY1**	**NY2**	**ΔNY2**	**$d\sigma_g/d\Omega$**	**$\Delta d\sigma_g/d\Omega$**	**$d\sigma_m/d\Omega$**	**$\Delta d\sigma_m/d\Omega$**
au	MeV	MeV/u	cm²/sr	cm²/sr	cm²/sr	cm²/sr	cm²/sr	cm²/sr	cm²/sr	cm²/sr
4.4700	6.00	0.50	1.13E-20	3.07E-22	6.21E-21	4.41E-22	2.76E-21	1.49E-21	5.45E-20	1.71E-20
5.4770	9.00	0.75	8.69E-21	2.73E-22	8.89E-21	4.16E-22	8.98E-21	4.89E-22	7.35E-21	3.65E-21
6.3246	12.00	1.00	1.03E-20	4.90E-22	7.21E-21	3.11E-22	6.57E-21	4.20E-22	2.48E-20	5.92E-21
7.0710	15.00	1.25	1.11E-20	2.78E-22	9.37E-21	5.27E-22	7.94E-21	2.10E-21	3.13E-20	2.73E-20

Table B.19: Normalized yields and beam component contributions for the $C^{4+} + Ar \rightarrow C^{3+}$ $(1s2s2p\,^2P_+)$ reaction. Same notation as in Table B.1.

$\mathbf{C^{4+}}$ + **Ar** $\rightarrow$ $\mathbf{C^{3+}}$ $(1s2s2p\,^2P_+)$										
V_p	**E_p**		**NY1**	**ΔNY1**	**NY2**	**ΔNY2**	**$d\sigma_g/d\Omega$**	**$\Delta d\sigma_g/d\Omega$**	**$d\sigma_m/d\Omega$**	**$\Delta d\sigma_m/d\Omega$**
au	MeV	MeV/u	cm^2/sr	cm^2/sr	cm^2/sr	cm^2/sr	cm^2/sr	cm^2/sr	cm^2/sr	cm^2/sr
4.4700	6.00	0.50	1.48E-20	5.31E-22	9.07E-21	4.51E-22	5.15E-21	1.69E-21	6.40E-20	1.97E-20
5.4770	9.00	0.75	9.17E-21	2.72E-22	8.54E-21	4.08E-22	8.26E-21	5.05E-22	1.35E-20	4.20E-21
6.3246	12.00	1.00	1.27E-20	5.76E-22	4.99E-21	2.90E-22	3.40E-21	6.87E-22	4.84E-20	1.29E-20
7.0710	15.00	1.25	1.04E-20	2.82E-22	6.65E-21	5.67E-22	3.56E-21	4.32E-21	5.39E-20	5.74E-20

Table B.20: Normalized yields and beam component contributions for the $C^{4+} + Ar \rightarrow C^{3+}$ $(1s2p^2\,^2D)$ reaction. Same notation as in Table B.1.

$\mathbf{C^{4+}}$ + **Ar** $\rightarrow$ $\mathbf{C^{3+}}$ $(1s2p^2\,^2D)$										
V_p	**E_p**		**NY1**	**ΔNY1**	**NY2**	**ΔNY2**	**$d\sigma_g/d\Omega$**	**$\Delta d\sigma_g/d\Omega$**	**$d\sigma_m/d\Omega$**	**$\Delta d\sigma_m/d\Omega$**
au	MeV	MeV/u	cm^2/sr	cm^2/sr	cm^2/sr	cm^2/sr	cm^2/sr	cm^2/sr	cm^2/sr	cm^2/sr
4.4700	6.00	0.50	5.08E-20	1.82E-21	3.48E-20	1.73E-21	2.39E-20	4.98E-21	1.88E-19	5.66E-20
5.4770	9.00	0.75	1.49E-20	4.43E-22	1.88E-20	9.00E-22	2.06E-20	1.44E-21	-1.19E-20	1.58E-20
6.3246	12.00	1.00	8.21E-21	3.73E-22	6.10E-21	3.54E-22	5.66E-21	4.15E-22	1.80E-20	4.33E-21
7.0710	15.00	1.25	5.57E-21	1.50E-22	6.10E-21	5.20E-22	6.53E-21	9.10E-22	-5.12E-22	1.01E-20

112

Appendix C

Construction - Technical notes

C.1 Introduction - Construction timeline

The following chapter is a detailed technical description of the experimental apparatus assembly, tuning and operation. The beam-line was assembled in the Red Target Room on the L45 beam-line of the 5.5 MV TANDEM accelerator laboratory located at the INPP at the NCSR in Athens. The first parts for the construction arrived midst July 2013 and by July 2014 the first spectrum had been recorded.

Significant construction milestones.

January 2013	The design of the experimental apparatus is finalized, along with the needed parts.The original design of the beam-line components together with the design of the collision chamber, the target and the post-stripping system is displayed in Fig. C.1.
February 2013	Tender announcement for the vacuum parts.
July 2013	Arrival of the parts to the laboratory. Beginning of construction. First vacuum tests of beam-line.
November 2013	First successful high-vacuum tests of the collision chamber and the gas cell chamber.
December 2013	Trial placement of the HDA. First announcement of the DAQ tender.
January 2014	Beam-line connected to the vacuum chamber. Final vacuum test.
February 2014	Disassembly and cleaning of the HDA. First ion beam transmission test using a 3 MeV proton (H^+) beam. Current measured on the first Faraday Cup (Before gas target) was 230 nA.
May 2014	First implementation and successful tests of the DAQ. First tests were conducted with a hot-wire e-gun.
July 2014	First spectrum using C^{4+} ions accelerated at 12 MeV (1 MeV/u).
October 2014	Installation of XYZ system for the Gas Cell.
February 2015	Change of gas cell apertures to larger ones.
November 2015	First FPS and GPS run
January 2016	DAQ freezing solved.
August 2016	Successful implementation of the GTS, allowing for lower metastable fraction beams.
February 2017	Complete set of measurements acquired.

C.2   Ion Optics design of complete beam-line

The optics of the entire accelerator were cross-checked with the Charged Particle Optics (CPO) code TRANSPORT [260] and compared to experimental beam conditions. Following that, beam-line optics were designed, where the L45 port was considered as the initial ion source. The ion beam optics study of L45 was conducted with the use of the MAD code [261] by Dr. Nikos Tsoupas - BNL. This determined the exact positions for the equipment in order to acquire highest transmission.

C.3   Beam-line Construction

Slits   A series a LED lights were installed inside both slits for illumination and making the alignment process easier. The LEDs were placed in such a way that:

- they can be powered by an external Power Supply Unit (PSU)(9-12 V), using the BNC feed-through, and

- they do not interfere with the **positive** ion measurements, since they are used for beam optimization. This is accomplished by connecting cathode of the LEDs to the slits and the anode to the ground and by applying negative voltage to the slits.

The 4-jaw slits are shown in Fig. 3.3. Fig. C.2 shows the electrical diagram for the slits illumination.

Quadrupoles   The electromagnetic quadrupole lens is designed to function as an accurate, strong-focusing device for the ion beam with controlled precision. It consists of four hyperbolically shaped pole pieces. Its disadvantage is that while focusing in one plane it defocuses in the other. This is solved by using a pair of Quadrupoles in series with the second been $90°$ rotated to the first, with respect to the beam axis [262, 263]. The magnetic quadrupole lens installed on the beam-line (HVI 1156 M-321 doublet) was acquired from the INPP. L45 quadrapole is controlled by the accelerator operator.

Steerers   The parallel steering electromagnets are used for small-angle corrections to the ion beam trajectories, and typically combine functions of steering along both transverse axes. The steering set installed in the beam-line is custom made, obtained from KSU and consists of two steerers (upstream and downstream steerer) each one equipped with two pairs of coils forming two dipoles in order to make corrections in two points along the ion beam. Thus, the user can either steer or parallel shift the ion beam. Each of the four dipoles has its own current power supply providing a maximum current of $\approx$ 6-10 A, depending on the distance (cable length) of the PSUs from the controller. The steerers and their power supplies are displayed in Fig. C.3. Proper connectivity, to avoid magnetic fields cancelling out, was achieved with the use of a small compass.

The controller of the steerers is mounted on the Tandem operator's console. The circuit of intermediate cabling is presented in Fig. C.4. The connection between each channel of the steerer and the respective PSU was achieved with a set of four 60-80 meters long UTP cables passing from the basement to the control room. The cable for each pair of coils is terminated with a DB9M connector on the control side and with a DB25M connector in the PSU side with the connections being"1-1": 1-1, 2-2, 3-3 etc.
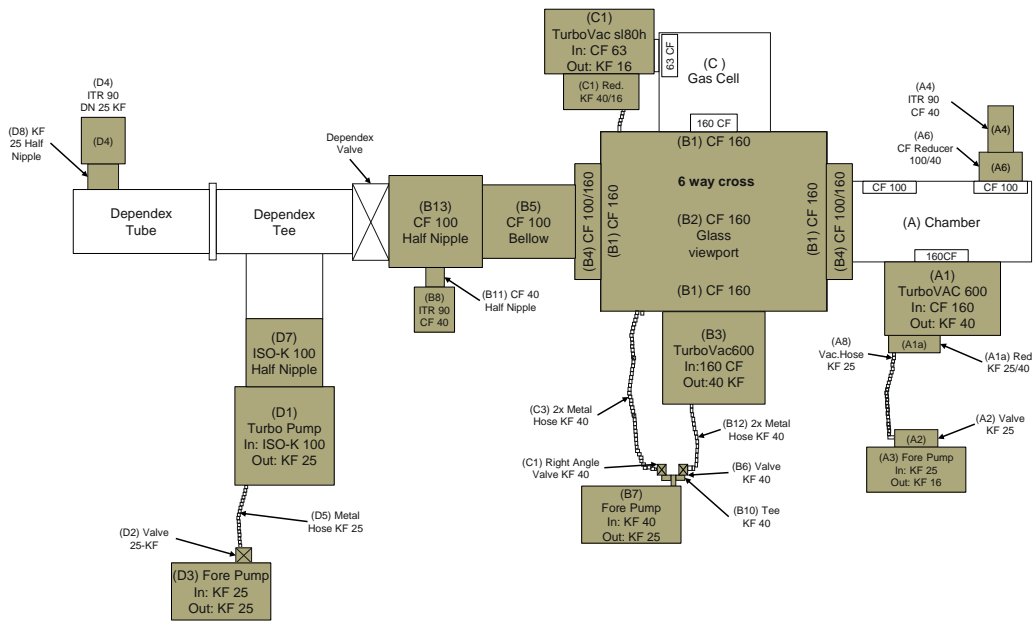
(a) Original design of beam-line components: Collision and analyzer chamber - January 2013.
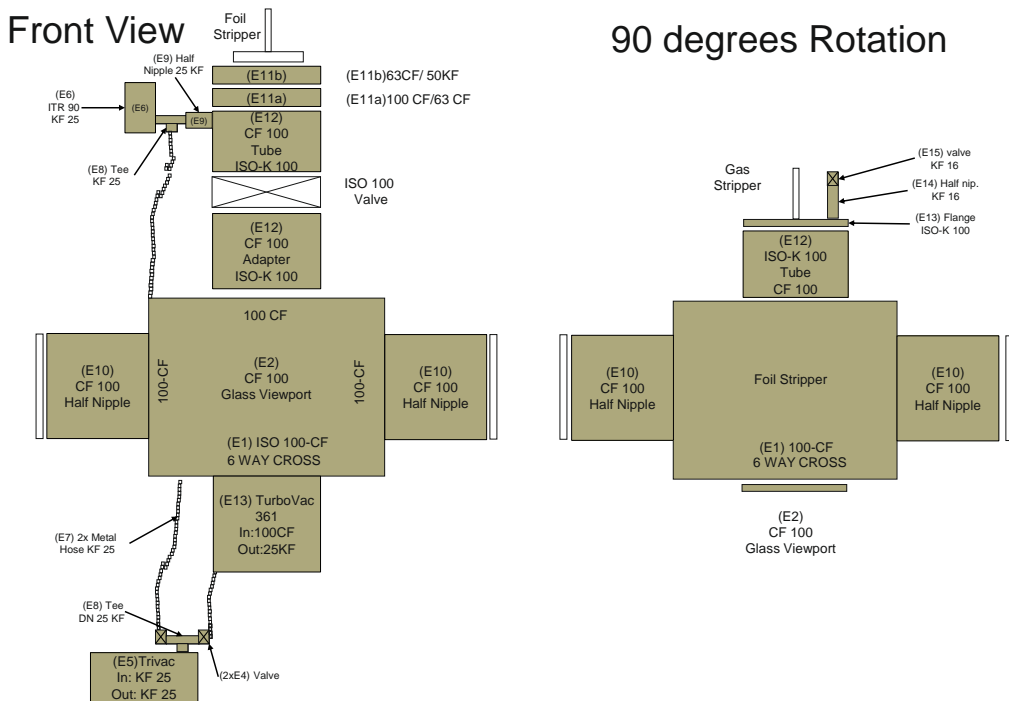
(b) Original design of beam-line components: Foil and gas post-strippers - January 2013.

Figure C.1: (a) Original design of beam-line components: Collision and analyzer chamber, (b) Original design of beam-line components: Foil and gas post-strippers. The colouring denotes the parts that needed to be purchased.
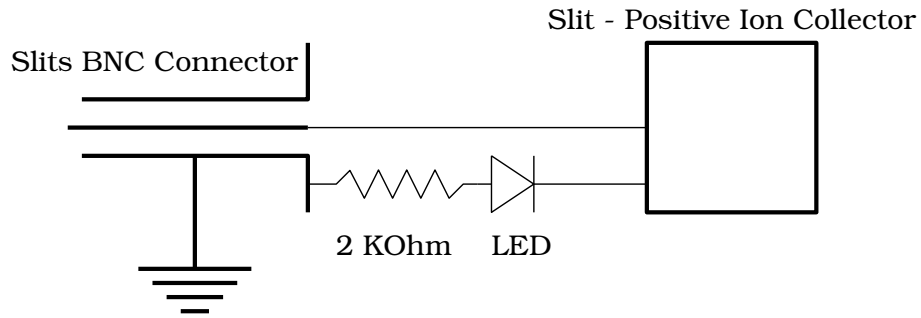
Figure C.2: Connections of internal LED lightning. During the beam-line alignment, a negative-tip 9 Volt DC cable is connected to the BNC adapters. The polarity of the diode ensures that positive ions collected on the plate can be measured with a BCI.

Figure C.3: Electromagnetic steerer coils and dedicated current supplies.
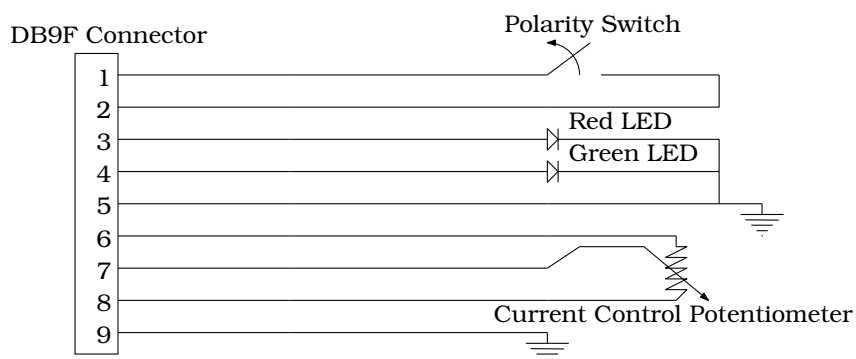
Figure C.4: Steerer Control Unit cabling. Image corresponds to one out of four current controls, each dedicated to a current supply.

Figure C.5: (Left) Photo of the inside of the Beam Profile Monitor (BPM) depicting motor and shaft of the rotating wire. The metal shield lining the inside of the beam-line is connected to the BPM signal collector. (Right) Photo of BPM controller box (down just above Nuclear Instrumentation Module (NIM) crate) and on top the oscilloscope viewer at the Tandem control console.

DB9F Connector	Function	Selected Cable	DB9F Connector
1	Power Status Control	Yellow	1
2	Collector	Grey (Shielded)	2
3	Collector Return	White (Shielded)	3
4	Fiducial	Yellow White	4
5	Shield (Ground)	Shield	5
6	S.C. Return	Blue	6
7	Gain Status Control	Purple	7
8	S.C. Return	Orange	8
9	Fiducial	Blue White	9

Figure C.6: BPM cabling schematics. The collector signals were connected through the shielded cables after suggestion of Dr. Béla Sulik

Beam Profile Monitors The BPM is a device that measures the beam intensity distribution as a function of the position. A single wire formed into a $45°$ arc is rotated about the axis of the arc in vacuum at a frequency of about 19 Hz. It sweeps across the beam in two independent directions in every cycle. The number of secondary electrons released from the wire as it intercepts the beam is a measure of the beam intensity at every instant. The two signals, representing beam intensity distributions in the $X-$ and $Y-$ directions perpendicular to the beam direction ($+Z$ direction), are displayed in an oscilloscope (Goldstar OS-9000SRS) [264]. The complete BPM system is shown in Fig. C.5. Two BPMs were installed, the first one, named BPM1, is placed inside the TANDEM room, right before the post stripper, between analysing and switching magnets. The second one, named BPM2, is placed at the end of the L45 beam-line and just before the target 6-way cross. The BPM controller and the oscilloscope are connected with both BPM1 and BPM2 and placed at the Tandem accelerator control room. Connectivity was achieved using the existing cabling of the previous BPMs[1]. Finally, right before the BPM2 and exactly above the turbo pump, a pneumatic Faraday Cup was installed (FC1). L45 beam-line and the collision chamber can be isolated by a manually operated vacuum valve.

---

[1]Currently removed

C.4 Assembly considerations

The spectrometer chamber along with the analyzer were modelled in full detail in the Solidworks™ CAD software for maximum design efficiency. The original chamber came with an XYZ alignment base table top. A supporting table was constructed with originally four legs. While the assembly of the apparatus advanced, an extension was decided, that would:

1. stabilize the apparatus,

2. handle the excessive weight of the instrumentation,

3. have the necessary space for the standard rack-sized mounted units and

4. provide the degrees of freedom to perform fine-adjustments to the overall alignment of the collision chamber.

This resulted in the solution shown in Fig. C.7 which depicts the final support stand for the apparatus. The upstream extension of the table was carefully designed so that the space beneath the target has the standard width of a typical rack unit(482.6 mm). Additionally, adjustable mounting feet were installed in every corner of the table for stability and control of the position and orientation of the table. Additional support was required and assembled (green support beam in Fig. C.7 for the support of the 3rd turbo pump and to set the final fixed point of the beam-line as the reference point for the apparatus alignment. After that, a bellow of standard beam-line diameter (101.6mm=4 in.) was placed between the beam-line and the chamber to ensure the required degrees of freedom for alignment. The support table for the two chambers was constructed in the TANDEM machine shop. Pictures from the construction and the placement of the support table can be seen in Fig. C.8 while the two chambers placed upon the support table before the connection with the beam-line can be seen in Fig. C.9.

The target's 6-way cross was bought by tender while for the collision chamber used was one of the two vacuum chambers obtained from KSU[2]. Two central turbo pumps (350-500 l/s) were bought, one for the collision chamber and one for the target's cross, and also a smaller one (80 l/s) for the differential pumping of the target gas cell. The collision chamber and the target's cross were designed along with the beam-line. Fig. C.7 is a CAD schematic view of the complete setup.

C.5 Vacuum considerations

All turbo pumps can be easily isolated from the backing pumps with the use of 24 VAC electropneumatic valves (High vacuum pneumatic Angle Valves - Leybold DN16). The control of these valves is done with custom made switches, as seen in Fig. C.10, that include status indicators. Initially, the switches were powered by the controllers of the turbo valves, however, since the controller could not deliver enough current, an external 240-to-24 VAC transformer was bought and installed in the apparatus, along with a "Master Valve Switch" which allows simultaneous control of all three valves. It should be noted that although these operate with either AC or DC voltages, AC supply resulted to less heating of the valves. Also, LED indicators presented no problem with the AC voltage applied. After the chamber system was connected with the beam-line, it was aligned

---

[2]A difference in the cross's dimensions is the primary reason for the different distance between the gas cell and the HDA compared to the previous setup in the KSU as seen in [166].
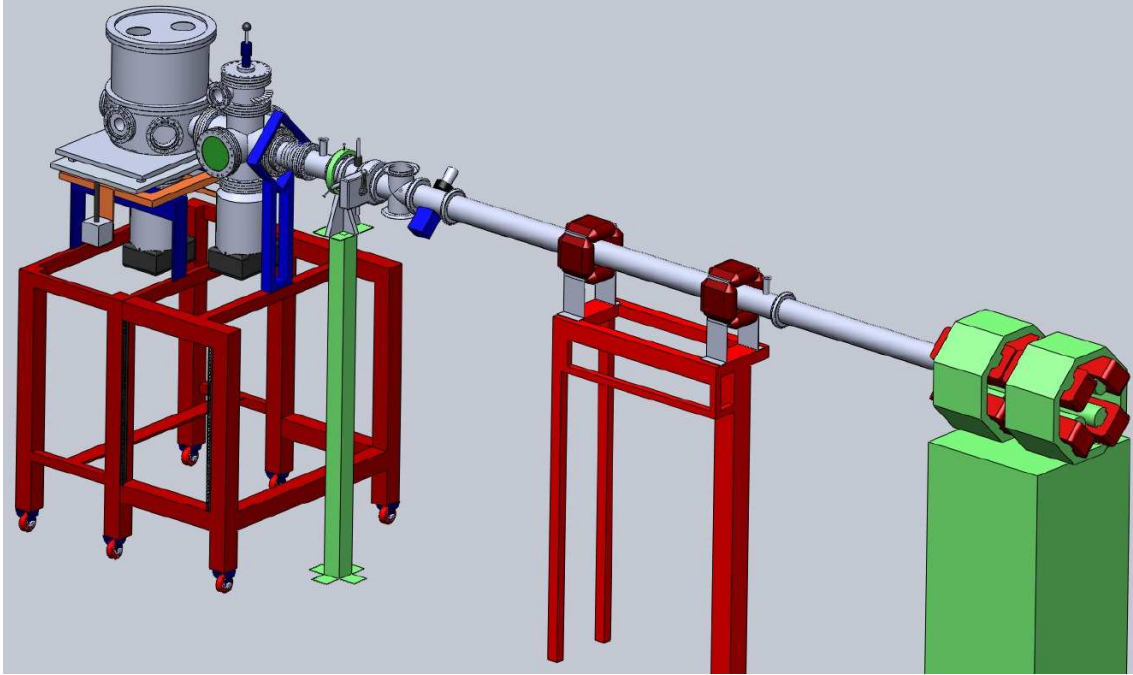
Figure C.7: CAD schematic of the L45 beam-line showing from left to right the analyzer chamber, the 6-way cross with target gas cell, the 4-jaw slits, the isolation valve, the beam profile monitor, the electromagnetic steerers and the focusing quadrupole. The beam enters from the right, is focused by the quadrupole, then collimated by the 4-jaw slits, collides with the gas in the target and continues through the HDA to FC2 at the end of the beam-line.

Figure C.8: Construction and placement of the support table.

with the use of the theodolite. Following the alignment, the whole setup was sealed for pumping and the final vacuum test was run.

The first full transmission tests were conducted using a 3 MeV proton beam. The current of the first FC1, right after the BPM2, was about 40 nA (with about 250 nA analyzed) and with the target gas cell pulled up and out of the ion beam path, the current in the FC2 was around 3-12 nA with SL2 set to about 2×2 mm opening. A second transmission test again with a 3 MeV proton beam was performed three days later with gas cell in the beam path with the current on the two Faraday cups being: FC1: 40 nA and FC2 0.7 nA with SL2 again quite open. In both cases, the missing current between FC1

Figure C.9: Photo of spectrometer chamber (left) on XYZ translation table and gas cell 6-way cross (right) with turbo pumps installed and supported by the table stand constructed in the TANDEM machine shop. The beam-line can be seen on the right.

Figure C.10: Various stages of the isolation valves. On the upper left corner is the first implementation of the isolation valves, powered by the turbo controllers, and having LED indicators for the valve status. Upper right corner is the isolation valve at the turbo under the analyzer chamber. Lower left corner shows the isolation valves both for the 6-way cross and the gas cell. At the lower right corner is the second scheme for powering the isolation valves using an external 24 VAC transformer through a master switch.

and FC2 was most likely lost inside the gas cell and alignment clearly was not optimal. SL2 was typically set between 1.5-2 mm on both axes, small enough to minimize the beam hitting the entry of the gas cell housing which had an internal diameter of 1.6 mm. In this case, FC2 typically showed only a few 0.5-3 nA.

C.6 μ-Metal Shielding

In Fig. C.12, the ^4P Auger line is seen to be misaligned from the other lines. This effect was attributed to insufficient μ-metal shielding as the length of the electron path from the center of the target gas cell to the lens entry is about 286 mm and was not yet properly shielded. This affected more the prompt Auger lines that were all emitted from the gas cell itself and to a lesser extent the ^4P peak which being metastable decayed mostly outside the gas cell and closer to the lens thus being less deflected from its trajectory. Two additional coaxial μ-metal cylinders were installed along this path (Fig. C.13) improving overall shielding. A new spectrum taken in September 2014 showed now that all Auger lines were properly aligned along the dispersion axis of the HDA. Testing with the e-gun

Figure C.11: As in Fig. C.9, but now finally connected to the beam-line.
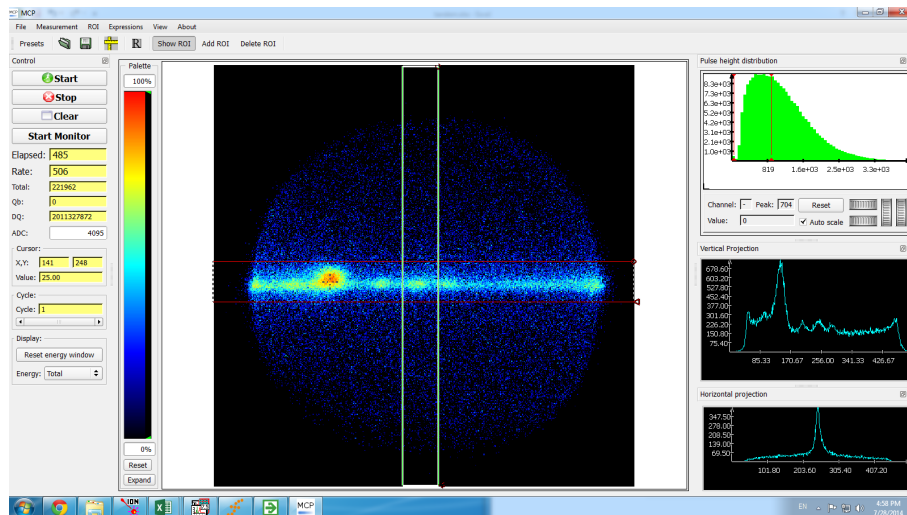
Figure C.12: Screenshot of the first spectrum. There seems to be a displacement of part of the spectrum perpendicularly to the energy (horizontal) axis.

provided with the minimum energy electrons could be measured, estimated to $\approx$80 eV.

C.7 Electronics

C.7.1 Computer Systems

The main computational systems used in APAPES are two identical PCs called the Lab Computer and the Analysis Computer. For both cases, the basic characteristics of the computers are as follows:

- Windows 7™ Ultimate Edition 64-bit

- Additional software MS Office™ 2007/2010 or later

Figure C.13: Placement of μ-metal tube. The tube is less that 5mm close to the exit of the Gas Cell, and it extends up to the entrance of the lens - V_{L6}.

- At least quad-core processor with minimum nominal speed 3.4 GHz

- 16 GB of RAM with capability of an extension up to 32 GB.

- Primary drive: Solid State for the operating system with minimum size 256 GB.

- Secondary drive: Hard Disk Drive with minimum size of 1 TB.

- LED-type monitor, at least 21".

- Autonomous graphics card with at least 1 GB RAM.

- Network connectivity.

- Two additional RAM modules of 8 GB each extending total RAM to 32 GB.

One of the two computers also required to have an extra Gigabit Ethernet port for the DAQ, since by the time of the tender, it was a known necessity. The first tender for the computer equipment ended unsuccessfully in January 2014, when a 2$^{\text{nd}}$ was publicised immediately. After the completion of the 2$^{\text{nd}}$ tender in February 2014, the PC assigned for the lab was bought, which allowed for further progress on the Control and DAQ work flow. The rest of the computer equipment were obtained later.

C.7.2   Micro-Channel Plates

One of the first necessities of the project was the storage of the MCPs used in the PSD. To date, the MCPs used were the same ones used when operating at KSU. These were stored in a desiccator and were found to work satisfactorily. A new larger desiccator was ordered by January 2014. On February 2014 a tender for MCPs replacement was announced, and by the end of April 2014, it was completed. The MCPs were bought from PHOTONIS and have not been utilized yet. They are safely stored in a desiccator for future use.

C.7.3   High Voltage Power supplies

Since the Tennelec HVPS's came with the chamber and the analyser, they were available early enough for testing. Also, research was done for the suitable floating HVPS for the MCPs and channeltron detector. On February 2014 all HVPSs were bought, including the custom-made HMI's, the counter and the Fasmatech multi-HVPS rack-mount unit. By March 2014, all additional purchases were made including a NIM crate,and a 4-channel 200MHz TDS200C digital storage oscilloscope. The testing for the correct integration of the DAQs 5$^{\text{th}}$ mode began on September 2014, and was finally debugged and completed by November 2014.

C.8 Preparation and placement of the HDA

After the first connection between the chamber housing the HDA and the beam-line was established. The HDA was carefully placed but only roughly aligned at this stage. In the same month, an order for electroformed mesh [211] (94% transmission) was placed. The purpose of the mesh is to minimize the intrusion of electric fields created by outside potentials, and thus isolate the HDA's electrostatic field. Furthermore, auxiliary mesh is also used to protect the detector surface from being hit by background electrons. This is the the mesh to which the potential V_{grid} is applied to, which is a little more negative that the plate potential V_p. However, the electron transmission is diminished by a factor proportional to each of the single mesh transmission and thus the overall transmission of N meshes is $T = T_{mesh}^N$ and should always be taken into consideration. According to the manufacturer, the transmission for a single grid is 90%, which translates to $T = 0.90^3 = 0.729$ or **72.9%**.
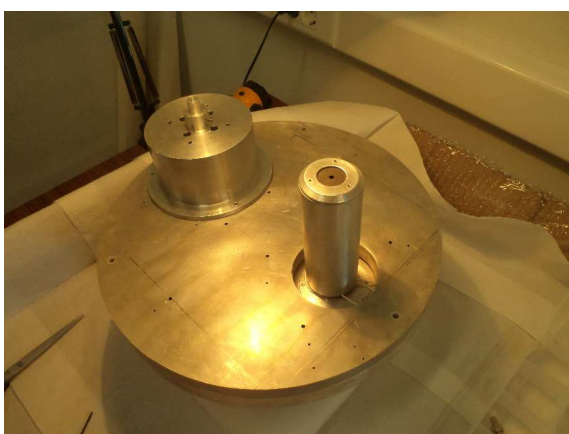
Figure C.14: Preparation for disassembly of the HDA. Although the analyser is made of large parts, there is a great number of tiny insulating sapphire balls, so extra caution is needed during this procedure.

On January 2014, a test of cable connectivity was ran, which, however, resulted, on the 12th of February, 2014, in complete disassembly of the HDA for cleaning and servicing (with the help of Prof. Emmanouil Benis) as shown in Fig. C.14. After the disassembly, all parts were cleaned from the any old coatings and dust. All screws were cleaned in the ultrasonic bath with the use of alcohol.

Figure C.15: Disassembly of the HDA. The carbon coated hemisphere is the inner sphere V_1 electrode. Beneath it, is located the plate electrode on potential V_p. The lower hole corresponds to the entrance of the analyser, and the upper hole to the exit. The HDA electrodes are stacked on the support plate and electrically isolated to about 5kV using sapphire balls of various radii.

After the cleaning process, a new carbon coat was applied over the V_1 and V_2 electrodes of the HDA using a special conducting Graphite Spray (Müller & Rössner). This procedure leads to a smooth surface and minimizes the effect of contact potentials and charge-up. In Fig. C.15 the coated V_1 electrode is visible.

Apart from the V_1, V_2 and V_p electrodes of the spectrograph, carbon coating was also applied to the inner surface of the injection lens electrodes. After that, the lens and the spectrograph were reassembled, ensuring at every step that all electrodes communicate with their corresponding cable, and that there was no electrical shorting between any of them.

The final stage of the assembly was the replacement of the electroformed grids. In total, there are three meshes used at the exit of the HDA between plate and PSD), resulting in an overall mesh transmission of $0.90^3 = 0.729$. After the assembly, in March 2014 the analyser was placed back into the chamber and was once again aligned, along with the target Gas Cell. The PSD was placed on the HDA and all the electrodes were checked for proper conductance. The MCPs were also checked by applying test voltages to them.

By April 2014, all parts of the analyser were designed with the use of Solidworks™CAD software (see Fig. 3.10). Since the CAD files were based on the official blueprints of the HDA this modelling of the setup increased significantly the design options. In addition, there were major corrections in the SIMION™ geometry files used to model the HDA.

Appendix D

Solid Angle Correction factor G$_\tau$

D.1 Introduction

As discussed in Ch. 4, zero-degree Auger electrons originating from long-lived projectile states such as $1s2s2p\,^4P_J$ [191, 239, 240] are characterized by lifetimes ranging from ns to ms depending on atomic number Z_p and total angular momentum J of the state. Therefore, the long-lived projectile states can Auger decay all along the path of the ion towards and even inside the spectrometer. Thus, their effective detection solid angle $\overline{\Delta\Omega}$ increases as the emitting ion approaches the spectrometer entry. Also, the state populations decay slowly so the correction factor must account both for the increase in the solid angle as well as the decrease due to the decay of the population. In this appendix, a summarized version of Refs [156, 241] for the correction of measured electron yields and the resulting cross sections is presented.

D.2 The solid angle correction factor G_τ : theoretical determination

D.2.1 Computational approach - Definitions and equations

As mentioned above, the distinction of projectile Auger transitions depends on the decay length $z_e \equiv V_p\tau$. If it is smaller or comparable to the length of the apparatus geometry, and particularly the target gas cell, the Auger transition is prompt, otherwise it is considered to be metastable. Most Auger states are considered prompt since $\tau \approx 10^{-6}$ ns, whereas V_p is 13.880 mm/ns at 1 MeV/u. The energy range of this thesis includes C^{3+} ions with energies from 6 up to 15 MeV. For these energies, projectile velocities range between 9.82 up to 15.515 mm/ns. In this velocity and lifetimes range, z_e is in the order of nm, therefore it decays well within the target gas cell volume. However, metastable states with $\tau > 10$ ns result to $z_e > 170$ mm decay lengths, and therefore contribute over a considerable length of the projectile path, well outside the target gas volume.

Thus, for prompt decays, Auger electrons are emitted from a small, well-defined volume and their detection solid angle depends mostly on the geometrical parameters of the experimental setup. For a ZAPS apparatus, Eq. 4.18 is appropriate for the prompt states under investigation. In the case of long-lived metastable projectile Auger states, the emission is spread out over a $V_p\tau_J$-dependent extended emission volume beyond the target gas cell and towards the spectrometer. This results in a different, comparatively to the $\overline{\Delta\Omega_0}$ for the prompt states, effective solid angle $\Delta\Omega_J$. To treat this problem, a correction

factor G_{τ_J} was defined, according to Eq. D.1:

$$\Delta\Omega_J = G_{\tau_J}\Delta\Omega_0 \tag{D.1}$$

The metastable state in question is $1s2s2p\,^4P_{1/2,3/2,5/2}$. The number of projectiles excited to component J in collision with a differential target length element dz' is given by Eq. D.2.

$$dN_0^J = N_0\sigma_J ndz' \qquad \left(0 \leq z' \leq L_c\right) \tag{D.2}$$

σ_J denotes the production cross section for direct population of the ^4P_J state in the collision of N_0 ions impinging on the target of surface density ndz', given in # atoms/cm^2. Following excitation at $z'(z=0)$, within the time $t = z/V_p$ and $t+dt$ later, dN_{τ_J} metastable states decay with the following rate:

$$dN_{\tau_J} = dN_0^J \left(\frac{e^{-z/V_p\tau_J}}{V_p\tau_J}\right) dz \qquad (0 \leq z \leq L - z') \tag{D.3}$$

In Eq. D.3, L is the maximal distance along the ion trajectory over which significant contributions to the overall electron line shape can be made.

Assuming electron emission at z, all electron contributions are integrated along the beam trajectory from $z = 0$ all the way to $z = L - z'$ to obtain the total number of accepted electron within $d\epsilon d\Omega$. $N_{\tau_J}^e(\epsilon)d\epsilon d\Omega$ is defined as follows:

$$N_{\tau_J}^e(\epsilon)d\epsilon d\Omega = N_0nL_c\sigma_J\xi_J d\epsilon \left[\frac{1}{L_c}\int_{z'=0}^{L_c}\Delta\Omega_0(L - z' - z)dz' \times \int_{z=0}^{L-z'}\frac{e^{-z/V_p\tau_J}}{V_p\tau_J}dz\right] \tag{D.4}$$

Figure D.1 presents the definitions of various terms.
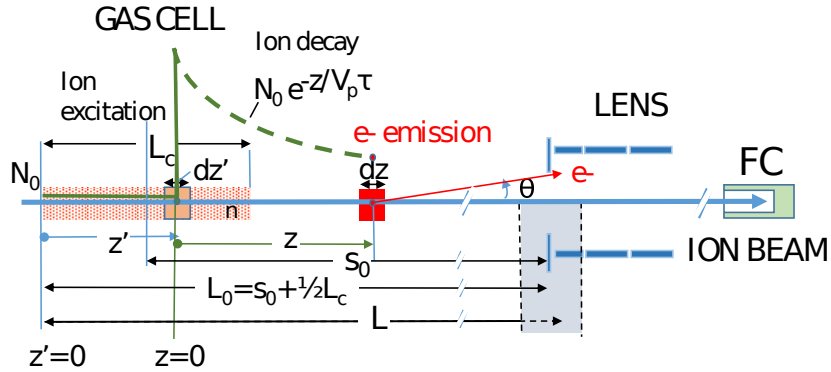
Figure D.1: Schematic of the integration region. N_0 ions (in the initial $1s2s\,^3S$ state enter the gas cell (length L_c an a distance s_0 from the lens entry) from the left with velocity V_p and get excited between z' and $z' + dz'$ to the $1s2s2p\,^4P_J$ state. Due to the long lifetimes τ_J, the excited ionic ^4P state travels further beyond the gas cell before it Auger decays. The Auger electron is emitted at angle θ, enters the lens and is eventually energy analysed by the HDA (not shown). The ions traverse the lens and part of the HDA, exiting at the back of the HDA and finally collected in the FC2 used for beam normalization.

For low-Z ions, like carbon, the different J components of the $1s2s2p\,^4P$ Auger line, cannot be experimentally resolved. Therefore, all contributions are added according to their statistical/population weight,

$$N_{\tau}^e d\epsilon d\Omega = \sum_J N_{\tau_J}^e(\epsilon)d\epsilon d\Omega \equiv N_0nL_c\sigma\xi d\epsilon G_\tau\overline{\Delta\Omega_0(s_0)}, \tag{D.5}$$

where the following symbols were implemented:

$$G_\tau \equiv \frac{\sum\limits_J a_J \xi_J G_{\tau_J}}{\sum\limits_J a_J \xi_J} = \frac{\sum\limits_J a_J \xi_J G_{\tau_J}}{\xi} = \frac{\sum\limits_J (2J+1)\xi_J G_{\tau_J}(L, V_p, s_0, L_c)}{\sum\limits_J (2J+1)\xi_J} \qquad (D.6a)$$

$$G_{\tau_J} = G_{\tau_J}(L, V_p\tau_J, s_0, L_c) \equiv \frac{\overline{\Delta\Omega_J}(L, V_p\tau_J, L_c)}{\overline{\Delta\Omega_0}(s_0, L_c)} \qquad (D.6b)$$

$$\alpha_J \equiv \frac{\sigma_J}{\sigma} = \frac{\sigma_J}{\sum\limits_J \sigma_J} = \frac{(2J+1)}{\sum\limits_J (2J+1)} \qquad (D.6c)$$

$$\xi = \sum_J \alpha_J \xi_J \qquad (D.6d)$$

G_τ is the J-averaged correction factor, G_{τ_J} is the correction factor for J component. α_J is the statistical weight for component J and ξ is the total Auger yield as a result of the statistically weighted Auger yields of the components J. The effective solid angle for the metastable state J averaged over the length of the gas cell is:

$$\overline{\Delta\Omega_J}(L, V_p\tau_J, L_c) \equiv \frac{1}{L_c} \int_{z'=0}^{L_c} \Delta\Omega_0(L - z' - z)dz' \times \int_{z=0}^{L-z'} \frac{e^{-z/V_p\tau_J}}{V_p\tau_J}dz \qquad (D.7)$$

and similarly to Eq.4.18, for a prompt state is defined as:

$$\overline{\Delta\Omega_0}(s_0, L_c) \equiv \left[\frac{1}{L_c} \int_{z'=0}^{L_c} dz' \Delta\Omega_0(L_c/2 + s_0 - z') \right] \qquad (D.8)$$

The only difference in both formulations is the reference point. In Eq.4.18 is defined as the center of the gas cell, whereas in Eq.D.8 is the beginning of the gas cell (upstream).
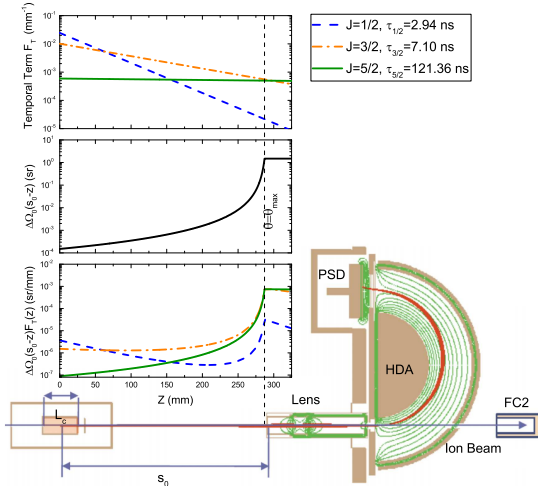
Figure D.2: z-Dependence along the ion trajectory for the probability decay density $F_T(z) = e^{(-z/V_p\tau)}/(-z/V_p\tau)$ (top), the point-source solid angle $\Delta\Omega_0(s_0 - z)$ (middle) and their product (bottom) as calculated for the $1s2s2p\,^4P_J$ states in the case of a 12 MeV C^{4+} ionic beam. The used lifetimes were obtained from [123]. The solid angle, computed by 4.17, increases over four orders of magnitude. However, due to kinematic effects, it reaches an upper limit a few mm's *before* entering the lens. $\approx$2.35 mm (12 MeV C^{4+}) before entrance, the acceptance angle reaches its maximum value.

D.2.2 SIMION Monte Carlo approach

The spectrograph layout, including the HDA, 4-element lens, PSD and the gas cell was built in the SIMION™ 8.1 geometry files design environment. Selected accuracy was

0.254 mm/gu. The same electrode voltages used in the experiment [220] were also applied to the model electrodes in order to simulate as closely as possible the experimental conditions. The numerical code was developed in the Lua programming language.

At each point of the ionic trajectory z, a number of emitted electrons is determined proportional to the product of the decay term and the solid angle term in Eq. D.7 as illustrated in Fig. D.2 and then multiplied by a starting indicative number N_i that determines the total number of electrons to be flown. The effects of the extended gas cell and ionic beam cylindrical shape are treated by creating electron distributions along the length of the gas cell in cylindrical disks having the radius of the ionic beam (≈ 0.8 mm). The electrons were emitted with the laboratory kinetic energy defined by the transformation equations for the corresponding Auger ϵ_A and cusp t_p energy. Regarding the direction, they were emitted within a cone distribution of angle θ, defined either by the lens aperture of radius d_{LE} at s_0 or the maximum allowed angle θ_{max}, if the computed θ was found to be larger than θ_{max}. Auger ϵ_A and cusp t_p energy values followed a Lorentzian and Gaussian pseudo-random distribution respectively, to describe more accurately the Auger widths and the ion beam energy width. The number of electrons created in this way was checked for solid angles smaller than the maximum kinematically allowed and found to be in good agreement.

D.2.3 Injection lens and the maximal distance of significant contributions

The number of electrons generated can increase to large numbers, exceeding the available RAM memory for large consecutive solid angles. As seen in Fig. D.2, the product of the decay and the temporal term can increase up to 4 orders of magnitude. For this reason, the effect of the lens on the long lived states that decay inside the region of the lens was examined. The target was to limit the decaying path of the ionic beam and thus the useful number of electrons. The $^4P_{\frac{5}{2}}$ J component of C^{3+} was chosen, having a relatively long lifetime of 121.36 ns [123] for the experimentally measured case of 12 MeV C^{4+} ionic beam. The study was performed for the lens voltages corresponding to pre-retardation factors $F = 1$ and $F = 4$. The result of the simulation shows that electrons generated inside the lens, even at the very beginning of the lens entry area, do not make it through and are largely filtered out before reaching the PSD area. This result can be justified by a number of reasons based on the fact that the electrons generated inside the lens cannot have a solid angle larger than θ_{max}, the kinematically allowed limit. This shows that:

- The main reason for the asymmetry exhibited by the metastable $1s2s2p\,^4P$ state is that the lens voltages of our HDA are optimized for prompt electrons originating from the gas cell volume. In other words, the lens is set as if its object is located at the gas cell center at a distance s_0 away. Delayed electrons emitted far from the object clearly will not be in focus, thus inheriting a broader and asymmetric energy distribution.

- The lens focuses primarily paraxial rays into the HDA. Thus, all electrons that deviate from the paraxial rays will largely depart from the central ray neighbourhood and will either hit the walls of the lens or the walls of the entry HDA aperture and not enter the HDA. For those few electrons that accidentally make it through the HDA aperture, these will have rather large entry angles resulting in detection at the PSD, but outside the range of the ^4P peak for paraxial rays and will thus be detected as background.

- The electrons that are generated at angles much larger than the paraxial values will have laboratory kinetic energies significantly different from the central energy

to which the HDA and the lens have been tuned. Thus, their rejection primarily by the lens is almost certain. In particular, in the case of forward emission considered here, it is clear that the laboratory energy $\epsilon_+(\theta)$ will always be smaller for $\theta \neq 0$. Therefore, contributions from non-zero θ angles will affect mostly the low energy side of the peak, as seen in the experimental line shape of the ^4P, also in Fig. D.3. This situation reverses for backward emission with contributions now broadening the peak on its high energy side (simulation not shown). Such backward emission for metastable Auger lines has never be reported to date and would therefore be of interest. This effect is probably also the cause of the broadening observed in the very low Auger energy prompt line shapes discussed in [265].

- Finally, electrons generated inside the lens will also have an altered kinetic energy by the amount of the value of the lens potential at the point of generation. Therefore, their kinetic energy will be out of the acceptance energy window of the lens/HDA. As a result, they will not be detected at all or will be detected as a random background signal on the PSD area. This effect is extended as the spectrometer is tuned to a pre-retardation factor $F > 1$, since this results in the narrowing of the energy acceptance window.
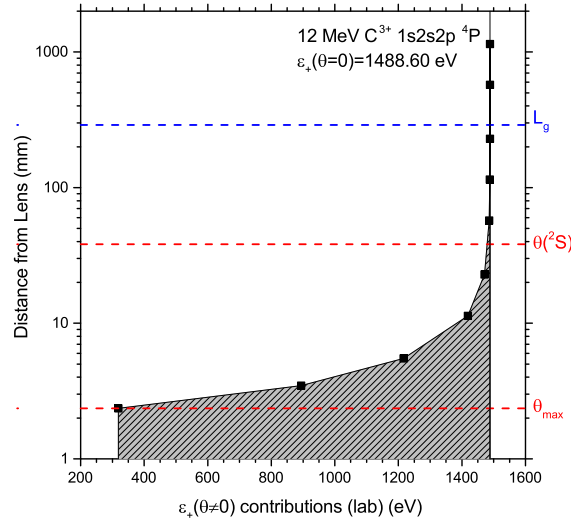
Figure D.3: Energy shift of $\theta \neq 0$ contributions as a function of distance from the lens for the ^4P state, for 12 MeV C^{4+} velocity. For a variety of distances, maximum θ is calculated, along with the corresponding maximum accepted shift $\epsilon_+(\theta)$. Due to kinematic effects, electrons emitted at $\theta \neq 0$, will have lower kinetic energies, and therefore will contribute to the low-energy side of the line. For example, ^4P states that Auger decay at$\approx$38 mm before the lens entry contribute to the **energy range** between ^2S and ^4P. Most of the electrons emitted are filtered out naturally due to the energy window of the analyzer. Exact value depends on tuning energy and deceleration mode, i.e. for $F = 4$ and $W = 1505$, lower limit is ≈ 1465 eV. Smaller F values yield larger energy windows.

In conclusion, the lens is found to act as an efficient filter rejecting electrons emitted outside the lens with large solid angles that substantially deviate from the paraxial values as well as those generated inside the lens itself. Its particular filtering action cannot be readily assessed theoretically. Here, it is simulated by SIMION showing that for the particular experimental setup, the end point L could be safely set outside the lens for all metastable state lifetimes considered. Therefore, the simulations carried out were

performed only in that area, since electrons emitted afterwards are practically filtered out.

D.2.4 Computational approach results

Table D.1: Theoretical parameters and Monte Carlo results for $1s2s2p\,^4P_J$ states of C^{4+} ions. Projectile energies E_p, total angular momentum component J, lifetimes τ_J, Auger yields ξ_J, measured area at Monte Carlo simulation, correction factor G_{τ_J}, statistical weight α_J, J-averaged Auger yield, and J-averaged G_τ. For all energies, pre-retardation factor $F = 4$. Table from Ref. [156].

E_p (MeV)	V_p (mm/ns)	J	τ_J(ns) [123]	Decay length (mm)	ξ_J	Number of eletrons	G_{τ_J}	α_J	ξ	G_τ
18	16.99	$^1/_2$	2.94	49.95	0.99	41767	1.88	$^1/_6$		
		$^3/_2$	7.10	120.63	0.94	84298	3.80	$^2/_6$	0.98	2.08
		$^5/_2$	121.36	2061.91	1.00	23580	1.06	$^3/_6$		
		Prompt				22192				
15	15.52	$^1/_2$	2.94	45.63	0.99	38608	1.74	$^1/_6$		
		$^3/_2$	7.10	110.19	0.94	80514	3.63	$^2/_6$	0.98	2.04
		$^5/_2$	121.36	1883.51	1.00	25504	1.15	$^3/_6$		
		Prompt				22192				
12	13.88	$^1/_2$	2.94	40.81	0.99	35404	1.60	$^1/_6$		
		$^3/_2$	7.10	98.55	0.94	75364	3.40	$^2/_6$	0.98	2.01
		$^5/_2$	121.36	1684.48	1.00	28398	1.28	$^3/_6$		
		Prompt				22192				
9	12.02	$^1/_2$	2.94	35.34	0.99	32170	1.45	$^1/_6$		
		$^3/_2$	7.10	85.34	0.94	67596	3.05	$^2/_6$	0.98	1.97
		$^5/_2$	121.36	1458.75	1.00	32349	1.46	$^3/_6$		
		Prompt				22192				
6	9.82	$^1/_2$	2.94	28.87	0.99	29092	1.31	$^1/_2$		
		$^3/_2$	7.10	69.72	0.94	56766	2.56	$^2/_6$	0.98	1.91
		$^5/_2$	121.36	1191.76	1.00	37845	1.71	$^3/_6$		
		Prompt				22192				

The procedure for obtaining solid angle correction factor G_τ in simulation is presented: Electrons simulated for every metastable state, and recorded by the PSD, correspond to the "observed" electrons, same as the experiment. Every J component is measured independently due to different lifetimes, along with every combination of projectile energy, due to various V_p. Following the above procedure, electron yields for the $1s2s2p\,^4P_J$ state are obtained, as well as for the corresponding reference prompt state, i.e., the state with the same energy as the $1s2s2p\,^4P_J$ state, but decaying promptly, inside the gas cell. The recorded number of this reference state corresponds to the "true" electrons, the electrons that should have been recorded, hadn't they decayed long after the HDA, and hadn't they encountered a geometrically variable solid angle. Simulating them as prompt is how this state can be compared with the other prompt states decaying inside the gas cell.

The correction factor G_{τ_J} was determined for the SIMION™ distance s_0 (see Fig. D.1) as the ratio of the number of PSD recorded electrons from the metastable state J under the peak of interest to that of the same energy but assuming a prompt decay which is equivalent to evaluating the ratio in Eq. D.6b) for each J, while both having the *same initial population*. Then, the J-averaged correction factors G_τ were determined according to Eq. D.6a. Non-isotropic angular distributions were not included in the calculations. Their effect is expected to be minimal in the case of the R_m ratio, defined as $\frac{\sigma_T[^4P]}{\sigma_T[^2P]}$. A

summary of the computed G_τ is presented on Table. D.1 from Ref. [156]. Lifetimes were obtained from Ref. [123], while ξ values from Ref. [238], and presented in Table. 4.4.

D.3 Summary and Conclusions

In this chapter the G_τ correction factor for auto-ionizing metastable projectile ion states was introduced. An analytical form regarding the dependence of the effective solid angle as a function of gas cell length, projectile velocity, J component lifetime and the distance of the gas cell was developed. A Monte Carlo type approach was combined with charged particle optics software based on the analytical approach. This approach is based on a comparison of prompt state electrons, and a Monte Carlo simulation of metastable state electrons, whose emittance was analogous to the effective solid angle. This comparison is equivalent to comparing the *true* number of electrons emitted with the *observed* number of electrons. By running Monte Carlo simulations, correction factors for every J component were calculated and then statistically averaged over total angular momentum, and Auger yield of each J component. For the validation of this study, the high resolution capabilities of the ZAPS technique was used to determine *experimentally* the effective detection solid angle $\overline{\Delta\Omega}$ of the long-lived $1s2s2p\,^4P$ state with respect to the point source solid angle $\Delta\Omega_0$ of the $1s(2s2p\,^3P)\,^2P_-$ prompt state whose solid angle can be readily computed. Measurements of $\overline{\Delta\Omega}$ were performed using the ZAPS spectrometer for collisions of 17.5 MeV O^{4+} and 6.6 MeV C^{2+} on H_2 target, where the $1s2s2p\,^4P$ and the $1s(2s2p\,^3P)\,^2P_-$ states are produced by $1s$ ionization of the $1s^22s2p\,^3P$ metastable component, inherent in Be-like beams. The solid angle correction factor G_τ, defined as the ratio of the solid angles $\overline{\Delta\Omega}/\Delta\Omega_0$, can be determined from the ratio of the $1s$ ionization cross sections of the two states, i.e. $\sigma_{1s}[^4P]/\sigma_{1s}[^2P_-]$, which is assumed to be 2, according to spin statistics. The $1s^22s2p\,^3P$ metastable component fraction was determined, and found in accordance with older measurements. In addition, older measurements of Lee *et al* [147] which used the conventional tandem PPA ZAPS spectrometer were also utilized, corrected and re-analysed using the same procedures. Aforementioned results of Monte Carlo type simulations realized using the SIMION electron optics package for both spectrometers, accounting for any electron optics effects due to electric fields in the two analyzer systems, were compared to the measurements and found to be in acceptable agreement. G_τ was found to sensitively depend on the lifetimes of the J-levels of the $1s2s2p\,^4P$ state resulting in a difference of 15% using SIMION for the HDA measurements. However, with the proper choice of the target distance to the spectrometer entry, the G_τ value can be tuned close to 1, minimizing the yield correction for the long-lived states, as well as reducing the sensitivity to their lifetimes, down to just a few percent, as is evident. This approach in the experimental determination of G_τ by $1s$ ionization of Be-like beams is that the ^4P and $^2P_-$ states can be assumed to be produced in a cascade-free environment, unlike the case of collisions with He-like ions where these same states are produced by capture to the metastable $1s2s\,^3S$ beam component, for which strong cascade feeding has been proposed.

Appendix E

Compton Profiles

The form of the Compton profile for each shell of the target is given by [266]:

$$J(p_z) = \sum_{n=1}^{M} \frac{\alpha_n}{\left[1 + \left(p_z/\xi_n \right)^2 \right]^{n+2}} \tag{E.1}$$

All $J(p_z)$ profiles must satisfy the following relation [267]:

$$\int_{-\infty}^{+\infty} J(p_z)dq = 2 \int_{0}^{+\infty} J(p_z)dp_z = 1 \tag{E.2}$$

For the H$_2$ and He Compton profiles, the α_n and ξ_n values are obtained from Ref. [266]. Regarding these gas targets, the multiplicity factor "2" is already included within the coefficients. They are presented in Table E.1 In the case of Ne and Ar, Compton profiles

Table E.1: Average coefficients of the polynomial used in the fitting of the H$_2$ and He Compton profiles. These parameters include both electrons. Taken from Ref. [266].

n	H$_2$ - $(1\sigma_g)^2$		He - $1s^2$	
	α_n	ξ_n	α_n	ξ_n
1	1.0012	0.9896	-0.0956	2.1828
2	0.5383	1.5566	0.0514	4.1598
3			0.1342	3.5200
4			0.7316	2.3948
5			0.2426	1.5732

are more complex. Every (sub)shell is characterized by a distinct momentum distribution. For RTEA calculations, the contributions of each subshell are calculated separately. Then, the distinct results are multiplied by subshell occupancy, to obtain a total calculation.

In Ref. [268] Biggs *et al* present $J(p_z)$ calculations for characteristic p_z values, for distinct subshells. Every Ne and Ar subshell was fit with functions similar to Eq. E.1, with M equal to 6 and 8 respectively. Results are presented in Tables E.2 and E.3. Fig. E.1 presents the relative deviation of the calculated $J(p_z)_{\text{calc}}$ values from the $J(p_z)_{\text{theory}}$ obtained from Ref. [268]. In the case of Ne, relative deviation does not exceed 2.6%, whereas in the case of Ar, maximum relative deviation is $\approx 3.6\%$. In both cases maximum deviations are for $p_z \geq 10$ (a.u.). For such values, $J(p_z)$ for non K-shell orbitals are 2-4 orders of magnitude smaller than $J(0)$. Considering that the fits cover a wide p_z range ($0 \leq p_z \leq 100$), results are satisfactory. For better quantization of the fitting quality, the

Table E.2: Average coefficients of the polynomial used in the fitting of the Ne Compton profiles.

	$1s^2$		$2s^2$		$2p^6$	
n	α_n	ξ_n	α_n	ξ_n	α_n	ξ_n
1	0.0404	11.1752	0.0140	8.2135	-0.0564	0.9715
2	0.0156	10.3239	0.2828	2.0386	0.2283	4.6427
3	0.0235	11.6496	0.0573	5.9148	-0.0908	5.7286
4	0.0385	10.8557	-0.0406	6.5976	-0.0004	12.0314
5	-0.0314	12.3119	0.1927	3.3889	0.0062	0.7585
6	0.0033	11.7149	-0.0532	7.1110	0.1871	3.8164

Table E.3: Average coefficients of the polynomial used in the fitting of the Ar Compton profiles.

	$1s^2$		$2s^2$		$2p^6$		$3s^2$		$3p^6$	
n	α_n	ξ_n	α_n	ξ_n	α_n	ξ_n	α_n	ξ_n	α_n	ξ_n
1	0.038	18.501	0.015	14.249	0.032	3.153	0.006	11.172	0.349	1.479
2	-0.075	9.492	0.013	3.776	0.112	9.349	-0.008	10.928	0.003	10.531
3	0.150	5.665	-0.128	5.882	-0.020	11.973	0.191	1.694	0.148	5.828
4	0.192	14.807	-0.001	0.292	0.038	10.641	0.216	1.965	0.043	2.444
5	-0.024	6.941	0.000	0.648	-0.064	6.834	-0.022	7.851	-0.192	1.344
6	-0.005	5.101	-0.024	14.443	-0.020	13.823	0.134	6.980	-0.116	7.689
7	-0.128	18.768	0.304	8.096	0.060	9.374	-0.190	4.688	0.278	3.367
8	-0.100	7.663	0.020	5.708	-0.034	5.507	0.321	2.424	-0.072	6.472
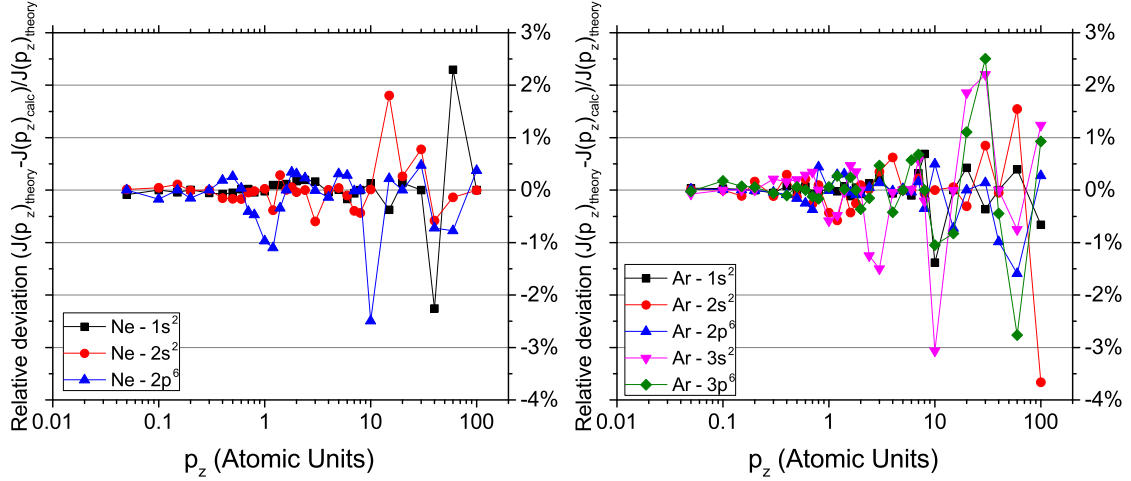
Figure E.1: Relative error for the α_n and ξ_n values, calculated for (Left) Ne and (Right) Ar. $J(p_z)_{\text{theory}}$ stands for the values obtained from Ref. [268] Biggs, while $J(p_z)_{\text{calc}}$ are the values obtained with the calculated α_n and ξ_n values.

convergence criterion was the absolute cumulative error $\left(= \sum\limits_{n=1}^{31 \text{ points}} \left| \frac{J(p_{z_n})_{\text{theory}} - J(p_{z_n})_{\text{calc}}}{J(p_{z_n})_{\text{theory}}} \right| \right)$ for each subshell. In the case of Ne, it did not exceed 0.0712, whereas for Ar, maximum value was 0.1335.

134

Appendix F

Selection rules

F.1 Autoionization transitions

In Table F.1 from Ref. [187] are presented the Auger selection rules. The tables' columns have been rearranged. The purpose is to identify for every transition the interaction mechanism along with the wave character of the emitted electrons.

Table F.1: Selection Rules for autoionization. α denotes the Sommerfeld fine-structure constant, m is the mass of the electron, and M is the proton mass. Table from Ref. [187] with rearranged columns.

Parity Change	ΔJ	ΔL	ΔS	Interaction	Relative transition rate
No	0	0	0	Coulomb	1
No	0	0,±1	0,±1	Spin-orbit / Spin-other-orbit	α^4
No	0	0,±1,±2	0,±1,±2	Spin-spin	α^4
No	0,±1	0,±1,±2	0,±1	Hyperfine	$\alpha^4 \left(m/M\right)^2$

Table F.2: Autoionization transitions for doubly excited $1s2lnl'$ states for Carbon and Oxygen. Table from Badnell $et\ al$ [269].

Intermediate	Final	
$1s2s\left({}^3S\right)nl \rightarrow$	$1s^2\,{}^1S + kl_c,$	$l_c = l$
$1s2s\left({}^1S\right)nl \rightarrow$	$1s^2\,{}^1S + kl_c,$	$l_c = l$
	$1s2s\,{}^3S + kl_c,$	$l_c = l$
	$\mathrm{C}^{4+}{:}n \geq 7$	$\mathrm{O}^{6+}{:}n \geq 8$
$1s2p\left({}^3P\right)nl \rightarrow$	$1s^2\,{}^1S + kl_c,$	$l_c = l \pm 1$
	$1s2s\,{}^3S + kl_c,$	$l_c = l \pm 1$
	$\mathrm{C}^{4+}{:}n \geq 7$	$\mathrm{O}^{6+}{:}n \geq 9$
$1s2p\left({}^1P\right)nl \rightarrow$	$1s^2\,{}^1S + kl_c,$	$l_c = l \pm 1$
	$1s2s\,{}^3S + kl_c,$	$l_c = l \pm 1$
	$\mathrm{C}^{4+}{:}n \geq 5$	$\mathrm{O}^{6+}{:}n \geq 7$
	$1s2s\,{}^1S + kl_c,$	$l_c = l \pm 1$
	$\mathrm{C}^{4+}{:}n \geq 8$	$\mathrm{O}^{6+}{:}n \geq 10$
	$1s2p\,{}^3P + kl_c,$	$l_c = l, l \pm 2$
	$\mathrm{C}^{4+}{:}n \geq 9$	$\mathrm{O}^{6+}{:}n \geq 10$

L is the orbit angular momentum, S is the spin, J is the total angular momentum and Π is the parity, defined as $\Pi = (-1)^{\sum_i l_i}$. As seen from Table F.1 parity is conserved

every time. Therefore, for every Auger transition parity should be conserved. Following the above reasoning, the next selection rule is defined as the conservation of J, as it is violated only through hyperfine interaction. Depending on the quantities that are ultimately preserved, the classification of the transition is made. What is more interesting is the existence of doubly excited states that decay to more than one states.

According to Badnell *et al* [269], doubly-excited $1s2lnl'$ states can decay by various autoionization transitions. Regarding C^{3+} and O^{5+} states, it can be seen in Table F.2 that the doubly-excited $1s2l2l'$ states of Carbon, under investigation in this thesis, decay exclusively to the $1s^2\,^1S$. Decay to any other $1s2l\,^{3,1}L + e_A(L')$ state for these states is not allowed energetically.

Considering the more general case of doubly-excited $1s2lnl'$ states presented on Table F.2, it is possible for the ion to decay to various $1s2l\,^{3,1}L + e_A(L')$ states. For this to be possible, the Binding Energy of the the $1s2lnl'$ configuration has to be larger than the Binding Energy of the corresponding $1s2l\,^{3,1}L$ state. This is primarily defined by the n-value of the $1s2lnl'$ configuration. Therefore, as seen in Table F.2, there are minimum n-values calculated for Carbon and Oxygen Li-like ions for which such transitions are possible. Also, the emitted electrons of these autoionization transitions are expected to be characterized by small energies, depending on the ion and the value of n. In Ref. [173] are calculations for the $1s^2ns$ and $1s^2np$ states with n ranging from 2 to 10. Considering the $1s2s\,^3S$ Binding Energy, rest Auger values are in the 1-10 eV region. For the ZAPS method, such values are expected near the Cusp energy.

Using the two selection rules for doubly-excited $1s2lnl'$ states, the orbit angular momentum of the emitted electron can be defined in the following transition assuming that the final state of the He-like ion is the $1s^2\,^1S$:

$$^{2S+1}L^{\Pi} \rightarrow (1s^2)^1S^e + e_A(L') \tag{F.1}$$

Below are examples that exhibit the use of the auto-ionization selection rules.

- $1s2s2p\,^4P_{5/2} \rightarrow (1s^2)^1S^e + e_A(f)$:
  In this case $J_i = \,^5/2$, while $\Pi_i = (-1)^{0+0+1} = (-1)^1 = -1$. Since $J_{f_i} = 0$ for the final ion, and $s_{f_e} = \,^1/2$ for the emitted electron, it's orbit angular momentum requires a minimum value of $l_{f_e} = 2$ to satisfy $J_{f_e} = l_{f_e} + s_{f_e} = \,^5/2$. However, the parity of the final state depends solely on the emitted electron, since $S_{f_i} = 0$. To ensure conservation of parity, $l_{f_e} = 3 \rightarrow \Pi_f = (-1)^{l_{f_e}} = -1 = \Pi_i$. Therefore, the emitted electron is an f-wave electron, that resulted from a spin-spin interaction ($\Delta L = 2, \Delta S = -1$).

- $(1s2p\,^3P)3s\,^4P_{3/2} \rightarrow (1s^2)^1S^e + e_A(p)$:
  In this case $J_i = \,^3/2$ while $\Pi_i = (-1)^{0+1+0} = (-1)^1 = -1$. Since $J_{f_i} = 0$ for the final ion, and $s_{f_e} = \,^1/2$ for the emitted electron, it's orbit angular momentum requires a minimum value of $l_{f_e} = 1$ to satisfy $j_{f_e} = l_{f_e} + s_{f_e} = \,^3/2$. This value also satisfies conservation of parity since $l_{f_e} = 1 \rightarrow \Pi_f = (-1)^{l_{f_e}} = -1 = \Pi_i$. Therefore, the emitted electron is an p-wave electron, that resulted from a spin(-other)-orbit interaction ($\Delta L = 0, \Delta S = -1$).

- $(1s2p\,^1P)3d\,^2F_{5/2} \rightarrow (1s^2)^1S^e + e_A(f)$:
  In this case $J_i = \,^5/2$ while $\Pi_i = (-1)^{0+1+2} = (-1)^3 = -1$. Since $J_{f_i} = 0$ for the final ion, and $s_{f_e} = \,^1/2$ for the emitted electron, it's orbit angular momentum requires a minimum value of $l_{f_e} = 2$ to satisfy $j_{f_e} = l_{f_e} + s_{f_e} = \,^5/2$. To ensure conservation of parity, $l_{f_e} = 3 \rightarrow \Pi_f = (-1)^{l_{fe}} = -1 = \Pi_i$. Therefore, the emitted electron is an f-wave electron, that resulted from a Coulomb interaction ($\Delta L = 0, \Delta S = 0$).

- $(1s2p\,^3P)3d\,^2P_{3/2} \rightarrow (1s^2)^1S^e + e_A(p)$:
  In this case $J_i = {}^3/_2$ while $\Pi_i = (-1)^{0+1+2} = (-1)^3 = -1$. Since $J_{f_i} = 0$ for the final ion, and $s_{f_e} = {}^1/_2$ for the emitted electron, it's orbit angular momentum requires a minimum value of $l_{f_e} = 1$ to satisfy $j_{f_e} = l_{f_e} + s_{f_e} = {}^3/_2$. To ensure conservation of parity, $l_{f_e} = 1 \rightarrow \Pi_f = (-1)^{l_{fe}} = -1 = \Pi_i$. Therefore, the emitted electron is an p-wave electron, that resulted from a Coulomb interaction ($\Delta L = 0, \Delta S = 0$).

- $(1s2p\,^1P)3p\,^2D_{3/2} \rightarrow (1s^2)^1S^e + e_A(d)$:
  In this case $J_i = {}^3/_2$ while $\Pi_i = (-1)^{0+1+1} = (-1)^2 = 1$. Since $J_{f_i} = 0$ for the final ion, and $s_{f_e} = {}^1/_2$ for the emitted electron, it's orbit angular momentum requires a minimum value of $l_{f_e} = 1$ to satisfy $j_{f_e} = l_{f_e} + s_{f_e} = {}^3/_2$. To ensure conservation of parity, $l_{f_e} = 2 \rightarrow \Pi_f = (-1)^{l_{fe}} = 1 = \Pi_i$. Therefore, the emitted electron is an d-wave electron, that resulted from a Coulomb interaction ($\Delta L = 0, \Delta S = 0$).

Since the $1s^2\,^1S$ final state is characterized by $S_{f_i} = 0$, and the free electron by $s_{f_e} = {}^1/_2$, then it appears that all the quartet states require a spin interaction mechanism ($\Delta S \neq 0$), for the required spin-flip.

F.2 Radiative transitions

In Table F.3 by Garstang [270], are the selection rules for electric dipole, magnetic dipole and electric quadrupole transitions. The notation used is as used above: L, S, and J are,

Table F.3: Selection Rules in atomic spectra. Table from Ref. [270]. Rules (1)-(3) are the rigorous selection rules while rules (4)-(6) are the approximate selection rules. Symbol $\nleftrightarrow$ indicates a forbidden transition.

	Electric Dipole	Magnetic Dipole	Electric Quadrupole
(1)	$\Delta J = 0, \pm 1$	$\Delta J = 0, \pm 1$	$\Delta J = 0, \pm 1, \pm 2$
	$(0 \nleftrightarrow 0)$	$(0 \nleftrightarrow 0)$	$(0 \nleftrightarrow 0, \frac{1}{2} \nleftrightarrow \frac{1}{2}, 0 \nleftrightarrow 1)$
(2)	$\Delta M = 0, \pm 1$	$\Delta M = 0, \pm 1$	$\Delta M = 0, \pm 1, \pm 2$
(3)	Parity change	No parity change	No parity change
(4)	One electron jump	No electron jump	One/no electron jump
	$\Delta l = \pm 1$	$\Delta l = 0$	$\Delta l = 0, \pm 2$
		$\Delta n = 0$	
(5)	$\Delta S = 0$	$\Delta S = 0$	$\Delta S = 0$
(6)	$\Delta L = 0, \pm 1$	$\Delta J = 0$	$\Delta J = 0, \pm 1, \pm 2$
	$(0 \nleftrightarrow 0)$		$(0 \nleftrightarrow 0, 0 \nleftrightarrow 1)$

respectively, the orbital, spin, and total angular momenta of the atomic state, M is the magnetic quantum number (component of J) and n is the principal quantum number. The parity is $\Pi = (-1)^{\sum_i l_i}$ where l_i is the orbital angular momentum of the i-th electron.

In most cases, the wavelengths λ of photons emitted/absorbed by an atom are much larger than its spatial dimensions. These electromagnetic transitions in atoms or molecules are treated in the Electric Dipole approximation [271]. The Selection Rules that arise in this approximation are presented in Table F.3, in the first column. Transitions that are not allowed through Electric Dipole transitions, can be made through higher-order approximations. Next order approximation leads to the Magnetic Dipole and the Electric Quadrupole Selection Rules, presented in the second and third column of Table F.3. However, transitions allowed by these are much weaker than Electric Dipole transitions.Therefore, the dominant transitions are these that are allowed by the Electric Dipole Selection Rules.

The allowed transitions of $1s2lnl'\,^{2,4}L$ states ($n > 2$) to lower-lying states, along with the respective Auger/radiative transition probabilities can provide insight to the formation of the KLL spectrum. Since capture to the $1s2s\,^{3}S$ can occur to $n > 2$, calculation of these transition probabilities can contribute to a better understanding of the time-dependence of the $1s2s2p\,^{2,4}P$ states.

Appendix G

The Carbon energy level diagram
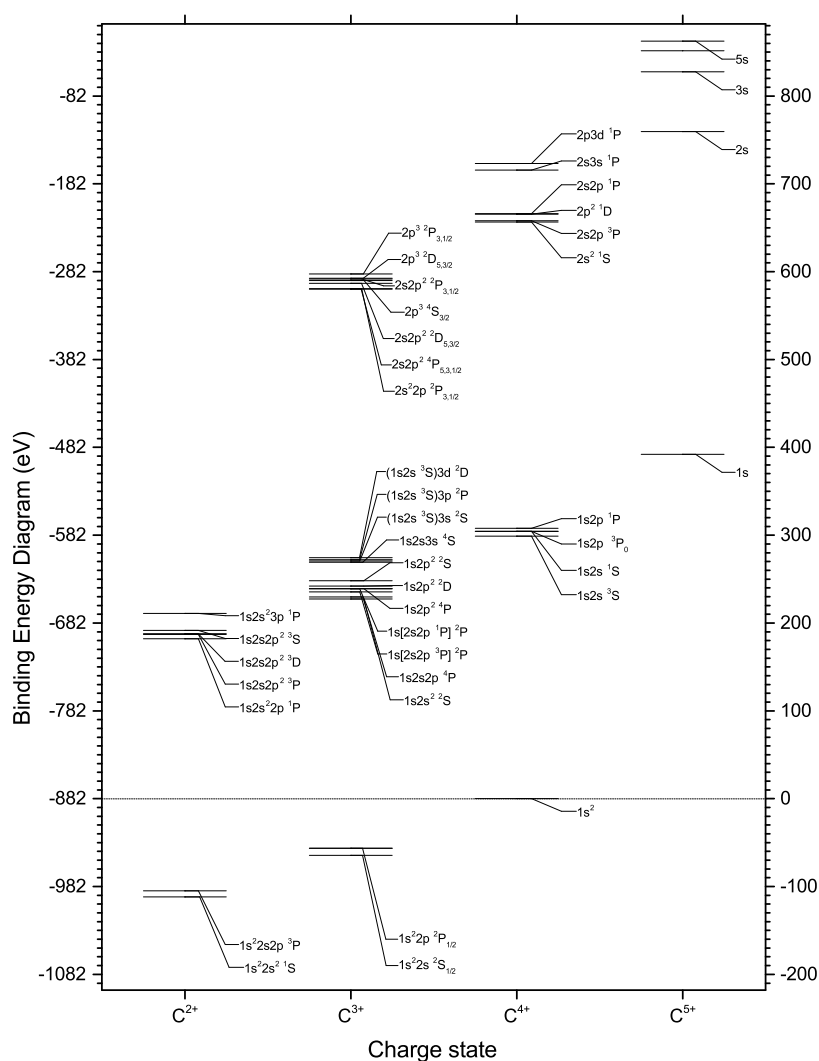
Figure G.1: The carbon energy level diagram. Values were obtained from [68, 155, 191, 235, 272–276].

Appendix H

1s2l2l' and 1s2l3l' spectrum of Li-like Carbon - C^{3+}

H.1 Introduction

This chapter summarizes the results of Chen [108] on calculations for the case of doubly-excited C^{3+}. Furthermore, additional Auger related parameters, such as ξ_A and lifetime are calculated. There have been extensive calculations and/or experimental validation for the various energy levels [68, 155, 191, 272–276] after the work of Chen. However, Ref. [108] was selected, as a consistent, full set of $1s2l2l'$ and $1s2l3l'$ configurations for the case of C^{3+}.

H.2 Formulas and definitions.

Table H.1: Binding Energy values, as obtained from NIST Database. Original source Ref. [277].

	Final state	NIST (eV)
	$1s^2$	-882.084
A	$1s^2 2s$	-946.577
B	$1s^2 2p$	-938.582
C	$1s^2 3s$	-909.029
D	$1s^2 3p$	-906.896
E	$1s^2 3d$	-906.297

All transition energies are converted to eV. Radiative rate $(A_r(if))$, total radiative rate $(A_r(i) = \sum_{f<i} A_r(if))$ and the Auger rate $(A_a(if))$ results are omitted. A total Auger rate $\left(A_a(i) = \sum_{f<i} A_a(if)\right)$ can also be defined, through the multiple Auger channels certain states exhibit. However, as stated in Table F.2, C^{3+} $1s2l2l'$ and $1s2l3l'$ states Auger decay exclusively to the $1s^2\,^1S$ state, therefore it is not needed. Although the mentioned quantities are omitted, they are still used to provide more Auger related parameters for each transition. The Auger yield ξ_A for each transition is defined by Eq. H.1:

$$\xi_A = \frac{A_a(if)}{A_r(i) + A_a(if)} \tag{H.1}$$

For the current study, an additional quantity was considered useful. Here, it is defined as PRDF. PRDF is the probability of the state under investigation to radiative de-excite to the respective "Final state". PRDF is defined by Eq. H.2:

$$\mathrm{PRDF} = \frac{A_r(if)}{\sum_{f<i} A_r(if)} \tag{H.2}$$

It represents the probability of every state to radiatively decay directly to the designated "Final state". These singly-excited states, although not ground states, cannot contribute

to neither a secondary Auger decay, nor to any cascading procedure. Therefore, the higher $\xi_A \times$ PRDF value a state presents, the less is its contribution to any cascading calculation. For example, the case of the transition $1s2s(^3S)3p\,^2P_{3/2} \to 1s^22s\,^2S_{1/2}$, with respective Auger energy 270.858 eV. With an Auger yield 60.94%, only $\approx \frac{2}{5}$ of the initial population decay radiatively. The PRDF value for this transition is 80.80%, which means only $\approx \frac{1}{5}$ does not decay directly to the ground state. This state can contribute only $\approx \frac{1}{5} \times \frac{2}{5} = \frac{2}{25} = 8\%$ of the initial population to any cascading procedure. The rest 92% of the initial population either Auger decays, or decays radiatively to the $1s^22s\,^2S_{1/2}$ state. However, it should be used carefully. There are many transitions, which begin with the same state, and result to various final, singly excited states. PRDF corresponds only to the particular final state. This is the reason the same states appear to have various PRDF values. In order to properly identify possible cascades, these PRDF values require to be summed.

The "Auger to $1s^2$" was calculated with respect to the NIST Binding Energy values found [277] for the various configurations listed as "Final state" in Table H.2. The "Auger to $1s^2$" energy is calculated by the following formula:

$$E_A = \lambda(\text{eV}) + (\text{Final state})_{B.E.} - \left(1s^2\right)_{B.E.} \tag{H.3}$$

Again, according to Badnell *et al* [269] all initial states in Table H.2 are expected to Auger decay to the $1s^2\,^1S$ state, so no summation of Auger rates is needed. The binding energies for the various final states are given in Table H.1. Finally, the lifetime of every initial state was calculated with the use of the following formula:

$$\text{Lifetime (ns)} = \frac{10^9}{A_a(i) + \sum_{f<i} A_r(if)} \tag{H.4}$$

considering that the rates provided by Chen were defined in s^{-1}.

H.3 Tabulated KLL/KLM transitions

As seen by Eq. H.3, the Auger energies stated in this appendix were not calculated in Ref. [108]. They were extracted with the use of the transition energies obtained from Ref. [108] and base energies as taken from NIST Database. This leads to two remarks:

- First of all the calculated energies for the $1s2l2l$ transitions do not exactly match the values used in this thesis. This is because the values in this thesis are based on the results of the work of Bruch *et al* [235]. The method used there relied on a combination of accurate $1s2s2p\,^4P$ determination combined with experimental data. $1s2s2p\,^4P$, with lifetimes in the ns regime, is characterised by a small natural line width, ≈ 0.223 µeV. Regarding states with sub-states with significantly different lifetimes, line width is calculated using the shorter lifetime. Therefore, in Bruch *et al* [235], $1s2s2p\,^4P$ was used as a calibration point due to its experimental determination accuracy. Work of Chen [108] is purely computational, using a multi-configuration Dirac-Fock model. These differences are especially seen in the case of $1s2s2p\,^4P$ where these two publications differ by a factor of ≈ 0.923 eV.

- The second is the fact that for every Initial State, only one Auger energy to $1s^2$ should be expected. However, for most cases, more than one transition energies were used to investigate the Auger to $1s^2$ value. This is not meant to imply that there are many possible Auger energies. This is just the result of different calculation methods,

along with multiple reference points for the *indirect* calculation of Auger energy in question. In any case, standard deviation of calculated Auger values for every state does not exceed 0.077 eV.

This list of Auger energies is not meant to serve as an accurate determination of energy levels. It's purpose is to function as a map to resolve lines appearing in experimental spectra, or to determine the contribution of various states to cascading procedures. For example, the $2s2p\,^{3,1}P$ states, produced by C^{4+} + target collisional excitations, Auger decay with characteristic energies 266 and 274 eV. As seen in Table H.2, there are various lines whose energies are in the vicinity of the $2s2p\,^{3,1}P$ lines. However, the combination of ξ_A and PRDF can rule certain possibilities out, and lead to a more in-depth line determination.

Table H.2: Dielectronic spectrum of Li-like Carbon - C^{3+}, obtained by Chen [108]. λ denotes the emitted photon energy for a radiative transition, ξ_A is the auto-ionization probability for the initial state, PRDF is the Probability of a Radiative decay Directly to Final. Auger to $1s^2$ is the expected Auger energy in the event of auto-ionization. Results are ordered with respect to the expected Auger energy.

Initial state	Final state	λ(Å)	λ(eV)	ξ_A	PRDF	Auger to $1s^2$ (eV)	Lifetime (ns)
$1s2s^2\ ^2S_{1/2}$	$1s^22p\ ^2P_{3/2}$	43.9390	282.173	99.96%	66.32%	225.688	1.336E-05
$1s2s^2\ ^2S_{1/2}$	$1s^22p\ ^2P_{1/2}$	43.9370	282.186	99.96%	33.44%	225.688	1.336E-05
$1s2s^2\ ^2S_{1/2}$	$1s^23p\ ^2P_{3/2}$	49.4656	250.647	99.96%	0.02%	225.839	1.336E-05
$1s2s^2\ ^2S_{1/2}$	$1s^23p\ ^2P_{1/2}$	49.4648	250.651	99.96%	0.01%	225.839	1.336E-05
$1s2s(^3S)2p\ ^4P_{1/2}$	$1s^22s\ ^2S_{1/2}$	42.3073	293.056	99.54%	100.00%	228.563	3.130E+00
$1s2s(^3S)2p\ ^4P_{3/2}$	$1s^22s\ ^2S_{1/2}$	42.3073	293.056	97.40%	100.00%	228.563	7.609E+00
$1s2s(^3S)2p\ ^2P_{1/2}$	$1s^22s\ ^2S_{1/2}$	41.4774	298.920	96.79%	99.80%	234.426	6.584E-05
$1s2s(^3S)2p\ ^2P_{3/2}$	$1s^22s\ ^2S_{1/2}$	41.4752	298.936	96.69%	99.80%	234.442	6.761E-05
$1s2s(^3S)2p\ ^2P_{1/2}$	$1s^23s\ ^2S_{1/2}$	47.4199	261.460	96.79%	0.16%	234.515	6.584E-05
$1s2s(^3S)2p\ ^2P_{3/2}$	$1s^23s\ ^2S_{1/2}$	47.4170	261.476	96.69%	0.16%	234.531	6.761E-05
$1s2s(^3S)2p\ ^2P_{1/2}$	$1s^23d\ ^2D_{3/2}$	47.9173	258.746	96.79%	0.05%	234.533	6.584E-05
$1s2s(^3S)2p\ ^2P_{3/2}$	$1s^23d\ ^2D_{5/2}$	47.9147	258.760	96.69%	0.04%	234.548	6.761E-05
$1s2s(^3S)2p\ ^2P_{3/2}$	$1s^23d\ ^2D_{3/2}$	47.9145	258.761	96.69%	0.00%	234.548	6.761E-05
$1s2p^2\ ^4P_{3/2}$	$1s^22p\ ^2P_{3/2}$	42.0997	294.501	3.06%	0.56%	238.016	1.443E+00
$1s2p^2\ ^4P_{1/2}$	$1s^22p\ ^2P_{1/2}$	42.0992	294.505	0.63%	0.29%	238.006	1.485E+00
$1s2p^2\ ^4P_{5/2}$	$1s^22p\ ^2P_{3/2}$	42.0992	294.505	56.06%	0.50%	238.020	6.549E-01
$1s2p^2\ ^4P_{3/2}$	$1s^22p\ ^2P_{1/2}$	42.0979	294.514	3.06%	0.06%	238.015	1.443E+00
$1s2s(^1S)2p\ ^2P_{3/2}$	$1s^22s\ ^2S_{1/2}$	40.8643	303.405	99.75%	97.58%	238.911	2.584E-05
$1s2s(^1S)2p\ ^2P_{1/2}$	$1s^22s\ ^2S_{1/2}$	40.8636	303.410	99.75%	97.62%	238.916	2.584E-05
$1s2s(^1S)2p\ ^2P_{3/2}$	$1s^23s\ ^2S_{1/2}$	46.6202	265.945	99.75%	0.11%	239.000	2.584E-05
$1s2s(^1S)2p\ ^2P_{1/2}$	$1s^23s\ ^2S_{1/2}$	46.6191	265.951	99.75%	0.11%	239.006	2.584E-05
$1s2s(^1S)2p\ ^2P_{3/2}$	$1s^23d\ ^2D_{5/2}$	47.1012	263.229	99.75%	0.99%	239.017	2.584E-05
$1s2s(^1S)2p\ ^2P_{3/2}$	$1s^23d\ ^2D_{3/2}$	47.1010	263.230	99.75%	0.11%	239.017	2.584E-05
$1s2s(^1S)2p\ ^2P_{1/2}$	$1s^23d\ ^2D_{3/2}$	47.1000	263.236	99.75%	1.07%	239.023	2.584E-05
$1s2p^2\ ^2D_{5/2}$	$1s^22p\ ^2P_{3/2}$	41.5330	298.520	99.70%	99.64%	242.035	1.070E-05
$1s2p^2\ ^2D_{3/2}$	$1s^22p\ ^2P_{3/2}$	41.5309	298.535	99.70%	15.09%	242.050	1.071E-05
$1s2p^2\ ^2D_{3/2}$	$1s^22p\ ^2P_{1/2}$	41.5291	298.548	99.70%	84.59%	242.049	1.071E-05
$1s2p^2\ ^2D_{5/2}$	$1s^22p\ ^2P_{3/2}$	46.4370	266.994	99.70%	0.16%	242.186	1.070E-05
$1s2p^2\ ^2D_{3/2}$	$1s^22p\ ^2P_{3/2}$	46.4344	267.009	99.70%	0.02%	242.201	1.071E-05
$1s2p^2\ ^2D_{3/2}$	$1s^22p\ ^2P_{1/2}$	46.4337	267.013	99.70%	0.13%	242.201	1.071E-05
$1s2p^2\ ^2P_{1/2}$	$1s^22p\ ^2P_{3/2}$	41.4065	299.432	0.06%	33.03%	242.947	1.154E-03
$1s2p^2\ ^2P_{1/2}$	$1s^22p\ ^2P_{1/2}$	41.4048	299.444	0.06%	66.40%	242.945	1.154E-03
$1s2p^2\ ^2P_{3/2}$	$1s^22p\ ^2P_{3/2}$	41.4041	299.449	1.12%	83.49%	242.964	1.142E-03
$1s2p^2\ ^2P_{3/2}$	$1s^22p\ ^2P_{1/2}$	41.4023	299.462	1.12%	16.05%	242.964	1.142E-03
$1s2p^2\ ^2P_{1/2}$	$1s^22p\ ^2P_{3/2}$	46.2791	267.905	0.06%	0.12%	243.097	1.154E-03
$1s2p^2\ ^2P_{1/2}$	$1s^22p\ ^2P_{1/2}$	46.2784	267.909	0.06%	0.25%	243.097	1.154E-03
$1s2p^2\ ^2P_{3/2}$	$1s^22p\ ^2P_{3/2}$	46.2760	267.923	1.12%	0.31%	243.115	1.142E-03
$1s2p^2\ ^2P_{3/2}$	$1s^22p\ ^2P_{1/2}$	46.2753	267.927	1.12%	0.06%	243.115	1.142E-03
$1s2p^2\ ^2S_{1/2}$	$1s^22p\ ^2P_{3/2}$	40.6033	305.355	98.62%	66.27%	248.870	5.419E-05
$1s2p^2\ ^2S_{1/2}$	$1s^22p\ ^2P_{1/2}$	40.6016	305.368	98.62%	32.59%	248.869	5.419E-05
$1s2p^2\ ^2S_{1/2}$	$1s^23p\ ^2P_{3/2}$	45.2779	273.829	98.62%	0.27%	249.021	5.419E-05
$1s2p^2\ ^2S_{1/2}$	$1s^22p\ ^2P_{1/2}$	45.2773	273.833	98.62%	0.13%	249.021	5.419E-05
$1s2s(^3S)3s\ ^2S_{1/2}$	$1s^22p\ ^2P_{3/2}$	38.0249	326.061	99.95%	28.24%	269.575	5.179E-05
$1s2s(^3S)3s\ ^2S_{1/2}$	$1s^22p\ ^2P_{1/2}$	38.0235	326.073	99.95%	14.29%	269.574	5.179E-05
$1s2s(^3S)3s\ ^2S_{1/2}$	$1s^23p\ ^2P_{3/2}$	42.0950	294.534	99.95%	0.23%	269.726	5.179E-05
$1s2s(^3S)3s\ ^2S_{1/2}$	$1s^22p\ ^2P_{1/2}$	42.0945	294.538	99.95%	0.13%	269.725	5.179E-05
$1s2s(^3S)3p\ ^4P_{1/2}$	$1s^22s\ ^2S_{1/2}$	37.0026	335.069	18.84%	3.92%	270.575	7.657E+00
$1s2s(^3S)3p\ ^4P_{3/2}$	$1s^22s\ ^2S_{1/2}$	37.0025	335.070	0.01%	11.78%	270.576	8.474E+00
$1s2s(^3S)3p\ ^4P_{3/2}$	$1s^23s\ ^2S_{1/2}$	41.6599	297.610	0.01%	0.53%	270.665	8.474E+00
$1s2s(^3S)3p\ ^2P_{3/2}$	$1s^22s\ ^2S_{1/2}$	36.9714	335.352	60.94%	80.80%	270.858	3.125E-03
$1s2s(^3S)3p\ ^2P_{1/2}$	$1s^22s\ ^2S_{1/2}$	36.9710	335.355	60.06%	80.80%	270.862	3.195E-03
$1s2s(^3S)3p\ ^2P_{3/2}$	$1s^23s\ ^2S_{1/2}$	41.6205	297.892	60.94%	7.24%	270.947	3.125E-03
$1s2s(^3S)3p\ ^2P_{1/2}$	$1s^23s\ ^2S_{1/2}$	41.6200	297.896	60.06%	7.10%	270.951	3.195E-03
$1s2s(^3S)3p\ ^2P_{3/2}$	$1s^23d\ ^2D_{5/2}$	42.0035	295.176	60.94%	0.04%	270.964	3.125E-03

144

Initial state	Final state	λ(Å)	λ(eV)	ξ_A	PRDF	Auger to $1s^2$ (eV)	Lifetime (ns)
$1s2s(^3S)3p\ ^2P_{3/2}$	$1s^23d\ ^2D_{3/2}$	42.0033	295.177	60.94%	0.00%	270.964	3.125E-03
$1s2s(^3S)3p\ ^2P_{1/2}$	$1s^23d\ ^2D_{3/2}$	42.0028	295.181	60.06%	0.04%	270.967	3.195E-03
$1s2s(^1S)3s\ ^2S_{1/2}$	$1s^22p\ ^2P_{3/2}$	37.6195	329.574	99.35%	2.19%	273.089	1.082E-04
$1s2s(^1S)3s\ ^2S_{1/2}$	$1s^22p\ ^2P_{1/2}$	37.6181	329.587	99.35%	1.12%	273.088	1.082E-04
$1s2s(^1S)3s\ ^2S_{1/2}$	$1s^23p\ ^2P_{3/2}$	41.5987	298.048	99.35%	55.78%	273.240	1.082E-04
$1s2s(^1S)3s\ ^2S_{1/2}$	$1s^23p\ ^2P_{1/2}$	41.5982	298.052	99.35%	28.14%	273.239	1.082E-04
$1s2s(^3S)3d\ ^2D_{3/2}$	$1s^22p\ ^2P_{3/2}$	37.5844	329.882	98.85%	4.95%	273.397	2.315E-04
$1s2s(^3S)3d\ ^2D_{5/2}$	$1s^22p\ ^2P_{3/2}$	37.5844	329.882	99.08%	37.37%	273.397	2.320E-04
$1s2s(^3S)3d\ ^2D_{3/2}$	$1s^22p\ ^2P_{1/2}$	37.5829	329.895	99.08%	31.23%	273.397	2.320E-04
$1s2s(^3S)3d\ ^2D_{5/2}$	$1s^23p\ ^2P_{3/2}$	41.5559	298.355	99.17%	4.29%	273.547	2.101E-04
$1s2s(^3S)3d\ ^2D_{3/2}$	$1s^23p\ ^2P_{3/2}$	41.5558	298.356	99.08%	0.74%	273.547	2.320E-04
$1s2s(^3S)3d\ ^2D_{3/2}$	$1s^22p\ ^2P_{1/2}$	41.5552	298.360	99.08%	3.65%	273.548	2.320E-04
$1s2p(^3P)3s\ ^4P_{1/2}$	$1s^22s\ ^2S_{1/2}$	36.5629	339.098	2.37%	0.01%	274.605	1.421E-01
$1s2p(^3P)3s\ ^4P_{3/2}$	$1s^22s\ ^2S_{1/2}$	36.5627	339.100	1.41%	0.13%	274.607	1.431E-01
$1s2p(^3P)3s\ ^4P_{1/2}$	$1s^23s\ ^2S_{1/2}$	41.1035	301.639	2.37%	0.09%	274.694	1.421E-01
$1s2p(^3P)3s\ ^4P_{3/2}$	$1s^23s\ ^2S_{1/2}$	41.1032	301.641	1.27%	0.24%	274.696	1.433E-01
$1s2p(^3P)3s\ ^4P_{3/2}$	$1s^23d\ ^2D_{5/2}$	41.4767	298.925	1.41%	0.01%	274.713	1.431E-01
$1s2s(^1S)3p\ ^2P_{1/2}$	$1s^22s\ ^2S_{1/2}$	36.5005	339.678	94.07%	64.96%	275.185	4.900E-04
$1s2s(^1S)3p\ ^2P_{3/2}$	$1s^22s\ ^2S_{1/2}$	36.5001	339.682	93.91%	64.43%	275.188	4.995E-04
$1s2s(^1S)3p\ ^2P_{1/2}$	$1s^23s\ ^2S_{1/2}$	41.0248	302.218	94.07%	16.45%	275.273	4.900E-04
$1s2s(^1S)3p\ ^2P_{3/2}$	$1s^23s\ ^2S_{1/2}$	41.0242	302.222	93.91%	16.72%	275.277	4.995E-04
$1s2s(^1S)3p\ ^2P_{1/2}$	$1s^23d\ ^2D_{3/2}$	41.3966	299.503	94.07%	16.20%	275.290	4.900E-04
$1s2s(^1S)3p\ ^2P_{3/2}$	$1s^23d\ ^2D_{5/2}$	41.3962	299.506	93.91%	14.43%	275.294	4.995E-04
$1s2s(^1S)3p\ ^2P_{3/2}$	$1s^23d\ ^2D_{3/2}$	41.3961	299.507	93.91%	1.60%	275.293	4.995E-04
$1s2p(^3P)3p\ ^4D_{1/2}$	$1s^22p\ ^2P_{3/2}$	37.2621	332.735	0.00%	10.04%	276.250	3.676E-01
$1s2p(^3P)3p\ ^4D_{3/2}$	$1s^22p\ ^2P_{3/2}$	37.2619	332.737	0.73%	32.02%	276.252	2.606E-01
$1s2p(^3P)3p\ ^4D_{5/2}$	$1s^22p\ ^2P_{3/2}$	37.2613	332.743	12.58%	0.03%	276.257	6.289E-01
$1s2p(^3P)3p\ ^4D_{1/2}$	$1s^22p\ ^2P_{1/2}$	37.2606	332.749	0.00%	19.71%	276.250	3.676E-01
$1s2p(^3P)3p\ ^4D_{3/2}$	$1s^22p\ ^2P_{1/2}$	37.2605	332.750	0.73%	6.51%	276.251	2.606E-01
$1s2p(^3P)3p\ ^2P_{3/2}$	$1s^22p\ ^2P_{3/2}$	37.2549	332.800	0.04%	52.60%	276.315	6.846E-03
$1s2p(^3P)3p\ ^2P_{1/2}$	$1s^22p\ ^2P_{3/2}$	37.2548	332.801	0.02%	21.16%	276.315	6.848E-03
$1s2p(^3P)3p\ ^2P_{3/2}$	$1s^22p\ ^2P_{1/2}$	37.2534	332.813	0.04%	10.75%	276.315	6.846E-03
$1s2p(^3P)3p\ ^2P_{1/2}$	$1s^22p\ ^2P_{1/2}$	37.2533	332.814	0.02%	43.01%	276.315	6.848E-03
$1s2s(^1S)3d\ ^2D_{3/2}$	$1s^23p\ ^2P_{3/2}$	41.1710	301.144	4.78%	12.69%	276.336	7.106E-03
$1s2p(^3P)3p\ ^4D_{1/2}$	$1s^23p\ ^2P_{3/2}$	41.1622	301.209	0.00%	5.50%	276.400	3.690E-01
$1s2p(^3P)3p\ ^4D_{3/2}$	$1s^23p\ ^2P_{3/2}$	41.1619	301.211	0.73%	14.80%	276.403	2.606E-01
$1s2p(^3P)3p\ ^4D_{1/2}$	$1s^23p\ ^2P_{1/2}$	41.1616	301.213	0.00%	10.99%	276.401	3.676E-01
$1s2p(^3P)3p\ ^4D_{3/2}$	$1s^23p\ ^2P_{1/2}$	41.1614	301.215	0.73%	5.49%	276.402	2.606E-01
$1s2p(^3P)3p\ ^4D_{5/2}$	$1s^23p\ ^2P_{3/2}$	41.1611	301.217	12.58%	0.96%	276.408	6.289E-01
$1s2p(^3P)3p\ ^2P_{1/2}$	$1s^23p\ ^2P_{3/2}$	41.1533	301.274	0.02%	9.25%	276.466	6.848E-03
$1s2p(^3P)3p\ ^2P_{3/2}$	$1s^23p\ ^2P_{3/2}$	41.1533	301.274	0.04%	23.77%	276.466	6.846E-03
$1s2p(^3P)3p\ ^2P_{3/2}$	$1s^23p\ ^2P_{1/2}$	41.1529	301.277	0.04%	5.03%	276.465	6.846E-03
$1s2p(^3P)3p\ ^2P_{1/2}$	$1s^23p\ ^2P_{1/2}$	41.1527	301.278	0.02%	19.25%	276.466	6.848E-03
$1s2p(^3P)3p\ ^4S_{3/2}$	$1s^22p\ ^2P_{3/2}$	37.1760	333.506	0.42%	0.17%	277.021	1.302E-01
$1s2p(^3P)3p\ ^4S_{3/2}$	$1s^22p\ ^2P_{1/2}$	37.1746	333.519	0.42%	0.07%	277.020	1.302E-01
$1s2p(^3P)3s\ ^2P_{1/2}$	$1s^22s\ ^2S_{1/2}$	36.2987	341.566	99.66%	0.07%	277.073	4.314E-05
$1s2p(^3P)3s\ ^2P_{3/2}$	$1s^22s\ ^2S_{1/2}$	36.2963	341.589	99.67%	0.08%	277.096	4.334E-05
$1s2p(^3P)3p\ ^4P_{1/2}$	$1s^22p\ ^2P_{3/2}$	37.1606	333.644	0.01%	0.01%	277.159	1.748E-01
$1s2p(^3P)3p\ ^4P_{3/2}$	$1s^22p\ ^2P_{3/2}$	37.1599	333.651	0.76%	0.01%	277.165	1.729E-01
$1s2p(^3P)3p\ ^4P_{1/2}$	$1s^22p\ ^2P_{1/2}$	37.1592	333.657	0.01%	0.04%	277.158	1.748E-01
$1s2p(^3P)3p\ ^2P_{1/2}$	$1s^23s\ ^2S_{1/2}$	40.7698	304.108	99.66%	90.74%	277.163	4.314E-05
$1s2p(^3P)3p\ ^4P_{3/2}$	$1s^22p\ ^2P_{1/2}$	37.1584	333.664	0.76%	0.06%	277.165	1.729E-01
$1s2p(^3P)3p\ ^4S_{3/2}$	$1s^23p\ ^2P_{1/2}$	41.0567	301.983	0.42%	0.01%	277.170	1.302E-01
$1s2p(^3P)3s\ ^2P_{1/2}$	$1s^23d\ ^2D_{3/2}$	41.1370	301.393	99.66%	0.78%	277.180	4.314E-05
$1s2p(^3P)3s\ ^2P_{3/2}$	$1s^23s\ ^2S_{1/2}$	40.7670	304.129	99.67%	90.37%	277.184	4.334E-05
$1s2p(^3P)3s\ ^2P_{3/2}$	$1s^23d\ ^2D_{5/2}$	41.1343	301.413	99.67%	0.71%	277.201	4.334E-05
$1s2p(^3P)3s\ ^2P_{3/2}$	$1s^23d\ ^2D_{3/2}$	41.1342	301.414	99.67%	0.08%	277.200	4.334E-05
$1s2s(^1S)3d\ ^2D_{3/2}$	$1s^22p\ ^2P_{3/2}$	37.1432	333.801	4.78%	1.37%	277.315	7.106E-03
$1s2p(^3P)3p\ ^4P_{1/2}$	$1s^23p\ ^2P_{3/2}$	41.0383	302.118	0.01%	0.04%	277.310	1.748E-01

Initial state	Final state	λ(Å)	λ(eV)	ξ_A	PRDF	Auger to $1s^2$ (eV)	Lifetime (ns)
$1s2s(^1S)3d\ ^2D_{5/2}$	$1s^22p\ ^2P_{3/2}$	37.1425	333.807	1.21%	7.45%	277.322	7.541E-03
$1s2p(^3P)3p\ ^4P_{1/2}$	$1s^23p\ ^2P_{1/2}$	41.0378	302.122	0.01%	0.03%	277.310	1.748E-01
$1s2p(^3P)3p\ ^4P_{3/2}$	$1s^23p\ ^2P_{3/2}$	41.0374	302.125	0.76%	0.12%	277.316	1.729E-01
$1s2s(^1S)3d\ ^2D_{3/2}$	$1s^22p\ ^2P_{1/2}$	37.1418	333.813	4.78%	6.48%	277.315	7.106E-03
$1s2p(^3P)3p\ ^4P_{3/2}$	$1s^23p\ ^2P_{1/2}$	41.0370	302.128	0.76%	0.13%	277.315	1.729E-01
$1s2p(^3P)3p\ ^4P_{5/2}$	$1s^23p\ ^2P_{3/2}$	41.0370	302.128	9.26%	0.72%	277.319	1.575E-01
$1s2s(^1S)3d\ ^2D_{3/2}$	$1s^23p\ ^2P_{1/2}$	41.0166	302.278	4.78%	57.54%	277.466	7.106E-03
$1s2s(^1S)3d\ ^2D_{5/2}$	$1s^23p\ ^2P_{3/2}$	41.0162	302.281	1.21%	69.92%	277.473	7.541E-03
$1s2p(^3P)3d\ ^4F_{3/2}$	$1s^23d\ ^2D_{5/2}$	41.0436	302.079	4.65%	5.07%	277.867	1.555E+01
$1s2p(^3P)3d\ ^4F_{3/2}$	$1s^23d\ ^2D_{3/2}$	41.0434	302.081	4.65%	42.74%	277.867	1.555E+01
$1s2p(^3P)3d\ ^4F_{5/2}$	$1s^23d\ ^2D_{5/2}$	41.0434	302.081	28.10%	25.69%	277.868	6.596E+00
$1s2p(^3P)3d\ ^4F_{5/2}$	$1s^23d\ ^2D_{3/2}$	41.0432	302.082	28.10%	16.24%	277.869	6.596E+00
$1s2p(^3P)3d\ ^4F_{7/2}$	$1s^23d\ ^2D_{5/2}$	41.0427	302.086	71.83%	32.72%	277.874	1.323E+01
$1s2p(^3P)3d\ ^2D_{3/2}$	$1s^23s\ ^2S_{1/2}$	40.6650	304.892	0.44%	0.01%	277.947	4.291E-02
$1s2p(^3P)3d\ ^2D_{3/2}$	$1s^23d\ ^2D_{5/2}$	41.0305	302.176	0.44%	2.38%	277.963	4.291E-02
$1s2p(^3P)3d\ ^2D_{3/2}$	$1s^23d\ ^2D_{3/2}$	41.0303	302.177	0.44%	25.91%	277.964	4.291E-02
$1s2p(^3P)3d\ ^2D_{5/2}$	$1s^23d\ ^2D_{5/2}$	41.0303	302.177	0.04%	26.61%	277.965	4.290E-02
$1s2p(^3P)3d\ ^2D_{5/2}$	$1s^23d\ ^2D_{3/2}$	41.0302	302.178	0.04%	2.47%	277.964	4.290E-02
$1s2p(^3P)3p\ ^2D_{3/2}$	$1s^22p\ ^2P_{3/2}$	37.0373	334.755	99.28%	14.47%	278.270	4.728E-05
$1s2p(^3P)3p\ ^2D_{5/2}$	$1s^22p\ ^2P_{3/2}$	37.0360	334.767	99.29%	87.50%	278.282	4.662E-05
$1s2p(^3P)3p\ ^2D_{3/2}$	$1s^22p\ ^2P_{1/2}$	37.0359	334.768	99.28%	73.03%	278.269	4.728E-05
$1s2p(^3P)3p\ ^2D_{3/2}$	$1s^23p\ ^2P_{3/2}$	40.8880	303.229	99.28%	1.97%	278.420	4.728E-05
$1s2p(^3P)3p\ ^2D_{3/2}$	$1s^23p\ ^2P_{1/2}$	40.8874	303.233	99.28%	8.68%	278.421	4.728E-05
$1s2p(^3P)3p\ ^2D_{5/2}$	$1s^23p\ ^2P_{3/2}$	40.8864	303.241	99.29%	10.33%	278.432	4.662E-05
$1s2p(^3P)3d\ ^4D_{1/2}$	$1s^23s\ ^2S_{1/2}$	40.5678	305.622	0.28%	0.03%	278.677	2.681E-02
$1s2p(^3P)3d\ ^4D_{3/2}$	$1s^23s\ ^2S_{1/2}$	40.5674	305.625	0.21%	0.02%	278.680	2.683E-02
$1s2p(^3P)3d\ ^4D_{1/2}$	$1s^23d\ ^2D_{3/2}$	40.9314	302.907	0.28%	0.03%	278.694	2.681E-02
$1s2p(^3P)3d\ ^4D_{3/2}$	$1s^23d\ ^2D_{5/2}$	40.9312	302.909	0.21%	0.01%	278.697	2.683E-02
$1s2p(^3P)3d\ ^4D_{3/2}$	$1s^23d\ ^2D_{3/2}$	40.9310	302.910	0.21%	0.01%	278.697	2.683E-02
$1s2p(^3P)3d\ ^4D_{5/2}$	$1s^23d\ ^2D_{5/2}$	40.9308	302.912	0.01%	0.01%	278.699	2.695E-02
$1s2p(^3P)3d\ ^4D_{5/2}$	$1s^23d\ ^2D_{3/2}$	40.9306	302.913	0.01%	0.01%	278.700	2.695E-02
$1s2p(^3P)3d\ ^4D_{7/2}$	$1s^23d\ ^2D_{5/2}$	40.9306	302.913	0.11%	0.02%	278.701	2.692E-02
$1s2p(^1P)3p\ ^2D_{3/2}$	$1s^23s\ ^2S_{1/2}$	40.5645	305.647	97.46%	82.71%	278.702	4.533E-05
$1s2p(^1P)3s\ ^2P_{3/2}$	$1s^22s\ ^2S_{1/2}$	36.1086	343.365	83.94%	0.37%	278.871	2.925E-04
$1s2p(^1P)3s\ ^2P_{1/2}$	$1s^22s\ ^2S_{1/2}$	36.1076	343.374	84.45%	0.38%	278.881	2.843E-04
$1s2p(^1P)3s\ ^2P_{3/2}$	$1s^23s\ ^2S_{1/2}$	40.5303	305.905	83.94%	93.44%	278.960	2.925E-04
$1s2p(^1P)3s\ ^2P_{1/2}$	$1s^23s\ ^2S_{1/2}$	40.5291	305.914	84.45%	93.42%	278.969	2.843E-04
$1s2p(^1P)3s\ ^2P_{3/2}$	$1s^23d\ ^2D_{5/2}$	40.8934	303.189	83.94%	3.84%	278.977	2.925E-04
$1s2p(^1P)3s\ ^2P_{3/2}$	$1s^23d\ ^2D_{3/2}$	40.8932	303.190	83.94%	0.41%	278.977	2.925E-04
$1s2p(^1P)3s\ ^2P_{1/2}$	$1s^23d\ ^2D_{3/2}$	40.8920	303.199	84.45%	4.20%	278.986	2.843E-04
$1s2p(^1P)3d\ ^2D_{3/2}$	$1s^23s\ ^2S_{1/2}$	40.4865	306.236	0.00%	9.37%	279.291	1.439E-03
$1s2p(^3P)3d\ ^2F_{5/2}$	$1s^23d\ ^2D_{5/2}$	40.8451	303.547	9.98%	6.19%	279.335	8.183E-03
$1s2p(^3P)3d\ ^2F_{5/2}$	$1s^23d\ ^2D_{3/2}$	40.8450	303.548	9.98%	78.91%	279.334	8.183E-03
$1s2p(^3P)3d\ ^2F_{7/2}$	$1s^23d\ ^2D_{5/2}$	40.8423	303.568	8.86%	85.56%	279.356	8.439E-03
$1s2p(^3P)3d\ ^4P_{3/2}$	$1s^23s\ ^2S_{1/2}$	40.4774	306.305	0.70%	0.15%	279.360	5.041E-02
$1s2p(^3P)3d\ ^4P_{1/2}$	$1s^23s\ ^2S_{1/2}$	40.4768	306.309	0.17%	0.05%	279.364	5.068E-02
$1s2p(^3P)3d\ ^4P_{5/2}$	$1s^23d\ ^2D_{5/2}$	40.8402	303.584	0.22%	0.01%	279.371	4.989E-02
$1s2p(^3P)3d\ ^4P_{5/2}$	$1s^23d\ ^2D_{3/2}$	40.8400	303.585	0.22%	1.46%	279.372	4.989E-02
$1s2p(^3P)3d\ ^4P_{3/2}$	$1s^23d\ ^2D_{3/2}$	40.8394	303.590	0.70%	0.01%	279.376	5.041E-02
$1s2p(^3P)3p\ ^2S_{1/2}$	$1s^22p\ ^2P_{3/2}$	36.8823	336.162	82.11%	28.42%	279.677	4.888E-04
$1s2p(^3P)3p\ ^2S_{1/2}$	$1s^22p\ ^2P_{1/2}$	36.8809	336.175	82.11%	14.43%	279.676	4.888E-04
$1s2p(^3P)3p\ ^2S_{1/2}$	$1s^23p\ ^2P_{3/2}$	40.6991	304.636	82.11%	37.70%	279.828	4.888E-04
$1s2p(^3P)3p\ ^2S_{1/2}$	$1s^23p\ ^2P_{1/2}$	40.6986	304.640	82.11%	17.73%	279.828	4.888E-04
$1s2p(^3P)3d\ ^2P_{3/2}$	$1s^22s\ ^2S_{1/2}$	35.9526	344.855	47.20%	0.01%	280.361	6.431E-03
$1s2p(^3P)3d\ ^2P_{1/2}$	$1s^22s\ ^2S_{1/2}$	35.9515	344.865	48.50%	0.01%	280.372	6.373E-03
$1s2p(^3P)3d\ ^2P_{3/2}$	$1s^23s\ ^2S_{1/2}$	40.3338	307.395	47.51%	54.93%	280.450	6.394E-03
$1s2p(^3P)3d\ ^2P_{1/2}$	$1s^23s\ ^2S_{1/2}$	40.3324	307.406	48.50%	54.70%	280.461	6.373E-03
$1s2p(^3P)3d\ ^2P_{3/2}$	$1s^23d\ ^2D_{5/2}$	40.6934	304.679	47.20%	20.58%	280.467	6.431E-03
$1s2p(^3P)3d\ ^2P_{3/2}$	$1s^23d\ ^2D_{3/2}$	40.6931	304.681	47.20%	1.64%	280.468	6.431E-03

Initial state	Final state	λ(Å)	λ(eV)	ξ_A	PRDF	Auger to $1s^2$ (eV)	Lifetime (ns)
$1s2p(^3P)3d\ ^2P_{1/2}$	$1s^23d\ ^2D_{3/2}$	40.6918	304.691	48.50%	22.03%	280.477	6.373E-03
$1s2p(^1P)3p\ ^2D_{5/2}$	$1s^22p\ ^2P_{3/2}$	36.7726	337.165	97.42%	0.56%	280.679	4.574E-05
$1s2p(^1P)3p\ ^2D_{3/2}$	$1s^22p\ ^2P_{3/2}$	36.7720	337.170	97.46%	0.13%	280.685	4.533E-05
$1s2p(^1P)3p\ ^2D_{3/2}$	$1s^22p\ ^2P_{1/2}$	36.7706	337.183	97.81%	0.39%	280.684	3.897E-05
$1s2p(^1P)3p\ ^2D_{5/2}$	$1s^23p\ ^2P_{3/2}$	40.5656	305.639	97.42%	98.05%	280.830	4.574E-05
$1s2p(^1P)3p\ ^2D_{3/2}$	$1s^23p\ ^2P_{3/2}$	40.5649	305.644	97.46%	15.29%	280.836	4.533E-05
$1s2p(^1P)3p\ ^2P_{1/2}$	$1s^22p\ ^2P_{3/2}$	36.7533	337.342	0.02%	5.88%	280.856	1.324E-03
$1s2p(^1P)3p\ ^2P_{3/2}$	$1s^22p\ ^2P_{3/2}$	36.7524	337.350	0.64%	14.46%	280.865	1.318E-03
$1s2p(^1P)3p\ ^2P_{1/2}$	$1s^22p\ ^2P_{1/2}$	36.7520	337.354	0.02%	11.40%	280.855	1.324E-03
$1s2p(^1P)3p\ ^2P_{3/2}$	$1s^22p\ ^2P_{1/2}$	36.7510	337.363	0.64%	2.88%	280.864	1.318E-03
$1s2p(^1P)3p\ ^2P_{1/2}$	$1s^23p\ ^2P_{3/2}$	40.5422	305.815	0.02%	26.75%	281.007	1.324E-03
$1s2p(^1P)3p\ ^2P_{1/2}$	$1s^23p\ ^2P_{1/2}$	40.5417	305.819	0.02%	55.10%	281.007	1.324E-03
$1s2p(^1P)3p\ ^2P_{3/2}$	$1s^23p\ ^2P_{3/2}$	40.5410	305.824	0.64%	68.97%	281.016	1.318E-03
$1s2p(^1P)3p\ ^2P_{3/2}$	$1s^23p\ ^2P_{1/2}$	40.5406	305.827	0.64%	12.86%	281.015	1.318E-03
$1s2p(^1P)3d\ ^2D_{3/2}$	$1s^23s\ ^2S_{1/2}$	40.1306	308.952	0.00%	0.00%	282.007	1.439E-03
$1s2p(^1P)3d\ ^2D_{3/2}$	$1s^23d\ ^2D_{5/2}$	40.4864	306.237	0.00%	85.90%	282.024	1.439E-03
$1s2p(^1P)3d\ ^2D_{5/2}$	$1s^23d\ ^2D_{5/2}$	40.4861	306.239	0.05%	88.49%	282.027	1.438E-03
$1s2p(^1P)3d\ ^2D_{5/2}$	$1s^23d\ ^2D_{3/2}$	40.4860	306.240	0.05%	6.74%	282.026	1.436E-03
$1s2p(^1P)3d\ ^2F_{7/2}$	$1s^23d\ ^2D_{5/2}$	40.4273	306.684	88.49%	95.37%	282.472	1.903E-04
$1s2p(^1P)3d\ ^2F_{5/2}$	$1s^23d\ ^2D_{5/2}$	40.4260	306.694	88.52%	6.75%	282.482	1.904E-04
$1s2p(^1P)3d\ ^2F_{5/2}$	$1s^23d\ ^2D_{3/2}$	40.4258	306.696	88.52%	88.56%	282.482	1.904E-04
$1s2p(^1P)3p\ ^2S_{1/2}$	$1s^22p\ ^2P_{3/2}$	36.5680	339.051	96.12%	2.06%	282.566	9.068E-05
$1s2p(^1P)3p\ ^2S_{1/2}$	$1s^22p\ ^2P_{1/2}$	36.5667	339.063	96.12%	0.99%	282.565	9.068E-05
$1s2p(^1P)3p\ ^2S_{1/2}$	$1s^23p\ ^2P_{3/2}$	40.3169	307.524	96.12%	31.78%	282.716	9.068E-05
$1s2p(^1P)3p\ ^2S_{1/2}$	$1s^23p\ ^2P_{1/2}$	40.3164	307.528	96.12%	31.78%	282.716	9.068E-05
$1s2p(^1P)3d\ ^2P_{1/2}$	$1s^22s\ ^2S_{1/2}$	35.6415	347.865	30.08%	0.24%	283.371	1.086E-03
$1s2p(^1P)3d\ ^2P_{3/2}$	$1s^22s\ ^2S_{1/2}$	35.6410	347.870	30.18%	0.24%	283.376	1.086E-03
$1s2p(^1P)3d\ ^2P_{1/2}$	$1s^23s\ ^2S_{1/2}$	39.9427	310.405	30.08%	1.22%	283.460	1.086E-03
$1s2p(^1P)3d\ ^2P_{3/2}$	$1s^23s\ ^2S_{1/2}$	39.9421	310.410	30.18%	1.21%	283.465	1.086E-03
$1s2p(^1P)3d\ ^2P_{3/2}$	$1s^23d\ ^2D_{3/2}$	40.2952	307.690	30.08%	95.03%	283.476	1.086E-03
$1s2p(^1P)3d\ ^2P_{3/2}$	$1s^23d\ ^2D_{5/2}$	40.2946	307.694	30.18%	85.69%	283.482	1.086E-03
$1s2p(^1P)3d\ ^2P_{3/2}$	$1s^23d\ ^2D_{3/2}$	40.2945	307.695	30.18%	9.42%	283.482	1.086E-03

Appendix I

Beamtime Preparation

Introduction

This is a manual for the experimentalist that summarizes all the steps that are taken to ensure proper operation during an experiment. Even though it is a detailed guide for the preparation, not all steps are always necessary before each experiment. Here, are described all the procedures for a thorough check of the various instrumentation modules. Time permitted, all preparation is conducted *before* the beginning of the experiment. This guide is designed to complement as a check-list. In case of a problematic device, any troubleshooting for any of the parts of the apparatus would render the present text far too extended.

I.1 Alignment

I.1.1 Breaking the vacuum

The first step for alignment is the breaking of the vacuum. For optimal alignment, the telescope has to be calibrated using the furthest set of slits, which is upstream SL1. Depending on the choice of alignment slits, the user can either break the vacuum only in the chamber and the target area, or up to the isolation valve of the switching magnet, as required for SL1. The procedure steps are the following:

1. Shutting down all Turbo-Molecular Pumps. Standstill time can vary, from 20 to 60 minutes, depending on the pump. By the time the turbo pumps slow down, the expected vacuum values are at the 10^{-6} to 10^{-4} Torr regime since the system is still supported by the backing pumps.

2. Closing of all the isolation valves with the use of the master control switch and the respective switch on the beam-line turbo pump.

3. The final step is the nitrogen purging. In order to avoid the deposition of moisture inside the MCP, atmospheric air should be avoided, and only clean gases that evaporate in ambient temperature and pressure should be used. Should the pressure reach atmospheric level, caution is needed for the event of over-pressurizing the chamber. This is done by periodic checking of the chamber's top lid.

I.1.2 Telescope alignment

Once the pressure is equivalent to atmospheric FC2 is removed along with the chamber lid. Then, the gas cell is lifted, along with FC1, and SL2 are set wide open. The next step

is to center the telescope to the SL1. The purpose of this step is to align the telescope with the optical axis of the beamline. This requires two points in space. The first one is the base of the telescope, and the second is set somewhere along the beamline, the "stable point". In the case of the L45 line, the second is defined twice along the beamline, with the use of SL1 and SL2. For each set of slits, the central settings, the settings for which each slit coincides with the optical axis, are written below each pair of slits. SL1 is considered the safest option regarding telescope alignment, as the furthest stable point of the beam-line. Optionally, SL2 can also be aligned but it is a necessity if there are major changes in the equipment before the last support rod. If this is the case, SL1 are set to the default zero position, as indicated, and the beam-line is set so that the telescope cross-hair matches the slits. First step is to set the horizontal and vertical displacement of the telescope to zero. Both SL1 and SL2 are equipped with LED lights, powered using the current outputs of the slits, along with an external power supply at ≈ 9 V. The routine is to set only two perpendicular slits to centered position, and align the telescope's cross-hair on their edges, and then repeating with the other two slits. Once the telescope is aligned, it is considered the guide with which everything else is aligned.

I.1.3 Chamber, gas target and HDA alignment

Typically, the chamber of the HDA should be aligned. Slight misalignment has been observed after extended periods of time, or after heavy-duty operations inside the chamber, however, the support table has sufficient degrees of freedom for corrections. In any case, alignment is always performed from outside to inside and from upstream to downstream. That means that if both the chamber and the HDA are misaligned (outside to inside) first the chamber is aligned, and then the HDA. Also, if both the chamber and the gas cell are misaligned (upstream to downstream), the gas-cell is corrected first . Once the chamber is aligned, the HDA is aligned, using the two screws that hold it in place. Gas cell apertures should be visible as circles, provided there is sufficient lighting during the alignment. Proper lighting can be achieved by opening the CF160 glass port.

Misaligned gas cell is observed as an ellipsoid. Depending on the long axis of the ellipsoid, the experimentalist can understand the correction needed, i.e. if the axis is vertical, then the gas cell requires to be turned horizontally, with the use of the gas cell alignment construction. All other alignment procedures involve the fine-tuning screws that support the target 6-way cross.

I.2 Electronics

Electronics are divided into three main categories:

1. Beam-line HVPS. These are necessary for proper beam pass, and require no calibration.

2. HDA HVPS. These are necessary for the proper execution of the experiment and most of them require calibration, with different limitations.

3. DAQ. These are also necessary for the experiment. For more information, refer to chapter C.

It should also be noted that since a part of the equipment has 120 V operational voltage, the very first test for the electronics is to ensure that the 240-120 V transformer (Big green one, below the steerers) is operational.

I.2.1 Power supplies

Steerers PSU These are current supplies for the double pair of steerers of the beam. Before each experiment, a test is ran for proper operation. Ideally, the four current supplies should be able to provide at least up to 2.5 to 3 Amperes each, both polarities. This test can be done with a simple multi-meter, although caution is required due to high current measurement. They should be turned on 1-2 days before beginning the experiment. Between experimental days they are kept operational to avoid any hysteresis to the currents.

Miscellaneous PSU Other than the steerers, there is also a number of HVPSs that need to be checked:

1. Suppressor power supply, currently (Sunday 28$^{\text{th}}$ February, 2021) is a Tennelec HVPS. Suppressor is an electrode located on either FC1 and FC2 that suppresses electrons emitted from the cups thus allows the proper beam current (=charge/time) measurement. The unit supplies -300 VDC, connected with BNC cables on either cup. A simple voltage check on both ends should be enough.

2. Isolating valves power supply. It is a transformer that provides 24 VAC from 240 VAC, and is connected to the valves through the hand-made "Master Valve Switch" Master Valve switch is connected in series with dedicated switches for each isolation valve.

3. MCP floating HVPS along with the voltage divider. By setting the MCP HVPS to a voltage less than 1 kV, the divider can be checked. Also, by setting V_{bias} +V_{MCP} to be less than 1 kV, the floating voltage can be also checked for proper operation.If not possible, V_{bias} can be checked independently.

HDA HVPS All the HDA HVPSs can be checked with the use of the rack-mounted voltage divider. The voltage division is by a factor of 10.900608, which means that i.e. for a value of 2000 Volts, the measured value should be $\frac{2000}{10.900608} = 183.476$ VDS. Ideally, depending on the projectile energy, one can calibrate the HVPS to the desired voltage range.

I.2.2 DAQ electronics

Data Acquisition Proper testing of the DAQ requires signal on the MCP, and needs to be conducted before the alignment procedure. This is because it is usually performed with the use of the e-gun. It can be performed after the alignment, with proper markings on the gas target positioning, so that the gas cell will return exactly on the optical axis of the beam.

Counter Testing of the counter can be done with the use of the INPP's pulse generator and the custom made *.vi in the laboratory computer.

I.2.3 Console Connectivity

There are four signal connections with the operator console during an experiment:

1. **Target**. This is the signal measured either in FC1 (during first beam pass) or in FC2 which serves as the final Faraday Cup for normalization during the experiment. During first beam transmission, in the case of low beam currents, proper calibration (pole zero check) of the lower 2 and 0.2 nA scales is required.

2. **Collimator**. This is a signal used by the operator for current maximization.

3. **BCI digital output**. This is the signal that is fed to the counter for ion measurement. A 50Ω terminator is used to avoid possible reflections of the signal.

4. **BCI analogue output**. This is a signal that is proportional to the beam current, and it is used to verify if the beam is "on" while in the experiment room. Optional.

Since all four signals go through three patch panels, proper testing is required before each experiment. Standard procedure is the documentation of every signal path, along with a conductivity test for each signal path. It should be noted that improper cable selection, especially in the case of the BCI Digital Output can lead to signal reflections, and a multiplication of the incoming pulse rate. This is the reason for placing the 50Ω terminator in parallel with the signal.

I.3   Miscellaneous

Gas targets   The gas delivery systems should be checked, properly purged, and during the experiment the pre-valve pressure should exceed atmospheric pressure in order to avoid any gas-target contamination.

Baratron   The Baratron unit should be warmed up at least 24 hours before the experiment and the final zeroing of the pressure depends on the total pumping time. If the vacuum seems stabilized, zeroing can be performed, otherwise, before the experiment should be sufficient.

Slits   Slits SL1 and SL2 should be set to an appropriate window. Usual settings are:

SL1 Upstream slits (usually) have a 6×8 mm window. The 8 mm on the horizontal axis provides a slight compensation for the widening of the beam after the switching magnet.

SL2 Downstream slits (usually) have a 3×3 mm window. This is an initial value for the slits. Since the gas cell has an aperture of 2.5 mm in diameter, SL2 are carefully tuned to minimize the background emerging from the secondary electrons that are emitted due to collision of the beam with the target gas cell.

Isolation Valve   Also, the L45 isolation valve requires checking from time to time.

Laboratory PC   Confirm the PC is operational, along with batteries for the wireless keyboard and mouse.

I.4   Checklist

☐ Alignment

☐ Steerer HVPS

☐ Suppressor HVPS

☐ Operation of FC1

☐ Isolating valves PS

☐ 240-to-120 VAC transformer

☐ MCP floating HVPS

☐ HDA HVPSs

☐ DAQ operation

☐ Counter operation

☐ Room connections

☐ Gas supply

☐ Baratron

☐ L45 Isolation valve

☐ Laboratory PC

Appendix J

Dissemination of results

International Publications

Articles in International Journals:

(1) *Determination of the solid angle and response function of a hemispherical spectrograph with injection lens for Auger electrons emitted from long lived projectile states*, S. Doukas, **I. Madesis**, A. Dimitriou, A. Laoutaris, T. J. M. Zouros and E. P. Benis, Review of Scientific Instruments 86 (2015) 043111

(2) *The Optimization of a 4-Element Input Lens on a Hemispherical Deflector Analyzer Using SIMION*, T. J. M. Zouros, A. Kanellakopoulos, **I. Madesis**, A. Dimitriou, M. Fernández-Martín, G. Martínez and T.J. Mertzimekis, Microscopy and Microanalysis 21 (suppl. 4) pp. 148-153 (2015).

(3) *Voltage optimization of a 4-element Injection Lens on a hemispherical spectrograph with virtual entry aperture*, G. Martínez, M. Fernández-Martín, O. Sise, **I. Madesis**, A. Dimitriou, A. Laoutaris and T.J.M. Zouros, Nuclear Instruments and Methods in Physics Research B **369**, 92-94 (2015)

(4) *High Resolution Auger Projectile Electron Spectroscopy of Li-like Ions Produced by Electron Capture in collision of He-like ions with Gaseous targets*, A. Dimitriou, A. Laoutaris, **I. Madesis**, S. Doukas, E. P. Benis, B. Sulik, O. Sise, A. Lagoyannis, M. Axiotis, T. J. M. Zouros, Journal of Atomic, Molecular, Condensate and Nano Physics, Vol.3, No. 2, 125-131 (2016)

(5) *The voltage optimization of a four-element lens used on a hemispherical spectrograph with virtual entry for highest energy resolution*, O. Sise and G. Martínez and **I. Madesis** and A. Laoutaris and A. Dimitriou and M. Fernández-Martín and T. J. M. Zouros, Journal of Electron Spectroscopy and Related Phenomena, 0368-2048, (2016)

(6) *High Resolution Auger Projectile Electron Spectroscopy of Li-like Ions Produced by Electron Capture in collision of He-like ions with Gaseous targets*, A. Dimitriou, A. Laoutaris, **I. Madesis**, S. Doukas, E. P. Benis, B. Sulik, O. Sise, A. Lagoyannis, M. Axiotis, T. J. M. Zouros, Journal of Atomic, Molecular, Condensate and Nano Physics, Vol.3, No. 2, 125-131 (2016)

(7) *Experimental determination of the effective solid angle of long-lived projectile states in zero-degree Auger projectile spectroscopy*, E. P. Benis, **I. Madesis**, A. Laoutaris, S.

Nanos, T. J. M. Zouros, Journal of Electron Spectroscopy and Related Phenomena 222, 31-39 (2017)

(8) *Mixed-State Ionic Beams: An Effective Tool For Collision Dynamics Investigations*, E.P. Benis, **I. Madesis**, A. Laoutaris S. Nanos, T.J.M. Zouros, ATOMS **6**, (2018) 66.

(9) *Projectile electron spectroscopy: new answers to old questions. Latest results at the new atomic physics beamline in Demokritos, Athens*, **I. Madesis**, A. Laoutaris, T.J.M. Zouros, S. Nanos and E. P. Benis, In: Book Series "Interdisciplinary Research on Particle Collisions and Quantitative Spectroscopy", Volume 2: Reviews on Ion-Atom and Ion-Molecule Collisions (Invited Lectures at ISIAC-2017), Edited by Dz. Belkic, A. Kadyrov and I. Bray (World Scientific Publishing Company, Singapore, 2018), pp. 1-31. (CALIBRA)

(10) *Population of the $1s2s(^3S)nl\,^2L$ states in collisions of mixed-state ($1s^2$, $1s2s\,^3$S) B^{2+} and C^{3+} ion beams with* He/H_2 *targets*, E. P. Benis and **I. Madesis** and A. Laoutaris and S. Nanos and A. Dubois and T. W. Gorczyca and T. J. M. Zouros, X-Ray Spectrometry **49X**, 54-59 (2020).

(11) *Pauli shielding and break-down of spin statistics in multi-electron, multi-open-shell dynamical atomic systems*, **I. Madesis**, A. Laoutaris, T. J. M. Zouros, E. P. Benis, J.W. Gao, A. Dubois, Phys. Rev. Lett. **124** (2020) 113401.

(12) *Radiative cascade repopulation of $1s2s2p\,^4P$ states formed by single electron capture in 2-18 MeV collisions of $C^{4+}(1s2s\,^3S$) with He*, T. J. M. Zouros, S. Nikolaou, **I. Madesis**, A. Laoutaris, S. Nanos, A. Dubois, E. P. Benis, ATOMS Atoms **2020**, 8, 61.

(13) *The Tandem Accelerator Laboratory of NCSR "Demokritos": Current status and perspectives*, S. Harissopulos, M. Andrianis, M Axiotis, A. Lagoyannis, A.G. Karydas, Z. Kotsina, A. Laoutaris, G. Apostolopoulos, A. Theodorou, T. J. M. Zouros, **I. Madesis**, E. P. Benis, European Journal of Physics X (2021) XX (submitted 6/1/21)

Articles in International Proceedings:

(1) *Atomic Physics with Accelerators: Projectile Electron Spectroscopy (APAPES)*, **I. Madesis**, A. Dimitriou, A. Lagoyannis, M. Axiotis, T. Mertzimekis, M. Andrianis, S. Harissopulos, E. P. Benis, B. Sulik, I. Valastyán, T. J. M. Zouros,Proceedings of HCI 2014 - 17th International Conferences on the Physics of Highly Charged Ions, Aug 31 - Sep 8, 2014, Bariloche, Argentina, Journal of Physics: Conference Series **583** (2015) 012014

(2) *Separation and solid angle correction of the metastable 1s2s2p ^4P Auger yield produced in ion-atom collisions using the biased as cell technique: A tool for the determination of the population mechanisms*, **I. Madesis**, A. Laoutaris, S. Doukas, A. Dimitriou, E. P. Benis, T. J. M. Zouros, Proceedings of XXIX International Conference on Photonic, Electronic, and Atomic Collisions (ICPEAC2015), J. of Physics: Conference Series **635** (2015) 052082

(3) *Monte Carlo Calculations of the Detection Solid Angle of electrons emitted from slowly decaying projectile ion Auger states*, S. Doukas, N. Angelinos, A. Kanellakopoulos, **I. Madesis**, A. Dimitriou, E. P. Benis, and T. J. M. Zouros, Conference Proceedings of the 6th IC-SCCE (2014) p. 282-288

(4) *Voltage optimization of a 4-element Injection Lens on a hemispherical spectrograph with virtual entry aperture*, G. Martínez, M. Fernández-Martín, O. Sise, **I. Madesis**, A. Dimitriou, A. Laoutaris and T. J. M. Zouros, Proceedings of PIPAMON 2015: Photon and fast Ion induced Processes in Atoms, MOlecules and Nanostructures, Mar 24-26, Debrecen, Hungary Nuclear Instruments and Methods in Physics Research B **369** (2015) 92-94

(5) *Evaluation of the effective solid angle of a hemispherical deflector analyser with injection lens for metastable Auger projectile states*, E. P. Benis, S. Doukas, **I. Madesis**, A. Dimitriou, A. Laoutaris, T. J. M. Zouros, F. Parente, C. Martins, J. P. Marques and J. P. Santos, Proceeding of SHIM-2015, Nuclear Instruments and Methods in Physics Research B **365** (2015) 457-461

(6) *Use of Gas and Foil strippers for the production of He-like ionic beams in both pure ground state ($1s^2$) and mixed states ($1s^2$, $1s2s$) for zero-degree Auger Projectile Electron Spectroscopy*, A. Laoutaris, **I. Madesis**, A. Dimitriou, A. Lagoyannis, M. Axiotis, E. P. Benis and T. J. M. Zouros, Proceedings of XXIX International Conference on Photonic, Electronic, and Atomic Collisions (ICPEAC2015), J. of Physics: Conference Series **635** (2015) 052062.

(7) *Investigation of the dependence of the energy resolution of a hemispherical deflection analyzer on the distance of the position sensitive detector from the focal plane*, C. Nounis, A. Laoutaris, **I. Madesis**, A. Dimitriou, O. Sise, E. P. Benis, T. J. M. Zouros, Proceedings of XXIX International Conference on Photonic, Electronic, and Atomic Collisions (ICPEAC2015), J. of Physics: Conference Series **635** (2015) 052063.

(8) *Optimal operation of a 4-element injection lens in a hemispherical spectrograph: FDM/BEM simulation and experimental demonstration*, G. Martínez, **I. Madesis**, A. Dimitriou, A. Laoutaris, O. Sise and T. J. M. Zouros, Proceedings of XXIX International Conference on Photonic, Electronic, and Atomic Collisions (ICPEAC2015), J. of Physics: Conference Series **635** (2015) 052083.

Bibliography

[1] P. Roncin, "Revisiting atomic collisions physics with highly charged ions, a tribute to Michel Barat," *J. Phys. B*, vol. 53, p. 202001, Sep 2020. i

[2] J. A. Tanis, A. L. Landers, D. J. Pole, A. S. Alnaser, S. Hossain, and T. Kirchner, "Evidence for Pauli Exchange Leading to Excited-State Enhancement in Electron Transfer," *Phys. Rev. Lett.*, vol. 92, p. 133201, Apr 2004. xv, xvii, 10

[3] J. A. Tanis, A. L. Landers, D. J. Pole, A. S. Alnaser, S. Hossain, and T. Kirchner, "Erratum," *Phys. Rev. Lett.*, vol. 96, no. 1, p. 019901, 2006. xv, xvii

[4] E. P. Benis, T. J. M. Zouros, T. W. Gorczyca, A. D. González, and P. Richard, "Erratum," *Phys. Rev. A*, vol. 73, p. 029901, Feb 2006. xv, xvii, 10, 22, 39, 66, 73, 91

[5] T. J. M. Zouros, B. Sulik, L. Gulyás, and K. Tökési, "Selective enhancement of $1s2s2p\,^4P_J$ metastable states populated by cascades in single-electron transfer collisions of $F^{7+}(1s^2/1s2s\,^3S)$ ions with He and H_2 targets," *Phys. Rev. A*, vol. 77, no. 5, p. 050701, 2008. xv, xvii, 6, 10, 11, 18, 20, 25, 26, 66, 82, 83

[6] D. Strohschein, D. Röhrbein, T. Kirchner, S. Fritzsche, J. Baran, and J. A. Tanis, "Nonstatistical enhancement of the $1s2s2p\,^4P$ state in electron transfer in 0.5–1.0-MeV/u $C^{4,5+}$ + He and Ne collisions," *Phys. Rev. A*, vol. 77, no. 2, p. 022706, 2008. xv, xv, xvii, xviii, 10, 11, 12, 23, 24, 25, 52, 66, 72, 82, 83, 85, 86, 91, 104

[7] I. Madesis, A. Laoutaris, T. J. M. Zouros, E. P. Benis, J. W. Gao, and A. Dubois, "Pauli shielding and breakdown of spin statistics in multielectron multi-open-shell dynamical atomic systems," *Phys. Rev. Lett.*, vol. 124, p. 113401, Mar 2020. xv, xviii, 5, 12, 13, 24, 79, 83, 84, 88, 103

[8] P. Richard, "Ion-atom collisions," in *Atomic Inner-Shell Processes* (B. Crasemann, ed.), vol. 1, (New York), pp. 73–158, Academic Press, 1975. 1

[9] M. Rødbro, R. Bruch, and P. Bisgaard, "High-resolution projectile Auger spectroscopy for Li, Be, B and C excited in single gas collisions i. line energies for prompt decays," *J. Phys. B*, vol. 12, p. 2413, 1979. 1, 7

[10] N. Stolterfoht, H. Gabler, and U. Leithäuser, "High resolution Ne-Auger spectrum produced in 4.2 MeV H^+–Ne collisions," *Phys. Lett.*, vol. 45A, p. 351, 1973. 1

[11] N. Stolterfoht, D. Schneider, R. Mann, and F. Folkmann, "Auger emission from highly ionised neon produced in 200 MeV Xe^{31+} + Ne collisions," *J. Phys. B*, vol. 10, p. L281, 1977. 1, 9

[12] D. Schneider, C. F. Moore, and B. M. Johnson, "High-resolution Ne K Auger-electron spectrum produced by 45 MeV Cl^{12+} ion impact," *J. Phys. B*, vol. 9, pp. L153–L156, 1976. 1

[13] D. Schneider, K. Roberts, W. Hodge, and C. F. Moore, "High-resolution Ar K Auger spectrum produced in 4-MeV H$^+$ on argon collisions," *Phys. Rev. Lett.*, vol. 36, pp. 1065–1067, Apr 1976. 1

[14] B. Breuckmann and V. Schmidt, "The K Auger spectrum of the free magnesium atom," *Zeitschrift für Physik*, vol. 268, no. 2, pp. 235–239, 1974. 1

[15] B. Breuckmann, V. Schmidt, and W. Schmitz, "The electron spectrum following ionization and excitation of L-shell electrons in magnesium vapour," *J. Phys. B*, vol. 9, pp. 3037–3046, dec 1976. 1

[16] P. Ziem, R. Bruch, and N. Stolterfoht, "Autoionization spectra of Li I and Li II excited by H$^+$ and He$^+$ impact," *J. Phys. B*, vol. 8, pp. L480–L484, 1975. 1

[17] E. Breuckmann, B. Breuckmann, W. Mehlhorn, and W. Schmitz, "L-Auger and autoionising spectrum of Na," *J. Phys. B*, vol. 10, pp. 3135–3150, oct 1977. 1

[18] D. L. Matthews, *Ion-induced Auger electron spectroscopy*, vol. 17 of *Methods of Experimental Physics*, pp. 433–527. New York: Academic Press, 1980. 1

[19] I. A. Sellin, D. J. Pegg, M. Brown, W. W. Smith, and B. Donnally, "Spectra of autoionization electrons emitted by fast, metastable beams of highly stripped oxygen and fluorine ions," *Phys. Rev. Lett.*, vol. 27, pp. 1108–1111, 1971. 1

[20] I. A. Sellin, D. J. Pegg, P. M. Griffin, and W. W. Smith, "Metastable autoionizing states of highly excited Heavy ions," *Phys. Rev. Lett.*, vol. 28, pp. 1229–1232, May 1972. 1

[21] N. Stolterfoht, D. Schneider, D. Burch, H. Wieman, and J. S. Risley, "Mechanisms for electron production in 30-MeV O^{n+}+O$_2$ collisions," *Phys. Rev. Lett.*, vol. 33, pp. 59–62, Jul 1974. 1

[22] N. Stolterfoht, P. Ziem, and D. Ridder, "Gas target experiments of K-shell vacancy sharing in asymmetric ion-atom collisions," *jpb*, vol. 7, pp. L409–L413, Oct 1974. 1

[23] D. J. Pegg, H. H. Haselton, R. S. Thoe, P. M. Griffin, M. D. Brown, and I. A. Sellin, "Core-excited autoionizing states in the alkali metals," *Phys. Rev. A*, vol. 12, pp. 1330–1339, Oct 1975. 1

[24] A. K. Pradhan and S. N. Nahar, *Atomic Astrophysics and Spectroscopy.* Cambridge: Cambridge University Press, 2011. 1

[25] P. Beiersdorfer, "Laboratory X-ray astrophysics," *Annu. Rev. Astron. Astrophys.*, vol. 41, no. 1, pp. 343–390, 2003. 1

[26] V. P. Shevelko and H. Tawara, eds., *Atomic Processes in Basic and Applied Physics.* Berlin Heidelberg New York: Springer, 2012. 1

[27] D. Belkić, "Review of theories on ionization in fast ion-atom collisions with prospects for applications to hadron therapy," *J. Math. Chem.*, vol. 47, pp. 1366–1419, May 2010. 1

[28] T. R. Kallman and P. Palmeri, "Atomic data for x-ray astrophysics," *Rev. Mod. Phys.*, vol. 79, no. 1, p. 79, 2007. 1

[29] N. Stolterfoht, "High resolution Auger spectroscopy in energetic ion atom collisions," *Phys. Rep.*, vol. 146, pp. 315–424, 1987. 1, 8, 20, 58, 59, 60

[30] R. K. Janev and L. P. Presnyakov, "Collision processes of multiply charged ions with atoms," *Phys. Rep.*, vol. 70, pp. 1–107, 1981. 2

[31] R. C. Isler and E. C. Crume, "Charge-transfer excitation of impurity ions in tokamaks," *Phys. Rev. Lett.*, vol. 41, pp. 1296–1300, Nov 1978. 2

[32] R. Isler, R. Neidigh, and R. Cowan, "Tungsten radiation from tokamak-produced plasmas," *Phys. Rev. A*, vol. 63, no. 3, pp. 295 – 297, 1977. 2

[33] M. Harrison, "Introductory paper 1. the role of atomic and molecular processes in fusion research," *Physics Reports*, vol. 37, no. 2, pp. 59 – 81, 1978. 2

[34] H. D. Betz, *Charge Equilibration of High-Velocity Ions in Matter*, vol. 17 of *Methods of Experimental Physics*, pp. 73–88. New York: Academic Press, 1980. 2

[35] A. A. Babaev and Y. L. Pivovarov, "Theory of resonant coherent excitation of relativistic hydrogen-like heavy ions under planar channelling in a si crystal," *J. Phys. B*, vol. 41, p. 195001, sep 2008. 2

[36] C. Kondo, S. Masugi, Y. Nakano, A. Hatakeyama, T. Azuma, K. Komaki, Y. Yamazaki, T. Murakami, and E. Takada, "Three-dimensional resonant coherent excitation of nonchanneling ions in a crystal," *Phys. Rev. Lett.*, vol. 97, p. 135503, Sep 2006. 2

[37] Y. Nakano, C. Kondo, A. Hatakeyama, Y. Nakai, T. Azuma, K. Komaki, Y. Yamazaki, E. Takada, and T. Murakami, "Polarization control in three-dimensional resonant coherent excitation," *Phys. Rev. Lett.*, vol. 102, p. 085502, Feb 2009. 2

[38] G. Kraft, "Tumor therapy with heavy charged particles," *Progress in Particle and Nuclear Physics*, vol. 45, pp. S473 – S544, 2000. 2

[39] E. Fokas, G. Kraft, H. An, and R. Engenhart-Cabillic, "Ion beam radiobiology and cancer: Time to update ourselves," *Biochimica et Biophysica Acta (BBA) - Reviews on Cancer*, vol. 1796, no. 2, pp. 216 – 229, 2009. 2

[40] J. Soltani-Nabipour, A. Khorshidi, F. Shojai, and K. Khorami, "Evaluation of dose distribution from 12c ion in radiation therapy by fluka code," *Nuclear Engineering and Technology*, vol. 52, no. 10, pp. 2410 – 2414, 2020. 2

[41] S. J. A. Atawneh, r. Asztalos, B. Szondy, G. I. Pokol, and K. Tőkési, "Ionization cross sections in the collision between two ground state hydrogen atoms at low energies," *Atoms*, vol. 8, no. 2, 2020. 2

[42] I. Ziaeian and K. Tőkési, "Interaction of Be^{4+} and ground state hydrogen atom|classical treatment of the collision," *Atoms*, vol. 8, no. 2, 2020. 2

[43] K. Igenbergs, J. Schweinzer, and F. Aumayr, "Charge exchange in be^{4+}{h(n= 1, 2) collisions studied systematically by atomic-orbital close-coupling calculations," *J. Phys. B*, vol. 42, p. 235206, nov 2009. 2

[44] J. Romazanov, S. Brezinsek, D. Borodin, M. Groth, S. Wiesen, A. Kirschner, A. Huber, A. Widdowson, M. Airila, A. Eksaeva, I. Borodkina, and C. Linsmeier, "Beryllium global erosion and deposition at jet-ilw simulated with ero2.0," *Nuclear Materials and Energy*, vol. 18, pp. 331 – 338, 2019. 2

[45] D. Borodin, J. Romazanov, R. Pitts, S. Lisgo, S. Brezinsek, I. Borodkina, A. Eksaeva, E. Safi, K. Nordlund, A. Kirschner, and C. Linsmeier, "Improved ero modelling of beryllium erosion at iter upper first wall panel using jet-ilw and pisces-b experience," *Nuclear Materials and Energy*, vol. 19, pp. 510 – 515, 2019. 2

[46] Y. Zhou, H. Bergsåker, I. Bykov, P. Petersson, V. Paneta, and G. Possnert, "Micro ion beam analysis for the erosion of beryllium marker tiles in a tokamak limiter," *Nucl. Instrum. Methods Phys. Res. B*, vol. 450, pp. 200 – 204, 2019. The 23rd International Conference on Ion Beam Analysis. 2

[47] M. W. Krasny, "The gamma factory proposal for cern," 2015. 2

[48] D. Budker, J. R. C. López-Urrutia, A. Derevianko, V. V. Flambaum, M. W. Krasny, A. Petrenko, S. Pustelny, A. Surzhykov, V. A. Yerokhin, and M. Zolotorev, "Atomic physics studies at the gamma factory at cern," 2020. 2

[49] Y. Nakano, Y. Takano, T. Ikeda, Y. Kanai, S. Suda, T. Azuma, H. Bräuning, A. Bräuning-Demian, D. Dauvergne, T. Stöhlker, and Y. Yamazaki, "Resonant coherent excitation of the lithiumlike uranium ion: A scheme for heavy-ion spectroscopy," *Phys. Rev. A*, vol. 87, p. 060501, Jun 2013. 2

[50] P. Richard, *Methods of Experimental Physics.: Atomic Physics Accelerators*. Academic Press, 1980. 3

[51] R. J. V. D. Graaff, "Tandem electrostatic accelerators," *Nucl. Instrum. Methods Phys. Res. B*, vol. 8, no. 2, pp. 195 – 202, 1960. 3

[52] K. Hill and R. Nelson, "A sputtering ion source," *Nucl. Instrum. & Methods*, vol. 38, pp. 15 – 18, 1965. 3

[53] H.-D. Betz, G. Hortig, E. Leischner, C. Schmelzer, B. Stadler, and J. Weihrauch, "The average charge of stripped heavy ions," *Physics Letters*, vol. 22, no. 5, pp. 643 – 644, 1966. 3

[54] H.-D. Betz, "Charge states and charge-changing cross sections of fast Heavy ions penetrating through gaseous and solid media," *Rev. Mod. Phys.*, vol. 44, pp. 465–539, Jul 1972. 3, 52

[55] V. N. I.S. Dmitriev, "Semi-empirical method for the calculation of the equilibrium distribution of charges in a fast-ion beam," *Soviet Physics J.Exptl. Theoret. Phys. (U.S.S.R)*, vol. 20, no. 2, pp. 409–415, 1965. 3, 52, 53, 54

[56] R. Sayer, "Semi-empirical formulas for heavy-ion stripping data," *Rev. Phys. Appl. (Paris)*, vol. 12, no. 10, pp. 1543–1546, 1977. 3, 52, 53, 54

[57] E.-M. Asimakopoulou, "Tardis (transmitted charge distribution)," technical report, Institute of Nuclear and Particle Physics and Department of Physics, University of Athens, 2014. 3

[58] E. P. Benis, I. Madesis, A. Laoutaris, S. Nanos, and T. J. M. Zouros, "Mixed-state ionic beams: An effective tool for collision dynamics investigations," *Atoms*, vol. 6, no. 4, p. 66, 2018. 3, 4, 15

[59] E. P. Benis, M. Zamkov, P. Richard, and T. J. M. Zouros, "Technique for the determination of the 1s2s ^{3}S metastable fraction in two-electron ion beams," *Phys. Rev. A*, vol. 65, p. 064701, 2002. 3, 15, 72, 84

[60] E. P. Benis, M. Zamkov, P. Richard, and T. J. M. Zouros, "Comparison of two experimental techniques for the determination of the $1s2s\,^3$S metastable beam fraction in energetic B^{3+} ions," *Nucl. Instrum. Methods Phys. Res. Sect. B*, vol. 205, pp. 517–521, 2003. 3, 15, 72

[61] A. Laoutaris, "Study and implementation of a system of ion poststrippers for use at the 5.5 MV Tandem Van de Graaff accelerator of the National Center for Science and Research Demokritos," M.Sc. dissertation, Dept. of Physics, National Technical University of Athens, 2015. (unpublished). 3, 4, 34, 37, 52, 53, 55, 79

[62] A. S. Schlachter, J. W. Stearns, W. G. Graham, K. H. Berkner, R. V. Pyle, and J. A. Tanis *Phys. Rev. A*, vol. 27, p. 3372, 1983. 4

[63] D. H. Jakubaba-Amundsen, "Theoretical models for atomic charge transfer in ion-atom collisions," *International Journal of Modern Physics A*, vol. 4, pp. 769–844, 1989. 4

[64] T. J. M. Zouros, K. L. Wong, S. Grabbe, H. I. Hidmi, P. Richard, E. C. Montenegro, J. M. Sanders, C. Liao, S. Hagmann, and C. P. Bhalla, "0° binary encounter electron production in 30-MeV O^{q+}+H$_2$, He, O$_2$, Ne, and Ar collisions," *Phys. Rev. A*, vol. 53, pp. 2272–2280, Apr 1996. 4, 95

[65] R. Abrines and I. C. Percival *Proc. Phys. Soc.*, vol. 88, p. 861, 1966. 4

[66] H. Ryufuku, K. Sasaki, and T. Watanabe, "Oscillatory behavior of charge transfer cross sections as a function of the charge of projectiles in low energy collisions," *Phys. Rev. A*, vol. 21, p. 745, 1980. 4, 6

[67] M. Mack and A. Niehaus, "Radiative and Auger decay channels in K-shell excited Li-like ions (z = 6-8)," *Nucl. Instrum. Methods Phys. Res. Sect. B*, vol. 23, no. 1-2, pp. 109 – 115, 1987. 4, 6, 20

[68] M. Mack and A. Niehaus, "K-shell excited Li-like ions: Electron spectroscopy of the doublet term system," *Nucl. Instrum. Methods Phys. Res. Sect. B*, vol. 23, no. 1-2, pp. 291 – 296, 1987. 4, 6, 139, 141

[69] E. M. Mack, *Electron capture to autoionizing states of multiply charged ions.* PhD thesis, Rijksuniversiteit te Utrecht, 1987. 4, 6, 17, 18

[70] B. Forsberg, "Classical over-the-barrier model for ionization of poly-cyclic aromatic hydrocarbons in kev-collisions with atomic ions," 2011. 4

[71] V. N. Ostrovsky, "Rydberg atom-ion collisions: classical overbarrier model for charge exchange," *Journal of Physics B: Atomic, Molecular and Optical Physics*, vol. 28, pp. 3901–3914, sep 1995. 4

[72] T. Kirchner, M. Keim, A. Achenbach, H. L?dde, O. Kroneisen, and R. Dreizler, "Basis generator method study of collisions between alpha particles and lithium-like ions," *Physica Scripta*, vol. T80, no. B, p. 270, 1999. 5

[73] W. Fritsch and C. D. Lin, "The semiclassical close-coupling description of atomic collisions: Recent developments and results," *Phys. Rev.*, vol. 202, no. 1, pp. 1 – 97, 1991. 5

[74] T. Kirchner, "Basis generator method calculations for charge-transfer collisions," tech. rep., 2017. 5

[75] T. Kirchner, "Charge-transfer collisions involving few-electron systems," tech. rep., 2016. 5

[76] T. R. Dillingham, J. R. Macdonald, and P. Richard, "Ionization of one-electron ions and capture by bare and one-electron ions of C, N, O, and F on He," *Phys. Rev. A*, vol. 24, pp. 1237–1248, 1981. 5

[77] J. L. Shinpaugh, J. M. Sanders, J. M. Hall, D. H. Lee, H. Schmidt-Böcking, T. N. Tipping, T. J. M. Zouros, and P. Richard, "Electron capture and target ionization in collisions of bare projectile ions incident on Helium," *Phys. Rev. A*, vol. 45, p. 2922, 1992. 5

[78] F. Hopkins, R. L. Kauffman, C. W. Woods, and P. Richard, "K x-ray transitions in one- and two-electron oxygen and fluorine projectiles produced in helium, neon, and argon targets," *Phys. Rev. A*, vol. 9, pp. 2413–2420, Jun 1974. 5, 9

[79] M. G. Suraud, R. Hoekstra, F. J. de Heer, J. J. Bonnet, and R. Morgenstern, "State selective electron capture into nl subshells in slow collisions of C^{5+} and N^{6+} with He and H2 studied by photon emission spectroscopy," *Journal of Physics B: Atomic, Molecular and Optical Physics*, vol. 24, pp. 2543–2558, may 1991. 5

[80] M. Trassinelli, C. Prigent, E. Lamour, F. Mezdari, J. Mérot, R. Reuschl, J.-P. Rozet, S. Steydli, and D. Vernhet, "Investigation of slow collisions for (quasi) symmetric heavy systems: what can be extracted from high resolution x-ray spectra," *J. Phys. B*, vol. 45, no. 8, p. 085202, 2012. 5

[81] D. Röhrbein, T. Kirchner, and S. Fritzsche, "Role of cascade and Auger effects in the enhanced population of the $C^{3+}(1s2s2p\ ^4P)$ states following single-electron capture in $C^{4+}(1s2s\ ^3S)$-He collisions," *Phys. Rev. A*, vol. 81, p. 042701, Apr 2010. 5, 11, 12, 22, 23, 24, 25, 26, 27, 66, 79, 82, 83, 84, 89, 90, 91

[82] M. Baxter, T. Kirchner, and E. Engel, "Time-dependent spin-density-functional-theory description of he^+-he collisions," *Phys. Rev. A*, vol. 96, p. 032708, Sep 2017. 5

[83] J. W. Gao, Y. Wu, J. G. Wang, N. Sisourat, and A. Dubois, "State-selective electron transfer in He^++He collisions at intermediate energies," *Phys. Rev. A*, vol. 97, p. 052709, May 2018. 5, 24

[84] N. Sisourat, I. Pilskog, and A. Dubois, "Non perturbative treatment of multielectron processes in ion-molecule scattering: Application to He^{2+}-H_2 collisions," *Phys. Rev. A*, vol. 84, p. 052722, Nov 2011. 5

[85] G. W. F. Drake, "Theory of relativistic magnetic dipole transitions: Lifetime of the metastable $2\,^3$S state of the Heliumlike ions," *Phys. Rev. A*, vol. 3, pp. 908–915, Mar 1971. 5

[86] L. Guillemot, P. Roncin, M. N. Gaboriaud, M. Barat, H. Laurent, S. Bliman, M. G. Suraud, D. Hitz, M. Bonnefoy, A. Chassevent, and A. Fleury, "Collisions of metastable He-like C^{4+} ions on He and H_2 targets," *J. Phys. B*, vol. 23, no. 19, p. 3353, 1990. 5

[87] R. Middleton, *A negative ion cookbook*. Department Of Physics, University of Pennsylvania, October 1989 (Revised February 1990). 5

[88] H. J. Zwally and D. W. Koopman, "Single-electron capture by C^{4+} in Helium, Neon, and Argon below 40 keV," *Phys. Rev. A*, vol. 2, pp. 1851–1861, Nov 1970. 6

[89] D. H. Crandall, R. E. Olson, E. J. Shipsey, and J. C. Browne, "Single and double charge transfer in C^{4+}-He collisions," *Phys. Rev. Lett.*, vol. 36, pp. 858–860, Apr 1976. 6

[90] D. H. Crandall, "Electron transfer between He-like ions and He," *Phys. Rev. A*, vol. 16, pp. 958–963, Sep 1977. 6

[91] D. H. Crandall, M. L. Mallory, and D. C. Kocher, "Charge exchange between multicharged ions of C, N, and O and molecular hydrogen," *Phys. Rev. A*, vol. 15, pp. 61–69, Jan 1977. 6

[92] D. H. Crandall, R. A. Phaneuf, and F. W. Meyer, "Electron capture by slow multicharged ions in atomic and molecular hydrogen," *Phys. Rev. A*, vol. 19, pp. 504–514, Feb 1979. 6

[93] J. Goldhar, R. Mariella, and A. Javan, "Observation of one- and two-electron transfer from noble-gas atom to highly stripped carbon ions," *Appl. Phys. Lett.*, vol. 29, no. 2, pp. 96–98, 1976. 6, 7

[94] R. E. Olson and A. Salop, "Electron transfer between multicharged ions and neutral species," *Phys. Rev. A*, vol. 14, pp. 579–585, Aug 1976. 6

[95] E. J. Shipsey, J. C. Browne, and R. E. Olson, "Theoretical charge-exchange total cross sections for B^{3+} + He and C^{4+} + He collisions," *Phys. Rev. A*, vol. 15, pp. 2166–2172, Jun 1977. 6

[96] R. E. Olson, E. J. Shipsey, and J. C. Browne, "Charge-transfer cross sections for B^{3+}, C^{4+}+H collisions," *jpb*, vol. 11, pp. 699–708, Feb 1978. 6

[97] S. Bliman, J. Aubert, R. Geller, B. Jacquot, and D. Van Houtte, "Electron-capture collisions at keV energies of multiply charged ions of carbon and argon with molecular deuterium," *Phys. Rev. A*, vol. 23, pp. 1703–1707, Apr 1981. 6

[98] S. Bliman, J. Bonnet, D. Hitz, T. Ludac, M. Druetta, and M. Mayo, "One and two electron transfer at low collision energy: Spectroscopic case studies," *Nucl. Instrum. Methods Phys. Res. B*, vol. 27, no. 4, pp. 579 – 583, 1987. 6

[99] R. Bruch, L. J. Dube, E. Trabert, P. H. Heckmann, B. Raith, and K. Brand, "Electron capture to Rydberg states: C^{4+} in collisions with H_2," *J. Phys. B*, vol. 15, pp. L857–L862, Dec 1982. 6

[100] D. Dijkkamp, A. Brazuk, A. G. Drentje, F. J. de Heer, and H. Winter, "State-selective single-electron capture by 80 keV C^{4+} ions from He, H_2 and Li," *J. Phys. B*, vol. 16, no. 11, p. L343, 1983. 6

[101] S. Bliman, J. J. Bonnet, G. Chauvet, S. Dousson, D. Hitz, B. Jacquot, and E. J. Knystautas, "Radiative decay of lithium-like ions following charge exchange collisions of 3 keV amu^{-1} C^{4+}ions with H_2," *J. Phys. B*, vol. 16, pp. L243–L245, Apr 1983. 6

[102] D. Dijkkamp, A. Brazuk, A. G. Drentje, F. J. de Heer, and H. Winter, "Single-electron capture into $C^{3+}(n,l)$ subshells in C^{4+} -Li collisions (20-80 keV)," *J. Phys. B*, vol. 17, no. 21, p. 4371, 1984. 6

[103] D. Dijkkamp, D. Ciric, E. Vileg, A. de Boer, and F. J. de Heer, "Subshell-selective electron capture in collisions of C^{4+} , N^{5+}, O^{6+} with H, H_2 and He," *J. Phys. B*, vol. 18, no. 24, p. 4763, 1985. 6

[104] D. Dijkkamp, D. Ćirić, F. D. Heer, and E. Vlieg, "(n,l)−subshell electron capture cross sections in collisions of C^{4+}, N^{5+} and O^{6+} with atomic hydrogen," *Nucl. Instrum. Methods Phys. Res. Sect. B*, vol. 9, no. 4, pp. 403 – 407, 1985. 6

[105] M. Kimura and R. E. Olson, "Electron capture to (nl) states in collisions of C^{4+} and C^{6+} with He," *J. Phys. B*, vol. 17, no. 21, p. L713, 1984. 6

[106] W. Fritsch and C. D. Lin, "Atomic-basis study of electron transfer into C^{3+} (nl) orbitals in C^{4+}+H and C^{4+}+Li collisions," *J. Phys. B*, vol. 17, pp. 3271–3278, aug 1984. 6

[107] T. R. Dillingham, J. Newcomb, J. Hall, P. L. Pepmiller, and P. Richard, "Projectile K-Auger-electron production by bare, one-, and two-electron ions," *Phys. Rev. A*, vol. 29, pp. 3029–3038, 1984. 6, 9

[108] M. H. Chen, "Dielectronic satellite spectra for He-like ions," *At. Data & Nucl. Data Tables*, vol. 34, no. 2, pp. 301 – 356, 1986. 6, 9, 13, 16, 20, 21, 22, 67, 141, 142, 144

[109] M. Zamkov, E. P. Benis, P. Richard, and T. J. M. Zouros, "Fraction of metastable $1s2s$ ^{3}S ions in fast He-like beams (Z = 5–9) produced in collisions with carbon foils," *Phys. Rev. A*, vol. 65, p. 062706, 2002. 6, 15, 52, 72, 84

[110] H. Cederquist, L. H. Anderson, A. Barany, P. Hvelplund, H. Knudsen, E. H. Nielsen, J. O. K. Pedersen, and J. Sorensen, "State-selective single- and double-electron capture processes in slow C^{4+}+He, Ne, Ar and Xe collisions," *J. Phys. B*, vol. 18, no. 19, pp. 3951–3969, 1985. 6

[111] A. Niehaus, "A classical model for multiple-electron capture in slow collisions of highly charged ions with atoms," *J. Phys. B*, vol. 19, pp. 2925–2937, 1986. 6

[112] I. Hoffmann, E. Jaäger, and U. Müller-Jahreis, "Z1-dependence of electronic energy straggling of light ions," *Radiation Effects*, vol. 31, no. 1, pp. 57–57, 1976. 7

[113] J. Rozet, C. Stéphan, and D. Vernhet, "ETACHA: a program for calculating charge states at GANIL energies," *Nucl. Instrum. Methods Phys. Res. Sect. B*, vol. 107, no. 1-4, pp. 67 – 70, 1996. 7

[114] A. Itoh, D. Schneider, T. Schneider, T. J. M. Zouros, G. Nolte, G. Schiwietz, W. Zeitz, and N. Stolterfoht, "Selective production of Li, Be and, B-like K vacancy states in fast Ne projectiles studied by zero-degree Auger spectroscopy," *Phys. Rev. A*, vol. 31, p. 684, 1985. 7, 8, 9, 66

[115] B. Johnson, D. Schneider, K. Roberts, J. Bolger, and C. Moore, "High resolution beam gas Auger electron spectra for oxygen ions excited by collisions with He, Ne, and Ar," *Physics Letters A*, vol. 53, no. 3, pp. 254 – 256, 1975. 7

[116] P. Dahl, M. Rødbrø, B. Fastrup, and M. E. Rudd, "Auger spectroscopy on heavy-ion–atom collisions i. kinematic effects and apparatus," *J. Phys. B*, vol. 9, pp. 1567–1579, 1976. 7

[117] P. Dahl, M. Rodbro, G. Hermann, B. Fastrup, and M. E. Rudd, "Auger spectroscopy on Heavy-ion-atom collisions ii. Na^+, Mg^+, Al^+, P^+, S^+, Cl^+-Ar collisions," *J. Phys. B*, vol. 9, pp. 1581–1599, 1976. 7

[118] G. B. Crooks and M. E. Rudd, "Experimental evidence for the mechanism of charge transfer into continuum states," *Phys. Rev. Lett.*, vol. 25, p. 1599, 1970. 7

[119] M. W. Lucas and K. G. Harrison, "Beam foil Auger spectroscopy," *J. Phys. B*, vol. 5, no. 2, pp. L20–L22, 1972. 7

[120] M. Rødbro, R. Bruch, P. Bisgaard, P. Dahl, and B. Fastrup, "High-resolution Auger spectra of boron excited in 200 keV B^+ single collisions," *J. Phys. B*, vol. 10, no. 13, pp. L483–L487, 1977. 7

[121] M. Rødbro, P. Bisgaard, and R. Bruch, "High-resolution Be Auger spectroscopy using fast Be ion beams excited in single gas collisions," *J. Phys. B*, vol. 10, no. 8, pp. L275–L279, 1977. 7

[122] P. Bisgaard, P. Dahl, B. Fastrup, and W. Mehlhorn, "Excitation of autoionising li i and He states in 20-500 keV li+-He collisions," *J. Phys. B*, vol. 14, no. 12, pp. 2023–2036, 1981. 7

[123] E. P. Benis, S. Doukas, T. J. M. Zouros, P. Indelicato, F. Parente, C. Martins, J. P. Santos, and J. P. Marques, "Evaluation of the effective solid angle of a hemispherical deflector analyser with injection lens for metastable Auger projectile states," *Nucl. Instrum. Methods Phys. Res. Sect. B*, vol. 365, pp. 457 – 461, 2015. 8, 9, 20, 65, 66, 69, 70, 85, 127, 128, 130, 131

[124] R. Morgenstern and A. N. U. Thielmann, "Quantum beats in quasimolecular electron emission," *Phys. Rev. Lett.*, vol. 37, no. 4, pp. 199–202, 1976. 8

[125] R. Morgenstern, A. Niehaus, and G. Zimmermann, "Autoionising states formed by electron capture in collisions of multiply charged Ne ions with He, H_2 and Xe," *J. Phys. B*, vol. 13, no. 24, pp. 4811–4831, 1980. 8

[126] A. Itoh, T. Schneider, G. Schiwietz, Z. Roller, H. Platten, G. Nolte, D. Schneider, and N. Stolterfoht, "Selective production of Auger electrons from fast projectile ions studied by zero-degree Auger spectroscopy," *J. Phys. B*, vol. 16, pp. 3965–3971, nov 1983. 8, 9

[127] J. C. Helmer and N. H. Weichert, "Enhancement of sensitivity in esca spectrometers," *Applied Physics Letters*, vol. 13, no. 8, pp. 266–268, 1968. 8

[128] J. A. Tanis, S. M. Shafroth, J. E. Willis, M. Clark, J. Swenson, E. N. Strait, and J. R. Mowat, "Simultaneous electron capture and excitation in S+Ar collisions," *Phys. Rev. Lett.*, vol. 47, p. 828, 1981. 8, 93

[129] J. A. Tanis, E. M. Bernstein, W. G. Graham, M. Clark, S. M. Shafroth, B. M. Johnson, K. W. Jones, and M. Meron, "Resonant behavior in the projectile X-ray yield associated with electron capture in S+Ar collisions," *Phys. Rev. Lett.*, vol. 49, p. 1325, 1982. 8, 19, 93

[130] D. Brandt, "Resonant Transfer and Excitation in ion-atom collisions," *Phys. Rev. A*, vol. 27, pp. 1314–1318, 1983. 8, 19, 93, 94, 101

[131] D. Brandt, "A simple classical model for the impact parameter dependence of electron capture," *Nucl. Instrum. Methods*, vol. 214, p. 93, 1983. 8, 19, 93

[132] J. M. Feagin, J. S. Briggs, and T. M. Reeves, "Simultaneous charge transfer and excitation," *J. Phys. B*, vol. 17, pp. 1057–1068, 1984. 8

[133] A. Itoh, T. J. M. Zouros, D. Schneider, U. Stettner, W. Zeitz, and N. Stolterfoht, "Transfer-Excitation in He$^+$+He collisions studied by zero-degree electron spectroscopy," *J. Phys. B*, vol. 18, pp. 4581–4587, 1985. 8, 71

[134] J. K. Swenson, Y. Yamazaki, P. D. Miller, H. F. Krause, P. F. Dittner, P. L. Pepmiller, S. Datz, and N. Stolterfoht, "Observation of Resonant Transfer and Excitation to specific LS-coupled states in O^{5+} + He collisions by high-resolution, $0°$ Auger-electron spectroscopy," *Phys. Rev. Lett.*, vol. 57, pp. 3042–3045, 1986. 8, 19

[135] N. Stolterfoht, "Techniques of high resolution Auger electron and x-ray spectroscopy in energetic ion atom collisions," in *Fundamental Processes in Energetic Atomic Collisions* (H. O. Lutz, J. S. Briggs, and H. Kleinpoppen, eds.), vol. 103, (New York), pp. 295–318, NATO Advanced Study Institute Series B: Physics, Plenum Publishing Corporation, 1983. 8

[136] N. Stolterfoht, C. C. Havener, R. A. Phaneuf, J. K. Swenson, S. M. Shafroth, and F. W. Meyer, "Evidence for correlated double-electron capture in low-energy collisions of o^{6+} with He," *Phys. Rev. Lett.*, vol. 57, pp. 74–77, Jul 1986. 8

[137] N. Stolterfoht, P. D. Miller, H. F. Krause, Y. Yamazaki, J. K. Swenson, R. Bruch, P. F. Dittner, P. L. Pepmiller, and S. Datz, "Surgery of fast, highly charged ions studied by zero-degree Auger spectroscopy," *Nucl. Instrum. Methods Phys. Res. Sect. B*, vol. 24/25, pp. 168–172, 1987. 8, 15, 66

[138] D. Schneider, N. Stolterfoht, G. Schiwietz, T. Schneider, W. Zeitz, R. Bruch, and K. T. Chung, "High Rydberg and Auger states in fast ion-atom collisions: zero-degree observations," *Nucl. Instrum. Methods Phys. Res. Sect. B*, vol. 24/25, pp. 173–179, 1987. 8

[139] R. Bruch, N. Stolterfoht, S. Datz, P. D. Miller, P. L. Pepmiller, Y. Yamazaki, H. F. Krause, and J. K. Swenson, "High-resolution KLL Auger spectra of multiply ionized oxygen projectiles studied by zero-degree electron spectroscopy," *Phys. Rev. A*, vol. 35, pp. 4114–4121, 1987. 8

[140] T. J. M. Zouros, D. Schneider, and N. Stolterfoht, "High resolution studies of two-electron processes observed in energetic ion-atoms collisions via zero-degree Auger spectroscopy," *Nucl. Instrum. Methods Phys. Res. Sect. B*, vol. 31, p. 349, 1988. 8

[141] T. J. M. Zouros, D. Schneider, and N. Stolterfoht, "State-selective observation of Resonant and Non-resonant Transfer Excitation in 50-500 keV ^{3}He$^+$ + H$_2$ collisions," *J. Phys. B*, vol. 21, pp. L671–L676, nov 1988. 8, 71

[142] D. H. Lee, T. J. M. Zouros, J. M. Sanders, J. L. Shinpaugh, T. N. Tipping, S. L. Varghese, B. D. DePaola, and P. Richard, "A zero-degree tandem electron spectrometer and Rydberg analyzer for projectile electron studies in ion-atom collisions," *Nucl. Instrum. Methods Phys. Res. Sect. B*, vol. 40/41, p. 1229, 1989. 8

[143] D. H. Lee, P. Richard, T. J. M. Zouros, J. M. Sanders, J. L. Shinpaugh, and H. Hidmi, "Binary encounter electrons observed at zero degrees in collisions of 1-2 MeV/amu H$^+$, C^{6+}, N^{7+}, O^{8+} and F^{9+}," *Phys. Rev. A*, vol. 41, pp. 4816–4823, 1990. 8

[144] D. H. Lee, P. Richard, T. J. M. Zouros, J. M. Sanders, and J. L. Shinpaugh, "State-Selective KLL RTEA measurements for collisions of 0.25-2 MeV/u F^{7+} with H$_2$ and He targets," in *12th Int. Conf. on Atomic Physics: Abstracts of Contributed Papers* (W. E. Baylis, G. W. F. Drake, and J. W. McConkey, eds.), (Ann Arbor, MI), Univ. of Michigan, 1990. 8, 72

[145] D. H. Lee, P. Richard, J. M. Sanders, T. J. M. Zouros, J. L. Shinpaugh, and S. L. Varghese, "Electron capture and excitation studied by state-resolved KLL Auger measurement in 0.25-2 MeV/u F$^{7+}(1s^2\,^1$S$, 1s2s\,^3$S$)$ + H$_2$/He collisions," *Nucl. Instrum. Methods Phys. Res. Sect. B*, vol. 56/57, pp. 99–103, 1991. 8, 10, 11, 19

[146] D. H. Lee, P. Richard, J. M. Sanders, T. J. M. Zouros, J. L. Shinpaugh, and S. L. Varghese, "KLL resonant transfer and excitation to F$^{6+}(1s2l2l')$ intermediate states," *Phys. Rev. A*, vol. 44, pp. 1636–1643, 1991. 8, 10, 11, 97, 98

[147] D. H. Lee, T. J. M. Zouros, J. M. Sanders, P. Richard, J. M. Anthony, Y. D. Wang, and J. H. McGuire, "K-shell ionization of O^{4+} and C^{2+} ions in fast collisions with H$_2$ and He gas targets," *Phys. Rev. A*, vol. 46, pp. 1374–1387, Aug 1992. 8, 66, 67, 85, 131

[148] N. Stolterfoht, "Zero-degree Auger spectroscopy in energetic, highly charged ion–atom collisions," *J. Electron Spectrosc. and Relat. Phenom.*, vol. 67, p. 309, 1994. 8

[149] T. J. M. Zouros, D. H. Lee, J. M. Sanders, J. L. Shinpaugh, T. N. Tipping, S. L. Varghese, and P. Richard, "High resolution studies of electron capture and excitation by 0° projectile electron spectroscopy," *Nucl. Instrum. Methods Phys. Res. Sect. B*, vol. 40/41, p. 17, 1989. 8

[150] T. J. M. Zouros, C. P. Bhalla, D. H. Lee, and P. Richard, "Effects of alignment and interference in resonant transfer and excitation for F^{6+} and O^{5+} collisions with H$_2$ in 0° Auger measurements," *Phys. Rev. A*, vol. 42, pp. 678–681, Jul 1990. 8

[151] M. O. Krause, "Atomic radiative and radiationless yields for K and L shells," *J. Phys. Chem. Ref. Data*, vol. 8, p. 307, 1979. 9

[152] D. Charalambidis, R. Brenn, and K. J. Koulen, "Transition rates of $1s2s2p\,^4$P^o_J states of Li-like ions (Z $= 8, 7, 6$)," *Phys. Rev. A*, vol. 40, pp. 2359–2364, 1989. 9

[153] J. M. Anthony, S. M. Shafroth, M. Benhenni, E. N. Strait, T. J. M. Zouros, L. D. Hendrik, and D. M. Peterson, "Production of doubly core-excited configurations in

C^{4+} projectiles through resonant transfer excitation," *J. de Phys. (Paris)*, vol. 48, pp. C9 301–306, 1987. 9, 10, 22, 23, 90

[154] J. M. Anthony, *Systematics of K-Auger Electron Production by 4-8 MeV Carbon Ions Following Collisions with Gas Targets*. PhD thesis, Univ. of North Carolina, Chapel Hill, 1987. unpublished. 9, 10, 22, 23, 90

[155] D. Schneider, R. Bruch, W. H. E. Schwarz, T. C. Chang, and C. F. Moore, "Identifications of Auger spectra from 2-MeV foil-excited carbon ions," *Phys. Rev. A*, vol. 15, pp. 926–934, 1977. 9, 139, 141

[156] S. Doukas, I. Madesis, A. Dimitriou, A. Laoutaris, T. J. M. Zouros, and E. P. Benis, "Determination of the solid angle and response function of a hemispherical spectrograph with injection lens for Auger electrons emitted from long lived projectile states," *Rev. Sci. Instrum.*, vol. 86, no. 4, p. 043111, 2015. 9, 58, 65, 66, 68, 85, 103, 125, 130, 131

[157] E. P. Benis and T. J. M. Zouros, "Improving the energy resolution of a hemispherical spectrograph using a paracentric entry at a non-zero potential," *Nucl. Instrum. Methods Phys. Res. A*, vol. 440, pp. 462–465, 2000. 9, 36, 37

[158] T. J. M. Zouros and E. P. Benis, "The hemispherical deflector analyser revisited. I. motion in the ideal $1/r$ potential, generalized entry conditions, Kepler orbits and spectrometer basic equation," *J. Electron Spectrosc. and Relat. Phenom.*, vol. 125, pp. 221–248, 2002. 9, 37

[159] E. P. Benis and T. J. M. Zouros, "The hemispherical deflector analyser revisited. II. Electron-optical properties," *J. Electron Spectrosc. and Relat. Phenom.*, vol. 163, pp. 28–39, 2008. 9, 37, 38, 39

[160] E. P. Benis, K. Zaharakis, M. M. Voultsidou, T. J. M. Zouros, M. Stöckli, P. Richard, and S. Hagmann, "A new hemispherical analyser with *2-D PSD* and focusing lens for use in $0°$ electron spectroscopy," *Nucl. Instrum. Methods Phys. Res. B*, vol. 146, pp. 120–5, 1998. 9, 36, 37

[161] E. P. Benis, T. J. M. Zouros, and P. Richard, "High resolution RTE measurements at zero degrees using a Hemispherical analyser with lens and 2-D PSD," *Nucl. Instrum. Methods Phys. Res. Sect. B*, vol. 154, pp. 276–280, 1999. 9

[162] E. P. Benis, T. J. M. Zouros, H. Aliabadi, and P. Richard, "Hemispherical analyser with 2-D PSD for zero-degree Auger projectile spectroscopy," *Phys. Scr.*, vol. T80B, pp. 529–31, 1999. 9

[163] R. Mann, F. Folkmann, and H. F. Beyer, "Selective electron capture into highly stripped Ne and N target atoms after heavy-ion impact," *J. Phys. B*, vol. 14, pp. 1161–1181, Apr 1981. 9

[164] P. D. Dumont, H. P. Garnir, Y. Baudinet-Robinet, and K. T. Chung, "Quartet system of C IV," *Phys. Rev. A*, vol. 32, pp. 229–236, Jul 1985. 10, 20, 21

[165] E. P. Benis, T. J. M. Zouros, T. W. Gorczyca, A. D. González, and P. Richard, "Elastic resonant and nonresonant differential scattering of quasifree electrons from B^{4+}(1s) and B^{3+}(1s^2) ions," *Phys. Rev. A*, vol. 69, p. 052718, 2004. 10, 22, 73

[166] E. P. Benis, *A novel high-efficiency paracentric hemispherical spectrograph for zero-degree Auger projectile spectroscopy.* Ph.D. dissertation, Dept. of Physics, University of Crete, 2001. (unpublished). 11, 29, 33, 37, 52, 59, 60, 61, 62, 63, 64, 65, 93, 94, 96, 101, 103, 118

[167] T. J. M. Zouros, S. Nikolaou, I. Madesis, A. Laoutaris, S. Nanos, A. Dubois, and E. P. Benis, "Radiative cascade repopulation of $1s2s2p\,^4$P states formed by single electron capture in 2-18 Mev collisions of $C^{4+}(1s2s\,^3$S) with He," *Atoms*, vol. 8, no. 3, 2020. 12, 25

[168] E. P. Benis and T. J. M. Zouros, "Determination of the $1s2\ell2\ell'$ state production ratios ^{4}P^o/^{2}P, ^{2}D/^{2}P and ^{2}P$_+$/^{2}P$_-$ from fast ($1s^2$, $1s2s\,^3$S) mixed-state He-like ion beams in collisions with H_2 targets," *J. Phys. B*, vol. 49, no. 23, p. 235202, 2016. 13, 57, 72, 73, 74, 76, 79, 84, 86, 107

[169] R. Hutton, N. Reistad, L. Engström, and S. Huldt, "Transition probabilities for the $1s^2\,^1$S$_0$-$1s2p\,^3$P$_1$ intercombination line in He-like carbon and nitrogen," *Phys. Scr.*, vol. 31, pp. 506–508, jun 1985. 16

[170] T. J. M. Zouros, D. H. Lee, P. Richard, J. M. Sanders, J. L. Shinpaugh, S. L. Varghese, K. R. Karim, and C. P. Bhalla, "State-selective observation of Resonance Transfer-Excitation (RTE) in collisions of F^{6+} with He and H_2 targets," *Phys. Rev. A*, vol. 40, p. 6246, 1989. 16, 19, 71

[171] T. J. M. Zouros, "Projectile-electron - target-electron interactions: Exposing the dynamic role of electrons in fast ion-atom collisions," *Comm. At. Mol. Phys.*, vol. 32, pp. 291–313, 1996. 16, 19, 94

[172] I. Mančev, N. Milojević, and D. Belkić, "State-selective and total single-capture cross sections for fast collisions of multiply charged ions with helium atoms," *Few-Body Systems*, vol. 54, pp. 1889–1900, Nov 2013. 17, 18, 25, 27

[173] I. Sakho and A. Wagué, "Energies for the ground-state and for the $ns(1s^2ns)^2$S^e, $np(1s^2np)^2$P^o, $(1sns^2)^2$S^e, $(1s2sns)^2$S^e, and $(1s2snp)^2$P^o excited states of Li-like ions," *Chinese Journal of Physics*, vol. 48, no. 5, pp. 567–591, 2010. 17, 136

[174] J. Burgdörfer, "Final-state angular momentum distributions in charge transfer collisions at high energies," *Nucl. Instrum. Methods Phys. Res. Sect. A*, vol. 240, no. 3, pp. 519 – 526, 1985. 18

[175] D. Belkić, "Electron transfer from hydrogenlike atoms to partially and completely stripped projectiles: CDW approximation," *Physica Scripta*, vol. 43, pp. 561–571, jun 1991. 17, 27

[176] M. Druetta, S. Martin, and J. Desesquelles, "VUV spectroscopy of charge exchange processes in collisions of multiply charged ions," *Nucl. Instrum. Methods Phys. Res. Sect. B*, vol. 23, no. 1, pp. 268 – 273, 1987. 17

[177] J. Newcomb, T. R. Dillingham, J. Hall, S. L. Varghese, P. L. Pepmiller, and P. Richard, "Electron capture by metastable projectiles on He and Ne," *Phys. Rev. A*, vol. 29, pp. 82–91, 1984. 18

[178] V. P. Shevelko, O. Rosmej, H. Tawara, and I. Y. Tolstikhina, "The target-density effect in electron-capture processes," *Journal of Physics B: Atomic, Molecular and Optical Physics*, vol. 37, pp. 201–213, dec 2003. 18

[179] J. Tanis, "Interactions involving two electrons in ion-atom collisions," *Nucl. Instrum. Methods Phys. Res. Sect. B*, vol. 40-41, pp. 70 – 76, 1989. 19

[180] T. J. M. Zouros, "Resonant Transfer and Excitation associated with Auger electron emission," in *Recombination of Atomic Ions* (W. G. Graham, W. Fritsch, Y. Hahn, and J. Tanis, eds.), vol. 296, (New York), pp. 271–300, NATO Advanced Study Institute Series B: Physics, Plenum Publishing Corporation, October 6-9, 1991 1992. 19, 25, 72, 89

[181] T. J. M. Zouros and D. H. Lee, "Zero degree Auger electron spectroscopy of projectile ions," in *Accelerator-Based Atomic Physics: Techniques and Applications* (S. M. Shafroth and J. C. Austin, eds.), ch. 13, pp. 426–479, Woodbury, NY: AIP, 1997. 19, 20, 39, 58, 65

[182] M. Schulz, R. Schuch, S. Datz, E. L. B. Justiniano, P. D. Miller, and H. Schöne, "Resonant Transfer and Excitation in Li-like F colliding with H_2," *Phys. Rev. A*, vol. 38, pp. 5454–5457, Nov 1988. 19

[183] M. Schulz, J. P. Giese, J. K. Swenson, S. Datz, P. F. Dittner, H. F. Krause, H. Schöne, C. R. Vane, M. Benhenni, and S. M. Shafroth, "Electron-electron interactions in transfer and excitation in F^{8+} →H_2 collisions," *Phys. Rev. Lett.*, vol. 62, pp. 1738–1741, Apr 1989. 19

[184] P. L. Pepmiller, P. Richard, J. Newcomb, J. Hall, and T. R. Dillingham, "Formation of doubly excited two-electron ions during F^{8+}+He, F^{8+}+Ne, and F^{8+}+Ar collisions," *Phys. Rev. A*, vol. 31, pp. 734–743, Feb 1985. 19

[185] E. Holøien and J. Midtdal, "On a metastable energy state of the negative helium ion," *Proceedings of the Physical Society. Section A*, vol. 68, pp. 815–823, sep 1955. 20

[186] E. Holoien and S. Geltman, "Variational calculations for quartet states of three-electron atomic systems," *Phys. Rev.*, vol. 153, pp. 81–86, 1967. 20

[187] P. Feldman and R. Novik, "Auto-ionizing states in the alkali atoms with microsecond lifetimes," *Phys. Rev.*, vol. 160, pp. 143–158, 1967. 20, 135

[188] J. D. Garcia and J. E. Mack, "Doubly excited states in lithium," *Phys. Rev.*, vol. 138, pp. A987–A991, 1965. 20

[189] B. F. Davis and K. T. Chung, "Spin-induced autoinization and radiative transition rates for the $(1s2s2p)\,^4P_j^o$ states in lithiumlike ions," *Phys. Rev. A*, vol. 39, pp. 3942–3955, 1989. 20

[190] E. P. Benis, I. Madesis, A. Laoutaris, S. Nikolaou, A. Dubois, T. W. Gorczyca, and T. J. M. Zouros, "Population of the $1s2s(^3S)nl\,^2L$ states in collisions of mixed-state ($1s^2\,^1S$, $1s2s\,^3S$) B^{3+} and C^{4+} ion beams with He/H_2 targets," *X-Ray Spectrom.*, vol. 49, no. 1, pp. 54–59, 2020. 20, 84, 85

[191] D. Schneider, R. Bruch, W. Butscher, and W. H. E. Schwarz, "Prompt and time-delayed electron decay-in-flight spectra of gas-excited carbon ions," *Phys. Rev. A*, vol. 24, pp. 1223–1236, Sep 1981. 20, 65, 66, 125, 139, 141

[192] W. S. Bickel, I. Bergström, R. Buchta, L. Lundin, and I. Martinson, "Mean lives of some doubly excited levels in Lithium I," *Phys. Rev.*, vol. 178, pp. 118–122, Feb 1969. 20

[193] S. Bliman and M. Cornille, "Spectroscopic studies of metastable ion-atom collisions: an overview of doubly excited systems," *Nucl. Instrum. Methods Phys. Res. Sect. B*, vol. 87, no. 1, pp. 51 – 57, 1994. 22

[194] J. A. Tanis, J. Y. Chesnel, F. Fremont, D. Hennecart, X. Husson, D. Lecler, A. Cassimi, J. P. Grandin, J. Rangama, B. Skogvall, B. Sulik, J. H. Bremer, and N. Stolterfoht, "One- and two-K-shell vacancy production in atomic li by 95-MeV/u Ar^{18+} projectiles," *Phys. Rev. A*, vol. 62, pp. 032715–1–10, 2000. 22

[195] M. Zapukhlyak, T. Kirchner, H. J. Lüdde, S. Knoop, R. Morgenstern, and R. Hoekstra, "Inner- and outer-shell electron dynamics in proton collisions with sodium atoms," *J. Phys. B*, vol. 38, pp. 2353–2369, jun 2005. 23

[196] L. J. Curtis, "A diagrammatic mnemonic for calculation of cascading level populations," *American J. Phys.*, vol. 36, pp. 1123–1125, 1968. 24

[197] R. D. Cowan, *The Theory of Atomic structure and spectra.* Berkeley, CA: University of California Press, 1981. 25, 82

[198] Oerlikon Leybold Vacuum GmbH, Bonner Str. 498, 50968 Köln, Germany, *Leybold ITR90 Gauge Specs Data Sheet*, January 2008. 30, 31, 33

[199] Oerlikon Leybold Vacuum GmbH, Bonner Str. 498, 50968 Köln, Germany, *Operating Instructions GA05118 1502*, December 2006. 32, 33

[200] Oerlikon Leybold Vacuum GmbH, Bonner Str. 498, 50968 Köln, Germany, *Leybold SC 5D, SC 15D, SC 30D, Dry Scroll Vacuum Pump*, December 2004. 32

[201] Oerlikon Leybold Vacuum GmbH, Bonner Str. 498, 50968 Köln, Germany, *TURBO-VAC SL 80, Wide-Range Turbomolecular Pump with Integrated or External Frequency Converter*, September 2009. 32

[202] D. H. Lee, *Electron-electron interactions in ion-atom collisions studied by projectile state-resolved Auger electron spectroscopy.* Ph.D. dissertation, Kansas State University, 1990. (unpublished). 33, 72

[203] MKS Instruments Inc., Six Shattuck Road Andover, MA 01810-2449, *Type: 390/590 Absolute 398 Differential High Accuracy Pressure Transducers*, June 1990. 34, 63

[204] MKS Instruments Inc., Six Shattuck Road Andover, MA 01810-2449, *MKS Type 248A/B/C Control Valve*, August 2006. 34

[205] MKS Instruments Inc., Six Shattuck Road Andover, MA 01810-2449, *MKS Type 250E Pressure/Flow Controller*, February 1997. 34

[206] MKS Instruments Inc., Six Shattuck Road Andover, MA 01810-2449, *MKS Type 270D High Accuracy Signal Conditioner*, November 1998. 34

[207] I. Madesis, A. Laoutaris, S. Doukas, A. Dimitriou, E. P. Benis, and T. J. M. Zouros, "Separation and solid angle correction of the metastable $1s2s2p\,^4$P Auger yield produced in ion-atom collisions using the biased gas cell technique: A tool for the determination of the population mechanisms," *J. Phys: Conf. Ser.*, vol. 635, no. 5, p. 052082, 2015. 35

[208] T. J. M. Zouros, O. Sise, M. Ulu, and M. Doğan, "Using the fringing fields of a hemispherical spectrograph to improve its energy resolution," *Meas. Sci. Technol.*, vol. 17, pp. N81–N86, 2006. 36

[209] O. Sise, T. J. M. Zouros, M. Ulu, and M. Dogan, "Novel and traditional fringing field correction schemes for the hemispherical analyzer: Comparison of 1rst order focusing and energy resolution," *Meas. Sci. Technol.*, vol. 18, pp. 1853–1858, 2007. 36

[210] A. Laoutaris, I. Madesis, A. Dimitriou, A. Lagoyannis, M. Axiotis, E. P. Benis, and T. J. M. Zouros, "Use of gas and foil strippers for the production of He-like ionic beams in both pure ground state ($1s^2$) and mixed states ($1s^2, 1s2s$) for zero-degree Auger projectile electron spectroscopy," *J. Phys: Conf. Ser.*, vol. 635, no. 5, p. 052062, 2015. 37

[211] Precision eForming, 839 NYS Route 13, Cortland, NY 13045 USA, *Precision Electroformed Mesh Product Catalog*, August 2006. 37, 123

[212] T. J. M. Zouros, E. P. Benis, and J. E. Schauer, "Charged particle trajectories in an ideal paracentric hemispherical deflection analyser," in *Application of Accelerators in Research and Industry* (J. L. Duggan and I. L. Morgan, eds.), vol. 576, (New York), pp. 76–79, American Institute of Physics, AIP Conference Proceedings, November 1-5 2001. 37

[213] T. J. M. Zouros and E. P. Benis, "Erratum to *The hemispherical deflector analyser revisited. I. Motion in the ideal $1/r$ potential, generalized entry conditions, Kepler orbits and spectrometer basic equation [J. Electron. Spectrosc. Relat. Phenom. **125**(2002)221]*," *J. Electron Spectrosc. and Relat. Phenom.*, vol. 142, pp. 175–176, 2005. 37

[214] T. J. M. Zouros and E. P. Benis, "Optimal energy resolution of a hemispherical analyzer with virtual entry," *Appl. Phys. Lett.*, vol. 86, p. 094105, 2005. 37, 40, 64

[215] M. Dogan, M. Ulu, G. G. Gennarakis, and T. J. M. Zouros, "Experimental energy resolution of a paracentric hemispherical deflector analyzer for different entry positions and bias," *Rev. Sci. Instrum.*, vol. 84, no. 4, p. 043105, 2013. 37, 38

[216] T. J. M. Zouros, A. Kanellakopoulos, I. Madesis, A. Dimitriou, M. Fernández-Martín, G. Martinez, and T. J. Mertzimekis, "The optimization of a 4-element input lens on a hemispherical deflector analyzer using SIMION," *Microscopy and Microanalysis*, vol. 21, pp. 148–153, 6 2015. 37, 38, 39, 71

[217] O. Sise and T. J. M. Zouros, "Position, energy, and transit time distributions in a hemispherical deflector analyzer with position sensitive detector," *Journal of Spectroscopy*, vol. 2015, no. 153513, p. 20, 2015. 37

[218] F. Hadjarab and J. L. Erskine, "Image properties of the hemispherical analyzer applied to multichannel energy detection," *J. Electron Spectrosc. and Relat. Phenom.*, vol. 36, p. 227, 1985. 39

[219] G. Martínez, M. Fernández-Martín, O. Sise, I. Madesis, A. Dimitriou, A. Laoutaris, and T. Zouros, "Voltage optimization of a 4-element injection lens on a hemispherical spectrograph with virtual entry aperture," *Nucl. Instrum. Methods Phys. Res. B*, vol. 369, no. 92, pp. 19–31, 2015. 39

[220] O. Sise, G. Martinez, I. Madesis, A. Laoutaris, A. Dimitriou, M. Fernandez-Martin, and T. J. M. Zouros, "The voltage optimization of a four-element lens used on a hemispherical spectrograph with virtual entry for highest energy resolution," *J. Electron Spectrosc. and Relat. Phenom.*, vol. 211, pp. 19 – 31, 2016. 39, 40, 41, 42, 43, 44, 103, 128

[221] I. Madesis, A. Dimitriou, A. Laoutaris, A. Lagoyannis, M. Axiotis, T. Mertzimekis, M. Andrianis, S. Harissopulos, E. P. Benis, B. Sulik, I. Valastyán, and T. J. M. Zouros, "Atomic Physics with Accelerators: Projectile Electron Spectroscopy (APAPES)," *J. Phys: Conf. Ser.*, vol. 583, p. 012014, 2015. 39, 103, 104

[222] http://www.simion.com 41, 43, 44

[223] Quantar Technology, 2620A Mission Street Santa Cruz, CA 95060, *3300/2400 Series System Installation and Operation Manual*, November 2012. 42

[224] J. L. Wiza, "Microchannel plate detectors," *Nucl. Instrum. & Methods*, vol. 162, pp. 587–601, 1979. 43

[225] Hahn-Meitner-Institut, Helmholtz-Zentrum Berlin für Materialien und Energie Hahn-Meitner-Platz 1 (formerly Glienicker Str. 100), 14109 Berlin, *HV-Versorgung N 97*, May 1979. 45

[226] Tennelec, Inc, 107 Union Valley Rd, Oak Ridge, TN, *Instruction Manual - TC 952 High Voltage Power Supply*, September 1983. 45

[227] Applied KiloVolts, Woods Way, Goring by Sea, BN12 4QY. United Kingdom, *HPZ Series Data Sheet*, May 2012. 46

[228] Applied KiloVolts, Woods Way, Goring by Sea, BN12 4QY. United Kingdom, *LS Series Data Sheet*, May 2012. 46

[229] M. Lampton and C. W. Carlson, "Low-distortion resistive anodes for two-dimensional position-sensitive MCP systems," *Rev. Sci. Instrum.*, vol. 50, no. 9, pp. 1093–1097, 1979. 49

[230] I. Valastyán, *CSPA Charge Sensitive Preamplifier and DSP module*. Precision eForming, Insitute for Nuclear Research, July 2014. 49, 50

[231] N. Instruments, *NI USB-621x User Manual*. National Instruments Corporation, 11500 North Mopac Expressway Austin, Texas 78759-3504 USA, April 2009. 50

[232] M. Zamkov, H. Aliabadi, E. P. Benis, P. Richard, H. Tawara, and T. J. M. Zouros, "Energy dependence of the metastable fraction in $B^{3+}(1s^2\,^1S, 1s2s\,^3S)$ beams produced in collisions with thin-foil and gas targets," *Phys. Rev. A*, vol. 64, p. 052702, 2001. 52

[233] M. Zamkov, H. Aliabadi, E. P. Benis, P. Richard, H. Tawara, and T. J. M. Zouros, "Stripping energy dependence of $B^{3+}(1s2s\,^3S)$ beam metastable fraction," *AIP*, vol. 576, pp. 149–52, 2001. 52

[234] A. M. Imai, M. Sataka, M. Matsuda, S. Okayasu, K. Kawatsura, K. Takahiro, K. Komaki, H. Shibata, and K. Nishio, "Quasi-equilibrium in charge-state evolution for carbon, sulfur, and tungsten ions after passing through carbon foils," *Journal of Physics: Conference Series*, vol. 635, no. 2, p. 022040, 2015. 53

[235] R. Bruch, K. T. Chung, W. L. Luken, and J. C. Culberson, "Recalibration of the KLL Auger spectrum of carbon," *Phys. Rev. A*, vol. 31, pp. 310–315, 1985. 61, 67, 84, 139, 142

[236] H. I. Hidmi, P. Richard, and I. Ben-Itzhak, "Energy calibration of an accelerator using cusp electron spectroscopy," *Nucl. Instrum. Methods Phys. Res. Sect. B*, vol. 88, pp. 313–316, 1994. 62

[237] C. W. Woods, R. L. Kauffman, K. A. Jamison, N. Stolterfoht, and P. Richard, "K-shell Auger-electron production cross sections from ion bombardment," *Phys. Rev. A*, vol. 13, pp. 1358–1369, Apr 1976. 64, 65

[238] M. H. Chen, B. Crasemann, and H. Mark, "Deexcitation of light Li-like ions in the $1s2s2p$ state," *Phys. Rev. A*, vol. 27, pp. 544–547, Jan 1983. 65, 66, 67, 69, 70, 131

[239] B. F. Davis and K. T. Chung, "Complex-rotation method for spin-induced autoionization," *Phys. Rev. A*, vol. 36, p. 1948, 1987. 65, 125

[240] T. J. M. Zouros, D. H. Lee, and P. Richard, "Projectile 1s→2p Excitation Due to Electron-Electron Interaction in Collisions of O^{5+} and F^{6+} Ions with He and H_2 Targets," *Phys. Rev. Lett.*, vol. 62, pp. 2261–2264, 1989. 65, 125

[241] E. P. Benis, I. Madesis, A. Laoutaris, S. Nanos, and T. J. M. Zouros, "Experimental determination of the effective solid angle of long-lived projectile states in zero-degree Auger projectile spectroscopy," *J. Electron Spectrosc. and Relat. Phenom.*, vol. 222, no. Supplement C, pp. 31 – 39, 2018. 65, 66, 67, 69, 84, 85, 104, 125

[242] G. Tachiev and C. F. Fischer, "Breit-Pauli energy levels, lifetimes, and transition data: beryllium-like spectra," *J. Phys. B*, vol. 32, no. 24, p. 5805, 1999. 66, 68

[243] C. Froese Fischer and G. Tachiev, "Breit-Pauli energy levels, lifetimes, and transition probabilities for the beryllium-like to neon-like sequences," *At. Data & Nucl. Data Tables*, vol. 87, pp. 1–184, May 2004. 66, 68

[244] C. D. Lin and W. R. Johnson, "Oscillator strengths for the beryllium isoelectronic sequence," *Phys. Rev. A*, vol. 15, pp. 1046–1052, Mar 1977. 66

[245] P. Shorer and C. D. Lin, "Magnetic quadrupole transition probabilities for the beryllium isoelectronic sequence," *Phys. Rev. A*, vol. 16, pp. 2068–2071, Nov 1977. 66

[246] E. P. Benis, S. Doukas, and T. J. M. Zouros, "Evidence for the non-statistical population of the $1s2s2p\,^4$P metastable state by electron capture in 4 MeV collisions of $B^{3+}(1s2s\,^3$S) with H_2 targets," *Nucl. Instrum. Methods Phys. Res. Sect. B*, vol. 369, pp. 83 – 86, 2016. 66, 69, 72, 103

[247] M. Wojdyr, "Fɪᴛʏᴋ: a general-purpose peak fitting program," *Journal of Applied Crystallography*, vol. 43, pp. 1126–1128, Oct 2010. 68, 70, 71, 76

[248] A.Dubois, "Preliminary results to be published," 2020. Private communications. 79, 84, 88, 89, 90

[249] D. J. Pole, "Understanding two-electron transitions in atomic collisions." Honors College Thesis, Western Michigan University (unpublished), 2002. 85, 86

[250] D. Strohschein, J. Baran, S. Hossain, and J. A. Tanis, "Investigation of the ^{4}D metastable state in Na-like ions," *Nucl. Instrum. Methods Phys. Res. Sect. B*, vol. 235, pp. 31–35, 2005. 86

[251] M. R. C. McDowell and J. P. Coleman, *Introduction to the Theory of Ion-Atom Collisions*. New York: North-Holland Publishing Co., 1970. 88

[252] M. Zamkov, *Multi-electron Processes In Ion-Atom Collisions*. unpublished, Kansas State University, 2003. 92

[253] I. Fourré and C. Courbin, "Classical trajectory study of orientation and alignment effects for charge exchange processes in H$^+$ - Na*($3p_m$) collisions," *Zeitschrift für Physik D Atoms, Molecules and Clusters*, vol. 38, pp. 103–111, Jun 1996. 92

[254] E. Y. Sidky and H.-J. T. Simonsen, "Velocity-matching model for electron capture in keV atomic collisions," *Phys. Rev. A*, vol. 54, pp. 1417–1429, Aug 1996. 92

[255] I. Y. Tolstikhina and V. P. Shevelko, "Collision processes involving heavy many-electron ions interacting with neutral atoms," *Physics-Uspekhi*, vol. 56, pp. 213–242, mar 2013. 92

[256] B. Friedman and G. DuCharme, "Semi-empirical scaling for ion-atom single charge exchange cross sections in the intermediate velocity regime," *J. Phys. B*, vol. 50, p. 115202, May 2017. 92

[257] K. R. Karim, "Compton profiles of variously ionized carbon atoms with configurations 1s^m 2s^n 2p^q," *Physica Scripta*, vol. 66, no. 3, p. 234, 2002. 92

[258] T. J. M. Zouros, P. Richard, and D. H. Lee, "Z_p and q-dependence of 0° binary encounter electrons in 1-2 MeV/u collisions of ions with H$_2$ and He targets," in *Proceedings of the 4th Workshop on High-Energy Ion-Atom Collision Processes, Debrecen, Hungary* (D. Berényi and G. Hock, eds.), (Berlin), Springer–Verlag, 1991. 97

[259] G. Martínez, M. Fernández-Martín, O. Sise, I. Madesis, A. Dimitriou, A. Laoutaris, and T. Zouros, "Voltage optimization of a 4-element injection lens on a hemispherical spectrograph with virtual entry aperture," *Nucl. Instrum. Methods Phys. Res. B*, vol. 369, pp. 92 – 94, 2016. 103

[260] D. Carey, K. Brown, and F. Rothacker, *Third-order TRANSPORT: A computer program for designing charged particle beam transport systems*. Stanford Linear Accelerator Center, Menlo Park, CA (United States): USDOE, Washington, DC (United States), May 1995. 114

[261] C. Iselin, *Computing in Accelerator Design and Operation: Proceedings of the Europhysics Conference Held at the Hahn-Meitner-Institut für Kernforschung Berlin GmbH Berlin, Germany, September 20–23,1983*, ch. The MAD program, pp. 146–151. Berlin, Heidelberg: Springer Berlin Heidelberg, 1984. 114

[262] Hermann Wollnik, "3 - quadrupole lenses," in *Optics of Charged Particles* (t. Wollnik, ed.), pp. 48 – 88, Cambridge, MA: Academic Press, 1st ed., 1987. 114

[263] J. D. Larson, *Electrostatic Accelerators: Fundamentals and Applications*, ch. Ion Optics and Beam Transport, pp. 278–298. Berlin, Heidelberg: Springer Berlin Heidelberg, 2005. 114

[264] Goldstar/LG Precision, 133, Gongdan Dong, Gumi shi, Gyeongsangbuk, Do 730-030, R.O.K., *OSCILLOSCOPE OS-9000SRS Operation Manual*, 1995. 117

[265] T. J. M. Zouros, G. Toth, C. Liao, E. C. Montenegro, S. Hagmann, P. Richard, S. Grabbe, C. P. Bhalla, and K. L. Wong, "Identification of very low energy projectile autoionizing transitions in high velocity collisions using zero-degree Auger electron spectroscopy," *Nucl. Instrum. Methods Phys. Res. Sect. B*, vol. 99, pp. 27–29, 1995. 129

[266] J. S. Lee, "Accurate determination of H_2, He, and D_2 compton profiles by high energy electron impact spectroscopy," *J. Chem. Phys.*, vol. 66, p. 4906, 1977. 133

[267] W. E. Duncanson and C. A. Coulson, "Theoretical shape of the compton profile for atoms from H to Ne," *Proceedings of the Physical Society*, vol. 57, no. 3, p. 190, 1945. 133

[268] F. Biggs, L. B. Mendelsohn, and J. B. Mann, "Hartree-fock compton profiles for the elements," *Atomic data and nuclear data tables*, vol. 16, no. 3, pp. 201–309, 1975. 133, 134

[269] N. R. Badnell, M. S. Pindzola, and D. C. Griffin, "Dielectronic recombination from the ground and excited states of C^{4+} and O^{6+}," *Phys. Rev. A*, vol. 41, pp. 2422–2428, Mar 1990. 135, 136, 142

[270] R. Garstang, "1 - forbidden transitions," in *Atomic and Molecular Processes* (D. BATES, ed.), vol. 13 of *Pure and Applied Physics*, pp. 1 – 46, Marquis One, 245 Peachtree Center Avenue, Suite 1900, Atlanta, GA 30303, USA: Elsevier, 1962. 137

[271] E. P. Benis, *Lecture notes on Atomic Physics*. Ioannina: University of Ioannina, 2013. 137

[272] R. Mann, "High-resolution K and L Auger electron spectra induced by single- and double-electron capture from h_2, He, and Xe atoms to C^{4+} and C^{5+} ions at 10–100-keV energies," *Phys. Rev. A*, vol. 35, pp. 4988–5004, Jun 1987. 139, 141

[273] U. I. Safronova and R. Bruch, "Triply excited states of the lithium isoelectronic sequence," *Phys. Scr.*, vol. 57, p. 519, 1998. 139, 141

[274] U. I. Safronova and R. Bruch, "Transition and Auger energies of li-like ions (1s2lnl' configurations)," *Phys. Scr.*, vol. 50, no. 1, p. 45, 1994. 139, 141

[275] S. W. J. Scully, A. Aguilar, E. D. Emmons, R. A. Phaneuf, M. Halka, D. Leitner, J. C. Levin, M. S. Lubell, R. Püttner, A. S. Schlachter, A. M. Covington, S. Schippers, A. Müller, and B. M. McLaughlin, "K-shell photoionization of Be-like carbon ions: experiment and theory for C^{2+}," *J. Phys. B*, vol. 38, no. 12, pp. 1967–1975, 2005. 139, 141

[276] H. A. Sakaue, Y. Kanai, K. Ohta, M. Kushima, T. Inaba, S. Ohtani, K. Wakiya, H. Suzuki, T. Takayanagi, T. Kambara, A. Danjo, M. Yoshino, and Y. Awaya, "Autoionization of $C^{4+}(2\ell n\ell')$ measured by electron spectroscopy in collisions of C^{6+} with He," *J. Phys. B*, vol. 23, pp. L401–L405, 1990. 139, 141

[277] J. Gallagher and C. E. Moore, *Tables of spectra of hydrogen, carbon, nitrogen, and oxygen atoms and ions.* CRC press, 1993. 141, 142

Acronyms